Max-Planck-Institut für Meteorologie
Max Planck Institute for Meteorology

Examensarbeit Nr. 88

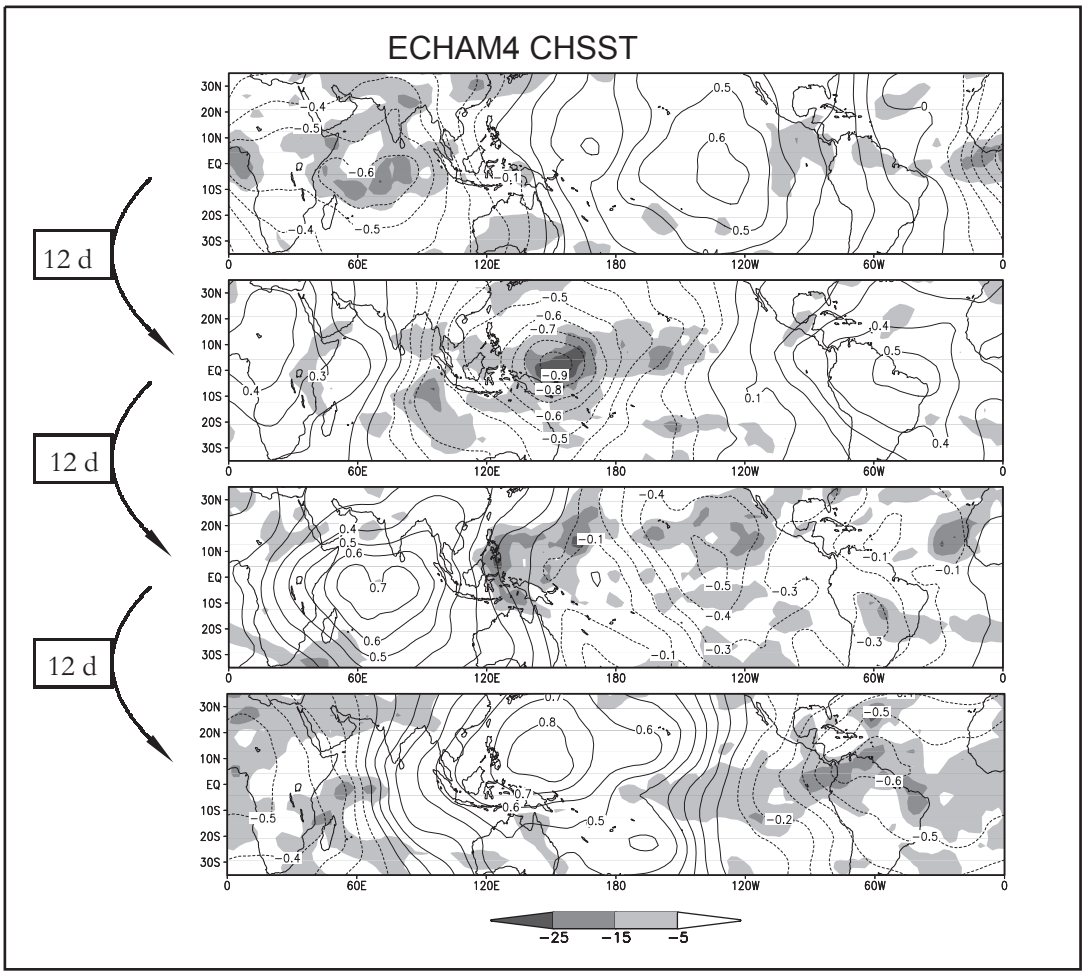

Model Studies of the Tropical 30 to 60 Day Oscillation

(Modelluntersuchungen der tropischen 30 bis 60 Tage Oszillation)

von

Stefan Liess

Hamburg, August 2002

Dissertation zur Erlangung des Doktorgrades

Autor:

Stefan Liess Max-Planck-Institut für Meteorologie

Max-Planck-Institut für Meteorologie
Bundesstrasse 55
D - 20146 Hamburg
Germany

Tel.: +49-(0)40-4 11 73-0
Fax: +49-(0)40-4 11 73-298
e-mail: <name>@dkrz.de
Web: www.mpimet.mpg.de

ISSN 0938-5177

Model Studies of the Tropical 30 to 60 Day Oscillation

(Modelluntersuchungen der tropischen 30 bis 60 Tage Oszillation)

Dissertation zur Erlangung des Doktorgrades
der Naturwissenschaften im Fachbereich
Geowissenschaften
der Universität Hamburg

vorgelegt von
Stefan Liess
aus Neumünster

Hamburg
2002

Als Dissertation angenommen vom Fachbereich Geowissenschaften
der Universität Hamburg

auf Grund der Gutachten von Prof. Dr. L. Bengtsson

und Prof. Dr. H. Graßl

Hamburg, den 3.4.2002

Prof. Dr. U. Bismayer
(Dekan des Fachbereichs Geowissenschaften)

Abstract

The tropical 30-60 day oscillation, also referred to as the intraseasonal oscillation (IO) or Madden-Julian oscillation is an important phenomenon in the tropical atmosphere on the intraseasonal timescale. The dominant characteristic of the IO is the eastward propagation of convection cells that organize themselves to super cloud clusters over the Indian Ocean and the West Pacific. The resulting eastward phase velocity of the super cloud cluster is about 5 m s^{-1}. East of the date line, the super cloud clusters vanish when Sea Surface Temperatures (SSTs) decrease. There, the circulation anomalies of the IO are confined to the upper tropospheric zonal wind and the IO consists of a faster, eastward propagating signal with a phase speed of about 10 m s^{-1}. The correct simulation of the initiation and propagation of the IO in General Circulation Models (GCMs) is important for the representation of convective clouds and the resulting radiation budget and precipitation in the tropical eastern hemisphere. The IO is a possible trigger of the Asian summer monsoon (Lau et al., 1998) and the Australian monsoon (Hendon and Liebmann, 1990a) and affects the position of subtropical jets (Knutson and Weickmann, 1987).

The present study discusses the representation of the IO in observations, reanalyses data and GCM simulations. The Principal Oscillation Pattern (POP) analysis (Hasselmann, 1988; von Storch et al., 1995) of daily 200 hPa velocity potential anomaly of the 5 years 1984 to 1988 is used to investigate the propagation speed, the location and the seasonal and interannual variability of the main IO activity. Case studies are performed to gain a detailed insight into the structure of the IO. The simulations are performed with (1) the fourth version of the European Centre Hamburg Atmospheric Model (ECHAM4; Roeckner et al., 1996a) GCM forced by monthly mean Atmospheric Model Intercomparison Project (AMIP) SSTs to point out the ability and deficiencies of the GCM to represent the IO; (2) the ECHAM4 GCM coupled to the third version of the ocean isopycnal (OPYC3) GCM to clarify possible air-sea interactions and connections of the IO and the El Niño/Southern Oscillation (ENSO) cycle; (3) ECHAM4 with increased vertical resolution and by this improved representation of the tropospheric stratification. To artificially force cooler (warmer) levels in the mid-troposphere and by this a changed stability, the melting rate for convective precipitation is doubled (halved) in two sensitivity studies. Additionally an experiment with suppressed snow melt for all precipitation is performed. (4) The horizontal resolution is increased to investigate the importance of a reasonable land-sea distribution over the maritime continent. (5) To distinguish this effect from general dynamical changes due to the changed resolution, the effects of the land-sea distribution are additionally studied in an experiment with land points associated with the maritime

continent replaced by sea points. (6) The ECHAM4 GCM is forced by a T42 version of the Optimum Interpolated SST (OISST) dataset (Reynolds and Smith, 1994) to study the influence of the SST as a boundary condition.

The main results are as follows: (1) The ECHAM4 T42 standard version simulates a too fast eastward propagation and an eastward shift of the main IO activity, as is common to many atmosphere GCMs (Slingo et al., 1996). (2) The coupled version reveals no improvements, although it is shown that the IO influences the El Niño/Southern Oscillation (ENSO) cycle and ENSO influences the interannual variability of the IO. The latter is depicted with 20 years of daily reanalyses data and 100 years of the coupled integration. (3) The increase in vertical resolution slightly improves the simulation of the vertical moisture profile, and thus slightly slows down the propagation speed of the IO. This result is not confirmed by the studies with artificially changed stability in the mid-troposphere. (4) Increasing the horizontal resolution from T42 to T106 results in a more precise representation of convection over the maritime continent. A consequence is a reduction of the erroneous eastward shift of the simulated IO activity, although the phase speed of the IO is increased. (5) These results are also obtained by replacing the maritime continent with sea points. (6) ECHAM4 forced by a changed SST dataset leads to the strongest improvements: Averaged over the maritime continent, the annual mean AMIP SST is only 0.14 K warmer than observations, but single grid points are more than 0.5 K warmer. Convection driving the IO is highly sensitive to a small reduction in surface temperature with lower level convection leading to a slower IO due to an increased influence of surface friction. ECHAM4 forced by the changed SST, which is only 0.04 K colder over the maritime continent than observations, produces a reasonable IO with a mean period of 48 days and a main IO activity near 140°E, as in the reanalysis. This illustrates the strong influence of the prescribed SST on the simulation of the IO.

Contents

Chapter 1

Introduction

This chapter describes the tropical 30-60 day oscillation and its impacts on tropical and extra-tropical climate. Since the 30-60 day oscillation has a slow evolution relative to synoptic weather systems, its prediction has the potential to improve extended-range weather forecasts.

After a brief review of current theories of the onset and propagation mechanisms of the 30-60 day oscillation, the current status in simulating the 30-60 day oscillation by General Circulation Models (GCMs) is discussed.

1.1 Description of the 30-60 day oscillation

The mean tropical easterlies, known as the trade winds, contribute to high sea surface temperatures (SSTs) in the Indian and western Pacific Oceans, since they cause warm surface water of the tropical Pacific to be transported westward. This body of warm surface water in the western tropical Pacific is known as the West Pacific warm pool (e.g. Wyrtki, 1989). The high SST is responsible for the deep atmospheric convection in this region, which influences synoptic to intraseasonal timescales from 2 to about 60 days. Typically, periodicities between 2 and 10 days are associated with synoptic, westward moving phenomena like the easterly waves, whereas lower frequencies tend to be dominated by periodicities between 30 and 60 days (Slingo et al., 1996). They are referred to as the tropical 30-60 day oscillation or intraseasonal oscillation (IO). The IO is dominated by an eastward propagating equatorial mode with zonal wave number one. Madden and Julian (1971, 1972) were the first in describing this phenomenon, therefore it is also called

the Madden-Julian oscillation. The original time period of the IO was thought to be 40 to 50 days, but numerous studies have broadened the period to cover a range of 30 to 60 days (e.g. Knutson and Weickmann, 1987; Chen and Chen, 1997).

A schematic depiction of the IO by Madden and Julian (1972) is shown in Figure 1.1. It describes the convective activity and the related tropopause height and sea level pressure. The signal in the equatorial zonal wind is present throughout the entire tropical belt in the upper troposphere. In the lower troposphere the IO is mostly confined to the Indian and western Pacific Oceans. The oscillation can be classified into two regimes: (1) In the convective (or active) regime (Figures 1.1F-1.1A), convection cells over the Indian Ocean induce updrafts. The associated diabatic heating due to latent heat release maintains Kelvin and Rossby wave modes (Sperber et al., 1997). Convection cells and updrafts move eastward to the date line with a speed of about 5 m s^{-1} until two equal circulation cells exist with negative sea level pressure anomaly near the date line. (2) In the dry regime (Figures 1.1B-1.1E), the circulation anomalies are confined to the upper tropospheric zonal wind. They take the form of a faster, eastward propagating Kelvin-wave signal with a speed of about 10 m s^{-1} until two equal circulation cells exist with maximum sea level pressure near the date line. In this regime, the sea level pressure anomaly is no longer in phase with the divergence in the upper troposphere.

The substantial modulation of tropical convection by the IO is apparent in satellite-observed Outgoing Longwave Radiation (OLR) data (e.g., Rui and Wang, 1990; Hendon and Salby, 1994; Salby and Hendon, 1994). The IO is best detectable in the upper tropospheric velocity potential field due to its planetary-scale structure (Slingo et al., 1996). Time-longitude Hovmöller diagrams are often used to characterize the general features of the IO. Figure 1.2 shows the IO for the years 1983-1988 in the European Centre for Medium Range Weather Forecasts (ECMWF) analysis upper troposphere velocity potential anomaly. With typical amplitudes of $\pm 6 \times 10^6$ $m^2 s^{-1}$ over the Indian Ocean and the West Pacific warm pool, it represents a substantial modulation of the climatic mean velocity potential field (Slingo et al., 1996).

According to numerical experiments (Lau et al., 1989) and observational studies (Rui and Wang, 1990; Jones and Weare, 1996), upper tropospheric easterlies increase during the passage of the mature phase of the IO. Lower troposphere westerlies have a maximum slightly after the passage, although the low-level convergence leads the convective anomalies in the mature phase of the IO, which is consistent with the influence of the equatorial Rossby waves (Matsuno, 1966; Wheeler et al., 2000). The vertical structure of the IO exhibits a deep baroclinic structure with the vertical node in zonal wind at about

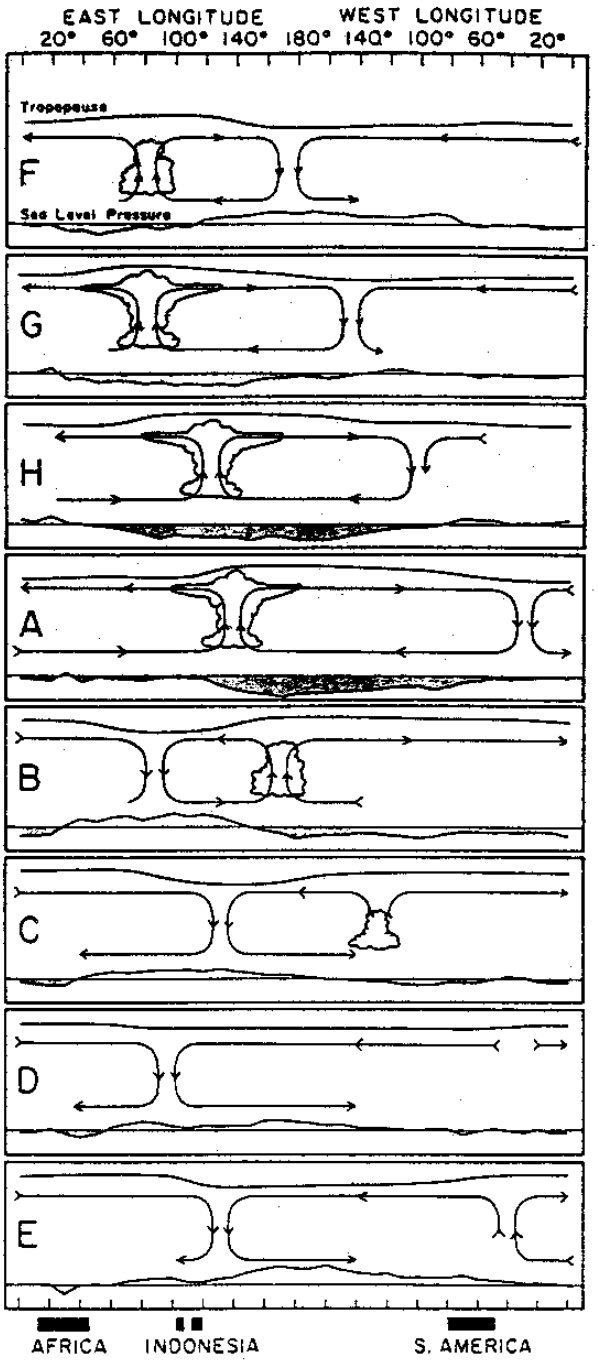

Figure 1.1: *Schematic depiction of the Madden-Julian oscillation. Dates are indicated symbolically by the letters on the left of each chart and correspond to dates associated with surface pressure in Canton Island (2°46'S, 171°43'W). A denotes minimum and E maximum surface pressure (Madden and Julian, 1972).*

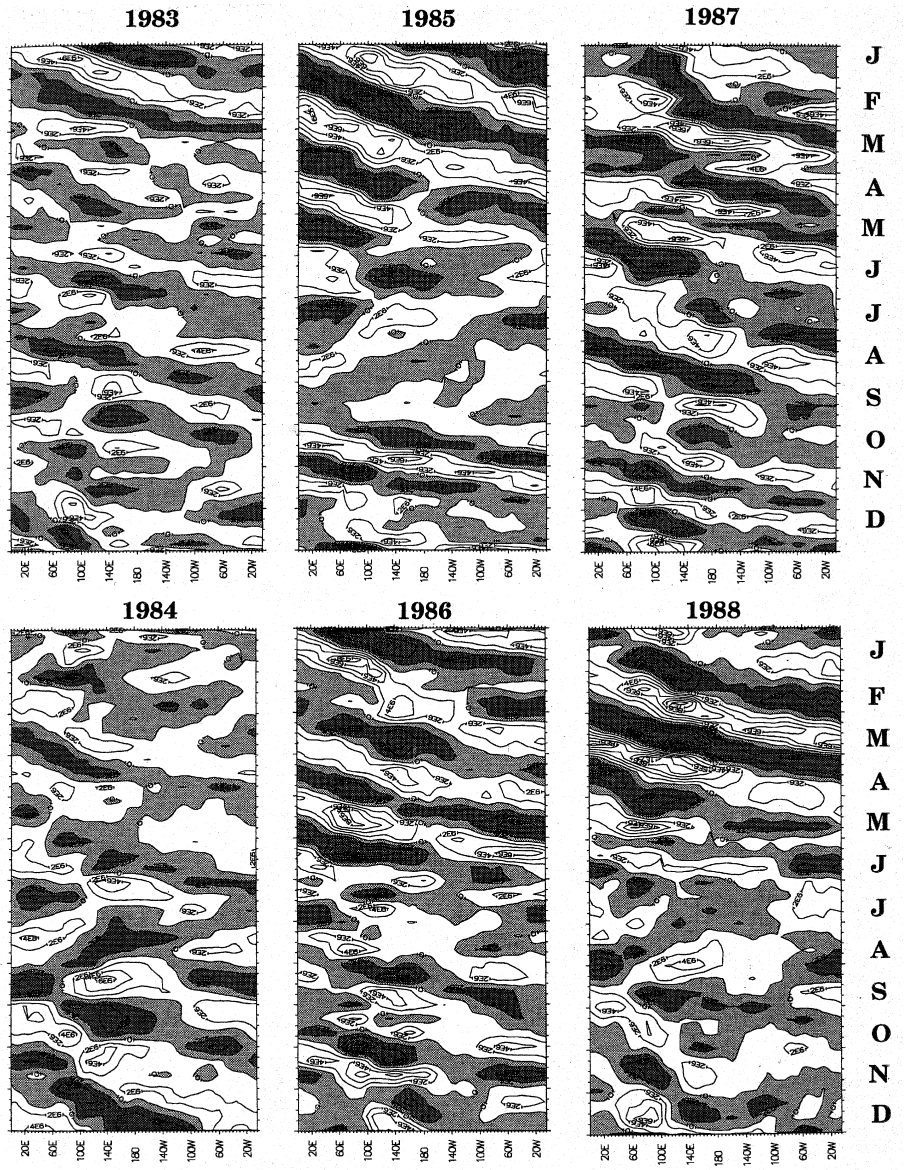

Figure 1.2: *Time-longitude diagrams of the 20-100 day filtered velocity potential anomaly at 150 hPa, averaged between 10°N and 10°S, from ECMWF analyses. The contour interval is* 2×10^6 m^2s^{-1} *and negative values are shaded (Slingo et al., 1996).*

300 hPa (Hendon and Liebmann, 1990b). The vertical tilt of the oscillation appears to systematically change from west to east. Hendon and Liebmann (1990b) revealed a westward tilt with height west of Darwin (12°S 130°E), at Darwin no tilt is observed and east of Darwin the vertical structure of the IO tilts eastward with height.

The IO is influenced by the annual cycle due to its sensitivity to the underlying SST. It is most pronounced in the October through May period, particularly from December onwards (e.g. Wang and Rui, 1990b; Salby and Hendon, 1994), when the SST is highest in the Indian Ocean and the West Pacific warm pool. During boreal summer, strong variance

of the convective activity is exhibited over the Indian Ocean and southeast Asia, but no pronounced eastward propagation is discernible along the equator (e.g. Rui and Wang, 1990). Figure 1.3 shows the time-longitude Hovmöller diagram of equatorial (5°N-5°S) observed Optimum Interpolated SST (OISST, Reynolds and Smith, 1994) in the Indian and Pacific Oceans for the years 1984-1988. The strong diurnal cycle of convection over land in the maritime continent is able to discharge the convective instability over this area (e.g. Rui and Wang, 1990; Salby and Hendon, 1994; Zhang and Hendon, 1997).

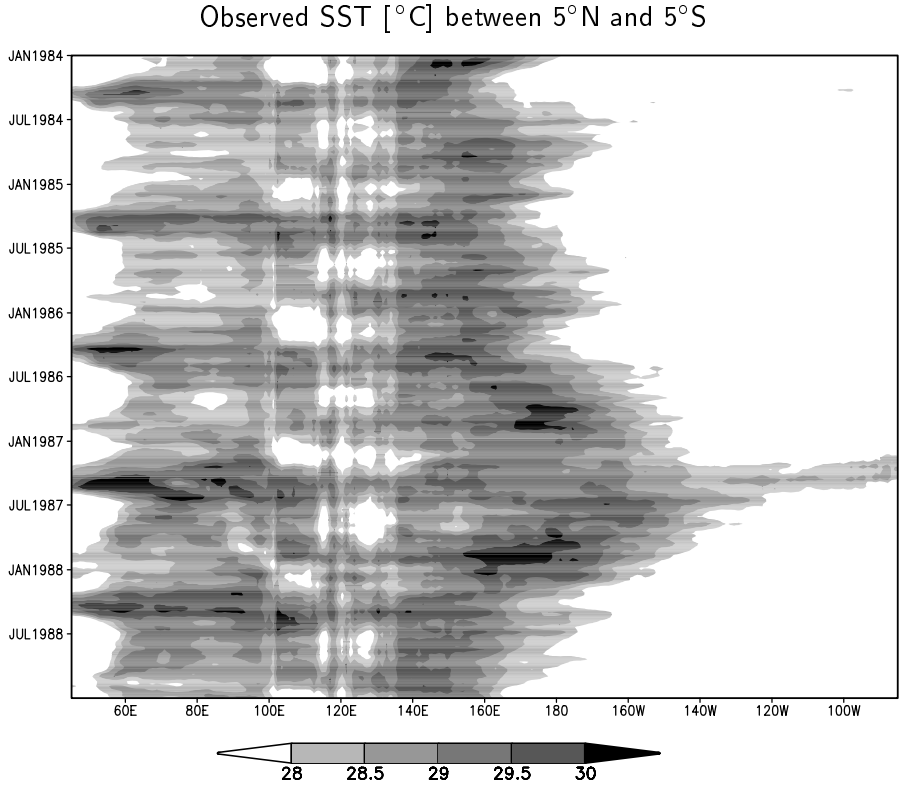

Figure 1.3: *Time-longitude Hovmöller diagram of equatorial (5°N-5°S) OISST [°C] for the years 1984-1988.*

1.2 Interactions with the tropical climate

The IO occurs in the Asian and Australian monsoon regions. Knutson and Weickmann (1987) attributed modulations of the strength of the Somali jet and anomalously clear or "break-monsoon" conditions over India, which appear on 30-60 day timescales, to the IO activity. On the contrary, Wang and Rui (1990b) described the northward propagating clouds of the Indian summer monsoon and the eastward propagating IO mode as generally independent from each other, since the eastward propagation of the IO occurs primarily

during boreal winter. Only during the transition from monsoon type circulation to IO type circulation, there is an interaction, and an east-north mode exists.

Knutson and Weickmann (1987) found statistically significant relations between midlatitude circulation anomalies in the winter hemisphere and the fluctuating tropical convective activity. For example, during northern winter the East Asian jet stream is retracted towards Asia and strong convection is occurring over the equatorial Indian Ocean. During the Australian winter, the jet stream over southern Australia is anomalously strong about 10 days after strong convective activity occured in the tropical western Pacific. Additionally, Hendon and Liebmann (1990b) showed that as the IO traverses northern Australia, upper-level tropical easterlies increase and expand in meridional width. This accompanies the increase and poleward displacement of the Australian subtropical jet. Interpretation of the IO as causing a substantial fluctuation of the local Hadley circulation seems to be consistent with these zonal wind changes.

A recent study by Lau et al. (1998) revealed that the large-scale convective systems connected with the IO lead to the first transition of the Asian summer monsoon, i.e., the abrupt transformation from land-locked convection over southern Thailand and northern Borneo to oceanic convection over the South China Sea (SCS) (Tao and Chen, 1987; Lau and Yang, 1997; Hsu et al., 1999). Lau et al. (1998) present a detailed description of the first transition of the Asian summer monsoon during the SCS Monsoon Experiment (SCSMEX) in May 1997. They describe the passage of the IO over the maritime continent as "abruptly 'hopping' from the Indian Ocean into the SCS, concomitant with enhanced convective activities over the entire tropical western Pacific."

Figure 1.4 depicts a sequence of satellite-observed OLR maps describing the evolution of large-scale convective systems associated with the IO and the SCS monsoon onset from the 9th to the 29th of May 1997 at 4-day intervals. On the 9th of May (Figure 1.4a), a major super cloud cluster was identified over the central equatorial Indian Ocean. When it reached the eastern Indian Ocean and the southern Bay of Bengal, the super cloud cluster became stationary and amplified just west of Sumatra (Figure 1.4b). There, it spun off convective clusters on opposite sides of the equator in the form of a "double cyclone" (see Section 1.3). Subsequently, the northern cyclone strongly developed while the southern one weakened. This led to intensified convective activity in the Bay of Bengal on the 17th of May (Figure 1.4c). Around the 21st of May, the SCS monsoon onset occurred, as indicated by the abrupt shift of convective activities from the Indian Ocean into the SCS (Figure 1.4d). On the 25th of May, a super cloud cluster became organized over the western Pacific and the SCS convection moved eastward over the Philippines

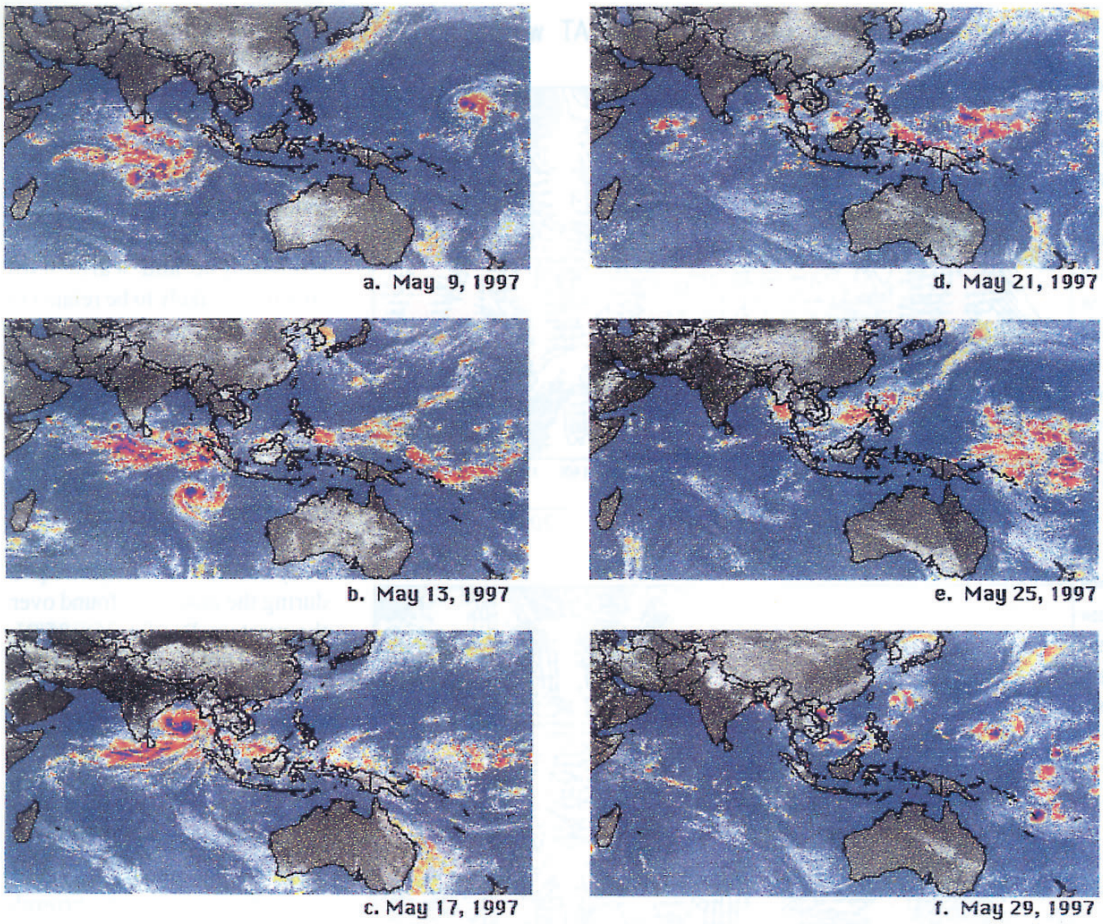

Figure 1.4: *Composite OLR maps showing the evolution of convective systems leading up to the SCS monsoon onset during 1997. Scales are relative. Areas of deep convection (OLR<240 W m^{-2}) are indicated in red and the deep convective cores (OLR<200 W m^{-2}) in dark blue (Lau et al., 1998).*

(Figure 1.4e). By the 29th of May, the super cloud cluster was dispersed over the western Pacific, spawning westward propagating cyclonic vortices on both sides of the equator (Figure 1.4f, see Section 1.3). At this time convective activity over the Indian Ocean was suppressed. Hence, the associated enhanced rainfall over the equatorial western Pacific Inter-Tropical Convergence Zone (ITCZ) and the South Pacific Convergence Zone (SPCZ) is triggered by the arrival of the ascending branch of the IO. The former "hopping" is thought to be due to the colder surface temperature over land on the maritime continent than the surrounding SST (Figure 1.3) with colder SSTs at the coastal regions of the maritime continent. A sensitivity study with the maritime continent replaced by sea points (Section 5.2) reveals the importance of the maritime continent for the tropical climate and especially the IO.

The transition of the Asian summer monsoon is socioeconomically important because the rainfall associated with this monsoon affects the entire region of southeast Asia and southern China, which is the home of about half the population of Asia. From the meteorological point of view the large-scale circulation changes associated with the onset of SCS monsoon foreshadow the subsequent development of a weak or strong summer monsoon over East Asia (Lau and Yang, 1997) and the occurrences of major drought and flood conditions over East Asia and Japan (Nitta, 1987; Huang and Sun, 1992).

Troup (1961) was the first to state that the monsoon in the Australian region resembles the Asian summer monsoon. In particular, both monsoons have a distinct onset (Hendon and Liebmann, 1990a). The onset of the Australian summer monsoon is defined as the first occurrence of 850 hPa westerlies with a speed of at least 5 m s^{-1} and a rainfall rate of at least 5 mm day^{-1} in Darwin. Hendon and Liebmann (1990a,b) proposed that this is strongly associated with the convective phase within the first IO per season that reaches northern Australia. In a composite study for the years 1957 to 1987, they found that 27 of the 30 onsets of the Australian summer monsoon were related to the IO. The average time between active episodes of the Australian monsoon is 40 days (Holland, 1986). Composite studies of observed OLR by Knutson and Weickmann (1987) clearly show that most of northern Australia is affected by the eastward passage of the IO.

In addition to the effects of the IO on the monsoon circulation, oceanic fluctuations associated with Westerly Wind Bursts (WWBs) are considered to be a consequence of the IO activity (see Section 1.3). These fluctuations significantly modify the structure of the thermocline in the equatorial Pacific Ocean on the intraseasonal time scale (e.g. McPhaden and Taft, 1988; Kessler et al., 1995; Zhang, 1997) and by this they could influence or even force oceanic Kelvin waves, which play an important role for the onset of an El Niño event (Weickmann, 1991; Kessler et al., 1995; Nakazawa, 1999; van Oldenborgh, 2000). The mechanism responsible for the organization of interannual oceanic Kelvin waves remains unclear (Zhang et al., 2001).

Four different explanations for the influence of the IO on the El Niño/Southern Oscillation (ENSO) cycle are summarized by Zhang et al. (2001): (1) The IO affects ENSO only as a source of stochastic forcing. No simple statistical relationship between the two should be expected. (2) Empirical relationships between the IO and ENSO depend on the IO indices used. IO effects on ENSO, if there are any, must take place through air-sea interaction in the Pacific. IO indices like the $\overline{u_{200}}$-variance index by Slingo et al. (1996) and Slingo et al. (1999) and the POP-coefficient index by Gualdi et al. (1999) (see Section 2.2) are based on global wind data, necessary as objective measures of the capability of atmosphere

General Circulation Models (AGCMs) to simulate the IO. These indices may not reflect local IO activity in the Pacific. When indices based on or including local signals of the IO in the Pacific are used, stronger statistical relationships between the IO and ENSO are found. (3) Influences of the IO on ENSO depend on the mean state of the coupled system and therefore on individual events. Cases of a strong ENSO warm event (1982/83) following a moderate IO season (1981/82), strong IO activity leading to no warm event (1989/90), and a warm event (1997/98) preceded by strong IO activity (1996/97) can all be found. (4) ENSO is influenced by intraseasonal or subseasonal variability because of WWBs instead of the IO. Not all WWBs are associated with the IO. The main distinctions between the two are the following: WWBs are more frequent and smaller in zonal extent; the IO has more coherent structures in winds, cloud, and precipitation than WWBs; the IO propagates eastward and WWBs do not necessarily.

The fluctuations in the ocean related to the IO are roughly 0.2-0.5 K in SST, 10-20 m in the thermocline depth and 0.1-0.2 m s^{-1} in mixed layer current (Zhang et al., 2001). These fluctuations are sensitive to the ocean mean state and an order of magnitude smaller than the oceanic variability associated with ENSO, i.e. air-sea coupling for the IO is weaker than for ENSO, but still present. The oceanic response in GCMs is also sensitive to the temporal resolution of surface cooling. Cooling due to high-frequency mixing induced by daily winds, for example, is much stronger than cooling due to monthly mean wind calculated from the same daily data (Zhang et al., 2001). The influence of ENSO on the IO, in contrast, is more evident. During an El Niño event, the heating in the Central and East Pacific increases; the winter upper-tropospheric equatorial westerlies in this region are weakened or even disrupted (Slingo et al., 1996) and the West Pacific warm pool is extended eastward (Picaut and Delcroix, 1995; Delcroix et al., 2000). This eastward extension of the West Pacific warm pool leads to an eastward shift of the main IO activity, as will be shown in Section 3.3.

The midlatitude response of the IO requires careful analysis due to the high background variability in the midlatitudes. Nevertheless, since the IO has a slow evolution relative to synoptic weather systems, prediction of the IO has the potential to improve extended-range weather forecast in the midlatitudes. Ferranti et al. (1990) constructed a composite of extratropical 500 hPa geopotential height correlated to the IO and analyzed the interactions of the IO and the midlatitudes. They also quantified the degree to which forecast skill in the extratropics is influenced by model errors in the tropics and conversely how tropical forecast skill is influenced by the extratropics by relaxing tropical and extratropical observations to the ECMWF forecast, respectively. The result of the relaxation of

tropical observations is a noticable improvement of the forecast skill scores in the range of 11 to 20 days in the extratropics, particular over the Pacific and North Amercian region. The relaxation of extratropical observations improves the tropical forecast skill scores and model systematic errors especially in the upper tropospheric streamfunction.

Mo and Higgins (1998a,b) and Jones (2000) investigated the linkage between the IO and California precipitation, whereby wet (dry) events are connected with the enhanced convection near 150°E (120°E) in the tropical Pacific through the eastward extension (retraction) of the Pacific jet. As a physical mechanism for the eastward extension, Higgins et al. (2000) propose the generation of the anomalous Rossby wave vorticity source in the subtropics, due to the anomalous divergent outflow associated with the tropical convection. The anomalous moisture transport during these events is typical of what has often been referred to as the "pineapple express", so called because a significant amount of the moisture traverses the Hawaiian Islands on its way towards western North America.

1.3 Theories about the origin and propagating mechanism

The origin of the convective forcing and the propagation of the IO has been a subject of many studies (e.g. Knutson and Weickmann, 1987; Lau and Peng, 1987; Wang and Rui, 1990a; Hayashi and Golder, 1993). They are briefly reviewed by Madden and Julian (1994). The three main theories for the propagation are (1) the frictional wave-CISK (Conditional Instability of the Second Kind), (2) the evaporation-wind feedback, also called wind-induced surface heat exchange (WISHE) and (3) the air-sea interaction that takes diabatic heating, entrainment cooling and thermocline variations in the ocean into account as reasons for the wave propagation (e.g. Krishnamurti et al., 1988; Lau and Sui, 1997; Wang and Xie, 1998). They are briefly described in the next paragraphs and illustrated in Figure 1.5.

Riehl and Malkus (1958) first showed that much of the tropical meteorology involves the collective interaction of large-scale circulations and cumulus convection. The physical mechanism for this interaction is the CISK mechanism, which was first described by Charney and Eliassen (1964) and Ooyama (1964). The CISK mechanism assumes that low-level convergence moistens the environment and destabilizes it through layer ascent leading to deep convection. Diabatic heating owing to the resulting release of precipitation drives the large-scale circulation and thus maintains the large-scale low-level convergence (e.g.

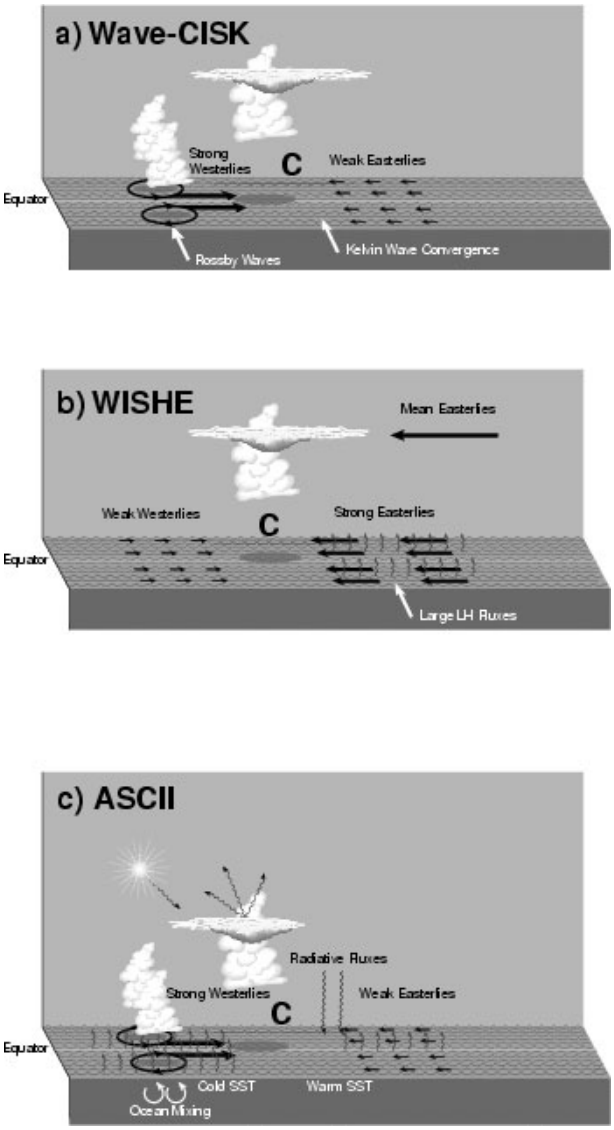

Figure 1.5: *Illustration of three conceptual models of the IO: a) Wave-CISK, b) wind-induced surface heat exchange (WISHE), c) air-sea convective intraseasonal interaction (ASCII) . "C" denotes the low-level convergence, that becomes the preferred site for the subsequent development of convection (Flatau et al., 1997).*

Holton, 1992). Yamasaki (1969) first investigated the production of low-level convergence due to equatorial waves, which is referred to as wave-CISK (Lindzen, 1974). Further details on equatorial waves can be found in e.g. Matsuno (1966) and Wheeler et al. (2000). In idealized experiments by Lau and Peng (1987), the phase speeds of the unstable modes were higher than observed and the smallest scales were the most unstable. Further insight was gained by Wang (1988) and Salby et al. (1994), who coupled the wave-CISK models to a frictional boundary layer. This led to the frictional wave-CISK mechanism. The strong correlation between surface convergence and convection during the amplification

and the lack of correlation during the decay suggests that moisture convergence in the boundary layer plays a key role in organizing anomalous convection in the IO (Hendon and Salby, 1994).

The evaporation-wind feedback mechanism (Neelin et al., 1987; Emanuel, 1987) seems to play a minor role for the propagation of the IO. It assumes mean surface easterlies that would lead to enhanced (reduced) low-level windspeed to the east (west) of the convection, where the easterlies increase (decrease) due to the low-level convergence. A result would be increased latent heat release below and to the east of the convection to evolve an eastward propagation of the convective activity. Observations reveal maximum latent heat release to the west and below the convection cells (Jones and Weare, 1996). The observed maximum latent heat release to the west of the convection is due to WWBs (Lau et al., 1989), which often occur after the passage of an IO. Thus, the WISHE mechanism does not appear to play a significant role in the propagation of the IO. Figure 1.6 shows a pair of cyclones leading to intense WWBs on the 18th of May 1986. These cyclones are generated by Rossby waves associated with the passage of the IO in the middle of May (Figure 1.2). Not all WWBs are associated with an IO (Zhang et al., 2001).

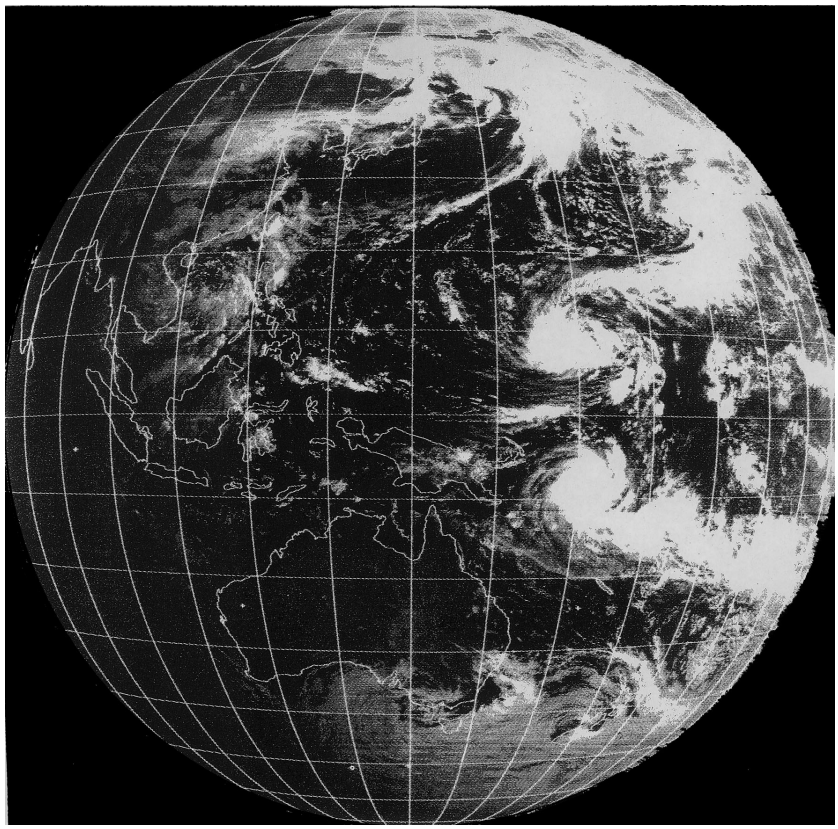

Figure 1.6: *GEOSAT satellite photograph of a pair of cyclones on opposite sides of the equator along 160°E on 18 May 1986 (Philander, 1990).*

The air-sea interaction theory is based on the fact that the potential energy for updrafts arises from the thermodynamic disequilibrium between the atmosphere and the underlying ocean. The potential energy to balance frictional dissipation depends on the rate of transfer of latent heat from the ocean to the atmosphere. Strong surface winds like the WWBs produce a rough sea surface and can greatly increase the evaporation rate (Holton, 1992) and the mixed-layer depth. Wang and Xie (1998) demonstrated that the coupling of the atmospheric wind with oceanic mixed layer entrainment and evaporation reduces the eastward propagation speed of the atmospheric moist Kelvin waves and increases the westward phase speed of the atmospheric moist Rossby waves. The air-sea interaction influences the SST variations with above normal SST to the east of the convection maintaining the eastward evolution, and decreasing SST near the western portion of the convective activity being associated with the cessation of convection (Sperber et al., 1997; Flatau et al., 1997; Wang and Xie, 1998; Waliser et al., 1999b). The warm SST anomaly acts to reduce the pressure hydrostatically and thus increases the convergent surface circulation. Since the WISHE-mechanism does not seem to produce a realistic IO (Kirtman and Vernekar, 1993), the current paradigm of the propagating mechanism of the IO is a combination of the frictional wave-CISK mechanism and air-sea interaction (e.g. Waliser et al., 1999b).

The active period of the IO is strongly controlled by the dynamic effect of the equator through the change of algebraic sign of the planetary vorticity and by the thermodynamic effect of the thermal equator where the maximum SST occurs (Salby et al., 1994). The meridional movement of the ITCZ is quite symmetric around the equator over the Indian Ocean and the West Pacific (Philander et al., 1996). It leads to enhanced convection during the equinoxes, especially the vernal equinox. At the autumnal equinox, the highest SST in the Pacific still lies in the northern hemisphere, and the migration of the mean ITCZ southward into the southern hemisphere does not occur until almost at the end of the year (Slingo et al., 1996). The IO is most active during these periods and it is weakest during the boreal summer solstice (Salby et al., 1994). When the maximum SST moves away from the equator in the western Pacific to about 7.5°N, the growth rate of the unstable coupled mode decreases significantly (Wang and Rui, 1990a).

Figure 1.7 shows that during the active period of the IO the forced Rossby waves in the eastern hemisphere lead to westward propagation of single cloud clusters with a zonal extension of about 1000 to 2000 km within the super cloud cluster with a zonal extension of about 2000 to 4000 km (Nakazawa, 1988; Lau et al., 1989). However, the Rossby waves are dissipating relatively fast. In contrast to this, the Kelvin waves propagate zonally

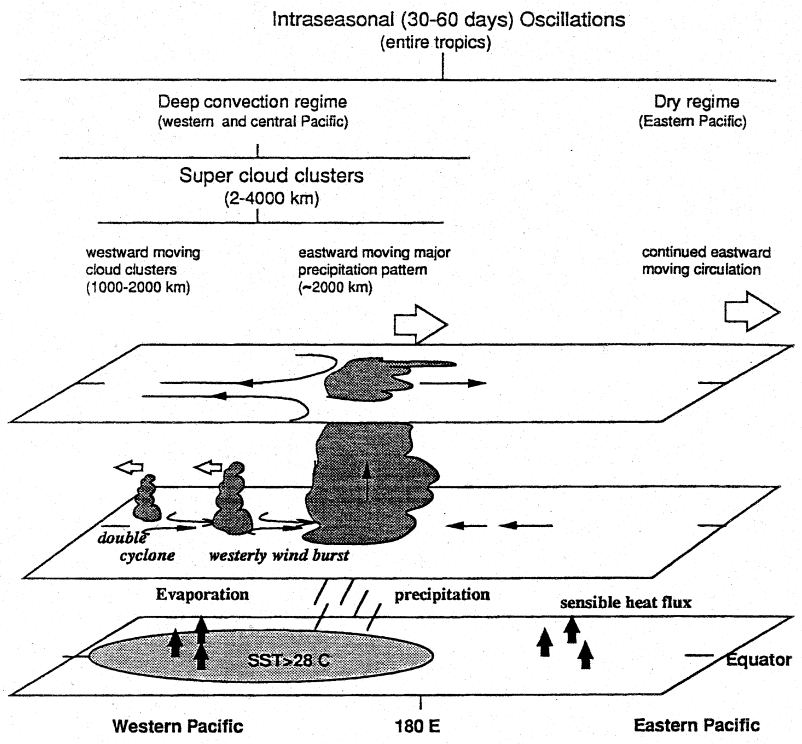

Figure 1.7: *Diagram of the hierarchy structure of the IO over the tropical Pacific. Horizontal scales shown are only approximate. Large overlap may occur within the super cloud cluster substructures (Lau et al., 1989).*

around the whole tropical belt. Moisture supply due to latent heat release from the Indian Ocean and the West Pacific warm pool reduces the propagation speed of the IO in this region (Jones and Weare, 1996). If C_a is a dry atmospheric Kelvin wave speed and I denotes the heating coefficient associated with wind-induced moisture convergence, then the moist Kelvin wave speed is $C_a^* = C_a(1-I)^{1/2}$ (Wang and Xie, 1998). The wind-induced moisture convergence and thus the vertical distribution of moist static energy of the basic state is closely related to the SST. With increasing SST the growth rate increases for all wavelengths, but the preferred scales shift to a shorter wavelength (Wang, 1988). A simplified study by Wang and Rui (1990a) reveals that the moist Kelvin mode becomes progressively less damped when moisture concentration gradually increases and finally begins to grow when the SST exceeds a critical value, whereas moist Rossby waves are always damped.

Idealized simulations by Salby et al. (1994) with different SSTs show that as surface temperature T_{00} and surface moisture increase, large-scale heating power at eastward frequencies also increases. Figure 1.8 describes the power spectrum of wavenumber-one heating over the equator for a barotropic atmosphere. For T_{00}=26 °C (dotted), heating

power is magnified at eastward periods of 25 days and longer. For T_{00}=28.5 °C (dashed), heating power is concentrated about an eastward period of 80 days, where the spectral density is increased by an order of magnitude. At T_{00}=29.5 °C (solid), the wavenumber-one heating spectrum is fully concentrated at an eastward period of about 80 days. For a baroclinic atmosphere, representative of equinox, the critical value of surface temperature is 26.5 °C and for conditions, which are representative of solstice, it is in excess of 30 °C (Salby et al., 1994).

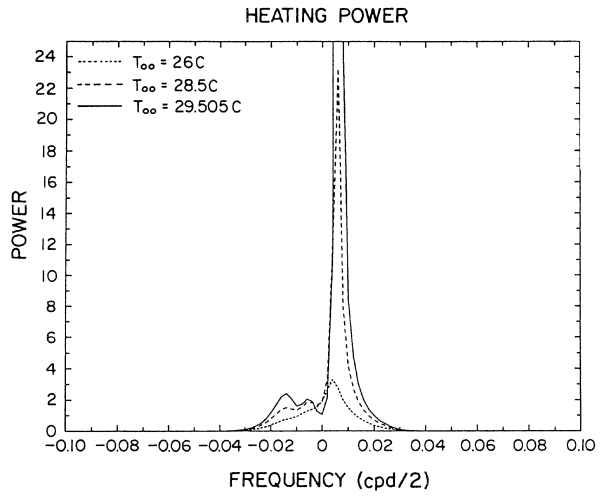

Figure 1.8: *Power spectrum of wavenumber-one heating over the equator and in the mid-troposphere for equatorial surface temperatures of T_{00}=26° C (dotted), T_{00}=28.5° C (dashed) and T_{00}=29.5° C (solid). Positive (negative) frequencies [cycles per day / 2] indicate eastward (westward) propagation (adapted from Salby et al., 1994).*

Hayashi and Sumi (1986) attribute the eastward propagation to wave-CISK convergence processes and wavenumber one zonal structure to the effects of convection-suppressing downdrafts occurring in a finite longitudinal domain. In this case, a new oscillation can begin once the convection-suppressing influences as subsidence and low-level moisture divergence of the previous event have moved "far enough" away to the east. As an origin of the convective forcing, Knutson and Weickmann (1987) pointed out the possibility that each new event is initiated by remnants of the previous IO approaching from the west. The smaller convection anomalies over the Central/South American sector could act to rejuvenate the IO after it has travelled over cooler sea surfaces. In contrast to this, Hsu et al. (1990) revealed in an observational study, that Rossby wave trains propagating from the midlatitudes into the tropics play a role in organizing tropical convection that triggers the IO. In addition, Bladé and Hartmann (1993) showed in a simplified two-level global nonlinear model that the midlatitude baroclinic eddies provide the quasi-stochastic forcing necessary to excite each new intraseasonal episode by organizing a

region of subtropical convection, which grows and expands equatorwards due to latent heating. They conclude, that independent redevelopment of the IO could occur even in the presence of a moist Kelvin wave (Figure 1.9) and that it is not obvious how an upper-level divergent wind anomaly can actually trigger convergence in the tropical boundary layer. In their "discharge-recharge" theory the IO period is determined by the recharge time for the moist static energy in the region of the Indian Ocean together with the time required for the convective event. Once the atmosphere becomes unstable to convection, any high-frequency extratropical or tropical wave could start the next IO cycle. Matthews and Kiladis (1999) observed an enhancement in such high-frequency activity just prior to the onset of the IO convection. The longitudinal variation in SST has a considerable impact on the development and propagation of an equatorial Kelvin wave (Bladé and Hartmann, 1993). Idealized model studies by Salby et al. (1994) show that static stability plays a key role in the IO.

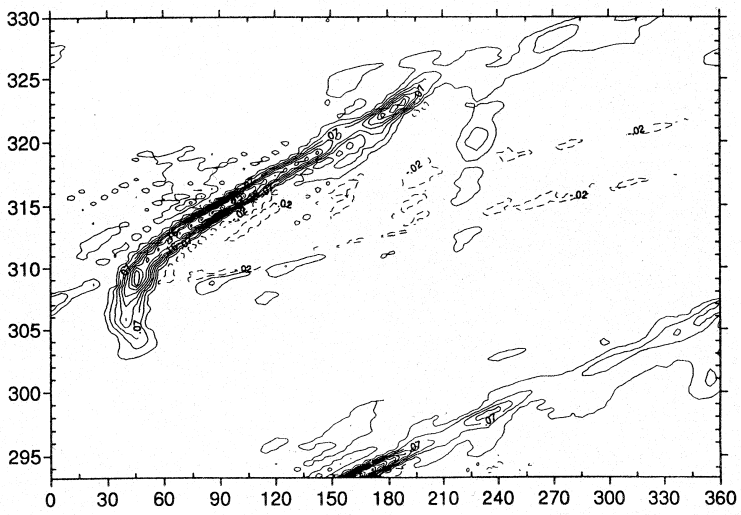

Figure 1.9: *Upper-level divergence at latitude 1.6°N simulated with a simplified two-level model. X-axis is longitude in degrees and y-axis is time in days. The contour interval is* 3×10^{-6} s^{-1} *(zero contour suppressed, first positive contour is* 1×10^{-6} s^{-1}*) (Bladé and Hartmann, 1993).*

However, Matthews (2000) pointed out a variety of mechanisms that are important in determining the behaviour of the IO. In addition to the "discharge-recharge" theory by Bladé and Hartmann (1993), the mean sea level pressure anomaly associated with the Kelvin wave that circuits around the equator is capable to initiate the next cycle of the IO. The blocking and delay of the surface Kelvin wave by the orographic barriers of the Andes in Central America and the East African Highlands are able to slow down the dry Kelvin wave. The meridional propagation of the mean sea level pressure anomaly

as a trapped wave against the Andes leads to a pressure torque across the mountain range (Weickmann et al., 1997). Currently, it is not clear to what extent one of these mechanisms dominates over the other.

1.4 Current status of the IO in GCM simulations

Observational studies indicate a non-negligible impact of the IO on the tropical climate. In addition to the direct effects of the modulated tropical convection, recent studies propose an influence of the IO on the ENSO-cycle and precipitation rates in the midlatitudes (see Section 1.2). These circumstances point out the importance of a correct representation of the IO in GCMs to further understand its propagating mechanism and its influence on tropical and global climate.

The representation of organized tropical convection at synoptic to intraseasonal timescales is extremely sensitive to the convective parameterization (Slingo et al., 1994). In a diagnostic subproject of the Atmospheric Model Intercomparison Project (AMIP; Gates, 1992), Slingo et al. (1996) compared 15 GCMs in their ability to simulate the IO. They found that GCMs that use the buoyancy closure for organized entrainment and detrainment in their convection schemes seem to simulate a more realistic IO than GCMs using the closure based on moisture convergence. The models with a weak seasonal cycle and a weak representation of the SPCZ also tend to have a weak IO. Errors in the basic equatorial zonal flow additionally affect the propagation characteristics of equatorial waves and the interaction of the extratropics and the tropics. Slingo et al. (1996) found some deficiencies common to many of these models: The eastward propagation is too fast, the strongest IO activity is shifted eastward from the maritime continent to the West and Central Pacific, and the change in phase speed from eastern to western hemispheres is missing. The eastward shift of the strongest IO activity is due to an erroneous distinct underestimation of intraseasonal variability over the maritime continent (Sperber et al., 1997). The disturbance of intraseasonal variability is weaker and less frequent in observations (see Figure 1.2).

Sperber et al. (1997) analyzed the IO in the Goddard Laboratory for Atmospheres (GLA) GCM, which is derived from an earlier version described by Kalnay et al. (1983), and the United Kingdom Meteorological Office (UKMO, Cullen, 1993) GCM. These are two of the models with the most realistic IO in the analysis by Slingo et al. (1996). The fourth version of the European Centre Hamburg Atmospheric Model (ECHAM4; Roeckner

et al., 1996a) GCM did not take part in this intercomparison project, but Gualdi et al. (1999) showed a quite realistic simulation of the IO and its interannual variability in this model. These three models still simulate an erroneous distinct underestimation of intraseasonal variability over the maritime continent. However, Waliser et al. (2001) selected the GLA, the ECHAM4 and the Geophysical Fluid Dynamics Laboratory (GFDL, Gordon and Stern, 1982) GCMs for a research proposal on the predictability study of the IO. These models simulate a reasonable realistic IO validated against the National Centers for Environmental Prediction (NCEP) reanalysis (Kalnay et al., 1996; Kistler et al., 2001) compared to other GCMs (Figure 1.10), although the GFDL GCM simulates a too strong IO (Hendon, 2000) and all three show the eastward shift of the strongest IO activity.

Several studies (e.g. Hayashi and Sumi, 1986; Swinbank et al., 1988; Flatau et al., 1997) reveal the presence of an IO-type oscillation in aqua-planet GCMs, which suggests the independence of the IO-propagation mechanism to land-sea distribution. Neale and Slingo (2001) performed a sensitivity study with the HadAM3 GCM whereby the land points associated with the maritime continent are substituted by sea points. They found, that the center of the simulated main IO activity is relocated from the Western and Central Pacific to the maritime continent and thus represents an IO more similar to observations. This indicates that the effect of land is misrepresented by this GCM. Since the IO is considered to be a coupled air-sea phenomenon, the necessity to study it with coupled atmosphere-ocean GCMs (CGCM) seems to be evident (Waliser et al., 1999b). However, Hendon (2000) found no indication of a feedback of the SST anomalies on the simulated IO in the GFDL GCM coupled to a one-dimensional ocean mixed layer model with variable mixed layer depth at each grid point.

In a recent study, Inness et al. (2001) illustrated the relevance of realistic convection to the IO in the HadAM3 aqua-planet GCM through increasing the vertical resolution from 19 to 30 levels by adding levels evenly between each original level except for the bottom and top three levels. The convection scheme assumes that solid precipitation melts as it falls from a model layer, where the temperature is below the freezing level to a layer where the temperature is above the freezing level. This melting is achieved at the expense of removal of heat from the atmosphere in that model level, thus cooling the layer. This results in an increase in stability above this level. For 19 vertical levels, the layer which is cooled has a thickness of about 100 hPa so the reduction in temperature and resulting change in stability are quite small. For 30 vertical levels, the layer which is cooled is only 50 hPa thick so the cooling and increase in stability are proportionally larger. The increase in stability then results in more convection terminating in mid-troposphere, giving

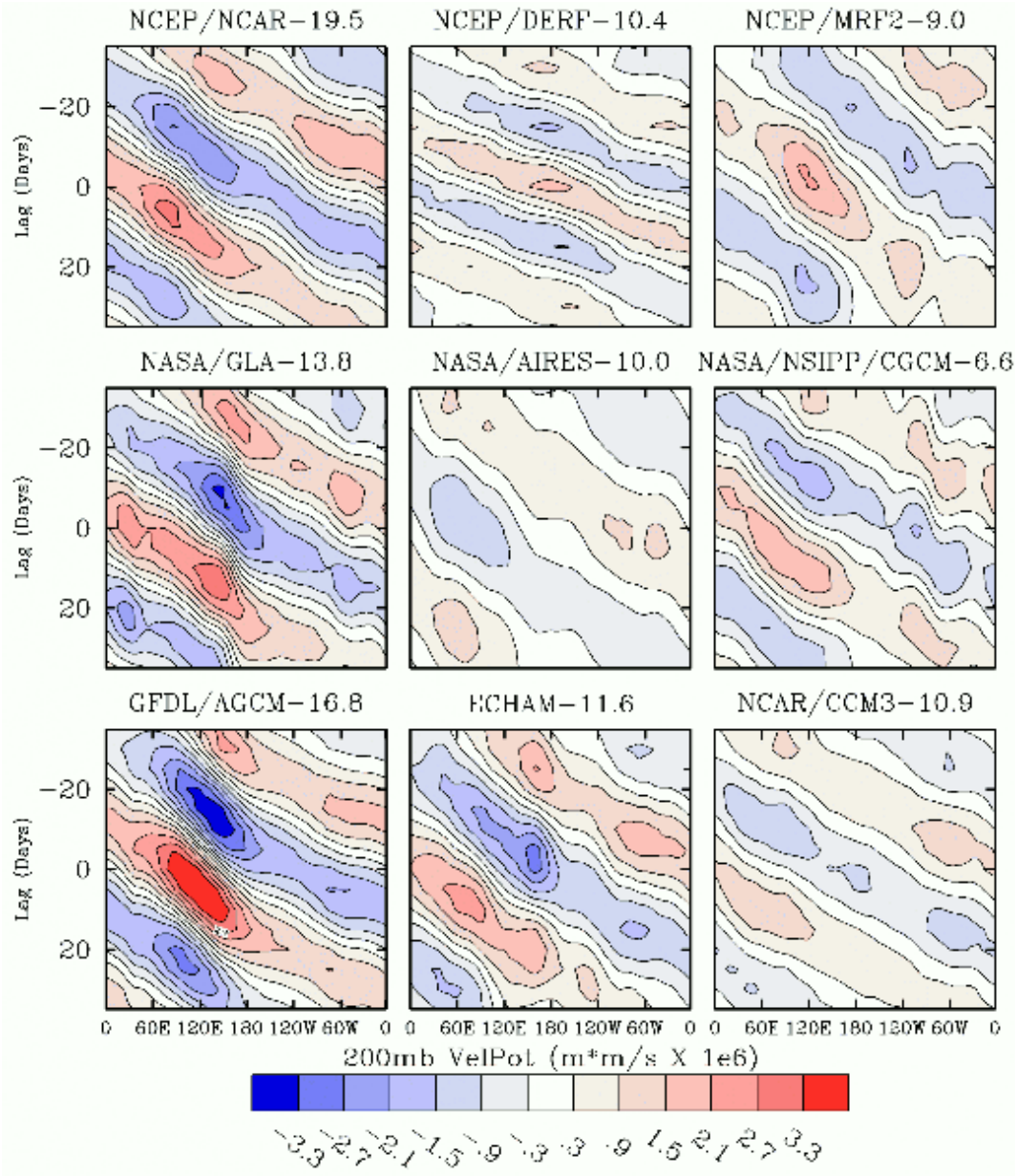

Figure 1.10: *Comparison of the NCEP/NCAR reanalysis (top left) to eight GCMs: Composites of time-longitude Empirical Orthogonal Functions (EOFs) of 200 hPa velocity potential anomalies for time lags from -35 days to +35 days. Numbers indicate the explained variance [%] (Waliser, pers. comm.).*

periods when the convective clouds are mainly cumulus congestus clouds. These clouds predominantly moisten the mid-troposphere, thus increasing the moist static energy and pre-conditioning the atmosphere for the next burst of deep convection.

Although Inness et al. (2001) analyzed this feature in aqua-planet GCMs, they propose that this mechanism is at least partly responsible for the difference in IO activity between two complete GCM simulations with different vertical resolutions. Most current GCMs

fail to simulate a peak in mid-level cloud cover, but this would lead to convective heating at these levels, which is important for the representation of the zonal wind field related to the IO and a reduced phase speed of the IO, as shown by Sui and Lau (1989) and Lau et al. (1989) in numerical experiments. They found a slower IO propagation due to an increase in convection in the lower troposphere between 500 and 700 hPa instead of the mid-troposphere between 300 and 500 hPa. Observational studies in the West Pacific warm pool region by Johnson et al. (1996) during the Tropical Ocean Global Atmosphere Coupled Ocean-Atmosphere Response Experiment (TOGA COARE; Webster and Lukas, 1992) period frequently exhibited thin stable layers near the freezing level, which are believed to be a consequence of melting precipitation in a layer of about 500 m thickness just below the melting level. At the altitude of this freezing level, 500 m is equivalent to 35 to 40 hPa. By increasing the vertical resolution of a GCM from 100 to 50 hPa in this region, the impact of melting precipitation on the stability of the atmosphere can be better resolved (Tompkins and Emanuel, 2000; Inness et al., 2001). Johnson et al. (1999) found in observations that the passage of an IO is associated with a trimodal structure in tropical cloud cover with peaks at high, low and mid levels.

A more realistic representation of water-vapor profiles, including the trimodal structure of the convection, was found in the ECHAM4 one-column model when the vertical resolution was increased from 19 to 40 levels or more (Tompkins and Emanuel, 2000). The ECHAM4 convection scheme (Tiedtke, 1989; Nordeng, 1996), which uses buoyancy closure for organized entrainment and detrainment, takes mid-level convection that reproduces the wave-CISK mechanism into account. However, this mechanism barely occurs in the boundary layer, thus the frictional wave-CISK mechanism, which would lead to slower eastward propagation of the super cloud clusters associated with the IO (Salby et al., 1994), is hardly active.

Jones et al. (2000) analyzed the prediction of the phase of the IO in 50-day forecasts of daily initialized 200 hPa zonal wind prior to different phases of the IO. They found in the National Centers for Environmental Prediction Dynamical Extended Range Forecast (NCEP-DERF) model a prediction skill of the phase of the IO of about 5 to 7 days, that is equal to the skill of current numerical weather forecasts (Bengtsson, 1999). Currently, purely statistical models (Waliser et al., 1999a) provide a better forecast of the phase of the IO with a prediction skill of 15 to 20 days. Hendon et al. (2000) discussed the prediction skill of the numerical weather forecasts during different phases of the IO. They discovered a reduced prediction skill of the NCEP-DERF during the active episodes of the IO.

1.5 Outline of this study

Zhang et al. (2001) pointed out that most current GCMs cannot simulate realistically the IO. Even the seasonality of the IO, one of the strongest signals in observations, is not consistently reproduced in GCM experiments. This is still not understood, due to the lack of comprehensive understanding of fundamental dynamics and thermodynamics of the IO. The purpose of this study is to assess the skill of the ECHAM4 GCM in representing the IO, and thereby to identify factors that offer scope for possible improvements in future model versions. The understanding and correct simulation of the IO and its variability is an important task to further reveal its influence on the global and especially the tropical climate. The present study emphasizes that improvements in the simulation of the IO in AGCMs are necessary, before the IO can reliably be analyzed in the simulated coupled atmosphere-ocean system.

To provide a detailed insight into the dynamics of the IO in reanalyses data, Chapter 2 of this study compares the representation of the IO in the NCEP and the ECMWF ERA15 (15 years of ECMWF Re-Analysis, Gibson et al., 1997) to global OLR derived from National Oceanic and Atmospheric Administration (NOAA) satellite data (Gruber and Krueger, 1984; Liebmann and Smith, 1996) and radiosonde measurements of relative humidity at Singapore airport. The radiosonde measurements are also compared to preliminary inofficial results of the new ECMWF ERA40 reanalysis. After the selection of an appropriate dataset, a detailed analysis of the IO for the 5 years period 1984 to 1988 is performed. This period is included in an AMIP subproject by Slingo et al. (1996). It contains the 1987 El Niño and the 1988 La Niña, with a dry and a wet Indian summer monsoon season, respectively. These features allow the study of the possible interactions of ENSO and Indian summer monsoon with the IO.

Simulations of the IO with the ECHAM4 AGCM forced with monthly-mean AMIP SSTs and ECHAM4 coupled to the third version of the Ocean isopycnal (OPYC3) OGCM are presented in Chapter 3. In addition, the aspects of the interannual variability of the IO are documented with the aid of 20 years of reanalyses data and 100 years of the coupled simulation.

Chapter 4 presents an approach to further understand the dynamics of the IO and to improve the simulation of the IO in the ECHAM4 AGCM. According to the suggestions by Inness et al. (2001), the vertical resolution is increased from 19 to 39 vertical levels to increase the stability in the mid-troposphere and thus producing a slower propagation of the simulated IO. To approve these results, the stability near the freezing level is increased

(decreased) by cooling (warming) the layer near the freezing level in two sensitivity studies. This is artificially achieved by doubling (halving) the melting rate in the calculation of the temperature change due to convective precipitation. Additionally, the influence of the suppression of snow melt for all precipitation is analyzed.

A second approach is chosen in Chapter 5. The horizontal resolution is increased to investigate the sensitivity to a reasonable land-sea distribution over the maritime continent. To distinguish this effect from general dynamical changes due to the increased horizontal resolution, the effects of the land-sea distribution are studied in a sensitivity experiment with the land points associated with the maritime continent replaced by sea points, similar to the study by Neale and Slingo (2001). Additionally, the ECHAM4 AGCM is forced with a different SST dataset to investigate the influence of the SST forcing on the IO, since the convection is very sensitive to changes in SST over the maritime continent region.

The results of this study are discussed in Chapter 6 and the conclusion is presented in Chapter 7. Appendix A provides a list of the acronyms used in this text. Appendix B shows the time-longitude Hovmöller diagrams of unfiltered 200 hPa velocity potential anomalies for ERA15 and selected GCM experiments. The 200 hPa level corresponds to a representative level of outflow from deep convective clouds (Inness et al., 2001). Appendix C gives a brief overview of the Principal Oscillation Pattern (POP) analysis, which is used to describe the characteristics of the IO in the present thesis.

Chapter 2

The IO in reanalyses data

In this chapter, the NCEP (Kalnay et al., 1996; Kistler et al., 2001) and ECMWF (Gibson et al., 1997) reanalyses are compared and briefly evaluated against observations with respect to their ability to represent the IO. Subsequently, the representation of the IO in the ERA15 reanalysis dataset is analyzed in more detail to introduce a method for the detection of the IO and to provide further insight into the characteristics of the IO.

2.1 Evaluation of reanalyses

It is important to have available several reanalyses to make an estimate of the reliability of their respective results, especially for quantities and trends that can not be accurately estimated from direct measurements.

Newman et al. (2000) investigated the differences in the NCEP, National Aeronautics and Space Administration (NASA), and ERA15 reanalyses over the tropical West Pacific warm pool (Figure 2.1). The standard deviations of both the NCEP and ERA15 reanalyses OLR data capture at least the overall pattern of satellite observed NOAA OLR variability on intraseasonal timescales, only the NASA dataset shows a pronounced double-banded structure around the equator. The NCEP dataset exhibits a too large standard deviation in the subtropics east of the date line, while near the equator the variability is too small. The standard deviation of 200 hPa divergence is dramatically different for each reanalysis. The amplitudes in ERA15 have twice the values of the other two reanalyses. The NASA dataset provides its characteristic double-banded structure and is thus omitted in the following analysis. NCEP has a coarser resolution than ERA15, with zonal waves up to

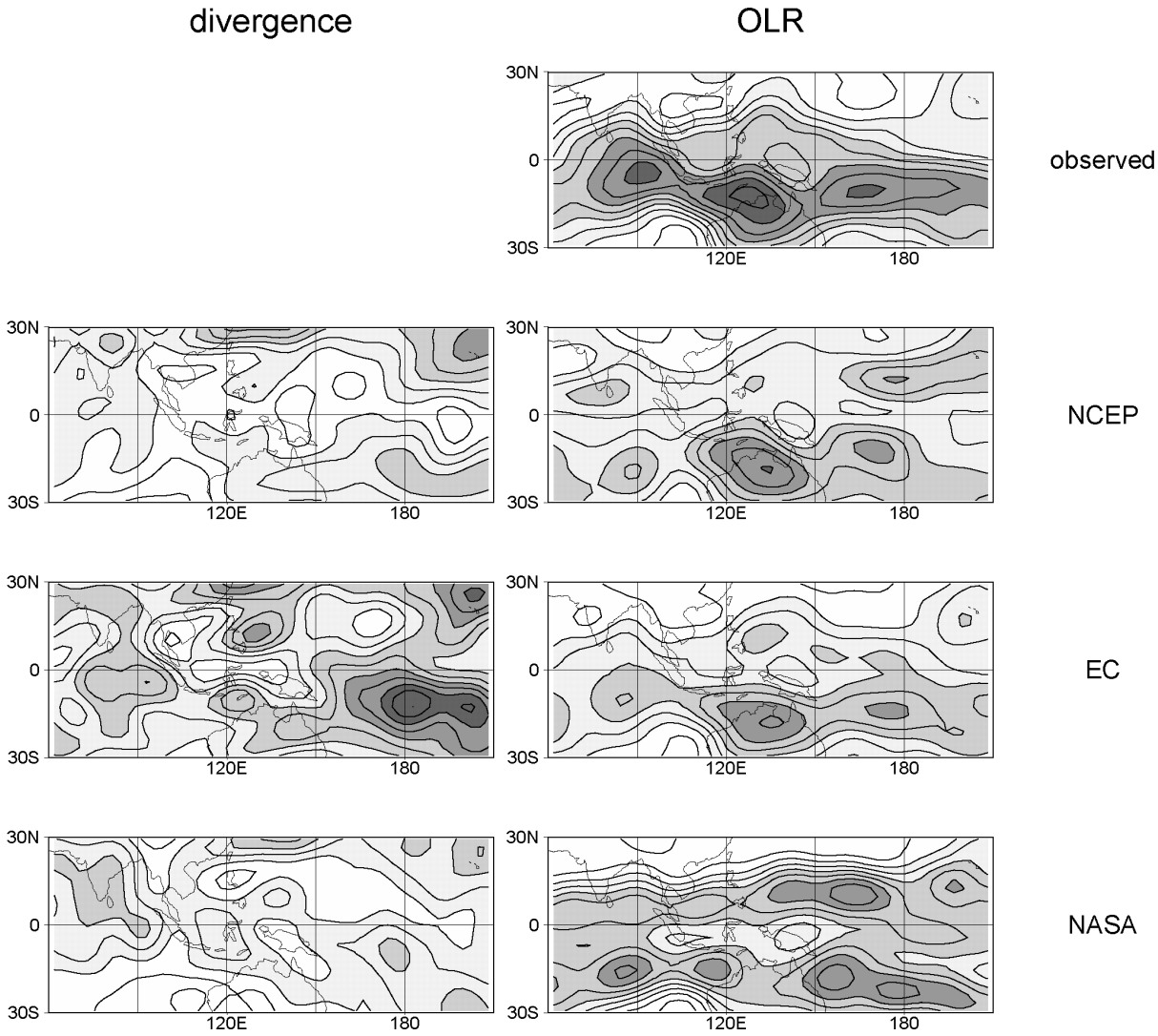

Figure 2.1: *Standard deviations of 30-70 day bandpass-filtered daily anomalies for the winter seasons 1980/81 to 1992/93. Left column: 200 hPa divergence for NCEP, ERA15 and NASA reanalysis. The lightest shading starts at* 9×10^7 s^{-1}. *The contour interval is* 1.5×10^7 s^{-1}. *Right column: OLR variability, represented by the standard deviation of brightness temperature, from satellite observations and each reanalysis. The lightest shading starts at 5 K. The contour interval is 1.25 K, darker shading indicating larger values (adapted from Newman et al., 2000).*

wavenumber 63 resolved on 28 vertical levels, instead of 106 zonal waves and 31 vertical levels resolved in ERA15. However, both datasets describe the overall characteristics of the IO, as shown in unfiltered daily 200 hPa velocity potential anomalies for the winter and spring seasons 1984/1985, 1985/1986 and 1987/1988 (Figure 2.2). Four IO events are present in every DJFMAM season. The weakest IO activity occurs in December and the strongest during February and March. The strongest amplitudes occur in the eastern

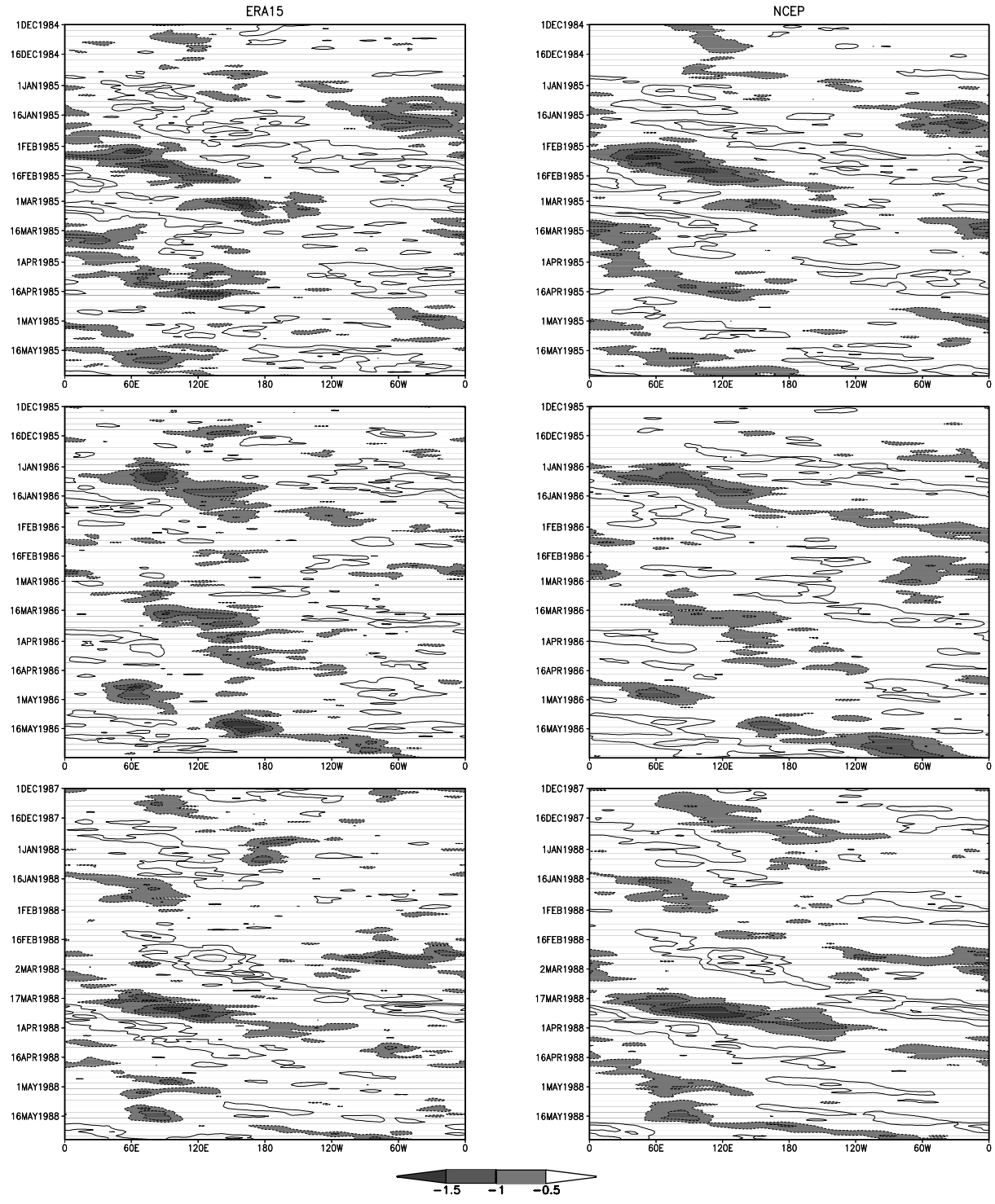

Figure 2.2: *Hovmöller diagrams of 200 hPa velocity potential anomaly [10^7 $m^2 s^{-1}$] averaged between 10°N and 10°S during northern winter and spring 1984/1985 (top), 1985/1986 (middle) and 1987/1988 (bottom) for ERA15 (left) and NCEP (right). Contour interval is 0.5×10^7 $m^2 s^{-1}$ with negative values dashed.*

hemisphere. The structure of every IO in both reanalyses resembles the observations derived from ECMWF analysis (see Figure 1.2). The amplitude is slightly stronger in NCEP, especially during 1984/1985 and 1987/1988. Hovmöller diagrams of ERA15 and ECHAM4 200 hPa velocity potential anomalies for the whole analyzed period 1984-1988 are presented in Appendix B.

As stated in the previous chapter, a suitable representation of the vertical moisture profile is essential for the representation of the IO. The vertical profiles of pentads – i.e. 5-day means – of radiosonde measurements at Singapore airport during the passage of an IO in March 1988 (Figure 2.3) are compared to reanalyses data at the corresponding grid

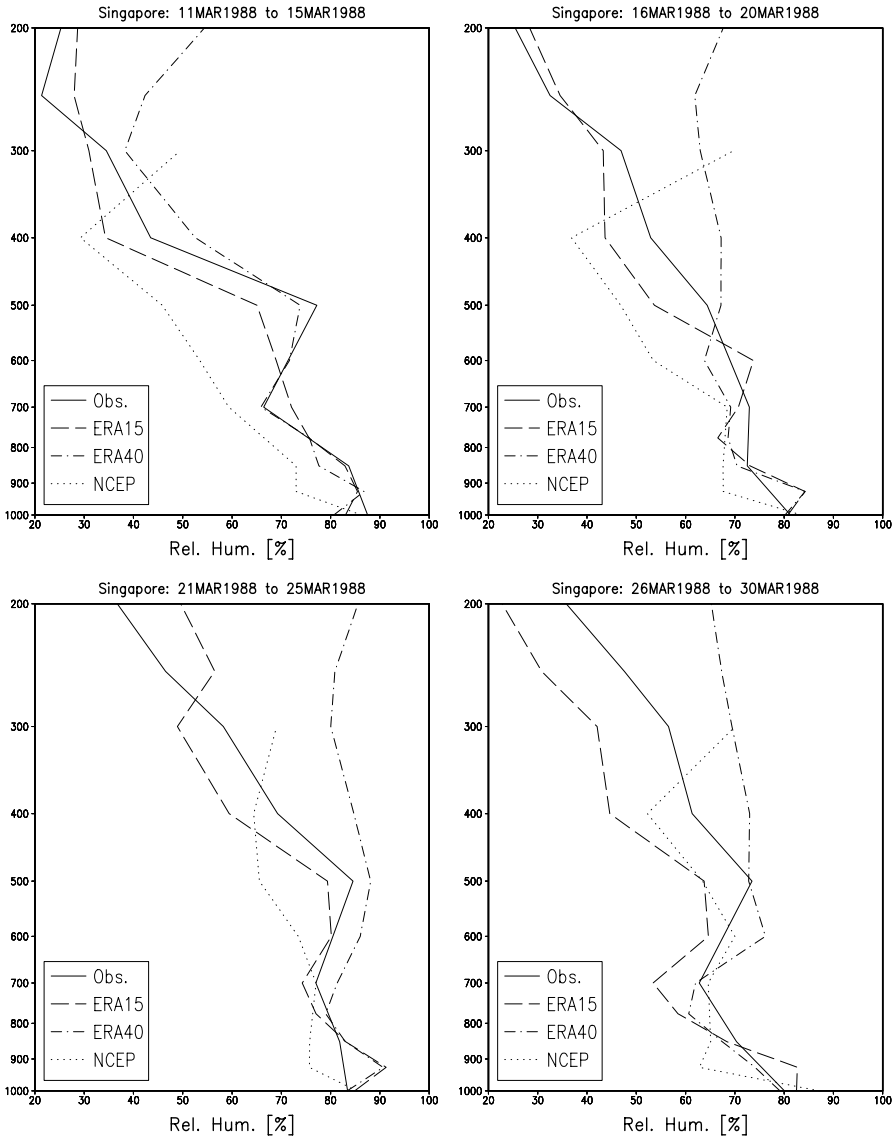

Figure 2.3: *Relative humidity during the passage of an IO in March 1988 at Singapore airport (1°22'N and 103°59'E) for radiosonde measurements (solid), ERA15 (dashed), ERA40 (dash-dotted) and NCEP (dotted).*

points. This period is also analyzed by Matthews et al. (1996) and Sperber et al. (1997). In addition to the NCEP and ERA15 reanalyses, preliminary inofficial results of the new ERA40 reanalysis are presented. The NCEP reanalysis is only available up to 300 hPa height. It overestimates the relative humidity in the upper troposphere. In the lower troposphere, where the moisture content is important for the wave-CISK mechanism to occur (see Section 1.3), the relative humidity is underestimated in NCEP. ERA40 follows the observations in the lower troposphere, but overestimates the relative humidity above 450 hPa height in the depicted period. ERA15 slightly underestimates the relative humidity between 500 and 300 hPa height.

Since the ERA15 reanalysis produces the most appropriate intraseasonal variability in OLR and relative humidity it is used in the following section to analyze the IO in fields that are not available in observations. The NCEP reanalysis will only be used in the study of interannual variability of the IO in Section 3.3 for periods where ERA15 and ERA40 data are currently not available.

2.2 Analysis of the IO in ERA15

The previous section indicates that the bandpass filtered 200 hPa divergence field is too noisy for a statistical analysis of the IO in the reanalyses data. The 200 hPa equatorial velocity potential between 10°N and 10°S is more appropriate due to the zonal wavenumber-one structure. Daily ERA15 data of the 5 years period 1984 to 1988 are used to perform a POP analysis (see Appendix C). The seasonal cycle of the data has been removed prior to POP analysis by subtracting multi-year monthly means from the original daily data as described in Hayashi and Golder (1988). A Fourier time filter with cosine tails is used for the bandpass-filtering. The reason for the cosine tails is to suppress erroneous secondary maxima that might occur for a pure rectangular filter (Gallagher et al., 1991). Many observational and modeling studies use a 20-100 day filter (e.g. Slingo et al., 1996). The present filter has a 20-100 day window with filter weights of zero below periods of 15 days and above 110 days, weights of one between 25 and 90 days and cosine tails between 15 and 25 days, and 90 and 110 days.

The top two panels in Figure 2.4 illustrate the spectra of the real and imaginary part of the dominant POP coefficient (left) and their squared coherence (right) (e.g. von Storch and Zwiers, 1999). Only periods between 10 and 100 days are depicted, since periods outside this domain are too strongly influenced by the bandpass filter. Chunk lengths

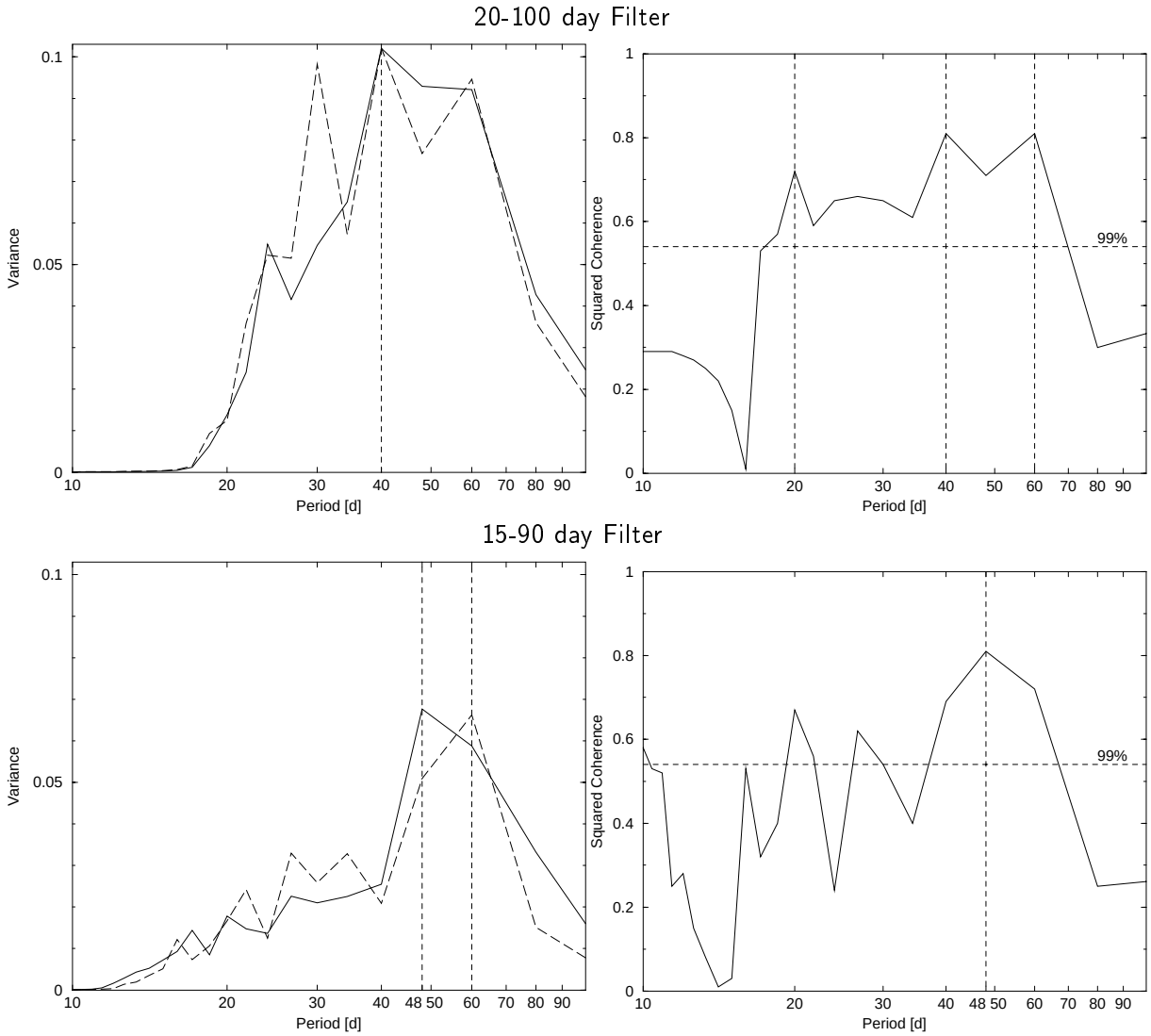

Figure 2.4: *Spectra of the real (solid line) and imaginary (long dashed line) dominant POP mode (left) and their squared coherence (right). The vertical dashed lines indicate the maxima. The horizontal dashed line depicts the 99% confidence interval of the squared coherence. Top: 20 to 100 day filtered data, bottom: 15 to 90 day filtered data.*

of $240/n$ days with $n \in \mathbb{N}$ are used to smooth the spectra. Both the spectra of the real and imaginary part reveal a maximum at 40 days. The squared coherence of both time series highlights the oscillation of both patterns. It depicts maxima at 40 and 60 days and a secondary maximum at 20 days. This secondary maximum is also found by Hayashi and Golder (1993) in observations during the first GARP global experiment (FGGE) in 1979. Sui and Lau (1989) showed with a simple dynamical model that the "fast" wave is excited by deep convection that has a heating maximum at or above the 500 hPa level. The "slow" wave is excited by heating maximized in the lower troposphere between 500 and 700 hPa. The occurrence of the secondary maximum in the cosine tail of the filter

induces reflections at the borders of the filter and might be responsible for the noisy structure of the spectrum of the imaginary POP coefficients. To avoid the noise and to take the secondary maximum into account, the filter window is changed to 15-90 days. The cosine tails are placed between 10 and 20 days and 80 and 100 days in this case. Now the spectra of the dominant POP coefficients have a distinct peak. It occurs at the 48 days period for the real part and 60 days for the imaginary (Figure 2.4, bottom left). Since the squared coherence of the spectra (Figure 2.4, bottom right) is used when the real and imaginary spectra differ from each other, the 48 day peak should be considered as the period of the dominant POP mode, although all periods between 37 and 67 days are well above the 99% confidence interval. The 99% confidence interval, which indicates the deviation from the normal distribution, is determined with an F test (von Storch and Zwiers, 1999).

The depicted dominant POP mode has an e-folding time of 56 days and its explained variance amounts to 23.8%. The relative phase of the imaginary and the real part appears to be around -90°(not shown), indicating that the imaginary part leads the real part, as theoretically expected (see Appendix C). Following von Storch et al. (1988) and Gualdi et al. (1997), the dominant complex POP coefficients that form an oscillation period, are used to obtain eight composites of 45° segments. Each of these composites represents a different phase of the oscillation. Only values of the complex POP coefficients with an amplitude larger than the mean amplitude plus 0.8 times the standard deviation are considered. These composites include about two to three events per year.

The compositing study is used to describe a typical IO in the reanalysis data and to compare ERA15 OLR with OLR observations available as pentad means in a horizontal resolution of 2.5°×2.5°, that are derived from NOAA satellite data. The eight POP phases of the unfiltered 200 hPa velocity potential anomaly (contour) are shown in Figure 2.5 with the NOAA OLR anomaly and in Figure 2.6 with ERA15 OLR anomaly. The time step from one panel to the next is 6 days. Strong negative OLR anomalies (shaded) indicate deep convective anomalies. The panels represent a kind of pseudo-Hovmöller diagram (von Storch et al., 1988) with time running from top to bottom. Since the POP coefficients are derived by the bandpass-filtered velocity potential and the observed OLR is only available as pentad means, the peaks of the POP coefficients do not necessarily match with the unfiltered datasets. A running mean over a 5-day window is used for the described datasets to diminish this effect. An additional advantage of the running mean is to accentuate the mean state of each segment.

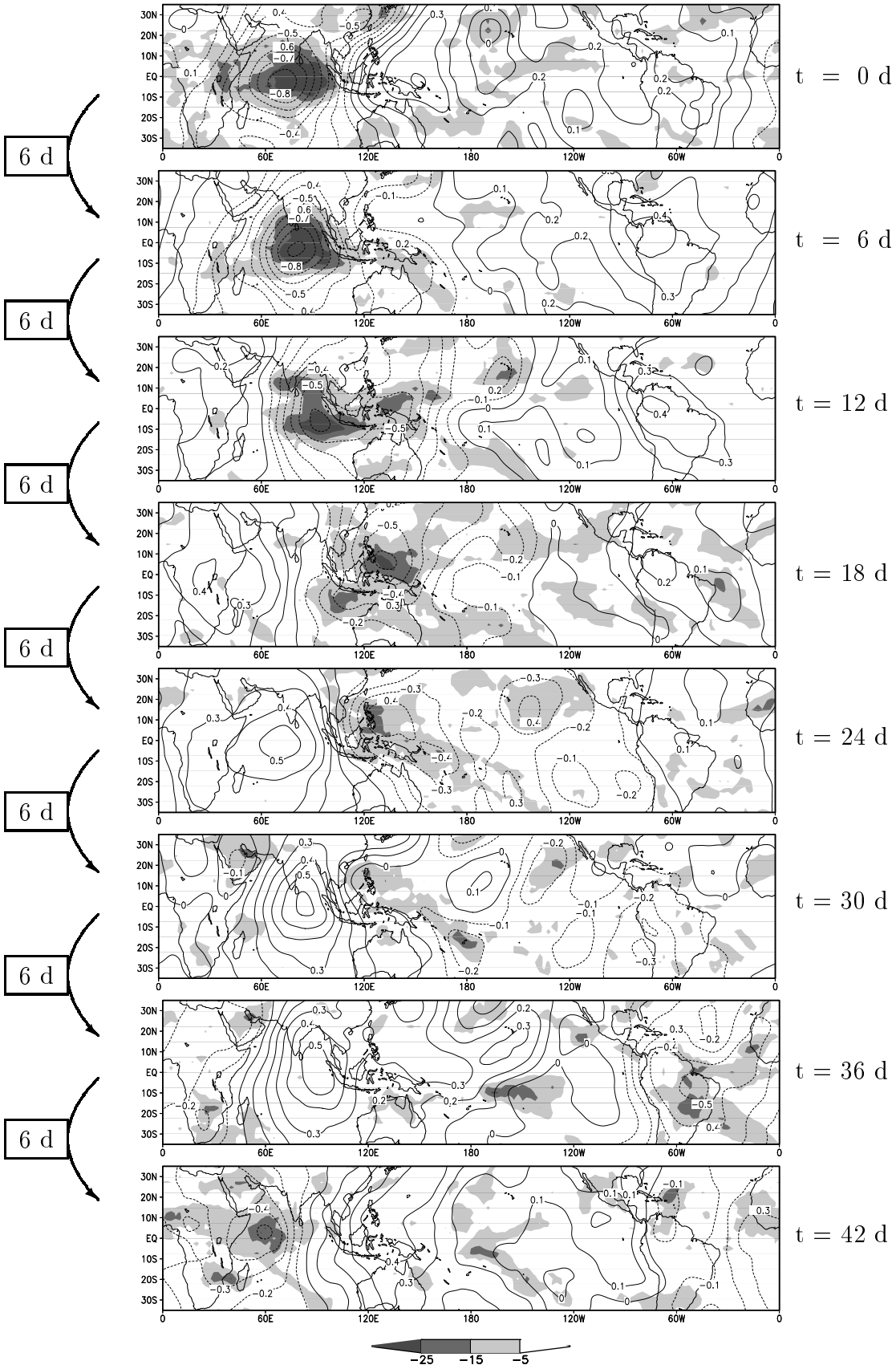

Figure 2.5: *Pseudo-Hovmöller diagrams of NOAA OLR anomaly [W m^{-2}] and ERA15 200 hPa velocity potential anomaly [10^7 m^{2}s^{-1}]. Negative OLR anomaly (shaded) indicates deep convective anomalies, and negative velocity potential anomaly (dotted) indicates large-scale divergent flow. Arrows on the left and the scale on the right point out the time step between the panels as derived by the POP analysis.*

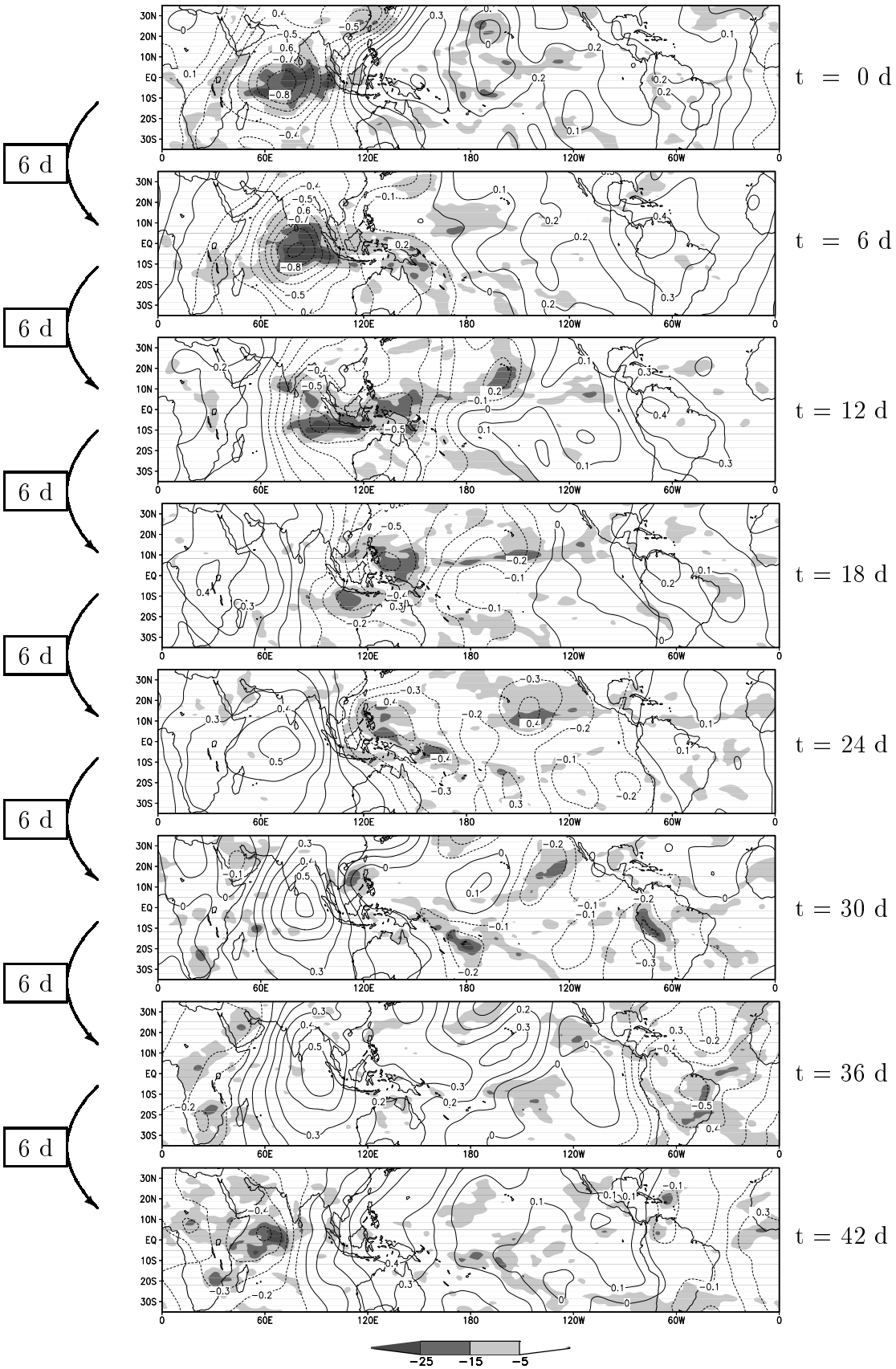

Figure 2.6: *As Figure 2.5, but for ERA15 OLR.*

The variance of OLR anomaly is slightly weaker in the reanalysis than in the satellite data, but the IO pattern is well represented in both datasets. A POP analysis of NOAA and ERA15 OLR would be a more direct way to compare both datasets, but OLR data are, even after filtering, too noisy for a firm POP analysis, since the dominant POP mode explains less than 9% of the total variance in both datasets (not shown). Figures 2.5 and 2.6 resemble the oscillation described by Madden and Julian (1971, 1972) and other authors. The onset, growing, eastward propagation and decay of the OLR anomaly is consistent with those presented in Figure 1.1. Also the 200 hPa velocity potential anomaly shows slow propagation of the large-scale divergent flow in phase with the OLR anomaly during the convective regime and faster propagation out of phase with the OLR during the dry regime. A secondary maximum of convective anomalies and large-scale divergent flow occurs over eastern tropical South America (panel seven) that might slow down the IO in this area (Matthews, 2000).

The SST increases before the passage of the IO convection center and decreases after its passage due to enhanced surface shortwave flux to the east of the convection and enhanced latent heat flux coincident with the convection and to the west of it (Lau and Sui, 1997; Waliser et al., 1999b). High SSTs to the east of the convection increase the meridional moisture flux convergence, which activates the wave-CISK mechanism and leads to the eastward propagation of the super cloud cluster (see Section 1.3). ERA15 is forced with observed weekly optimum interpolated SST (OISST) data (Reynolds and Smith, 1994). Figure 2.7 depicts composites of the OISST anomalies corresponding to the first four panels in Figures 2.5 and 2.6. The amplitude of about 0.1 K is lower than the expected 0.1 to 0.5 K from TOGA Tropical Atmosphere Ocean project (TAO) observations (Kessler et al., 1995; Jones et al., 1998), due to the compositing process. The first panel shows the positive SST anomaly over the Indian Ocean that forms the deep convective anomaly. Panels two to four describe the cooling below and to the west of the deep convective anomalies over the Indian Ocean and a slight warming to the east of the deep convective anomalies over the maritime continent, consistent with the air-sea interaction depicted in Figure 1.5 c.

The syntheses of the individual IO events are somewhat complicated because of the great diversity of the phenomenon (Wang and Rui, 1990b), e.g. the propagation speed and the location of main IO activity differ from event to event. Averaging over many IO events might lead to an incorrect picture, since local disturbances are compared that might belong to different IO events. Additionally, the IO signal is harder to detect in a composite study due to the smoothed peaks after averaging. Hence, in addition to the

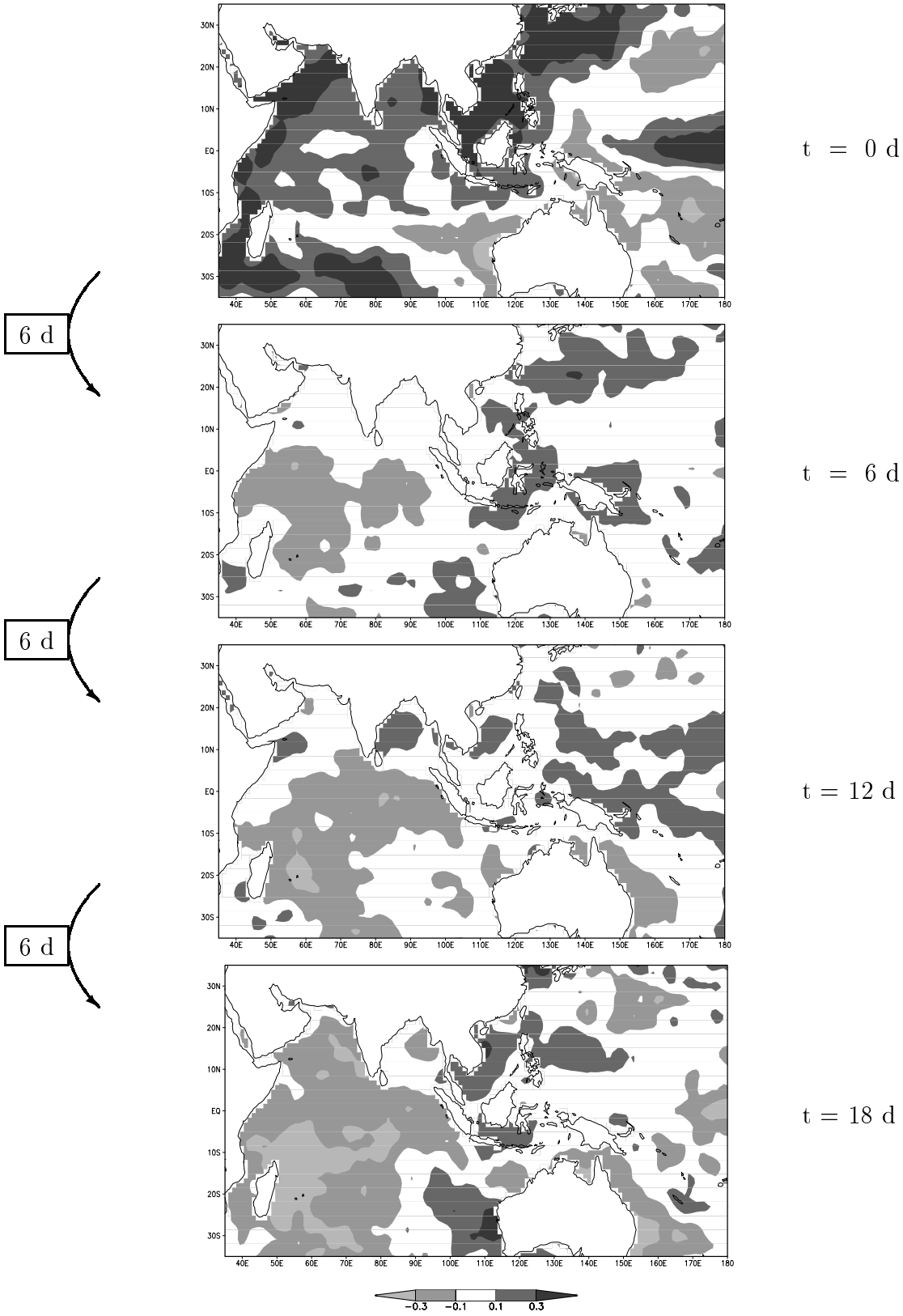

Figure 2.7: *Pseudo-Hovmöller diagrams of observed OISST anomaly [K] during the convective regime, as described by the first four panels in Figures 2.5 and 2.6.*

POP analysis, this study utilizes case studies to compare individual events of different datasets. It is important to note that case studies lack statistical significance, and thus are only valid for the presentation of existing mechanisms. Numerical values are only discussed, if they are representative for the whole dataset.

For the detection of a representative IO event it is important to find an index that describes the activity of the IO. Many indices have been discussed before, e.g. the power spectrum of eastward propagating OLR waves with wavenumbers one to three described by Salby and Hendon (1994), the variance within a 100-day moving window of 200 hPa zonal mean zonal wind ($\overline{u_{200}}$) established by Slingo et al. (1996) and Slingo et al. (1999), and the 100-day running mean of the squared amplitude of the POP coefficients of 200 hPa velocity potential anomaly (Gualdi et al., 1999). These indices seem to be useful in representing the interannual variability in the activity of the IO, but they are temporally too coarse to coincide with a single oscillation.

According to Slingo et al. (1999), who tested several indices, an EOF analysis of the 15-90 day bandpass filtered daily 200 hPa velocity potential anomaly between 10°N and 10°S is performed. The first EOF (Figure 2.8) shows the dominant circulation anomalies produced when the active phase of the IO is located over the eastern Indian Ocean and the western Pacific (Slingo et al., 1996). It explains 37.0% of the total variance. The minimum is located at 140°E, indicated by the dark shading. Figure 2.9 shows the corresponding first principal component (PC1), normalized by its standard deviation. High values of PC1 indicate the presence of typical IOs, but it has to be kept in mind that the dominant EOF mode can not be regarded as an index of the full IO activity, since one EOF cannot describe the propagating features.

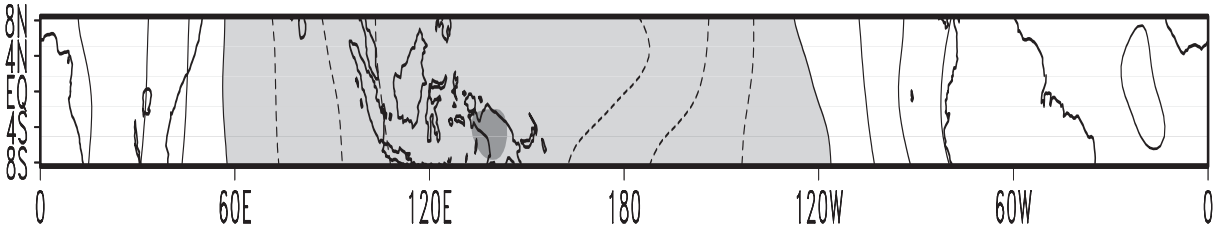

Figure 2.8: *ERA15 first EOF of 200 hPa velocity potential anomaly in the equatorial region. Contour interval is 0.005, negative values are light shaded and the minimum at 140°E is indicated by dark shadings. The EOF pattern explains 37.0% of the total variance.*

The maximum of PC1 occurs on the 23rd of March 1988. The corresponding IO is taken as a case study. This is consistent with the studies by Salby and Hendon (1994), Sperber et al. (1997), Slingo et al. (1999) and Gualdi et al. (1999), who also detected strong IO activity during spring 1988. Matthews et al. (1996) investigated the interaction of the SPCZ and the IO by means of this event.

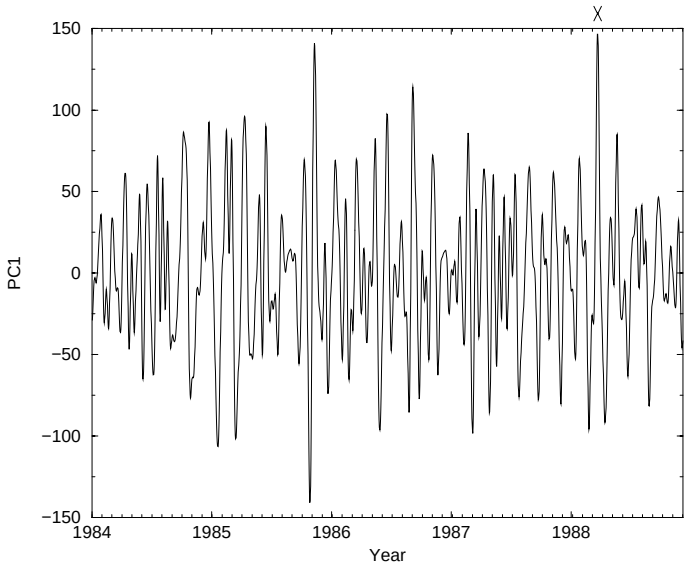

Figure 2.9: *ERA15 PC1 which is used as an index of the activity of the IO (Slingo et al., 1999). X marks the maximum at the 23rd of March 1988 as an identifier for a typical IO.*

The EOF-based index reflects the interannual variability very well compared to the $\overline{u_{200}}$-variance index (Figure 2.10, left) by Slingo et al. (1996) and the POP-coefficient index (Figure 2.10, right) by Gualdi et al. (1999). Slingo et al. (1996) showed that the zonal mean of the upper tropospheric zonal wind responds to the IO with a transition from the mean westerlies in northern winter to strong easterlies, associated with the active phase of the IO. This can be seen for example in spring 1988 in Figure 1.2 (corresponding to Figure 6 in Slingo et al., 1996). However, the $\overline{u_{200}}$-variance index should by handled with care, because it does not take zonal variations of the zonal wind into account. The eastward shift of the main IO activity and the associated strong easterlies and negative velocity potential anomalies during spring 1987 are accompanied by strong positive velocity potential anomalies and associated strong westerlies over the Indian Ocean at the same time. Both zonal wind patterns cancel out each other in the zonal mean field, leading to the underestimation in the $\overline{u_{200}}$-variance index in 1987 (Figure 2.10 left, corresponding to Figure 14 in Slingo et al., 1996). Hence, only the IO index of the POP coefficients of 200 hPa velocity potential anomalies is used in the further study.

The maximum in the POP coefficient index occurs during spring 1985 instead of spring

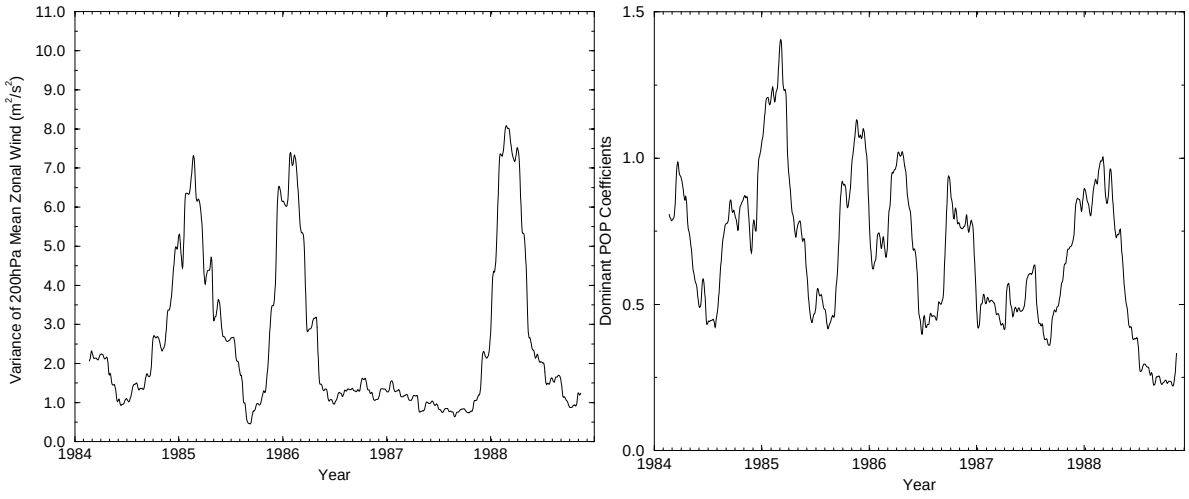

Figure 2.10: *ERA15 $\overline{u_{200}}$-variance averaged between 10°N and 10°S within a 100-day moving window (left) and 100-day running mean of the squared amplitude of the POP coefficients of 200 hPa velocity potential anomalies (right), both reflecting the interannual variability of the IO activity.*

1988, which illustrates the effects of the filtering with the 100-day running mean and the difference between the EOF pattern and the POP. Unlike the PC1 index, the POP coefficient index is already smoothed, since the POP analysis is performed with EOF-filtered data (see Appendix C). Appendix B shows the time-longitude Hovmöller diagrams of unfiltered 200 hPa velocity potential anomalies for ERA15 and the GCM experiments. This is currently the best way to represent the interannual variability of the IO, since each IO event and its zonal position is presented.

The weak IO activity during 1987 in the present indices is related to weak convective activity over the Indian Ocean due to the concurrent El Niño, as suggested by Gualdi et al. (1999). However, Figure 1.2 suggests an eastward shift of IO activity prior to and during an El Niño event. This feature is also present in Figure B.3. The shift is not captured by the present indices, which depend on the dominant spatial pattern of the IO activity. The teleconnections associated with the transition from the 1987 El Niño to the 1988 La Niña and the concurrent westward shift of the west Pacific warm pool due to a downwelling Rossby wave are described by Picaut and Delcroix (1995).

In the present indices, strong IO activity occurs prior to the La Niña in 1988, as indicated in Figure 2.11 by the NINO3 (the region between 150°W, 90°W, 5°N and 5°S) sea surface temperature anomaly (SSTA) of the observational dataset. The two vertical lines mark 20 days before and 40 days after the maximum in PC1, respectively. This feature is a hint that the present indices do not capture a possible zonal shift of the IO with the

Figure 2.11: *Monthly mean NINO3 SSTAs [K] and the PC1 maximum (20 days before and 40 days after the maximum, indicated by the two vertical lines).*

ENSO cycle. Although the detected IO activity is strongest at the time of steepest NINO3 SSTA decrease, other strong IO events occur in 1985 and 1986, which are not related to the ENSO cycle. During the mature phase of La Niña during northern summer after the onset of the monsoon, the ITCZ is shifted north of the equator (Figure 2.12). Wang and Rui (1990a) showed that the growth rate of equatorial Kelvin waves decreases substantially when the SST maximum shifts northward to 7.5° N. At that time the deep convection north of the equator generates only weak equatorial Kelvin waves, and therefore the IO activity shifts northward and decreases (Salby et al., 1994) or turns into an east-north mode (Wang and Rui, 1990b) instead of propagating further eastward.

In addition to the POP analysis and the general description of the detected IO event, longitude-time Hovmöller diagrams are used to investigate the onset and characteristics of the IO in time and space. Figure 2.13 (top) presents the negative OLR anomalies for NOAA satellite observations and ERA15 reanalysis data, respectively. The data of 20 days before and 40 days after the maximum of PC1 are depicted meridionally averaged between 10°N and 10°S. The maximum of convective anomaly is indicated by negative OLR anomaly. Since the NOAA data are only available as pentads, the reanalysis and GCM OLR data used in this study are also averaged to 5-day means. All other data are daily mean values. The latent heat flux anomaly of ERA15 is added to both panels. The main characteristics of the OLR anomaly are well represented by ERA15. The super cloud cluster propagates eastward over the Indian Ocean and the West Pacific between 60°E and 150°E during March 16th to 26th for the detected IO event and during April 18th to

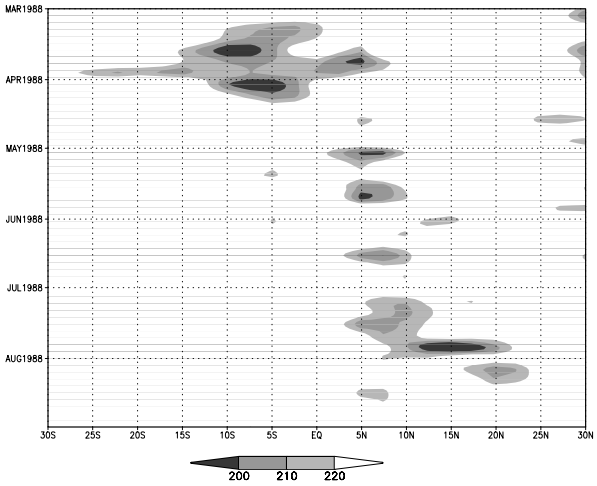

Figure 2.12: *Time-latitude Hovmöller diagram of NOAA OLR [W m^{-2}] over the West Pacific warm pool averaged between 120°E and 180°E. Dark shading indicates deep convective anomalies.*

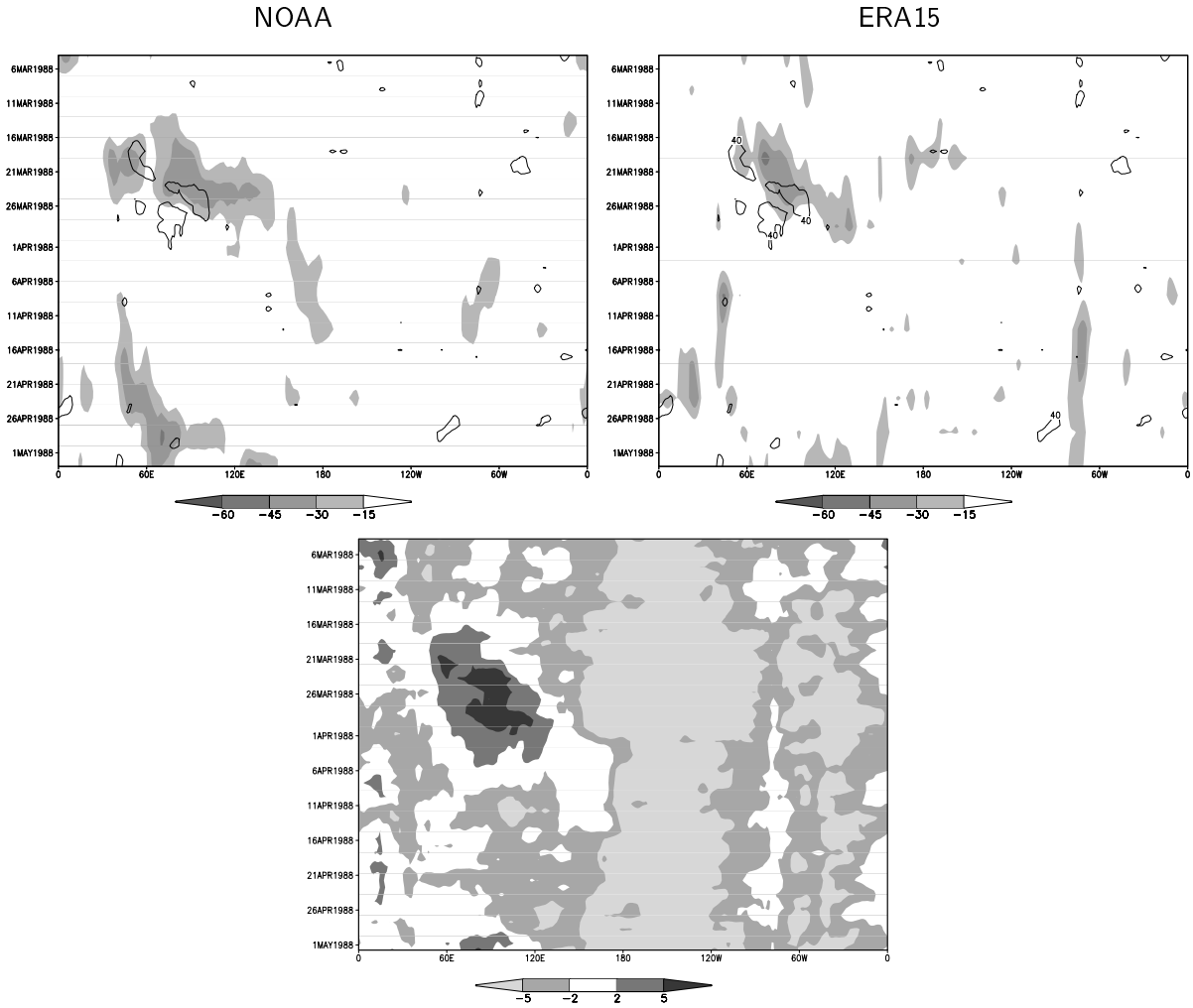

Figure 2.13: *Top: NOAA (left) and ERA15 (right) OLR anomalies [W m^{-2}] (shaded), contour: 40 W m^{-2} isoline of ERA15 latent heat flux anomaly. Bottom: ERA15 850 hPa zonal wind [m s^{-1}]. All data are averaged between 10°N and 10°S.*

May 1st for a subsequent event. The slow decay of convective anomalies for the detected IO between 150°E and the date line is hardly detectable in the reanalysis data. Non-propagating convection anomalies occur around 70°W and 0°W over the South American and West African rainforest, respectively. The latent heat flux anomalies below and to the west of the deep convective anomalies indicate the presence of the wave-CISK mechanism in ERA15 (Sperber et al., 1997). The WWBs between 50°E and 120°E (Figure 2.13, bottom), which induce the positive latent heat flux anomalies, occur slightly after the passage of the IO.

The present chapter compares different reanalysis datasets. The ERA15 reanalysis is further analyzed, since it represents observational data such as OLR most realistically. The reanalysis data are used for variables for which no sufficient observations are available. The 200 hPa velocity potential anomaly is used to detect the IO in ERA15. The POP analysis shows that the IO in the ERA15 reanalysis has a mean period of 48 days during the analyzed 5-year period 1984-1988. A composite study points out the existence of a relatively slow propagation of the IO during the convective regime and a faster propagation during the dry regime. In the convective regime, colder SSTs below and to the west of the convection and warmer SSTs to the east of the convection are found. The influence of the IO on the low-level wind field, as suggested by the wave-CISK theory, is also present in the ERA15 reanalysis.

Chapter 3

The IO in ECHAM4 and ECHAM4/OPYC3

This chapter describes the ability of the ECHAM4 AGCM with T42 horizontal resolution and 19 vertical levels (ECHAM4 T42L19) to represent the IO. For a detailed description of the ECHAM GCM, the reader is referred to Roeckner et al. (1996a) and Roeckner et al. (1992). The ECHAM4 AGCM is forced with monthly-mean AMIP SSTs. For the investigation of possible impacts of air-sea interaction, the ECHAM4 T42L19 AGCM is coupled to the OPYC3 OGCM (ECHAM4/OPYC3; Roeckner et al., 1996b; Bacher et al., 1998). In addition, the interannual variability of the IO, especially the interaction with the ENSO cycle, is investigated with 20 years of daily reanalyses data and pentad NOAA OLR. The ENSO cycle is simulated by the ECHAM4/OPYC3 CGCM. Hence, the interannual variability of the IO is also analyzed with 100 years of this coupled simulation. Since the IO indices by Slingo et al. (1996) and Gualdi et al. (1999) do not represent zonal variations of the main IO activity during the ENSO cycle, the interaction of the IO and ENSO is described with time-longitude Hovmöller diagrams.

3.1 ECHAM4 T42L19

Gualdi et al. (1997) studied the simulation of the IO in previous ECHAM GCM versions. In these versions, the closure for deep convection and organized entrainment in the convective mass flux scheme is based on moisture convergence (Tiedtke, 1989). As shown in Section 1.4, Slingo et al. (1996) emphasized the advantage of a closure scheme for organized entrainment based on buoyancy for the simulation of the IO in GCMs. In

ECHAM4, this is included together with an adjustment-type closure for deep convection (Nordeng, 1996). The ability of ECHAM4 to simulate the IO was previously analyzed by Gualdi et al. (1999). They used an ensemble of 15 experiments with the relatively low T30 horizontal resolution to investigate the interannual variability of the IO. The characteristics of the simulations are an erroneous eastward shift in the main IO activity and a too fast propagation speed of the IO.

To highlight these model deficiencies, ECHAM4 T42L19 is analyzed analogously to the ERA15 reanalysis in Section 2.2. The POP analysis is applied to 15-90 day bandpass filtered 200 hPa velocity potential anomaly between 10°N and 10°S. The spectra of the real and imaginary parts of the dominant POP mode (Figure 3.1 left) reveal a peak at the 34-day period in both time series, indicated by the vertical dashed line. Their squared coherence (Figure 3.1 right) provides a somewhat noisy spectrum. The peak occurs at the 18-day period, which is in the cosine tail of the filter window (see Section 2.2) and could be regarded as an erroneous maximum (Gallagher et al., 1991). However, the large amount of energy between 18 and 24-day periods and at 34-day periods leads to a bimodal squared coherence with all periods between 15 and 38 days above the 99% confidence interval. The bimodal structure is also found in the GFDL GCM, but with a more pronounced peak at longer periods thus better resembling the observations (Hayashi and Golder, 1993). In the present dataset, the secondary maximum at 34 days is close to the peak in the spectra, and thus considered as the propagation speed of the simulated IO.

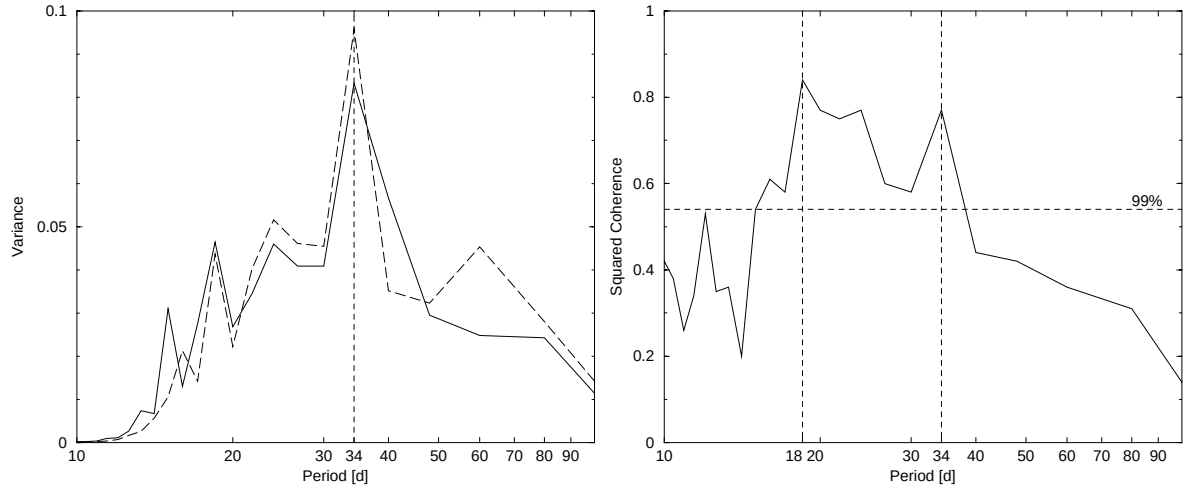

Figure 3.1: *ECHAM4 T42L19: Spectra of the real (solid line) and imaginary (long dashed line) dominant POP mode (left) and the corresponding squared coherence (right). The vertical dashed lines indicate the maxima. The horizontal dashed line depicts the 99% confidence interval of the squared coherence.*

The dominant mode explains 49.8% of the total variance of the data, which is considerably more than the variance explained by the corresponding dominant POP mode in the reanalysis data. The e-folding time of 58 days resembles the reanalysis data. The high ratio of e-folding time to period indicates the too far eastward extension of large amplitudes, and the larger portion of explained variance indicates less variability in the simulated IO than in the reanalysis data.

The eight composites obtained from the dominant POP mode are depicted in Figure 3.2. The increment from one panel to the next is about 4.3 days. Compared to OLR observations and reanalysis data (see Figures 2.5 and 2.6), the model produces a more distinct oscillation. The onset, growing and eastward propagation are simulated at the right phase during the convective regime. The onset of eastward propagating convection cells occurs too far eastward, and the propagation of the super cloud cluster also fades away too far eastward over the eastern Pacific. This seems to be due to the erroneous underestimation of convective anomalies over the maritime continent, most obvious in panel two. Observations show a weaker discharge of the convective instability over the maritime continent due to the strong diurnal cycle of convection over land in this area (e.g. Rui and Wang, 1990; Salby and Hendon, 1994; Zhang and Hendon, 1997). A consequence of the eastward shift is an eastward shift of the SPCZ in panels four to six. Noteworthy is the relatively slow propagation of the signal in the convective regime, due to the strong influence of deep convection. Unlike OLR observations and reanalysis velocity potential, the slow propagation of the IO occurs stepwise in the West and Central Pacific in panels one to three, over equatorial South America in panels four to six, and again in the second minimum of the velocity potential anomaly in panels six to one. In contrast to the reanalysis data, the convection and the upper-troposphere divergent flow are nearly always in phase. The second minimum of the velocity potential anomaly over the South American rainforest is stronger than in the observations. This reinforcement in convection explains the relative decrease in phase speed of the simulated IO over this region.

The strongest IO activity, as represented by the first EOF of the 15-90 day bandpass filtered 200 hPa velocity potential anomaly, occurs slightly west of the date line at 170°E (Figure 3.3). Thus, it is shifted eastward compared to the reanalyses data, as previously shown by the POP analysis. The pattern of the first EOF explains 34.7% of the total variance. Figure 3.4 (left) shows the PC1 time series and Figure 3.4 (right) illustrates the 100-day running mean of the squared amplitude of the POP coefficients. The PC1 time series and the POP index both show the presence of the interannual variability of the IO in the model, but the main activity occurs too late during the year, appearing in spring

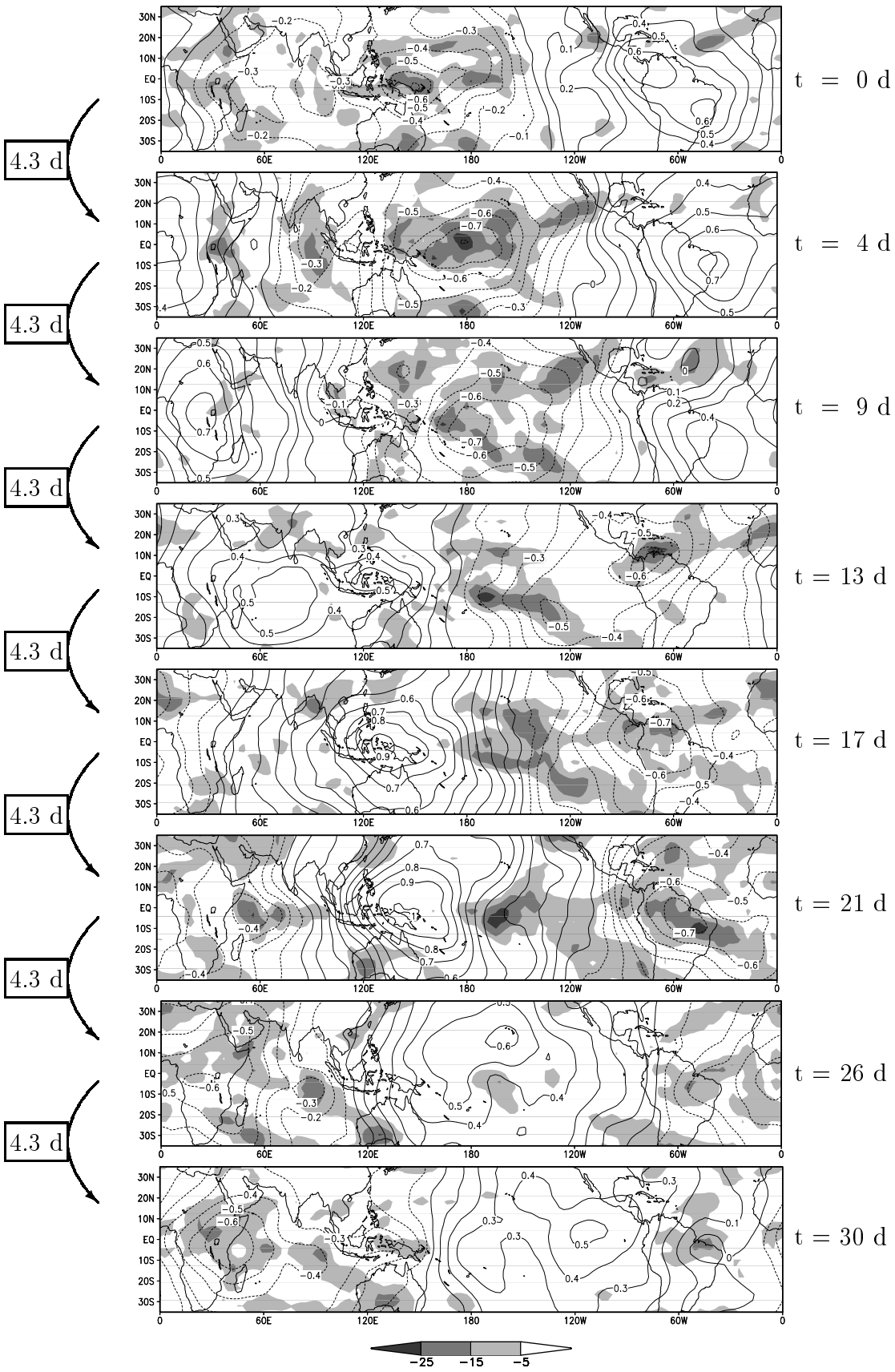

Figure 3.2: *Pseudo-Hovmöller diagrams of ECHAM4 T42L19 OLR anomaly [W m^{-2}] and 200 hPa velocity potential anomaly [10^7 $m^2 s^{-1}$]. Negative OLR anomaly (shaded) indicates deep convection, and negative velocity potential anomaly (dotted) indicates large-scale divergent flow. Arrows on the left and the scale on the right point out the time step between the panels as derived by the POP analysis.*

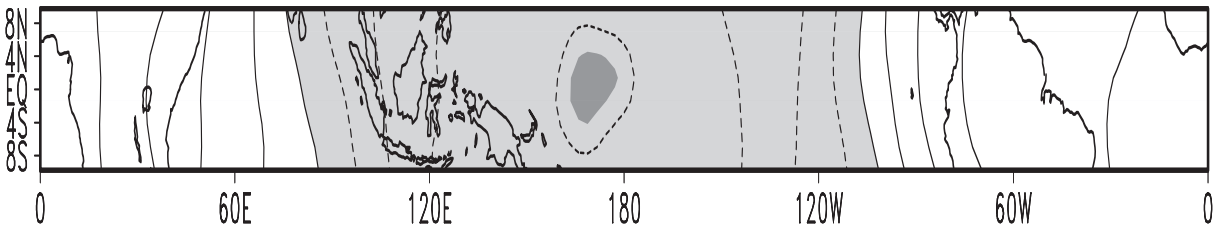

Figure 3.3: *ECHAM4 T42L19 first EOF of 200 hPa velocity potential anomaly in the equatorial region. Contour interval is 0.01, negative values are light shaded and the minimum at 170°E is indicated by dark shadings. The EOF pattern explains 34.7% of the total variance.*

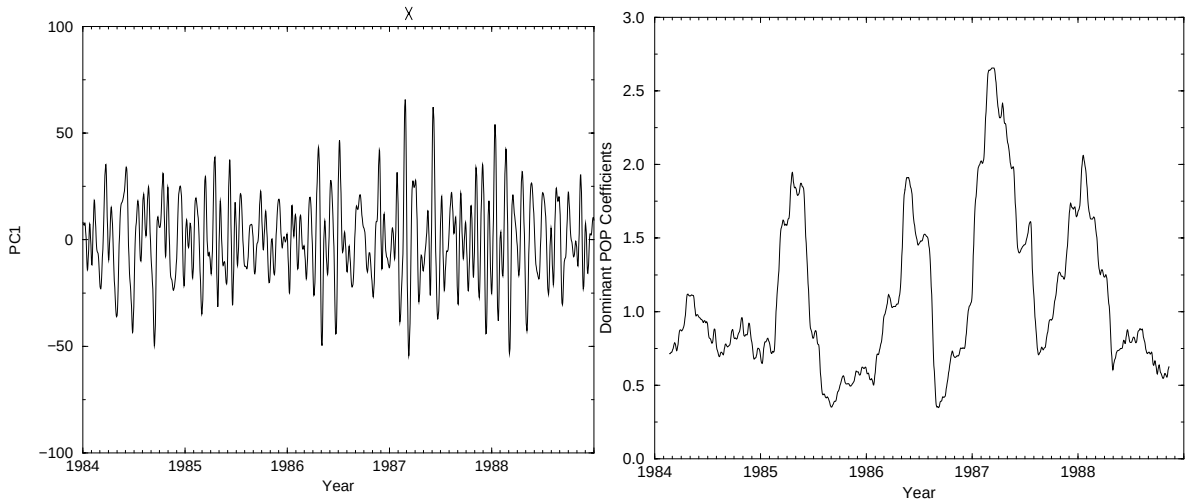

Figure 3.4: *Left: ECHAM4 T42L19 PC1, which is used as an index of the activity of the IO. X marks the maximum at the 8th of March 1987 as an identifier for a typical IO. Right: 100-day running mean of the squared amplitude of the POP coefficients of 200 hPa velocity potential anomalies, reflecting the interannual variability of the IO activity.*

and summer instead of winter and spring as in the reanalyses data.

The maximum of PC1 occurs on March 8th 1987. Slingo et al. (1996) also found, as shown in their Figure 15, that the GLA and the UKMO GCMs have their maximum IO activity during the 1987 season. Observations and ERA15 data show an eastward shift of the IO activity during this El Niño year (Slingo et al., 1996; Gualdi et al., 1999). This indicates the eastward shift of the simulated IO activity in GLA, UKMO and ECHAM4, which leads to a simulation of IOs characteristic of El Niño years: The strongest activity is shifted eastward (Gualdi et al., 1999) due to the eastward extension of maximum equatorial SST (Picaut and Delcroix, 1995; Delcroix et al., 2000).

The time-longitude Hovmöller diagram of negative OLR anomaly and the positive latent heat flux anomaly from 20 days before to 40 days after the maximum of PC1 is shown in

Figure 3.5 for the NOAA OLR anomaly and the 40 W m^{-2} isoline of ERA15 latent heat flux anomaly (top left) and ECHAM4 T42L19 data (top right). The observed OLR shows the end of the convective regime of an IO during end of February 1987 with increased latent heat flux anomaly to the west due to the WWB, which occurs at the same time (Figure 3.5, bottom left). The observed IO is shifted eastward compared to the general structure of the IO, due to the relatively warm Central Pacific in this pre-El Niño condition (Figure 1.3). The OLR anomaly is restricted to a narrow band near the date line, and the eastward propagating signal is hardly detectable. However, the eastward propagation is conspicuous in the 200 hPa velocity potential anomalies in Figure B.3.

The three convective regimes of the simulated IO during end of February, middle of March

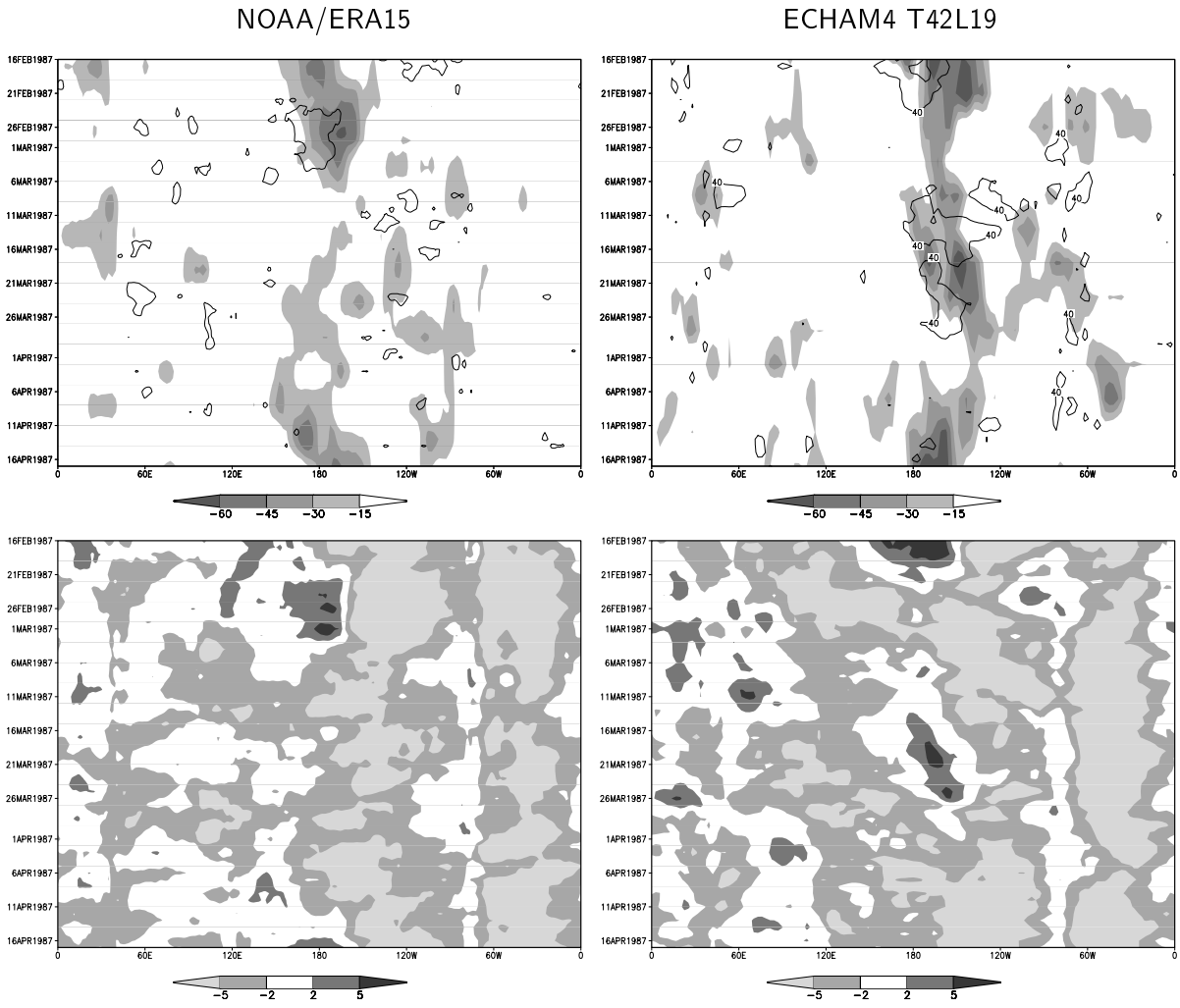

Figure 3.5: *Top: OLR anomaly [W m^{-2}] (shaded) and the 40 W m^{-2} isoline of latent heat flux anomaly. Bottom: 850 hPa zonal wind [m s^{-1}]. All data are averaged between 10°N and 10°S. Left: NOAA OLR and ERA15 latent heat flux and zonal wind, right: ECHAM4 T42L19 data.*

and beginning of April still occur too far east of the date line. The increase in latent heat flux below and to the west of the super cloud clusters as described by e.g. Lau et al. (1989) is only present during end of February for the first IO event, and during the middle and end of March 1987 for the second. In the first half of March, the increased latent heat flux also occurs to the east of the super cloud cluster, where it is not associated with distinct eastward propagation.

Figure 3.5 (bottom right) shows the two simulated WWBs related to the first two IO events around the 17th of February and the 19th of March. The WWB around the 11th of March is related to the deep convection over the Indian Ocean that is not associated with the IO. The eastern extension of the main IO activity leads to westerlies over the Andes at about 80°W. The associated stronger low-level convergence over the South American continent reinforces the convection leading to the relative decrease in phase speed of the simulated IO over this region, as presented in the composite study.

Although the general features of the IO are present in ECHAM4 T42L19, an improved simulation is desirable for a more realistic representation of the tropical climate (see Section 1.2). To compare different simulations, the ECHAM4 T42L19 experiment is referred to as the control experiment in the further studies. Since the air-sea interaction is suggested to play an important role on the propagation of the IO, the next section deals with the IO in the ECHAM4/OPYC3 CGCM.

3.2 ECHAM4 T42L19 / OPYC3

The ECHAM4 AGCM at T42 horizontal resolution has been coupled to the OGCM OPYC3 (Roeckner et al., 1996b; Bacher et al., 1998). The flux correction of the CGCM is restricted to annual means of heat and freshwater. Since the flux correction is fixed, it can not produce erroneous periodic forcings to influence the IO. The seasonal cycle simulated by the CGCM is in good agreement with that of the atmospheric model component forced with observed SSTs (Roeckner et al., 1996b; Bacher et al., 1998).

Daily 200 hPa velocity potential anomalies of the simulated 25 CGCM-years 251 to 275 are 15-90 day bandpass-filtered and analyzed concerning the ability of the CGCM to represent the IO. The spectra of the real and imaginary parts of the dominant POP coefficients show a bimodal structure with peaks for the fast mode at about 22 days and for the slow mode at 60 days for the real part and 48 for the imaginary (Figure 3.6, left). However, the spectra are quite noisy. The squared coherence reveals a clear oscillation period of the

dominant POP mode of about 27 days (Figure 3.6, right) with an e-folding time of more than 60 days, an explained variance of 54.7% and periods between 15 and 41 days above the 99% confidence interval. Thus, the IO in ECHAM4/OPYC3 is faster, less damped and has a slightly larger range of periods than the IO in the control experiment.

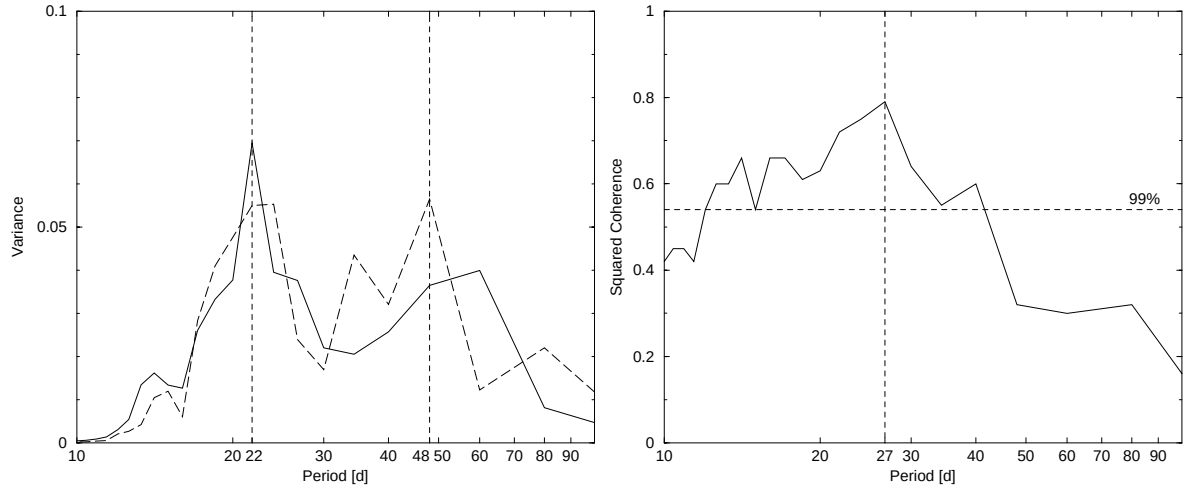

Figure 3.6: *ECHAM4/OPYC3: Spectra of the real (solid line) and imaginary (long dashed line) dominant POP mode (left) and their squared coherence (right). The vertical dashed lines indicate the maxima. The horizontal dashed line depicts the 99% confidence interval of the squared coherence.*

Figure 3.7 depicts the composites of velocity potential anomaly and OLR anomaly resulting from the POP analysis. The time step from one panel to the next is about 3.4 days. The IO in the CGCM is even more pronounced than in the AGCM. The western super cloud cluster forms a standing oscillation in the velocity potential anomaly over the Indian Ocean indicated by the local minimum in phase one and two, and the local maximum in phase five. In contrast, a study by Zhang and Hendon (1997) shows that the observed IO is not dominated by a standing oscillation. The super cloud cluster over the West Pacific warm pool grows and propagates eastward. As in the AGCM, the eastward propagation occurs too far to the east. The velocity potential anomaly is during all phases in phase with the convection, so it is not possible to distinguish between a convective and a dry regime very clearly. In all phases the two propagating cells have about the same size and propagation speed.

Figure 3.8 shows the composites of the OPYC3 SST anomalies during the convective regime that correspond to the first four panels in Figure 3.7. As implied by the patterns of the deep convection, the negative SST anomaly associated with the IO is restricted to the West Pacific warm pool. The convection over the Indian Ocean does not produce SST anomalies relevant for the eastward propagation. Compared to observations (Figure 2.7),

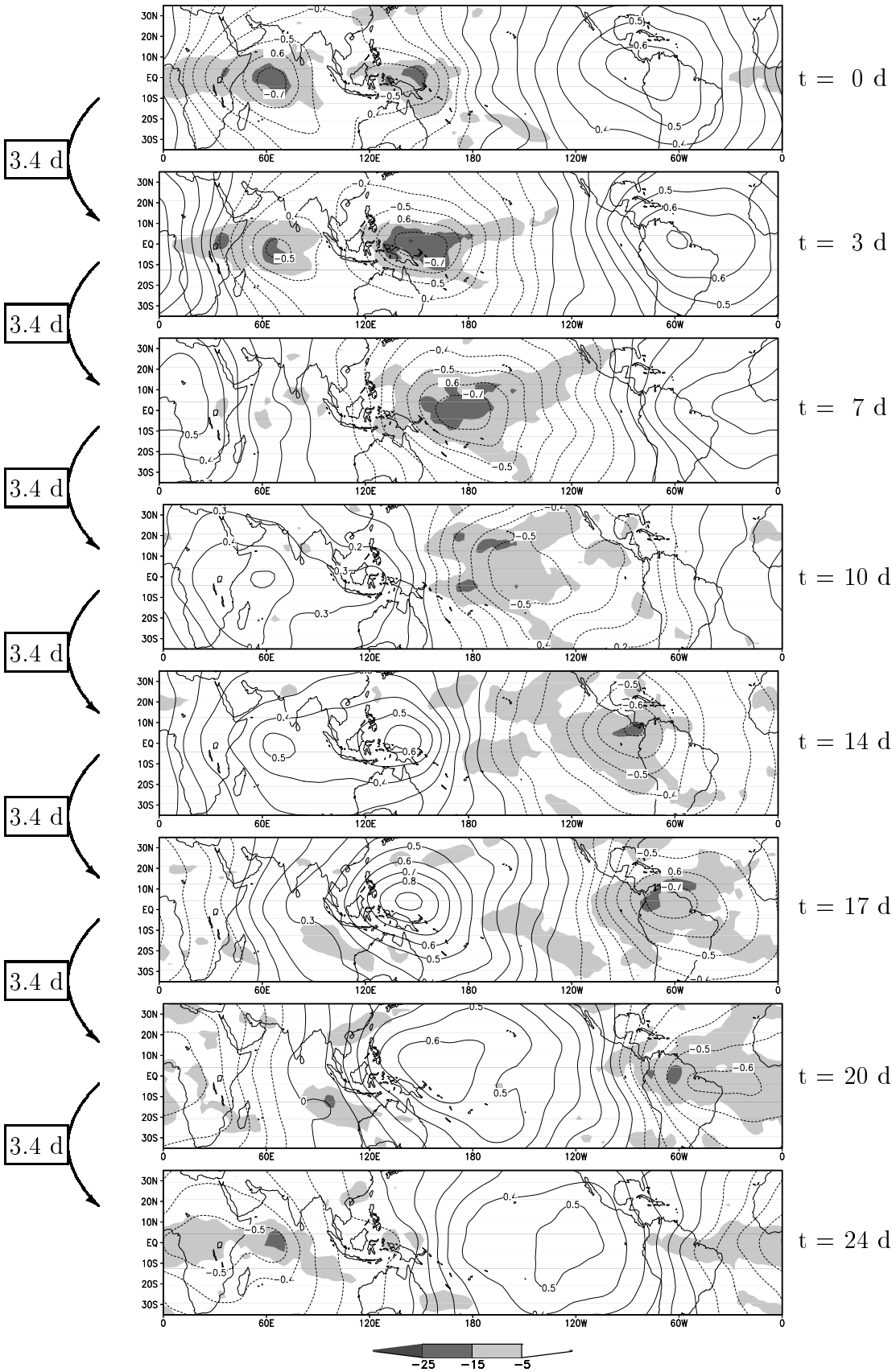

Figure 3.7: *As Figure 3.2, but for ECHAM4/OPYC3.*

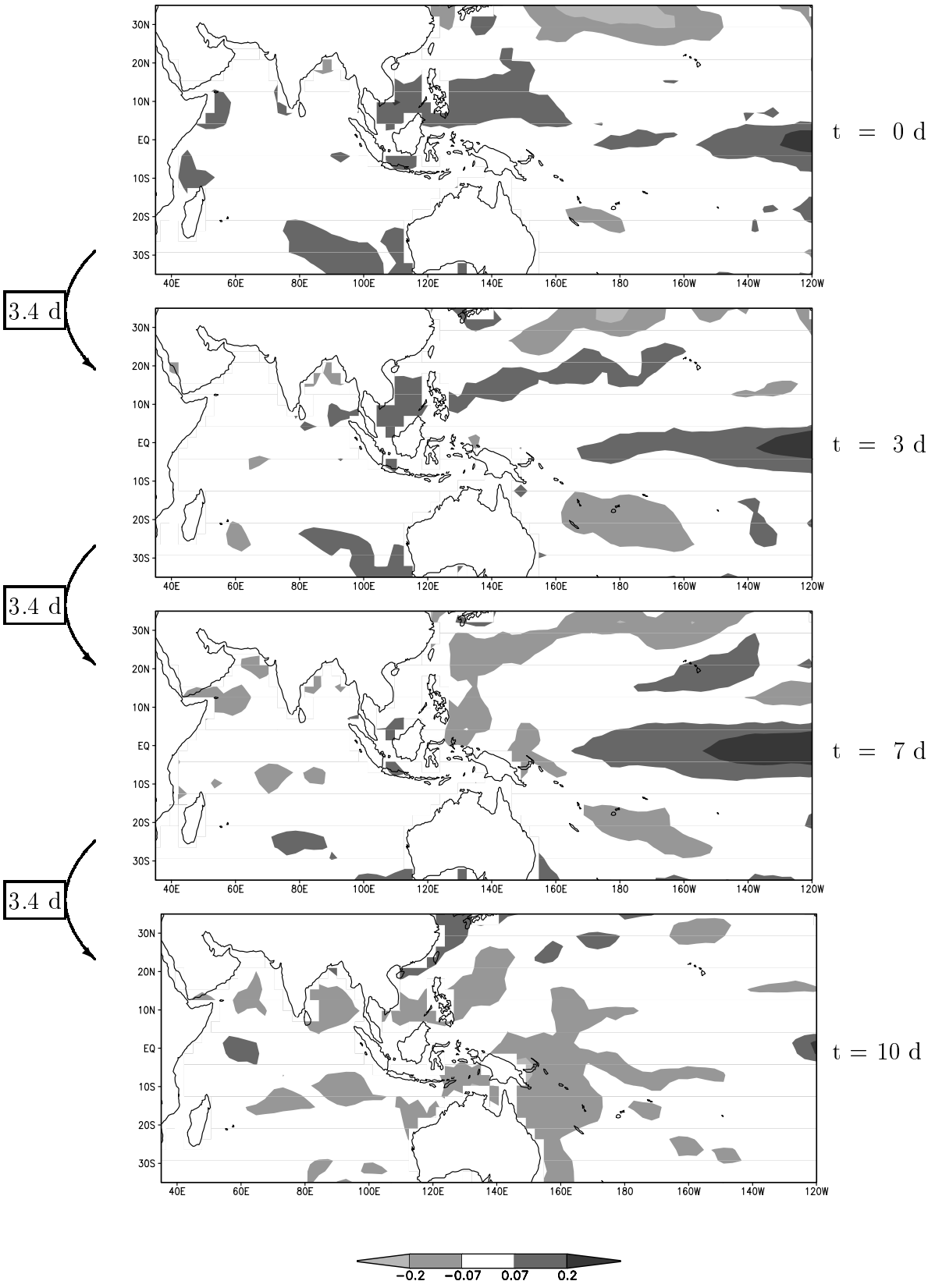

Figure 3.8: *Pseudo-Hovmöller diagrams of ECHAM4/OPYC3 SST anomaly [K] during the convective regime, as described by the first four panels in Figure 3.7. The shading interval is slightly reduced compared to Figure 2.7.*

the negative SST anomaly below and to the west of the deep convection is underestimated compared to the positive SST anomaly to the east of the convection. The latter occurs too far eastward over the Central Pacific in OPYC3.

The first EOF of the 200 hPa velocity potential anomaly (Figure 3.9) explains 35.6% of the total variance. The minimum is located at 145°E, near the ERA15 pattern. However, this should not be considered as an improvement compared to the control experiment (see Figure 3.3), since the mean SST in the Central Pacific is about 1 K colder in the CGCM than the observed AMIP SST (shown later in Section 3.3), and the West Pacific warm pool is slightly warmer. Figure 3.10 (left) depicts the time series of PC1. It is confined to the years 270 to 274 for the sake of clarity. The absolute maximum occurs at the 24th of March in the model year 274. The interannual variability of the IO activity is simulated reasonably well by the model (Figure 3.10, right), but as in the control experiment the main activity occurs too late in the year, appearing in spring and summer instead of winter and spring as observed.

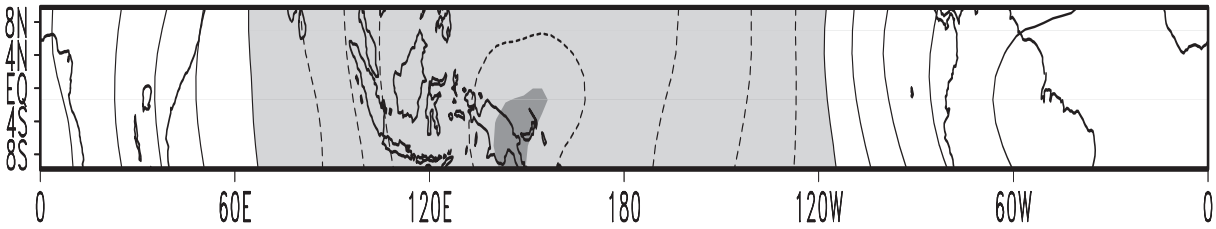

Figure 3.9: *ECHAM4/OPYC3 first EOF of 200 hPa velocity potential anomaly in the equatorial region. Contour interval is 0.01, negative values are light shaded and the minimum at 145°E is indicated by dark shadings. The EOF pattern explains 35.6% of the total variance.*

Figure 3.11 describes the time series of the simulated monthly-mean NINO3 SSTA and the occurrence of the strong IO event in the model. The ENSO cycle is present in the CGCM (Roeckner et al., 1996b). As in Figure 2.11, the two vertical lines mark 20 days before and 40 days after the PC1 maximum in spring of the model year 274. The simulated IO occurs prior to a La Niña, at the time of steepest NINO3 SSTA decrease, as in the ERA15 data. This feature is only a hint that the present indices do not capture a possible interaction of the IO and the ENSO cycle, and should not be regarded as an interaction of the IO and La Niña, as discussed in Section 2.2.

Longitude-time Hovmöller diagrams of the simulated IO in spring of the model year 274 show a distinct eastward propagation of the OLR anomaly (Figure 3.12, left). The related local maximum in latent heat flux anomaly occurs rather to the west of the OLR anomaly, indicating the dominance of the wave-CISK mechanism in the coupled model (Sperber

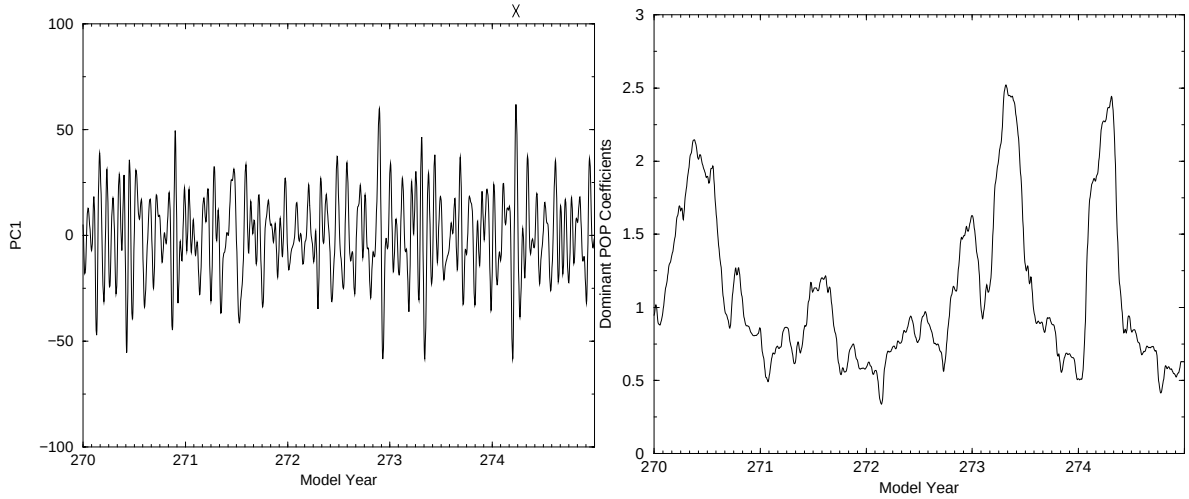

Figure 3.10: *Left: ECHAM4/OPYC3 PC1, which is used as an index of the activity of the IO. X marks the maximum at the 24th of March 274 as an identifier for a typical IO. Right: 100-day running mean of the squared amplitude of the POP coefficients of 200 hPa velocity potential anomalies, reflecting the interannual variability of the IO activity.*

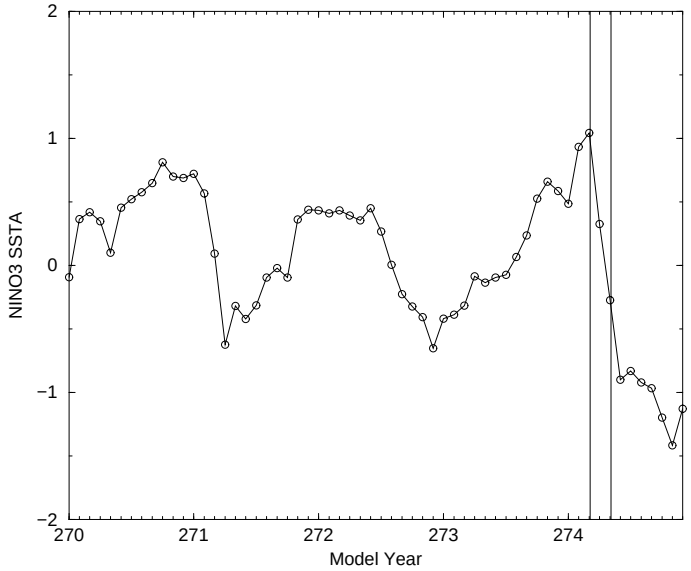

Figure 3.11: *Comparison of NINO3 SSTA to the PC1 maximum with 20 days before and 40 days after the PC1 maximum indicated by the two vertical lines.*

et al., 1997). The WWBs (Figure 3.12, right) are the dominant factor for the production of latent heat flux anomalies between 60°E and 180°E.

The main conclusion of the CGCM results is that no pronounced improvement of the representation of the IO is achieved by the coupling. Hendon (2000) found similar results with the GFDL GCM coupled to a one-dimensional ocean mixed layer model with variable mixed layer depth atop a layered model extending to a depth of 1000 m at each grid

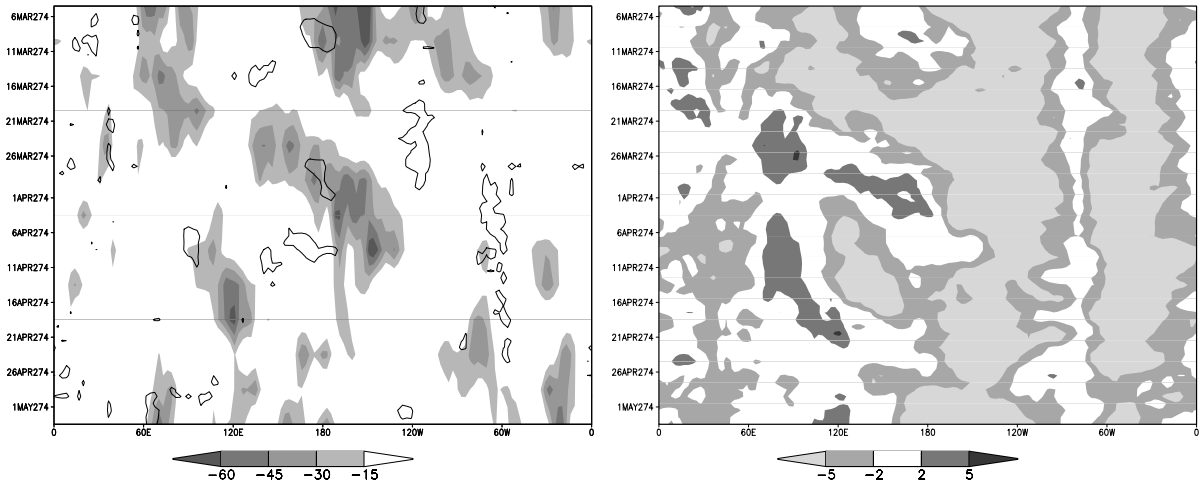

Figure 3.12: *ECHAM4/OPYC3. Left: OLR anomaly [W m^{-2}] (shaded) and the 40 W m^{-2} isoline of latent heat flux anomaly. Right: 850 hPa zonal wind [m s^{-1}]. Both panels are averaged between 10°N and 10°S.*

point. Unlike in the present study, the latent heat flux anomalies do not systematically propagate eastward. However, ERA15 latent heat flux anomalies (see Figures 2.13 and 3.5) do not necessarily propagate eastward. The latent heat flux anomalies depend on the occurrence of WWBs, which are more frequent, smaller in zonal extent, and potentially less predictable than the IO (Zhang et al., 2001). In the study by Hendon (2000), the latent heat flux anomalies occur nearly symmetrically around the deep convection indicating the presence of wave-CISK and WISHE mechanisms. In the ECHAM4/OPYC3 CGCM they are predominantly confined below and to the west of the deep convection, as in the reanalysis data.

It should be kept in mind that the failure of the present CGCMs to improve the simulation of the IO does not necessarily exclude the importance of air-sea interaction. It is only pointed out that neither the ECHAM4/OPYC3 CGCM nor the GFDL/mixed layer model resolve any coupled phenomena that lead to an improved simulation of the IO, although both models exchange heat, momentum and freshwater once per day (Bacher et al., 1998; Hendon, 2000). However, Section 5.3 investigates the influence of a different SST dataset, which takes the small-scale land-sea distribution into account which is important for the propagation of the IO, but can not be resolved by present OGCMs. Despite these deficiencies of the simulation of the IO in ECHAM4/OPYC3, the next section describes the influence of the IO on the interannual variability of tropical climate and the interannual variability of the IO with observations, reanalyses and CGCM data.

3.3 Interannual variability and the IO

Nakazawa (1999) presents a possible connection of the IO to the ENSO cycle. Figure 3.13 shows time-longitude Hovmöller diagrams of NOAA satellite OLR, NASA Scatterometer (NSCAT) surface zonal wind, TOPEX/Poseidon sea level height (SLH) anomaly and TOGA/TAO SST anomalies (SSTA) from September 1996 to July 1997 averaged between 5°N and 5°S. This period covers the conditions prior to the 1997 El Niño. The OLR data (left panel) show evidence of the IO signal at 150°E in early November, middle December, late February, early April and middle May. WWBs (second left panel) occur slightly after the passage of the IO, as described in the previous chapters.

Wyrtki (1975) was the first to suggest that the appearance of warm water in the eastern Pacific results from westerly wind anomalies in the central western Pacific, which generate equatorial downwelling oceanic Kelvin waves. This is seen in Figure 3.13 (second right panel), where downwelling Kelvin waves induce strong positive SLH anomalies at 160°E in late December, middle March and middle April. The weak positive SLH anomaly at the beginning of December is associated with the WWB in middle November. The phase speed of the eastward propagating oceanic Kelvin waves is about 2 m s^{-1}. The warming in the eastern Pacific (Figure 3.13, right panel) results mainly from the deepening of the thermocline, inhibition of the mean upwelling and eastward advection of warm water from the west (Picaut and Delcroix, 1995; Delcroix et al., 2000).

A comparable mechanism is present in the ECHAM4/OPYC3 CGCM, which is shown by a focus on the simulated period from September 258 to July 259 (Figure 3.14), although the SSTs over the eastern Pacific are lower in the CGCM (Roeckner et al., 1996b). Unfortunately, the sea level height anomalies are only available as monthly mean values and thus give only a smooth picture. It has to be kept in mind that the described mechanism is only one possible case of the IO significantly influencing ENSO, as described in Section 1.2. Both Figures 3.13 and 3.14 reveal a slight eastward shift of the main IO activity, as represented by OLR, prior to the El Niño event. This is due to the eastward shift of the West Pacific warm pool (Picaut and Delcroix, 1995; Delcroix et al., 2000).

The interannual variability of the IO in reanalyses data and AGCM ensembles has recently been investigated by Slingo et al. (1999) and Gualdi et al. (1999). At least Gualdi et al. (1999) found an eastward shift of the IO prior and during El Niño events, and a similar characteristic is seen in Figure B.3 for the 1987 El Niño event. This study highlights the fact, that the IO indices used by Slingo et al. (1999) and Gualdi et al. (1999) fail to represent the proposed eastward shift of the IO due to the eastward extension of the

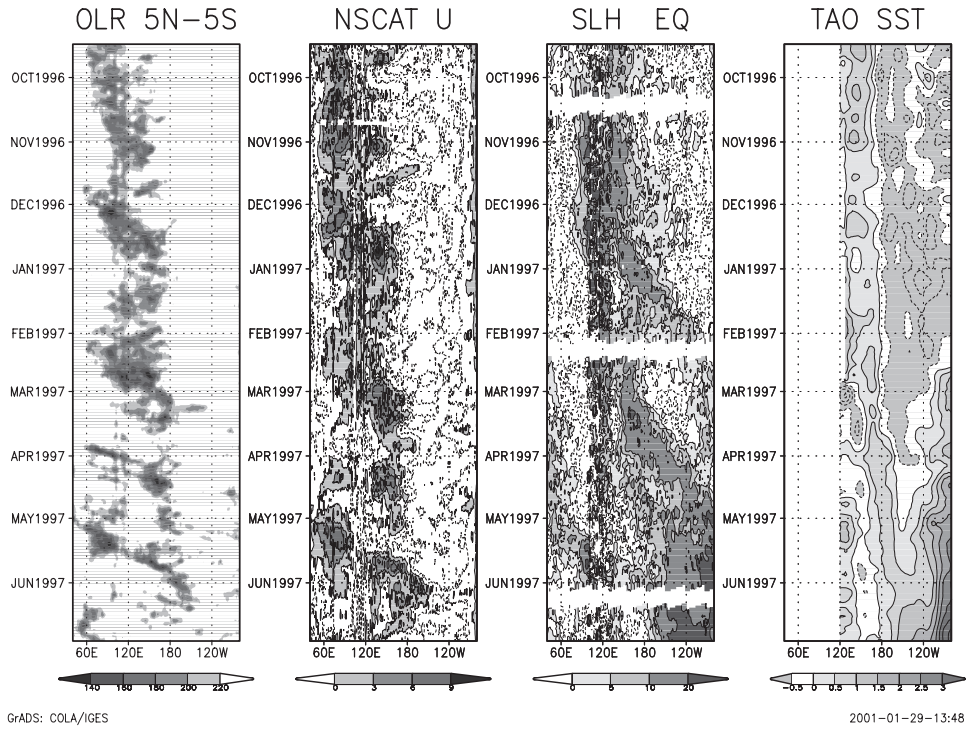

Figure 3.13: *Time-longitude cross section of OLR [W m^{-2}] (left), NSCAT surface zonal wind [m s^{-1}] (second left), TOPEX/Poseidon sea level height (SLH) anomaly [cm] (third left) and TOGA/TAO SST anomaly [K] (right) for the period from September 1996 to July 1997 (Nakazawa, 1999).*

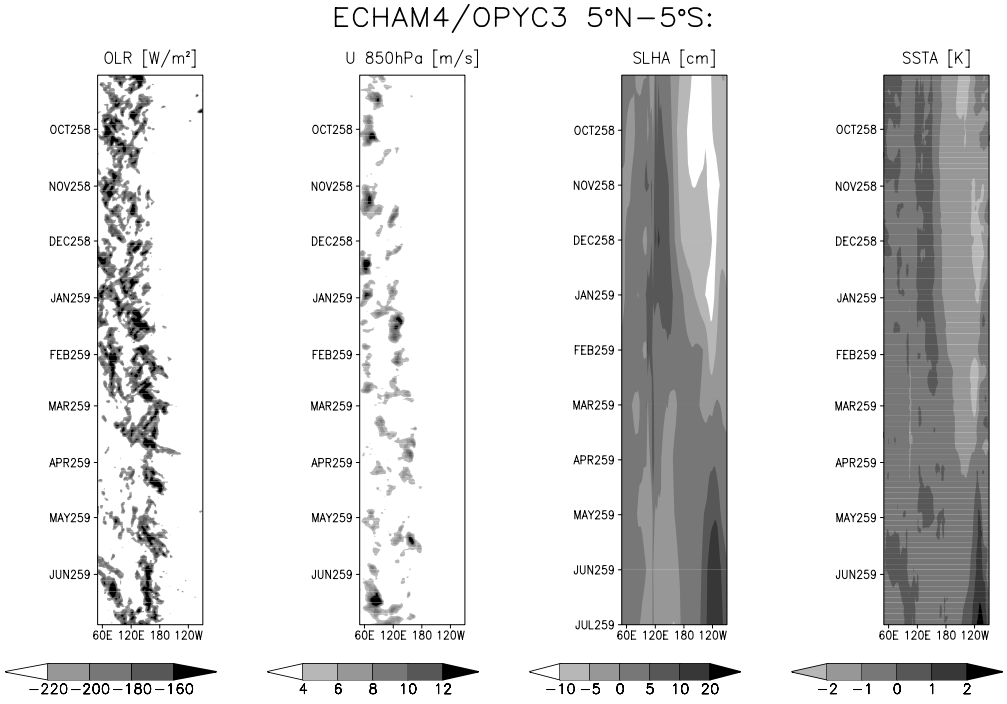

Figure 3.14: *As Figure 3.13, but for ECHAM4/OPYC3 data.*

West Pacific warm pool during and prior to El Niño events. Gualdi et al. (1999) also distinguished between an index for cold ENSO conditions and one for warm conditions (not shown), but for a detailed analysis of the zonal shift, time-longitude Hovmöller diagrams should be used.

In addition to the previous case studies, 20 years (1979-1998) of pentad OLR observations from NOAA polar orbiting satellites are used as a proxy for deep tropical convection, to indicate regions of possible IO activity. Daily data from 15 years (1979-1993) of the ERA15 reanalysis and 5 years (1994-1998) of the NCEP reanalysis are also analyzed. Despite the differences described in Section 2.1, the combination of both reanalysis datasets is reasonable for the depicted accuracy. These 20 years include the four El Niño events 1982/83, 1987, 1992/93 and 1997. The ENSO cycle and the associated displacement of the West Pacific warm pool are described with the ERA15 and NCEP SSTs and Pathfinder sea level elevation data (Koblinsky et al., 1998, 1999). The latter are only available for the period 1985-1988 from GEOSAT observations and from 1992 until present from TOPEX/Poseidon satellite observations. Only these periods are shown in the time-longitude Hovmöller diagram in Figure 3.15. For such long periods, single IO events are not detectable in the Hovmöller diagrams of OLR. However, Figure 3.16 shows that the deep convection over the maritime continent and by this the possible IO activity splits from one super cloud cluster into two super cloud clusters during an El Niño event, one remaining over the maritime continent and the other moving eastward towards the Central Pacific. There are two main differences between the two weaker El Niño events 1987 and 1992/1993 and the two stronger events 1982 and 1997: (1), re-organization of deep convection occurs over the West Pacific after the weak events in contrast to the connection of the convection over the Central Pacific to the convection over the South American continent after the strong events. (2), the location of WWBs during weak events is restricted mainly to the Indian Ocean and the West Pacific, whereas during strong events it follows the IO activity over the Central Pacific. The 28 °C SST isotherm also illustrates the ENSO cycle. Additionally, it is a reasonable threshold for the active generation of organized convection (e.g. Graham and Barnett, 1987). Deep convection, represented by OLR values less than 200 W/m^2, is restricted to SSTs higher than 28 °C (Figure 3.16). The strongest convection occurs over the eastern Indian ocean.

The interannual variability of the IO is also analyzed using a 100-year simulation of the ECHAM4/OPYC3 CGCM. Figure 3.17 shows a 20-year part of this time series including eight simulated El Niño events during the model years 276, 277, 281, 285, 287, 289, 290 and 292. Since the SST in the East Pacific is lower than in the observations (Roeckner

et al., 1996b), the 27 °C isotherm is additionally shown. Compared to observations, the simulated ENSO period is nearly halved. The sea level height anomaly in the ocean part of the CGCM resembles the observed structure of the strong events of 1982 and 1997. The model produces strong WWBs quite frequently over the Indian Ocean, but the strongest convection is shifted from the Indian Ocean to the West Pacific warm pool, where it is stronger than in the satellite data. The importance of this displacement will be further analyzed in Section 5.3. The strong convection is underestimated over the maritime continent, which leads to a nearly permanent splitting of the super cloud clusters (Figure 3.18). In observations, the super cloud clusters are predominantly split during El Niño events. In contrast to the connection of deep convection over the Central Pacific and the South American continent during strong El Niño events, the simulated strong convective activity over the Central Pacific does not merge with the convection over tropical South America during El Niño events due to the lower SST over the Central and East Pacific. Hence, the atmospheric part of the CGCM mostly simulates the IO as observed during moderate El Niño events (1987 and 1992/1993). To improve the representation of the IO in the AGCM and to gain further insight into the characteristics of the IO, the following two chapters describe sensitivity experiments with different resolutions, changes in atmospheric stratification and prescribed boundary conditions in the ECHAM4 AGCM.

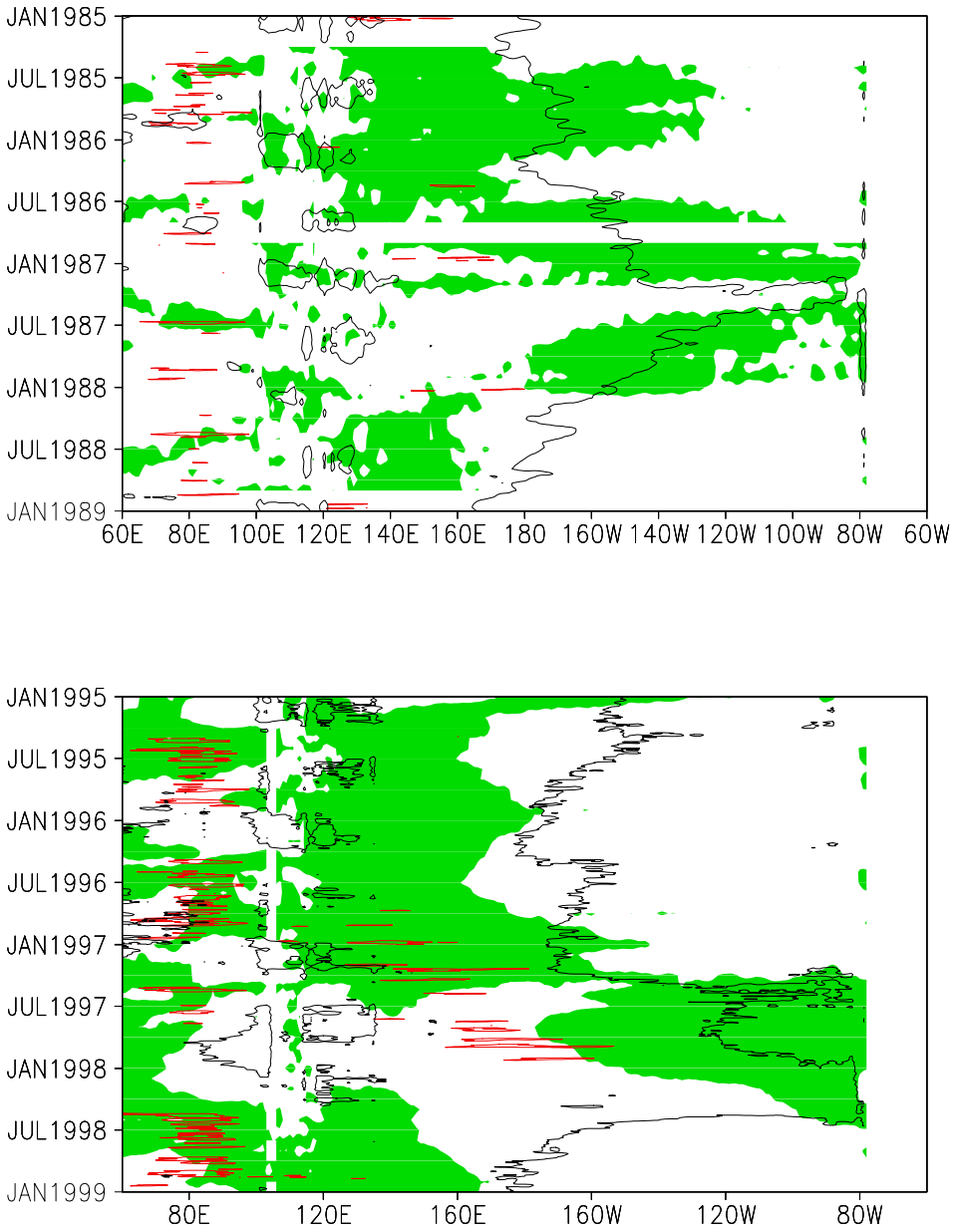

Figure 3.15: *Time-longitude cross section of Pathfinder sea level elevation anomaly (green shadings for values higher than +2 cm) with 850 hPa zonal wind (red contour for values higher than +10 m s^{-1}) and 28° C SST isotherm (black) overlayed. SST and zonal wind data are from ERA15 (top) and NCEP (bottom) reanalysis. Pathfinder data is from GEOSAT (top) and TOPEX/Poseidon (bottom) satellite measurements. Pathfinder data is not available for other El Niño periods. All values are averaged between 5°N and 5°S.*

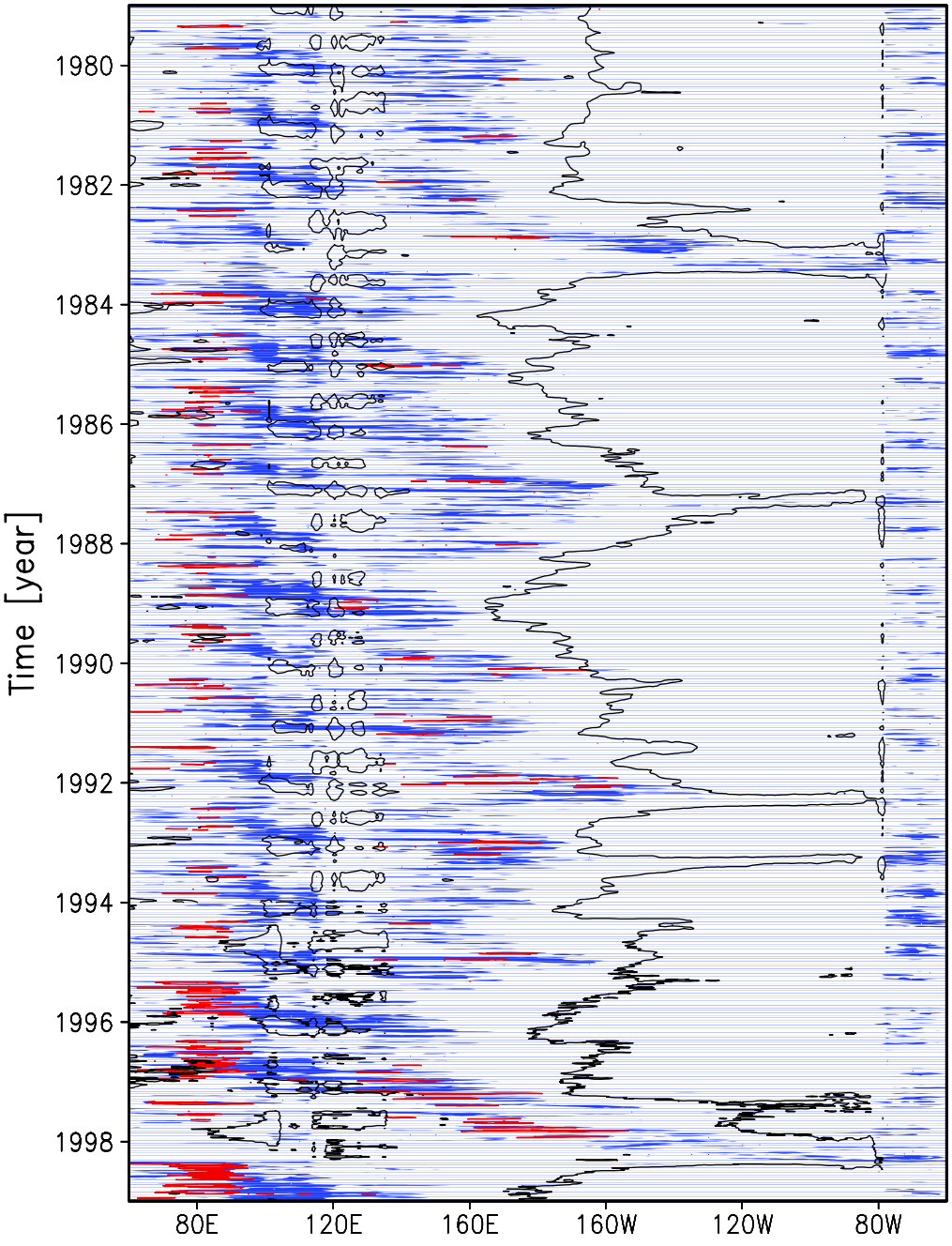

Figure 3.16: *Time-longitude cross section of NOAA OLR (blue shadings for values less than 200 W/m^2) with 850 hPa zonal wind (red contour for values higher than +10 m s^{-1}) and 28° C SST isotherm (black) overlayed. SST and zonal wind data are from ERA15 and NCEP reanalyses. All values are averaged between 5°N and 5°S.*

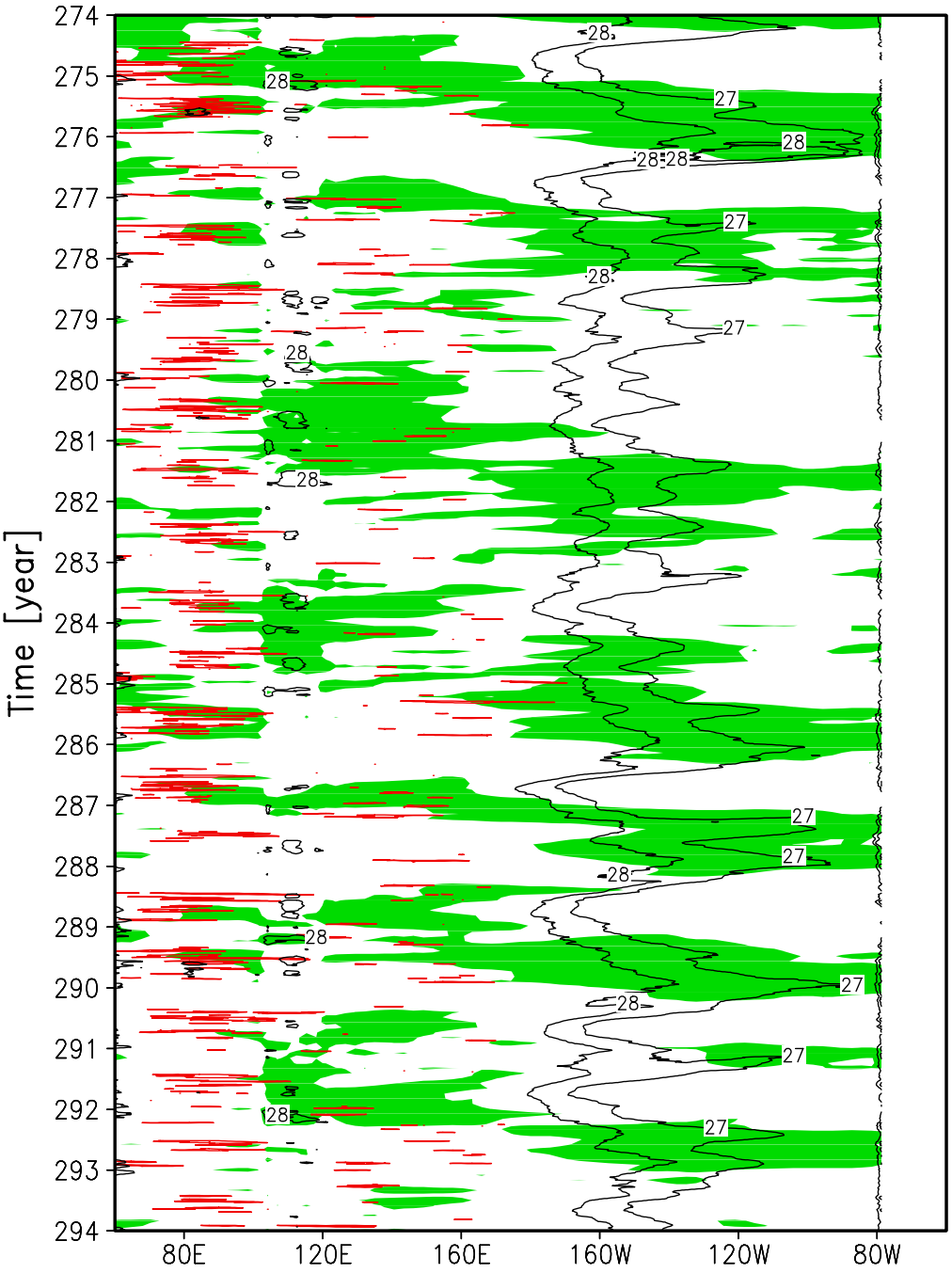

Figure 3.17: *Time-longitude cross section of ECHAM4/OPYC3 data: sea level elevation anomaly (green shadings for values higher than +2 cm) with 850 hPa zonal wind (red contour for values higher than +10 m s^{-1}) and 28° C and 27° C SST isotherms (black) overlayed. All values are averaged between 5° N and 5° S.*

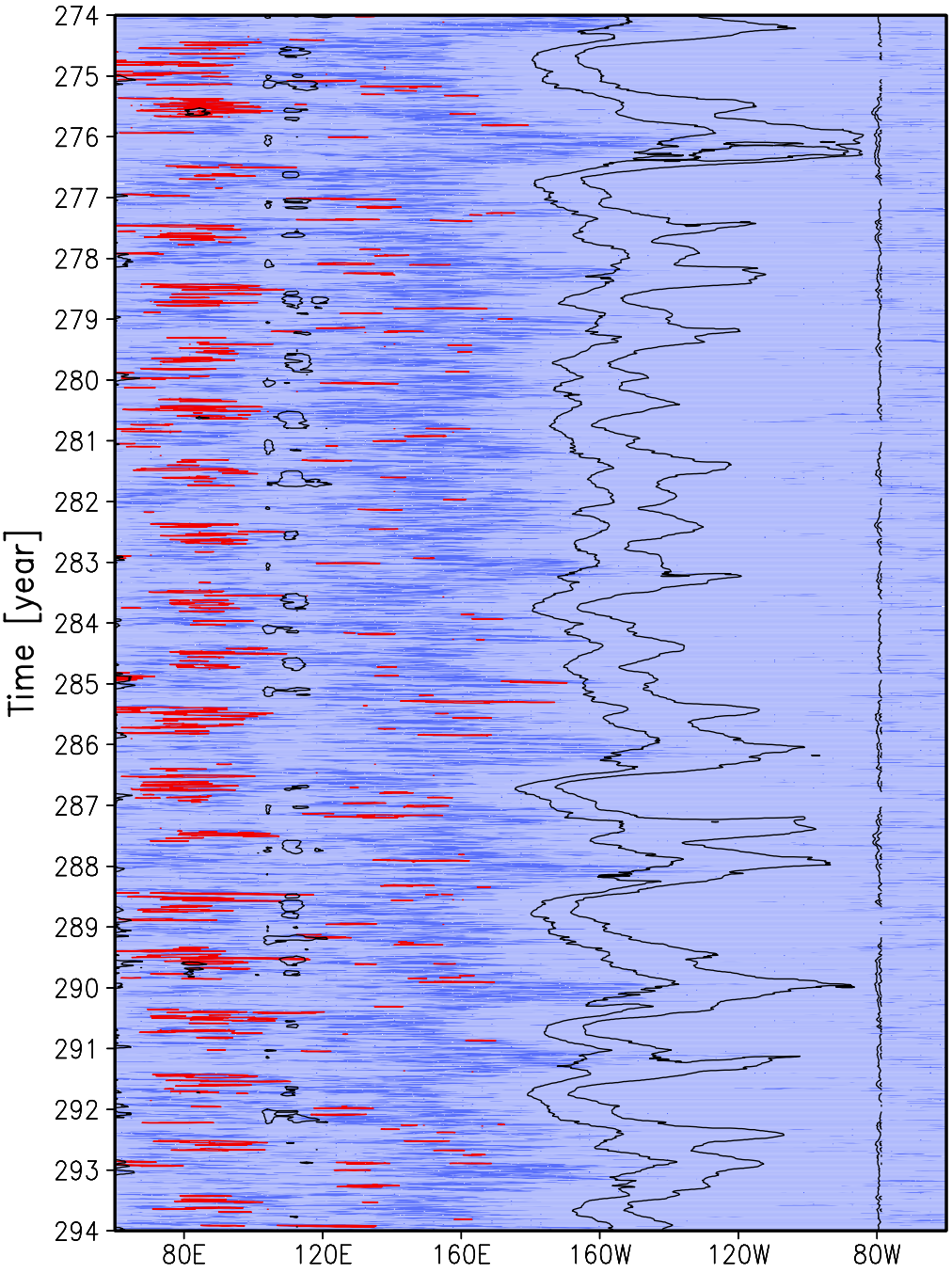

Figure 3.18: *Time-longitude cross section of ECHAM4/OPYC3 data: OLR (blue shadings for values less than 200 W/m^2) with 850 hPa zonal wind (red contour for values higher than +10 m s^{-1}) and 28°C and 27°C SST isotherms (black) overlayed. All values are averaged between 5°N and 5°S.*

Chapter 4

Sensitivity experiments I: The mid-troposphere

As previously stated, current GCMs often simulate a too fast IO, whose main activity is shifted too far eastward. The reasons for this behaviour are currently not fully understood. The present and the following chapter contain two approaches to further understand the dynamics of the IO and to improve the simulation of the IO in the ECHAM4 AGCM.

The present chapter investigates the influence of a stable layer in the mid-troposphere on the propagation of the IO. The approach is to change the stability in the mid-troposphere by cooling/warming the layer below the freezing level. This is achieved with four different model experiments. First, the vertical resolution is increased to 39 levels, to improve the simulation of the stable layer due to snow melt below the freezing level as proposed by Inness et al. (2001) and described in Section 1.4. In two other experiments, the layer near the freezing level is cooled (warmed) by artificially doubling (halving) the melting rate of convective precipitation for the calculation of the temperature change due to latent heat release. In the fourth experiment, no snow melt for convective and stratiform precipitation is allowed. This sets the melting rate for all precipitation to zero. The increase (decrease) in melting rate cools (warms) the tropical mid-troposphere below the freezing level, since energy required for melting is not available for heating.

4.1 Increased vertical resolution: T30L39

Observational studies of tropical convection have pointed out the importance of cumulus congestus clouds in moistening the mid-troposphere prior to periods of deep cumulonimbus convection. Cumulus congestus clouds constitute over half the precipitating convective clouds in the TOGA-COARE experiment and contribute over one quarter of the total convective rainfall (Johnson et al., 1999). Together with shallow cumulus and cumulonimbus clouds, the cumulus congestus clouds contribute to a trimodal vertical distribution of fractional cloudiness in the tropics. The peaks in this distribution are in close proximity to stable layers that exist over the West Pacific warm pool: the trade stable layer near 2 km height, the freezing level near 5 km height and the tropopause near 15-16 km height (Johnson et al., 1999). These stable layers inhibit cloud growth and promote cloud detrainment. The stable layer near the freezing level can produce detrainment from cumulonimbi and by this help to retard the growth of strongly entraining cumulus congestus clouds. Moreover, the restriction of cumulus congestus clouds to just above the freezing level limits further enhancement of cloud buoyancy through glaciation (Johnson et al., 1999). Since the cumulus congestus clouds influence the vertical distribution of the moist static energy, they play a major role in the development of the IO (Bladé and Hartmann, 1993). Sui and Lau (1989) and Lau et al. (1989) found in idealized model experiments that lower convection is responsible for a slower propagation of the IO due to the increased influence of frictionally dominated surface convergence (Hendon and Salby, 1994).

A recent work by Tompkins and Emanuel (2000) has revealed the sensitivity of the vertical distribution of water vapor on the vertical resolution in the one-column version of the ECHAM4 GCM. They question the ability of GCMs with currently about 19 vertical levels to represent correctly some of the physical processes which determine the distribution of water vapor in the atmosphere, e.g. the representation of the stable layer near the freezing level. As described in Section 1.4, Inness et al. (2001) analyzed the influence of vertical resolution in the HadAM3 aqua-planet GCM on the representation of tropical convection, and associated the improved tropical convection with the more realistic representation of the IO in the HadAM3 GCM with increased vertical resolution. Although they stated that the signal of improved convection is too noisy in a GCM with complex land-sea distribution, the present study attempts to point out these improvements in the ECHAM4 AGCM with increased vertical resolution. Due to a lack of computing power, the simulation with vertical resolution increased to 39 vertical layers is performed with a reduced horizontal resolution of T30 (ECHAM4 T30L39). For consistency, this version is compared to the T30 version with 19 vertical levels (ECHAM4 T30L19). The ECHAM4

T30L39 version was developed at the Deutsches Luft-und Raumfahrtzentrum (DLR) for tracer transport studies (Land et al., 1999). ECHAM4 T30L39 consists of an irregularly spaced hybrid sigma-pressure coordinate system with the highest resolution in the atmospheric boundary layer, as in the standard 19 level version (Roeckner et al., 1996a). Thus, the vertical resolution is nearly uniformly increased in the model domain.

The POP analysis of the 200 hPa velocity potential anomalies of ECHAM4 T30L19 and ECHAM4 T30L39 is performed as described in Section 2.2 and Appendix C. The spectra of the dominant complex POP coefficients of ECHAM4 T30L19 (Figure 4.1, top) depict periods of 30 and 27 days for the real and imaginary parts, respectively. Their squared

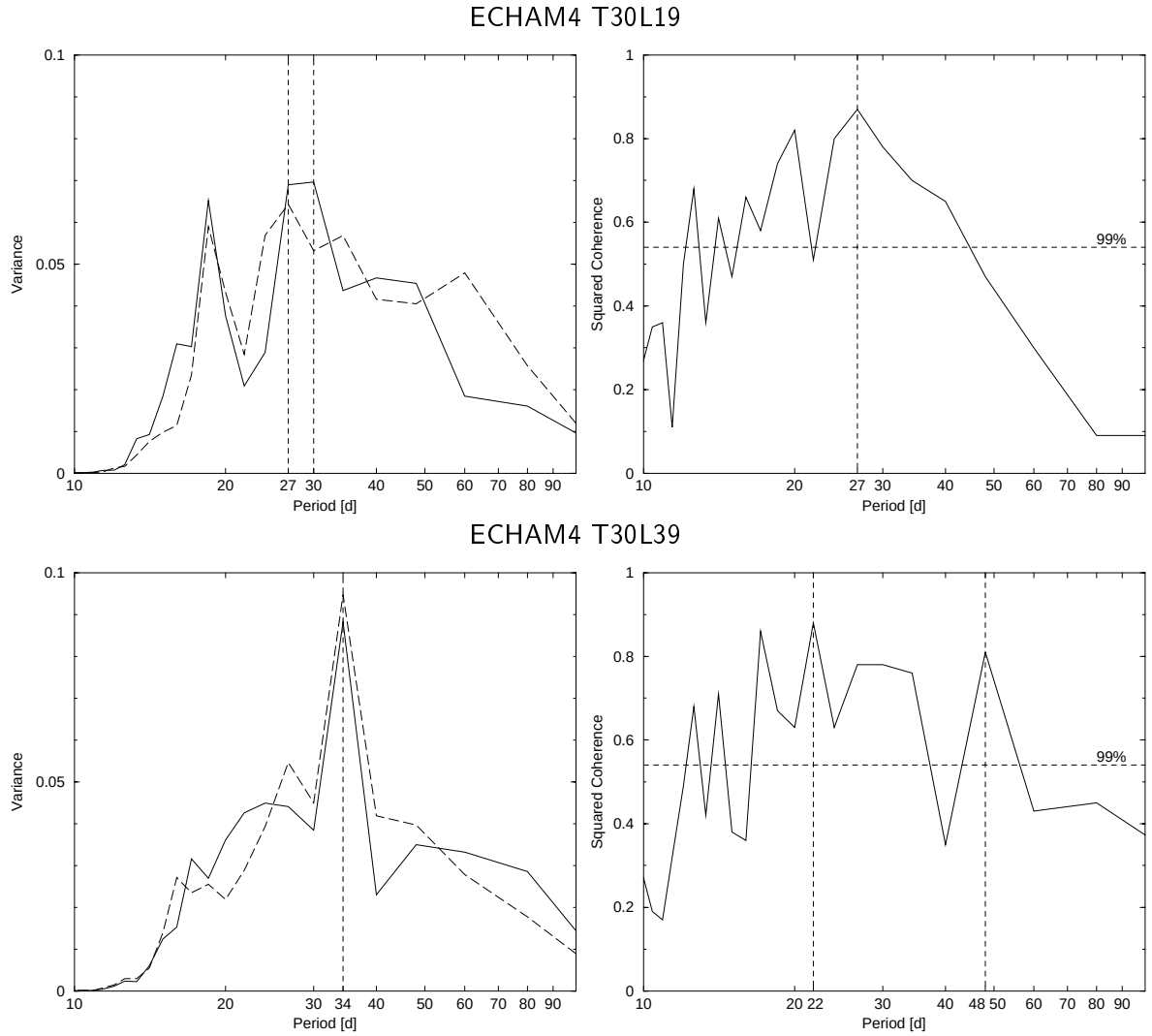

Figure 4.1: *Spectra of the real (solid line) and imaginary (long dashed line) dominant POP mode (left) and their squared coherence (right). The vertical dashed lines indicate the maxima. The horizontal dashed line depicts the 99% confidence interval of the squared coherence. Top: ECHAM4 T30L19, bottom: ECHAM4 T30L39.*

coherence confirms the peak at 27 days. In the 39-layer simulation (Figure 4.1, bottom), the period in the spectra changes to 34 days, which is the same value as in ECHAM4 T42L19 (see Section 3.1). The squared coherence for ECHAM4 T30L39 is noisier and does not confirm the period of 34 days. The peak occurs at 22 days and only a secondary peak at 48 days well above the 99% confidence interval depicts the tendency towards slower propagation. However, since both spectra revealed the 34 day period, this period is suggested as the main phase velocity in this model integration. The periods above the 99% confidence interval within the filter window change from 15-21 days and 22-45 days for ECHAM4 T30L19 to 16-37 days and 43-56 days for ECHAM4 T30L39. The explained variances of the described POP modes for ECHAM4 T30L19 and ECHAM4 T30L39 are 50.3% and 47.2%, respectively. The e-folding times are around 59 and 67 days. Compared to the ERA15 data, this indicates the lack in spatial variability and too far eastward extension of large amplitudes as in the control experiment (see Section 3.1).

Although the spectra and the periods above the 99% confidence interval of the squared coherence show a tendency towards slower propagations in ECHAM4 T30L39, the squared coherence of the ECHAM4 T30L39 data is noisier. This may be the result of a change in the convection scheme. Parameters as e.g. the conversion rate of cloud droplets to rain droplets had to be readapted to restore the long-term mean radiative balance at the top of the atmosphere. A detailed description of these differences is presented by Land et al. (1999).

Figure 4.2 displays the eight composites of the 45° segments for ECHAM4 T30L39 as derived by the POP analysis. For a period of 34 days, the time step from one panel to the next is 4.3 days. The underestimation of convective anomalies over the maritime continent is slightly enlarged. As in the control experiment (see Figure 3.2), the maximum of convective anomaly is shifted eastward towards the date line. Due to stronger variability in the vertical cloud distribution (Land et al., 1999), the negative peaks in OLR anomaly are broadened leading to erroneously enhanced large-scale divergent flow anomalies near the tropopause as indicated by the too strong minima in 200 hPa velocity potential anomaly. The composites of ECHAM4 T30L19 resemble the ones of ECHAM4/OPYC3 (not shown). The minimum of the first EOF of the 200 hPa velocity potential anomaly is located at 148°E in ECHAM4 T30L19 (Figure 4.3, top) and at 165°E in ECHAM4 T30L39 (Figure 4.3, bottom). As in the composites, the result for ECHAM4 T30L19 is similar to ECHAM4/OPYC3 (see Figure 3.9). In ECHAM4 T30L39, the spatial structure of the IO is deteriorated, but the representation of phase velocity is slightly improved compared to ECHAM4 T30L19.

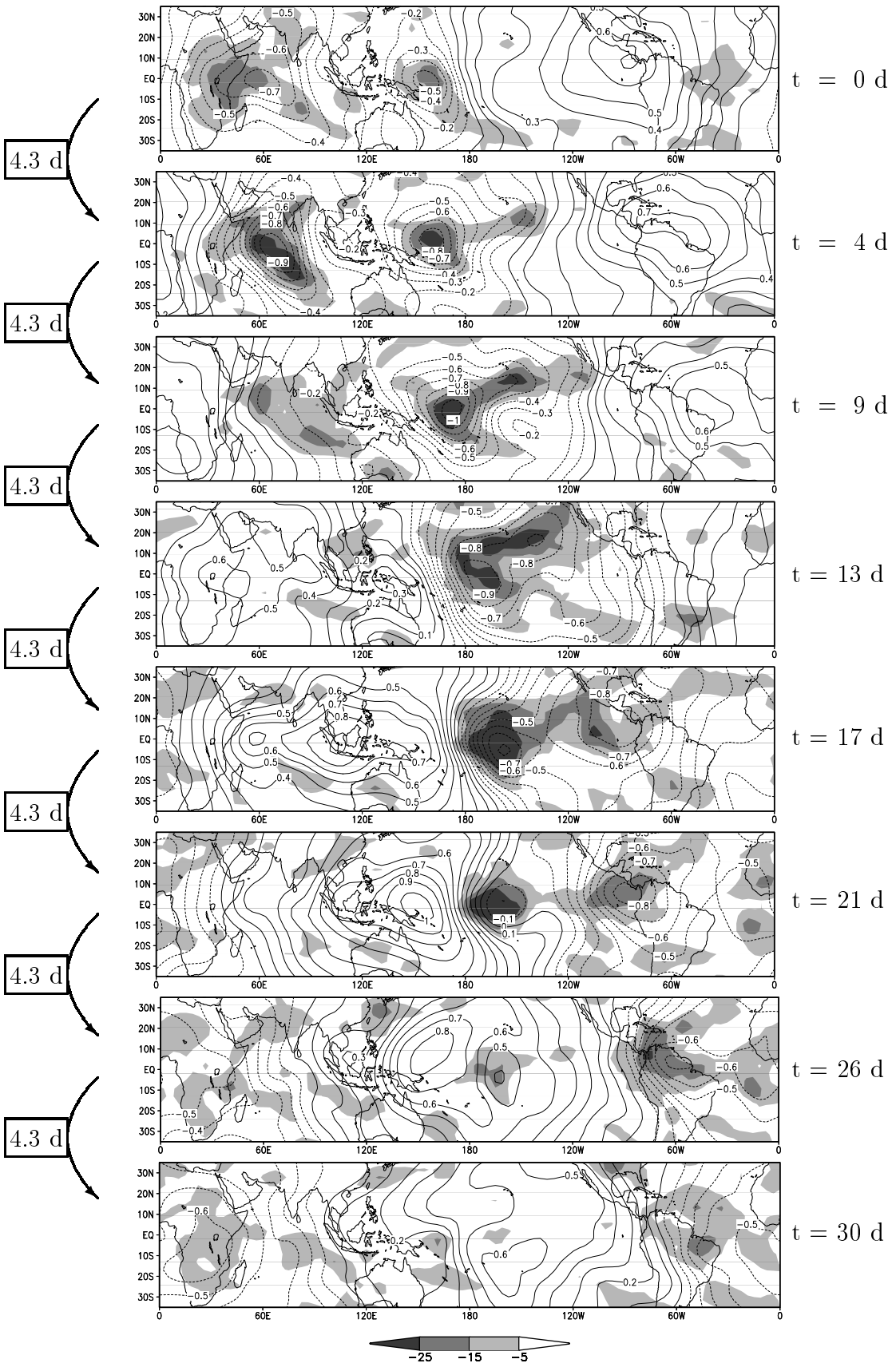

Figure 4.2: *Pseudo-Hovmöller diagrams of ECHAM4 T30L39 OLR anomaly [W m^{-2}] and 200 hPa velocity potential anomaly [10^7 m^{2}s^{-1}]. Negative OLR anomaly (shaded) indicates deep convective anomalies and negative velocity potential anomaly (dotted) indicates large scale divergent flow. Arrows on the left and the scale on the right point out the time step between the panels.*

The PC1 time series for ECHAM4 T30L39 (Figure 4.4, left) has its peak at the 3rd of February 1988, which is in the same season as the detected IO in the ERA15 reanalysis data (see Section 2.2). The representation of the interannual variability with the POP index (Figure 4.4, right) shows an inconsistency to the PC1 time series with the peak in interannual variability in spring 1987. This is due to an eastward shift of the dominant POP compared to the first EOF (not shown), indicating the inaccuracy of current IO

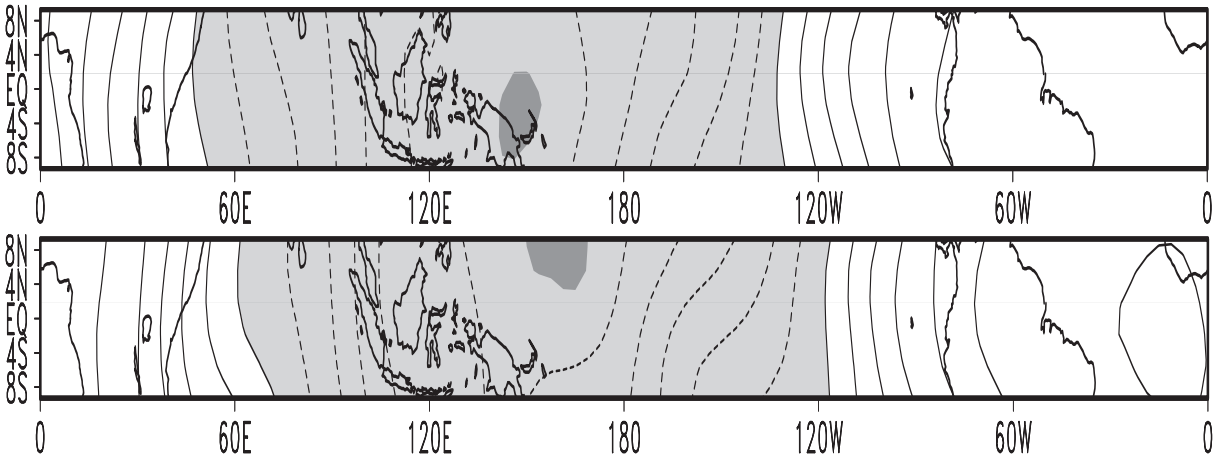

Figure 4.3: *ECHAM4 T30L19 (top) and ECHAM4 T30L39 (bottom) first EOF of 200 hPa velocity potential anomaly in the equatorial region. Contour interval is 0.01, negative values are light shaded and the minima at 148°E and 165°E are indicated by dark shadings. The EOF pattern explain 35.2% of the total variance for ECHAM4 T30L19 and 34.6% for ECHAM4 T30L39.*

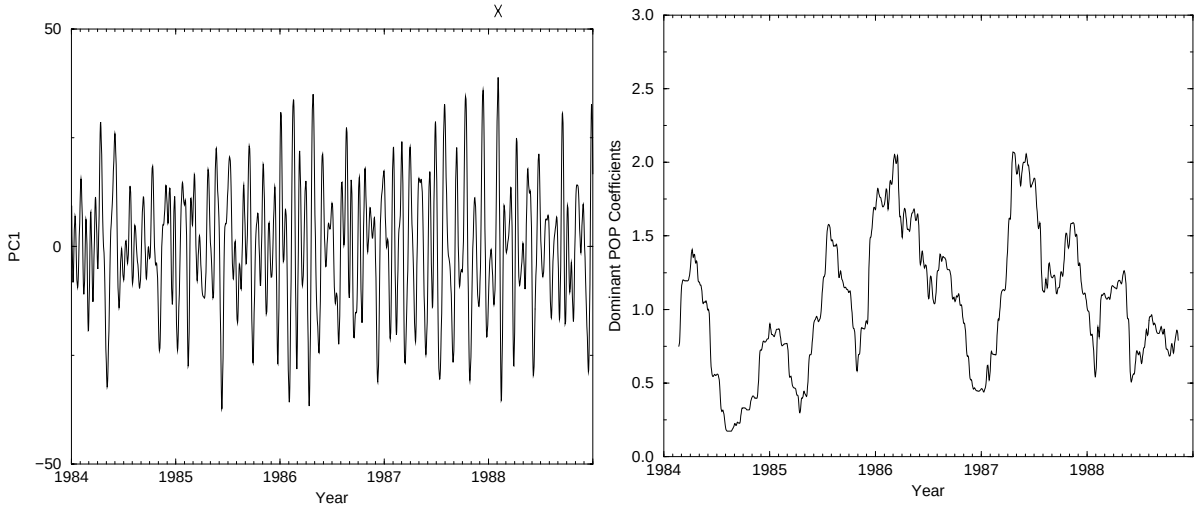

Figure 4.4: *Left: ECHAM4 T30L39 PC1, which is used as an index of the activity of the IO. X marks the maximum at the 3rd of February 1988 as an identifier for a typical IO. Right: 100-day running mean of the squared amplitude of the POP coefficients of 200 hPa velocity potential anomalies, reflecting the interannual variability of the IO activity.*

indices in describing the zonal variations of the main IO activity. However, the peak in the POP index during spring 1987 is not as conspicuous as in the ECHAM4 control experiment.

Hovmöller diagrams show an eastward propagating IO in NOAA OLR during February 1988 (Figure 4.5, left). The IO in ECHAM4 T30L39 (Figure 4.5, right) is accompanied by non-propagating OLR anomalies and it is disrupted near 140°E. The simulated strong convective anomaly in the western Indian Ocean near 60°E does not propagate eastward on the intraseasonal time scale. It resembles the convective anomalies in the case study of the control experiment (see Figure 3.5). The positive anomalies of latent heat flux to the west of the deep convective anomalies are present between 19th and 26th of February

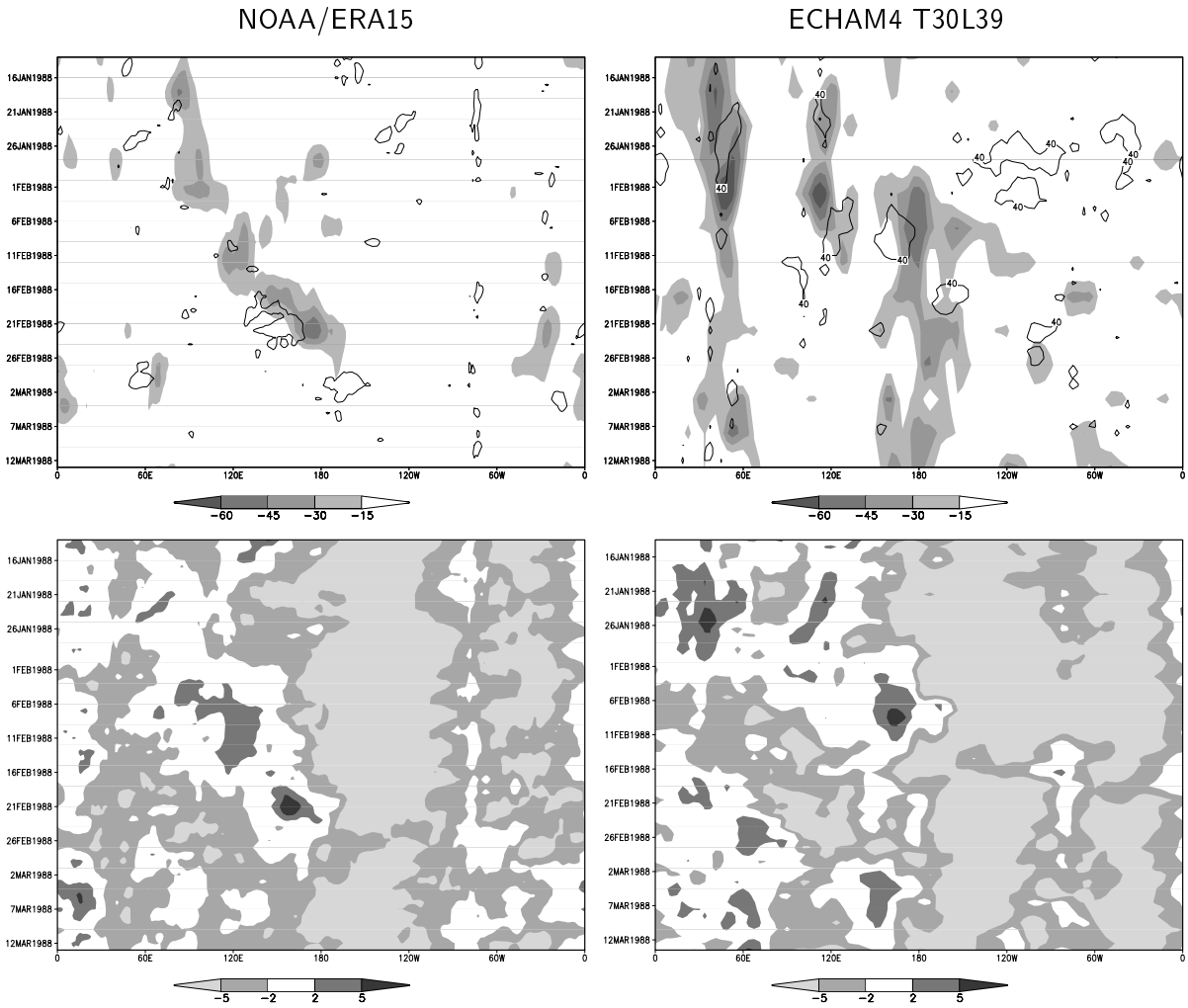

Figure 4.5: *Top: OLR anomaly [W m^{-2}] (shaded) and the 40 W m^{-2} isoline of latent heat flux anomaly. Bottom: 850 hPa zonal wind [m s^{-1}]. All data are averaged between 10°N and 10°S. Left: NOAA OLR and ERA15 latent heat flux and zonal wind, right: ECHAM4 T430L39 data.*

in ERA15 and between 6th and 11th of February in ECHAM4 T30L39. The positive latent heat flux anomalies are due to the WWBs (Figure 4.5, bottom). ECHAM4 T30L39 also simulates WWBs and positive latent heat flux anomalies below the non-propagating convective anomaly in the western Indian Ocean.

To describe the effect of increased vertical resolution on the simulation of the IO, the instability index by Kemball-Cook and Weare (2001) is used. This index is based on the moist static energy h and describes the passage of the IO in the "discharge-recharge" theory by Bladé and Hartmann (1993), as described in Section 1.3. The index is formed by subtracting *h(500hPa)* from *h(1000hPa)* and calculating the anomaly. This provides a measure of instability analogous to the vertical gradient of the equivalent potential temperature. The convective available potential energy (CAPE) curve, which is a measure of the maximum possible kinetic energy that a statically unstable air-parcel can acquire (Holton, 1992), closely follows the changes in the instability index but tends to be noisier. The evolution of h is produced almost entirely by the moisture field (Hendon and Liebmann, 1990b). The temperature field evolves out of phase with the rainfall (cool, when it is raining, warm when it is not) and has little impact on h. The coherence between zonal wind and OLR is greater than that between rainfall and OLR, thus emphasizing the noisy nature of tropical rainfall (Kemball-Cook and Weare, 2001).

Only non-maritime continent station data are used for a composite analysis of the instability index (Figure 4.6), since the distribution of moist static energy is rather noisy over the maritime continent (Kemball-Cook and Weare, 2001). During the suppressed phase of the IO, the instability index increases steadily, indicating that the atmosphere becomes more unstable. Until day 0, when the convection sets in, the instability index roughly parallels the *h(1000 hPa)* anomaly curve, while the *h(500 hPa)* curve remains negative. As the IO event begins, the *h(500 hPa)* curve increases sharply, becoming positive and dominating the instability index. The deep convection, described by brightness temperature anomaly T_b is in all stages concurrent with the instability index.

Figure 4.7 shows the instability index (left), and the vertical profile of the related zonal wind (right) for ERA15, ECHAM4 T30L19 and ECHAM4 T30L39 at 120°E, where the convective anomalies corresponding to the IO are located (see Figure 4.5). ERA15 shows mostly negative values in the instability index between the 6th and 26th of February 1988, indicating the duration of a stable period after the onset of convection. The associated zonal wind field shows lower-tropospheric westerlies up to 500 hPa height during this period. The upper-tropospheric easterlies right above the westerlies indicate the mature phase of the IO (see Section 1.1). ECHAM4 T30L39 captures this long time scale and the

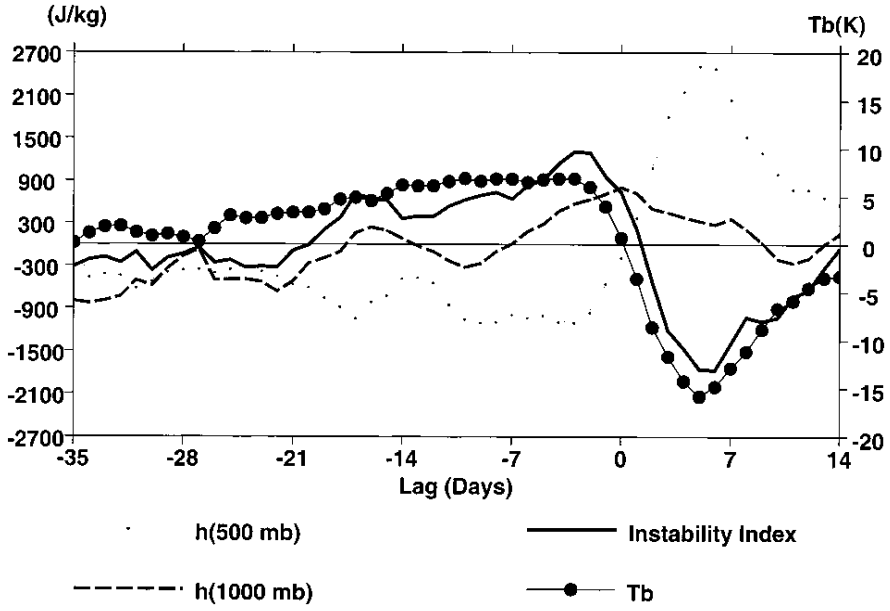

Figure 4.6: *Non-maritime continent station composite of moist static energy anomalies (h) at 1000 and 500 hPa, instability index h(1000 hPa)-h(500 hPa) and brightness temperature anomaly (T_b), adapted from Kemball-Cook and Weare (2001). Day 0 indicates the onset of convection.*

minimum below -6000 J kg^{-1} for the stable period between the 21st of January and 9th of February 1988. The upper-tropospheric easterlies around the 28th of January lead the lower-tropospheric westerlies by about 7-14 days, indicating the growing phase of the IO, which is shifted eastward compared to ERA15. The erroneous underlying westerlies in the tropical eastern hemisphere are a systematic error in the ECHAM4 AGCM (Roeckner et al., 1996a). Mentionable stable periods occur in ECHAM4 T30L19 between the 21st of January and 1st of February 1988, and again between the 7th and 14th of March 1988. Their amplitude is lower than in ERA15 and ECHAM4 T30L39. As in ECHAM4 T30L39, the associated zonal wind field indicates the growing phase of the IO in both cases.

The moisture static energy anomalies are considerably larger in the case studies in Figure 4.7, which present typical values for the detected unfiltered events, than in the composite values in Figure 4.6. Although the case study is only valid for the selected events, composite studies (not shown) illustrate the resemblance of the instability index with the deep convection. Thus, the differences in phase speed between ECHAM4 T30L19 and ECHAM4 T30L39 might be explained by the different time scales of the stable period after the onset of convection. It is questionable, if the decrease in propagation speed of the IO is based on the representation of the stable layer near the freezing level or the differences in convective parameterization. The mean 500 hPa temperatures for the 5

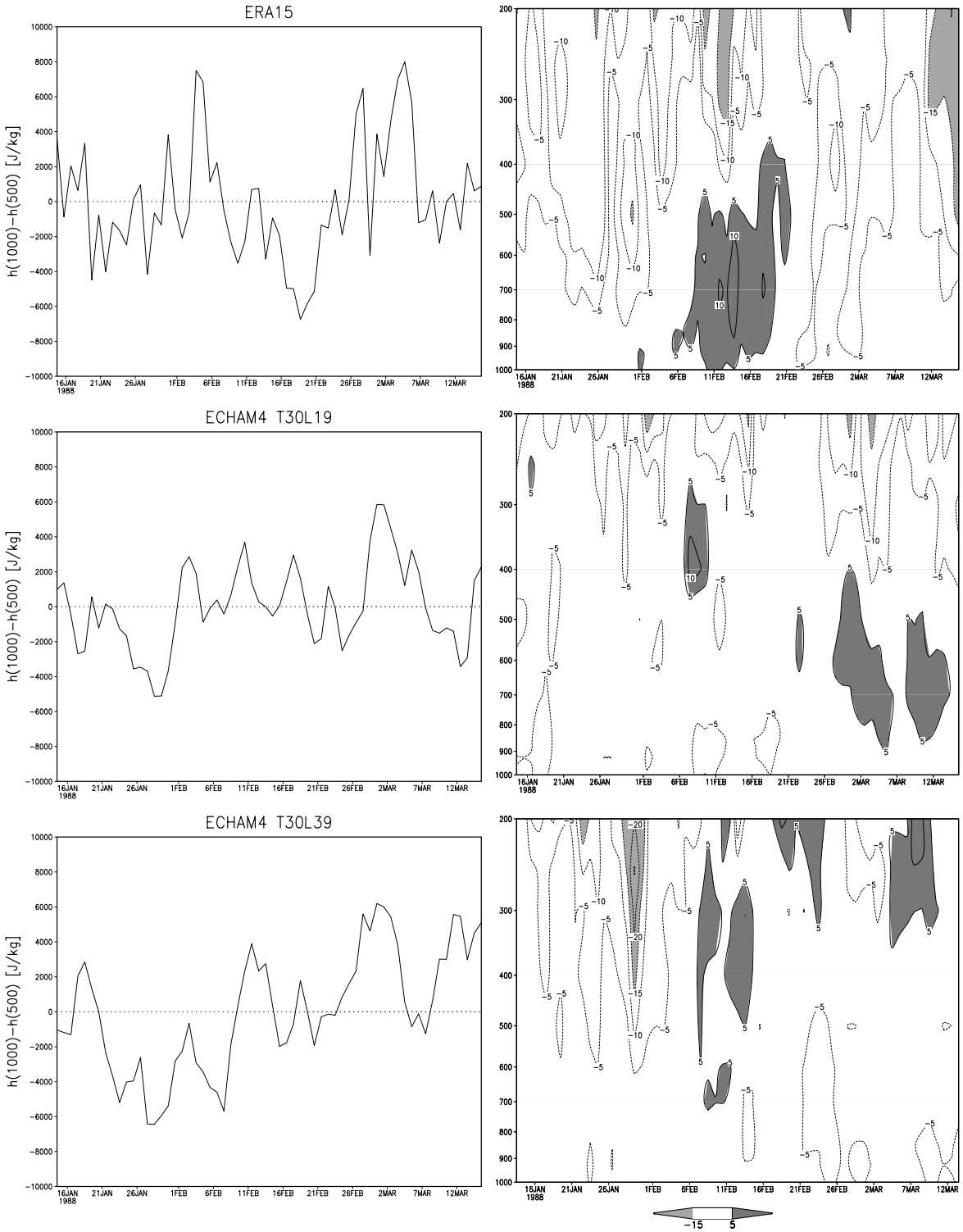

Figure 4.7: *Moisture static energy anomalies and the instability index (left) and the vertical profile of the related zonal wind (right) at the equator at 120° E. Top: ERA15, middle: ECHAM4 T30L19, bottom: ECHAM4 T30L39.*

years 1984 to 1988 over the tropical Indian Ocean and the West Pacific warm pool are about 1.8 K higher in ECHAM4 T30L19 than in ERA15. Due to the stronger cooling in ECHAM4 T30L39, the difference in mean 500 hPa temperatures over this region is reduced to about 1.3 K. To analyze the importance of the improved 500 hPa temperature field and the associated stratification, the next section describes sensitivity studies with a changed heating profile in the ECHAM4 AGCM.

4.2 Changing the melting rate

Three sensitivity studies are performed with ECHAM4 at T42 horizontal resolution and 19 vertical levels, to investigate a possible influence of the atmospheric stratification in the mid-troposphere on the IO. The three experiments are designed to change the effects of the melting precipitation, since the stratification at the freezing level depends on thin stable layers, which are a consequence of melting precipitation in a layer of about 500 m thickness just below the freezing level (see Section 1.4).

In ECHAM4, the cooling due to the melting of convective precipitation is parameterized as

$$\frac{\Delta T}{\Delta t} = -M \cdot \frac{L_f}{C_p} \tag{4.1}$$

where ΔT is the temperature change within one time step Δt, M is the melting rate (s $^{-1}$), L_f is the latent heat of fusion (L_f=334000 J kg^{-1}) and C_p is the heat capacity of air (C_p=1005 J kg^{-1} K^{-1}).

Melting occurs in each layer, whenever the temperature exceeds 2 °C (Roeckner et al., 1992). In the tropics, the layer thickness near the freezing level is about 1.2 km for ECHAM4 T42L19. When this relatively thick layer is cooled due to melting of precipitation, the cooling rate is less than if only a thin layer would be cooled (see Section 1.4). In the first experiment (ECHAM4 2.0xMR) the representation of the mid-troposphere stability and by this the effect of a doubled vertical resolution is forced by doubling the melting rate M in Equation (4.1) and thus doubling the cooling near the freezing level.

Compared to the control experiment, this artificial change cools the 500 hPa model level by about 0.4 K over the maritime continent, averaged over the simulated years 1984 to 1988. This is consistent to the cooling of about 0.5 K due to doubled vertical resolution (see Section 4.1). To corroborate the results obtained from such a sensitivity study, the

opposite experiment design is also analyzed and the opposite result is expected. Thus, in a second experiment (ECHAM4 0.5xMR), the melting rate for convective precipitation is halved in Equation (4.1). In a third experiment (ECHAM4 NSMT), snow melting for convective and stratiform precipitation is suppressed. Both of the latter experiments have nearly the same effect on the temperature near the freezing level: They warm the corresponding layer by about 0.2 K. It should be mentioned that all three model integrations are stable within the five simulated years and do not produce pronounced trends.

Figure 4.8 indicates an increase in phase speed in ECHAM4 2.0xMR and ECHAM4 0.5xMR compared to the control experiment (see Figure 3.1). ECHAM4 2.0xMR shows a pronounced peak at about 25 days. Although the propagation speed is increased, the squared coherence is stronger than in any other realization, since the differences in moist static energy between convective and dry events have increased. The POP analysis of ECHAM4 0.5xMR shows rather noisy spectra with a small peak at periods around 20 days. Thus, a firm conclusion about the change in phase speed after cooling or warming the layer near the freezing level can not be drawn from these experiments. On one hand, the changes in the convection scheme result in only small differences in 500 hPa temperature and the associated stratification. On the other hand, the changed energy cycle strongly disturbs the slow IO mode in the upper-tropospheric divergent flow.

If snow melt is not allowed (ECHAM4 NSMT), the cooling of the mid-troposphere due to melting precipitation is inhibited and a stable layer can not develop. The spectra of the POP coefficients and their squared coherence illustrate a trimodal structure with peaks at the 25, 30 and 49 day periods in ECHAM4 NSMT. The peaks at 12 and 15 days in the squared coherence occur too far in the cosine tail of the filter window and should not be interpreted. This splitting of the spectra compared to the control experiment is a hint of a connection between the melting of precipitation and the bimodal structure in the propagation speed of the IO simulated in the control experiment. However, the spectra of ECHAM4 2.0xMR, ECHAM4 0.5xMR and ECHAM4 NSMT do not confirm the suggestions by Inness et al. (2001), that an increased cooling due to the improved representation of the energy required for melting precipitation and thus an increased stability near the freezing level reduces the phase speed of the IO. The results of the present chapter are too weak to present a reliable connection of the representation of the stable layer near the freezing level and the propagation of the IO. Hence, these sensitivity experiments are not further analyzed. Instead of this, the next chapter investigates the influence of different boundary conditions on the propagation of the IO as an additional approach to explain the too fast IO propagation and the eastward shift of the main IO

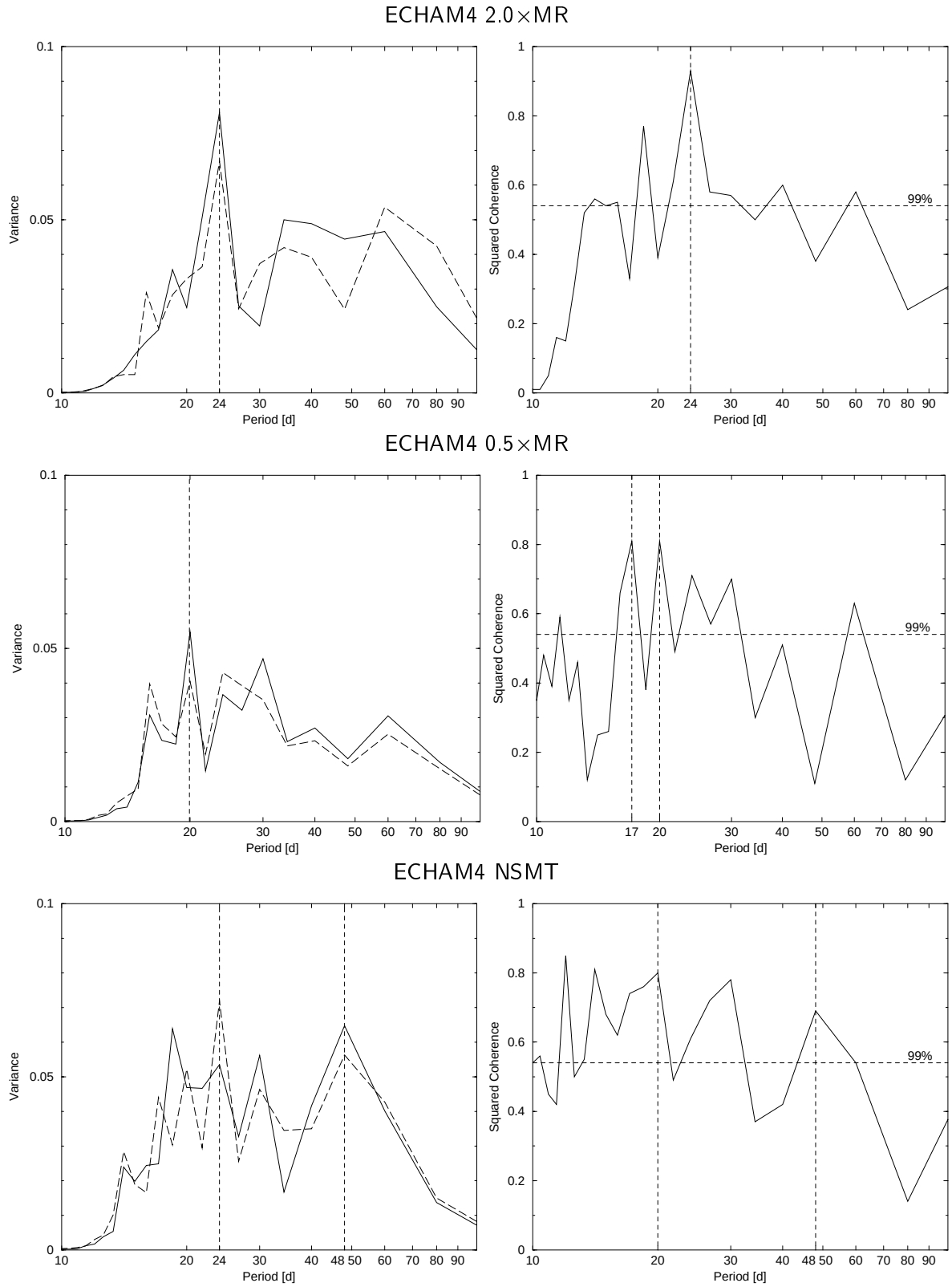

Figure 4.8: *Spectra of the real (solid line) and imaginary (long dashed line) dominant POP coefficients (left), and their squared coherence (right) for ECHAM4 2.0xMR, ECHAM4 0.5xMR and ECHAM4 NSMT. The vertical dashed lines indicate the maxima. The horizontal dashed line depicts the 99% confidence interval of the squared coherence.*

activity in GCMs, since Neale and Slingo (2001) found an improved spatial structure of the IO in a sensitivity experiment with the maritime continent replaced by sea points in the HadAM3 GCM.

Chapter 5

Sensitivity experiments II: Boundary conditions and horizontal resolution

In addition to the too fast propagation of the IO, the previous chapters point out the eastward shift of the main IO activity as a characteristic in the ECHAM4 GCM. Both deficiencies are common to many GCMs with similar horizontal and vertical resolutions (Slingo et al., 1996). The results of Section 4.1 do not show a pronounced improvement of the simulated IO in a GCM with increased vertical resolution. Sensitivity studies with different heating patterns in the mid-troposphere also do not reveal a significant influence on the IO. However, Neale and Slingo (2001) found the absence of the erroneous eastward shift of the simulated IO's in a sensitivity experiment with the maritime continent replaced by sea points in the HadAM3 GCM. This leads to the question: Is the zonal shift of the main IO activity related to the coarse horizontal resolution of current GCMs or at least to their land-sea distribution?

The present chapter analyzes the impact of different boundary conditions on the simulated IO. The importance of the representation of the land-sea distribution is investigated with three GCM experiments. In the first, the horizontal resolution is increased to T106, which leads to a finer and by this more realistic land-sea distribution. In the second experiment, the land points associated with the maritime continent are replaced by sea points (ECHAM4 NOMARI) to point out the importance of land points in the convective regime for the propagation of the IO. In the third experiment, the effect of the prescribed SST is analyzed. The AMIP SST, which is used as a boundary condition for the control experiment, is replaced by a T42 version of the optimal interpolated SST (OISST, Reynolds and Smith, 1994). In this model version, the "SST" consists partly of land

surface temperatures. This sensitivity study points out the importance of the prescribed SST on the representation of the IO, since convection is very sensitive to small changes in surface temperature near values of 26 to 29.5 °C , which are typical for the West Pacific warm pool and the maritime continent region (Salby et al., 1994, see Section 1.3).

5.1 Increased horizontal resolution: T106L19

In this section, the ECHAM4 GCM at T106 horizontal resolution (ECHAM4 T106L19) is used to analyze possible improvements of the simulation of the characteristic horizontal structure of the IO. The POP analysis of the 15-90 day bandpass filtered 200 hPa velocity potential anomaly between 10°N and 10°S shows relatively low amplitudes in the spectra and their squared coherence (Figure 5.1). This noisy structure is consistent with results by Fox-Rabinovitz and Lindzen (1993). They used the GLA GCM with no filters applied to point out the importance of an appropriate ratio between horizontal and vertical resolution on the stability of atmospheric waves in GCM simulations. Extrapolating their results to the T106 horizontal resolution suggests the requirement of a vertical resolution finer than 0.6 km to obtain distinct spectra of atmospheric waves for the T106 horizontal resolution. This corresponds to more than 39 layers. However, the required computing power to perform experiments with such high horizontal and vertical resolution does not currently exist at bearable costs.

Despite the large amount of noise, the spectra of the dominant POP coefficient show peaks at about 24 days, indicating an even faster propagation of the simulated IO than in the control experiment. The shorter periods in ECHAM4 T106L19 and ECHAM4 T30L19 (see Section 4.1) highlight the influence of non-linear effects. The convection scheme is not changed for the different horizontal resolutions. Within the filter window, only periods between 21 and 30 days occur above the 99% confidence interval. The peak in the squared coherence at 27 days is accompanied by a secondary peak at 15 days in the cosine tail of the filter, that has no equivalence in the spectra. The detected mode explains 27.7% of the total variance and has an e-folding time of about 46 days. These values are less than in the previously analyzed model versions but they resemble the ERA15 data, suggesting the dependence of the IO on the horizontal resolution.

The eight composites of the 45° segments (Figure 5.2) reveal no underestimation of the convective anomalies over the maritime continent in ECHAM4 T106L19. For the detected period of 24 days the time step from one panel to the next is 3 days. Analogous to the

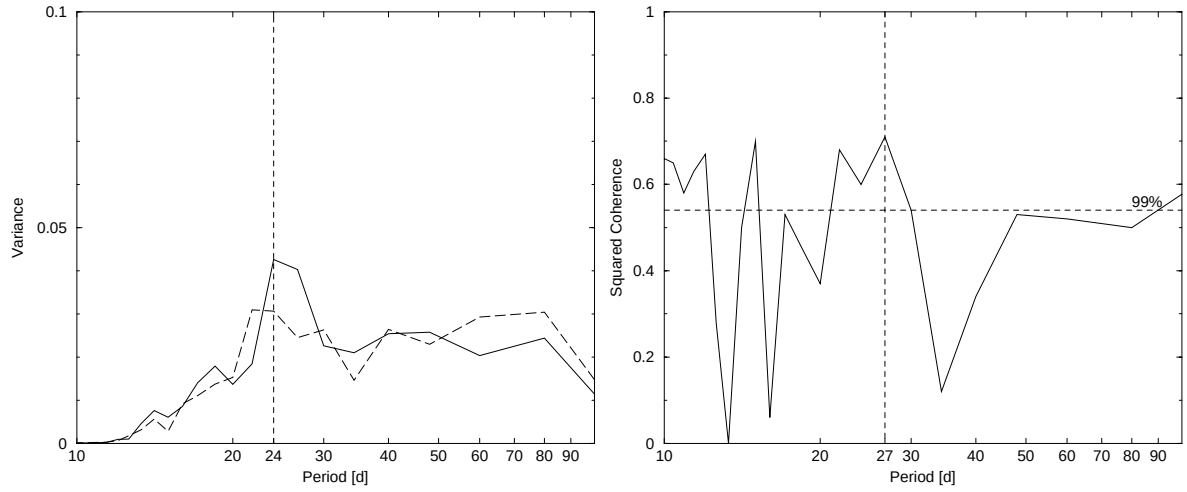

Figure 5.1: *ECHAM4 T106L19: spectra of the real (solid line) and imaginary (long dashed line) dominant POP mode (left) and their squared coherence (right). The vertical dashed lines indicate the maxima. The horizontal dashed line depicts the 99% confidence interval of the squared coherence.*

IO in ERA15 200 hPa velocity potential anomaly and NOAA OLR anomaly as presented in Figure 2.5, the eastward propagation of the negative velocity potential anomaly in the convective regime over the Indian Ocean and the West Pacific warm pool (panels one to four) is slower than in the dry regime elsewhere (panels five to eight). This characteristic change in phase speed has so far only been detected in the GLA and NCAR GCMs, which are included in the model intercomparison by Slingo et al. (1996).

As a result of the improved spatial distribution of convective anomalies over the maritime continent, the minimum in the EOF pattern at 117°E (Figure 5.3) is even shifted to the west of the minimum in ERA15 (see Figure 2.8). The maximum of the associated PC1 (Figure 5.4, left), which leads to a typical IO event, occurs on 1st of May 1986. The POP index in Figure 5.4 (right) also shows the strongest IO activity during spring 1986. The annual cycle with strongest IO activity in winter and spring is well established. From the analyzed model versions with AMIP SSTs, only ECHAM4 T106L19 represents the weak IO activity in 1987 consistent to the ERA15 data (see Figure 2.10). However, the strong IO activity during spring 1988 is underestimated (see also Figure B.2).

Since the POP analysis produces a relatively noisy IO, it is noteworthy that the improvements of ECHAM4 T106L19 in spatial distribution compared to ECHAM4 T42L19 are also shown in the time-longitude Hovmöller diagrams in Appendix B. The IO event detected by the PC1 time series shows an eastward propagation of the convection anomaly and the associated anomaly in latent heat flux (Figure 5.5, top) over the western Indian

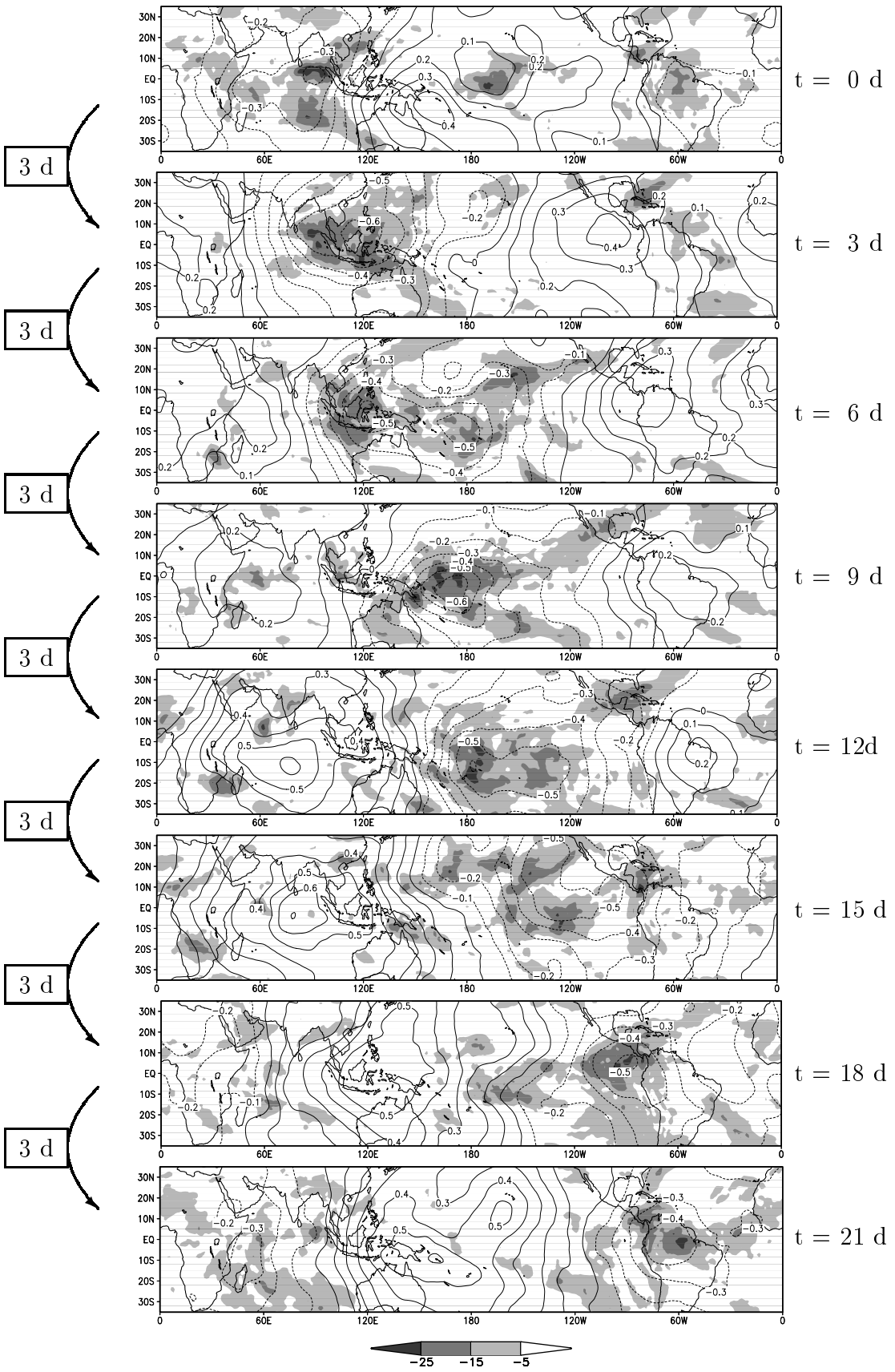

Figure 5.2: *Pseudo-Hovmöller diagrams of ECHAM4 T106L19 OLR anomaly [W m^{-2}] and 200 hPa velocity potential anomaly [10^7 $m^2 s^{-1}$]. Negative OLR anomaly (shaded) indicates deep convective anomalies and negative velocity potential anomaly (dotted) indicates large scale divergent flow. Arrows on the left and the scale on the right point out the time step between the panels.*

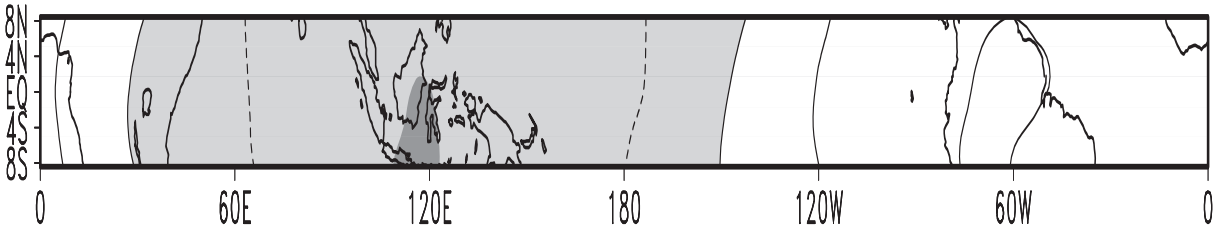

Figure 5.3: *ECHAM4 T106L19 first EOF of 200 hPa velocity potential anomaly in the equatorial region. Contour interval is 0.005, negative values are light shaded and the minimum at 117°E is indicated by dark shadings. The EOF pattern explains 34.3% of the total variance.*

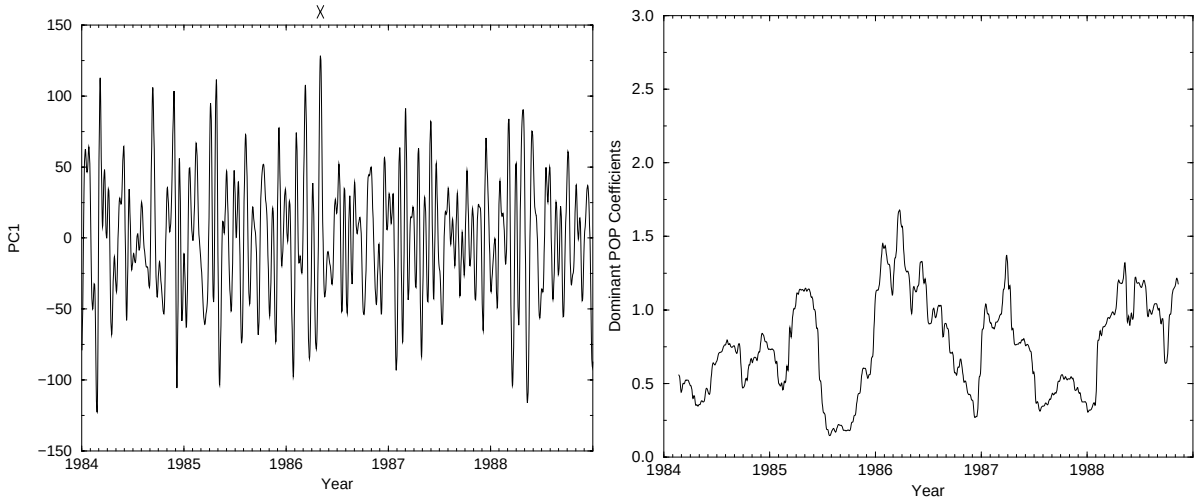

Figure 5.4: *Left: ECHAM4 T106L19 PC1, which is used as an index of the activity of the IO. X marks the maximum at the 1st of May 1986 as an identifier for a typical IO. Right: 100-day running mean of the squared amplitude of the POP coefficients of 200 hPa velocity potential anomalies, reflecting the interannual variability of the IO activity.*

Ocean in the NOAA and ERA15 data as well as in the ECHAM4 T106L19 simulation, although the simulated deep convection propagates eastward too fast. During the selected IO event, both datasets show a reduction in convective anomaly over the maritime continent at about 110°E, where the largest equatorial land mass (Borneo) is located, and a deceleration near the date line. In addition to the increased latent heat flux anomaly to the west of the deep convection anomalies, the ERA15 dataset also shows strong latent heat flux anomalies in the Central and East Pacific between 170°E and 80°W below low-level easterlies from the middle of May 1986 onwards (Figure 5.5, bottom left). ECHAM4 T106L19 simulates strong westerlies at this stage (Figure 5.5, bottom right). Only the NOAA OLR anomaly shows a reinforcement of the IO over the South American continent

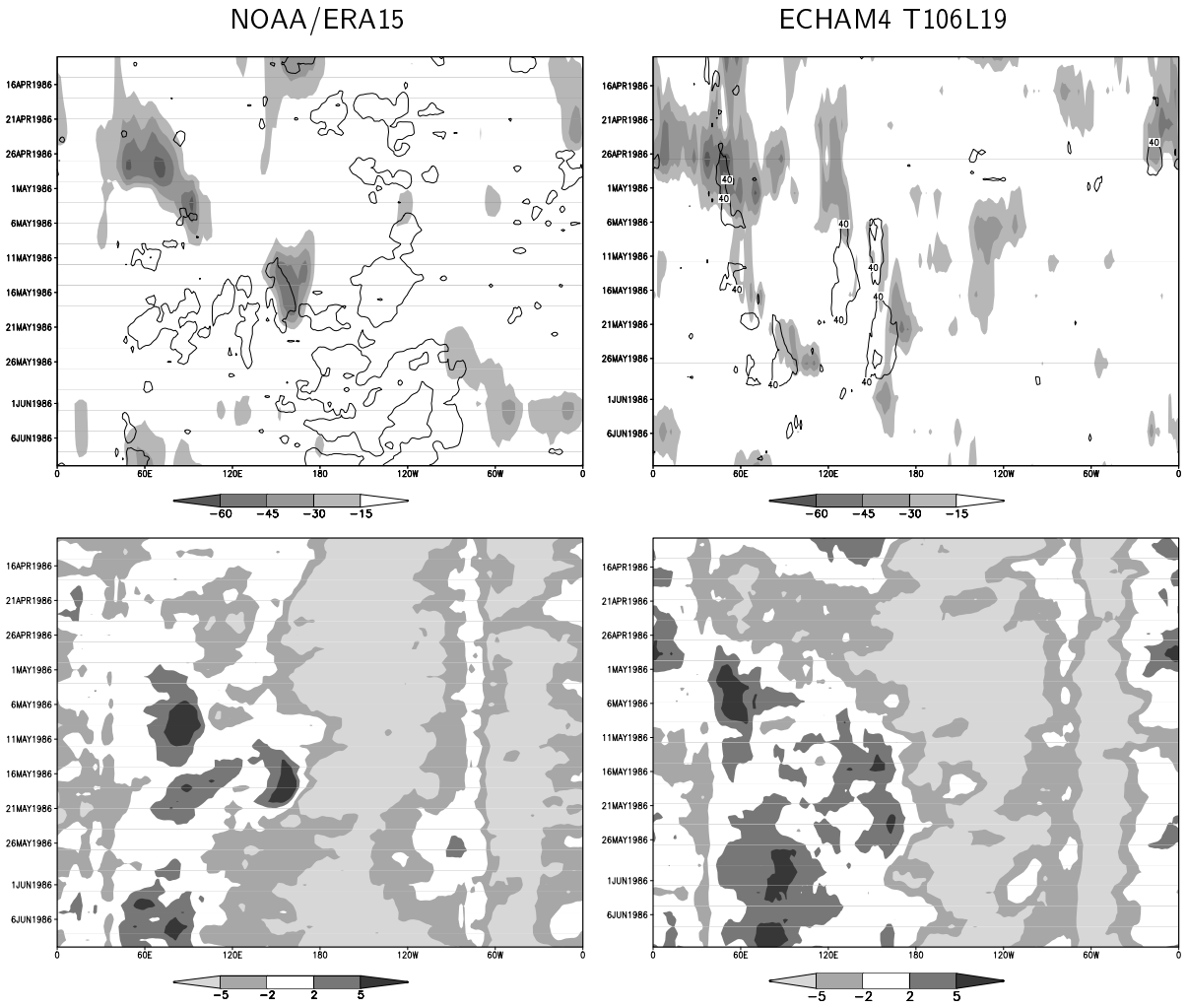

Figure 5.5: *Top: OLR anomaly [W m^{-2}] (shaded) and the 40 W m^{-2} isoline of latent heat flux anomaly. Bottom: 850 hPa zonal wind [m s^{-1}]. All data are averaged between 10°N and 10°S. Left: NOAA OLR and ERA15 latent heat flux and zonal wind, right: ECHAM4 T106L19 data.*

between 80°W and 40°W at the end of May and beginning of June 1986.

Although the underestimation of convective anomalies over the maritime continent is present in the case studies, the composite studies of ERA15 and ECHAM4 T106L19 data do not confirm these results. The spatial structure of the simulated IO is in good agreement with the ERA15 data. Since the propagation speed is even faster than in the control experiment, the analysis of ECHAM4 T106L19 suggests no connection of the too fast propagation of the IO to the eastward shift of the main IO activity. To confirm the dependence of the spatial structure of the IO on the different land-sea distribution in different horizontal resolutions, a sensitivity study with the land mass of the maritime continent replaced by ocean similar to the study by Neale and Slingo (2001) but with the ECHAM4 GCM is described in the next section.

5.2 Replacing the maritime continent by ocean

To further analyze the effect of land-sea distribution on the IO, the land mass of the maritime continent between 90°E, 160°E, 10°N and 10°S is replaced by sea points in ECHAM4 with T42 horizontal resolution (ECHAM4 NOMARI). The change in the land-sea mask replaces all surface parameters from land to sea values, except for the surface orography, since the orography in the ECHAM4 GCM is calculated in the spectral space. Thus, a change in the spectral coefficients of the orography would lead to a globally changed orography. However, Neale and Slingo (2001) showed with the HadAM3 gridpoint GCM, that the removal of orographic forcing over the maritime continent has only a small contribution on the deep convection compared to the replacement of the land surface temperature by the interpolated SST. The new SST dataset is obtained by interpolation of the SST from the surrounding sea points. Over the maritime continent, the values for annual mean surface temperatures over land are about 24-26 °C. This is up to 5 K cooler than over the ocean, with temperatures of 28-29 °C due to the accumulation of warm surface water from the West Pacific warm pool. Thus, this modification drastically increases the mean surface temperature over the maritime continent (Figure 5.6).

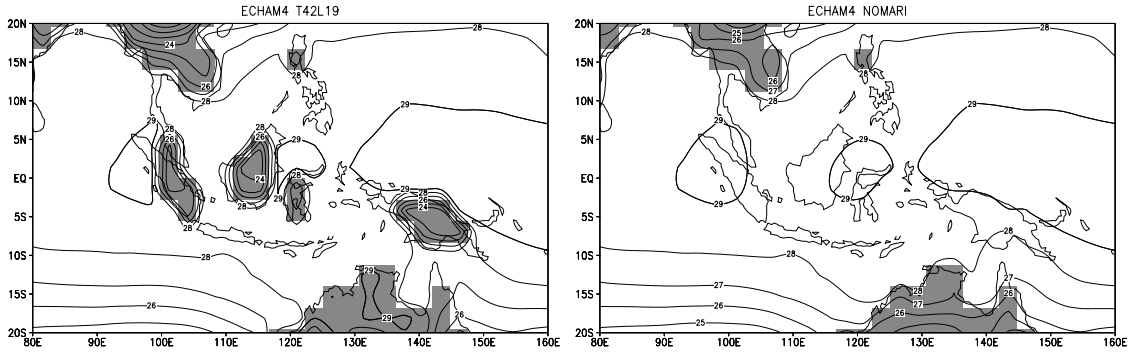

Figure 5.6: *Land-sea distribution (land points shaded) and mean surface temperature [°C] for 1984-1988 of the control experiment (ECHAM4 T42L19, left) and the experiment with the land mass of the maritime continent replaced by sea points (ECHAM4 NOMARI, right).*

As in ECHAM4 T106L19, the results of the POP analysis reflect an increase in phase speed of the simulated IO compared to the control experiment. The spectrum (Figure 5.7, left) shows a distinct peak at 27 days for the real and the imaginary part of the dominant POP coefficient; the imaginary part has a second maximum near 20 days. Both maxima are confirmed by the squared coherence (Figure 5.7, right). The slower mode is referred to as the IO-mode. The dominant POP explains 46.9% of the total variance and has an e-folding time of about 60 days. The increase in phase speed, compared to the control

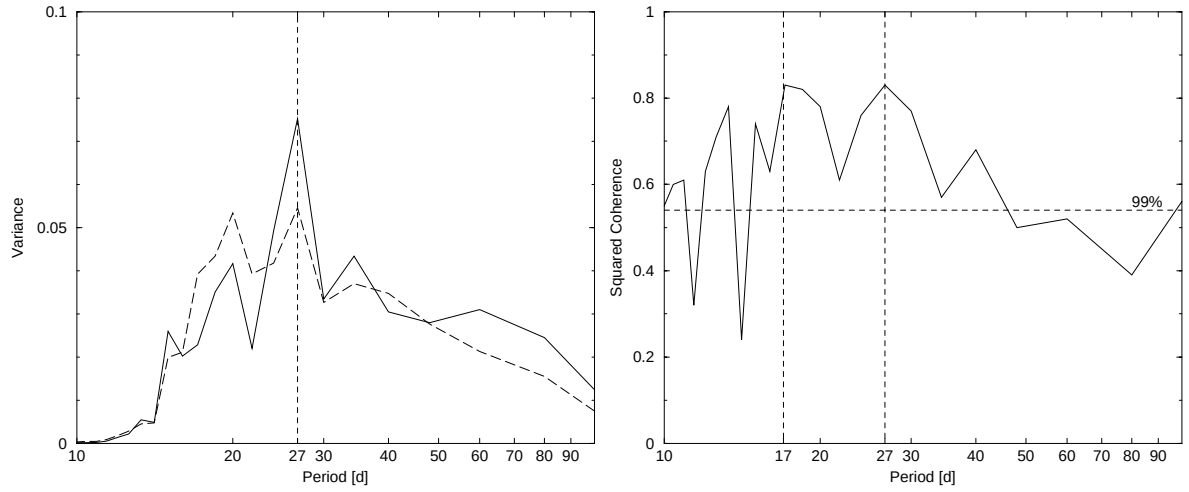

Figure 5.7: *ECHAM4 NOMARI: spectra of the real (solid line) and imaginary (long dashed line) dominant POP coefficients (left) and their squared coherence (right). The vertical dashed lines indicate the maxima. The horizontal dashed line depicts the 99% confidence interval of the squared coherence.*

experiment, reveals the importance of the land mass on the maritime continent to reduce the propagation of the IO, since the land mass induces frictional processes (Hendon and Salby, 1994), and the strong diurnal cycle of convection over land in the maritime continent is able to discharge the convective instability over this area (e.g. Rui and Wang, 1990; Salby and Hendon, 1994; Zhang and Hendon, 1997).

The composite study (Figure 5.8) shows a strengthened convective anomaly over the maritime continent due to the higher SSTs. Also the spatial structure of the main IO activity is improved, compared to the control experiment. This is in agreement with the study by Neale and Slingo (2001), who replaced the maritime continent by ocean in the HadAM3 AGCM. The improvement in the simulated spatial structure of the IO resembles the effect of increased horizontal resolution (Section 5.1); only the convective anomalies over the eastern Indian Ocean, where the changes in land-sea distribution are not effective, is still underestimated in ECHAM4 NOMARI. The EOF analysis (Figure 5.9) reveals the main IO activity at about 122°E, also similar to ECHAM4 T106L19.

The PC1 time series (Figure 5.10, left) and the POP index time series (Figure 5.10, right) both show the presence of the annual cycle of the IO after removal of the land surface over the maritime continent. The IO event, which is detected with the maximum of PC1, occurs around the 20th of May 1985. The case studies illustrate that the IO is barely seen in the NOAA and ECHAM4 NOMARI OLR anomalies during this period (Figure 5.11, top). However, the Hovmöller diagrams in Figure B.2 show an eastward propagation of

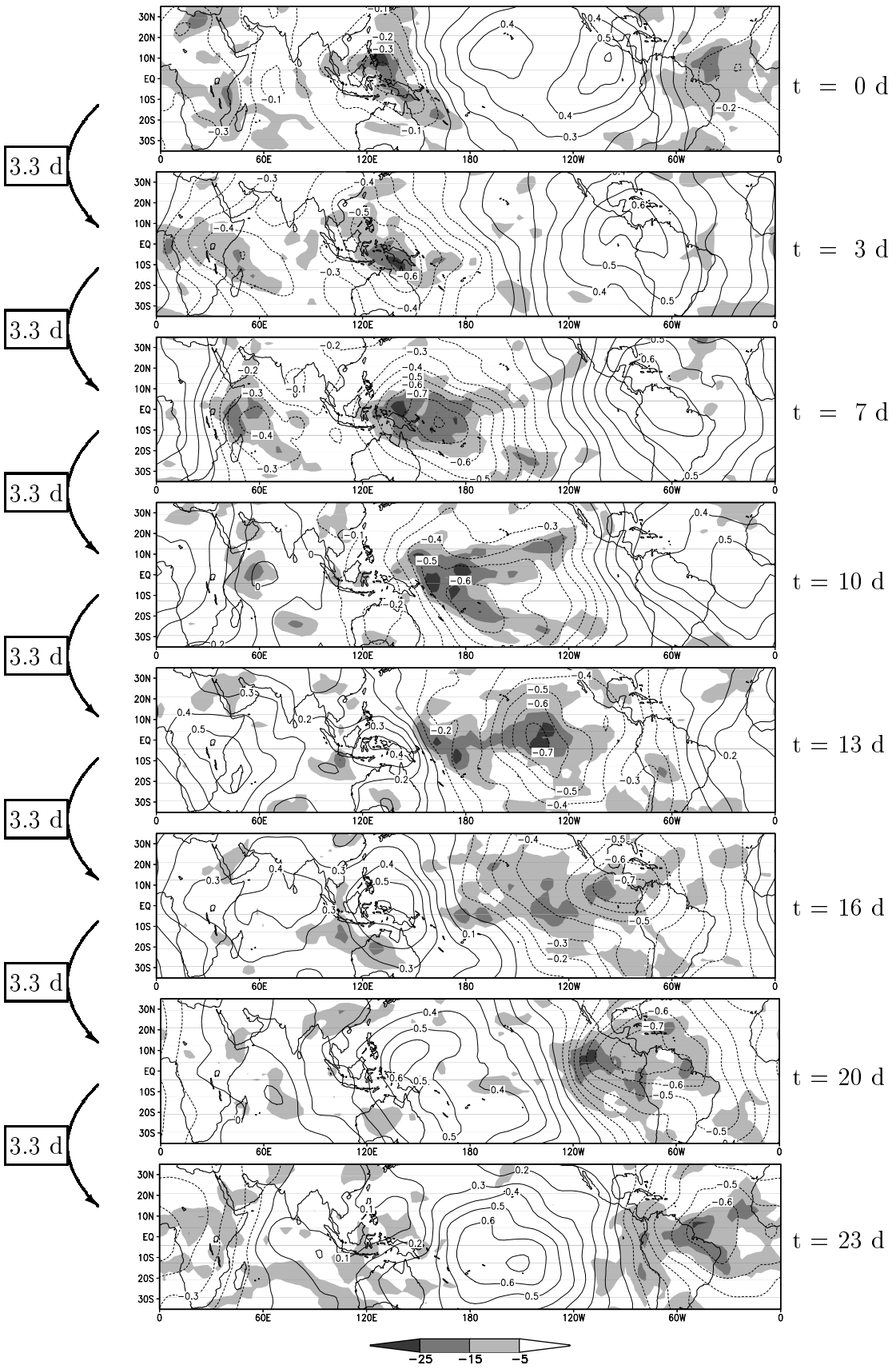

Figure 5.8: *Pseudo-Hovmöller diagrams of ECHAM4 NOMARI OLR anomaly [W m^{-2}] and 200 hPa velocity potential anomaly [10^7 $m^2 s^{-1}$]. Negative OLR anomaly (shaded) indicates deep convective anomalies and negative velocity potential anomaly (dotted) indicates large-scale divergent flow. Arrows on the left and the scale on the right point out the time step between the panels as derived by the POP analysis.*

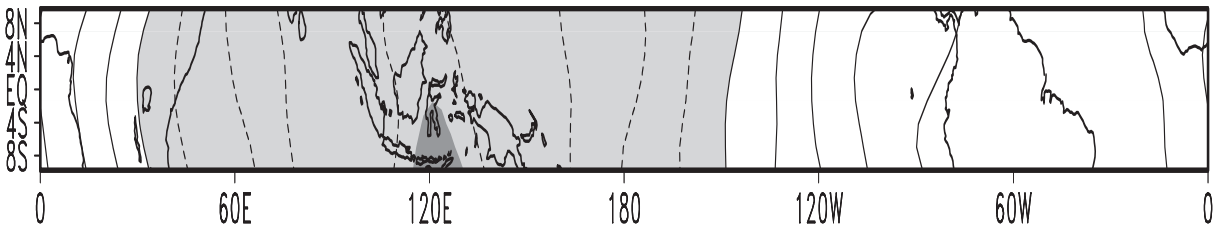

Figure 5.9: *ECHAM4 NOMARI first EOF of 200 hPa velocity potential anomaly in the equatorial region. Contour interval is 0.01, negative values are light shaded and the minimum at 122°E is indicated by dark shadings. The EOF pattern explains 33.1% of the total variance.*

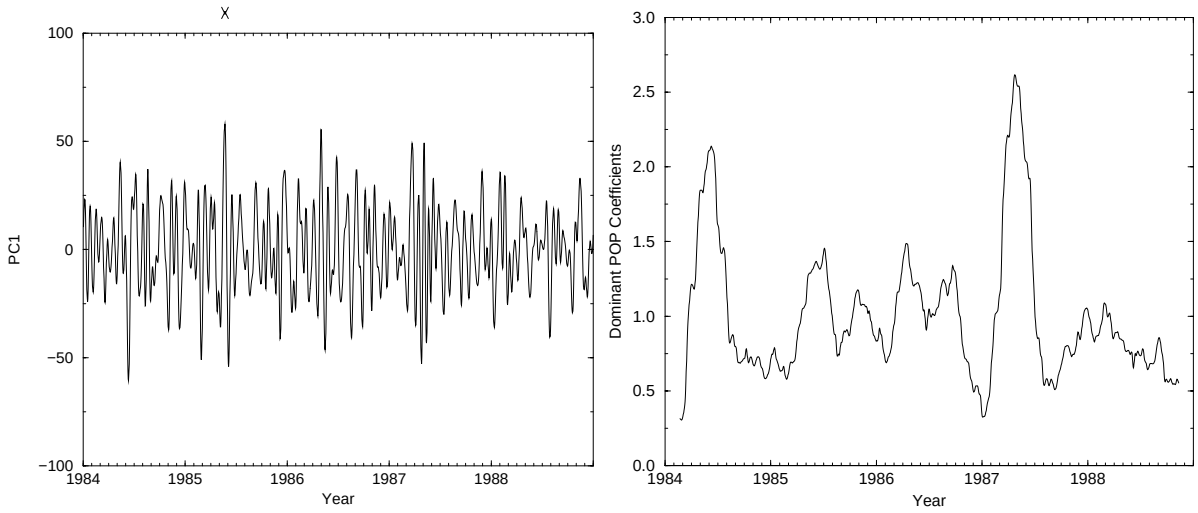

Figure 5.10: *Left: ECHAM4 NOMARI PC1, which is used as an index of the activity of the IO. X marks the maximum at the 20th of May 1985 as an identifier for a typical IO. Right: 100-day running mean of the squared amplitude of the POP coefficients of 200 hPa velocity potential anomalies, reflecting the interannual variability of the IO activity.*

200 hPa velocity potential anomaly in both datasets for the depicted time period. Also the positive latent heat flux anomalies below and to the west of the deep convective anomalies indicate an eastward propagation due to the wave-CISK mechanism. However, the WWBs are slightly weaker in ECHAM4 NOMARI compared to ERA15 (Figure 5.11, bottom).

The explanation of the different representation of the IO due to different boundary conditions requires a closer study of the simulated mean climate. Figure 5.12 (top left) shows the 5-year mean of the years 1984 to 1988 of NOAA satellite observed OLR. To highlight the small differences in deep convection, only OLR values in the range of 206 to 226 W m^{-2} are shown with a 2 W m^{-2} interval. The strongest convective activity occurs between 90°E and 115°E and also east of 130°E. It is disrupted between 120°E and

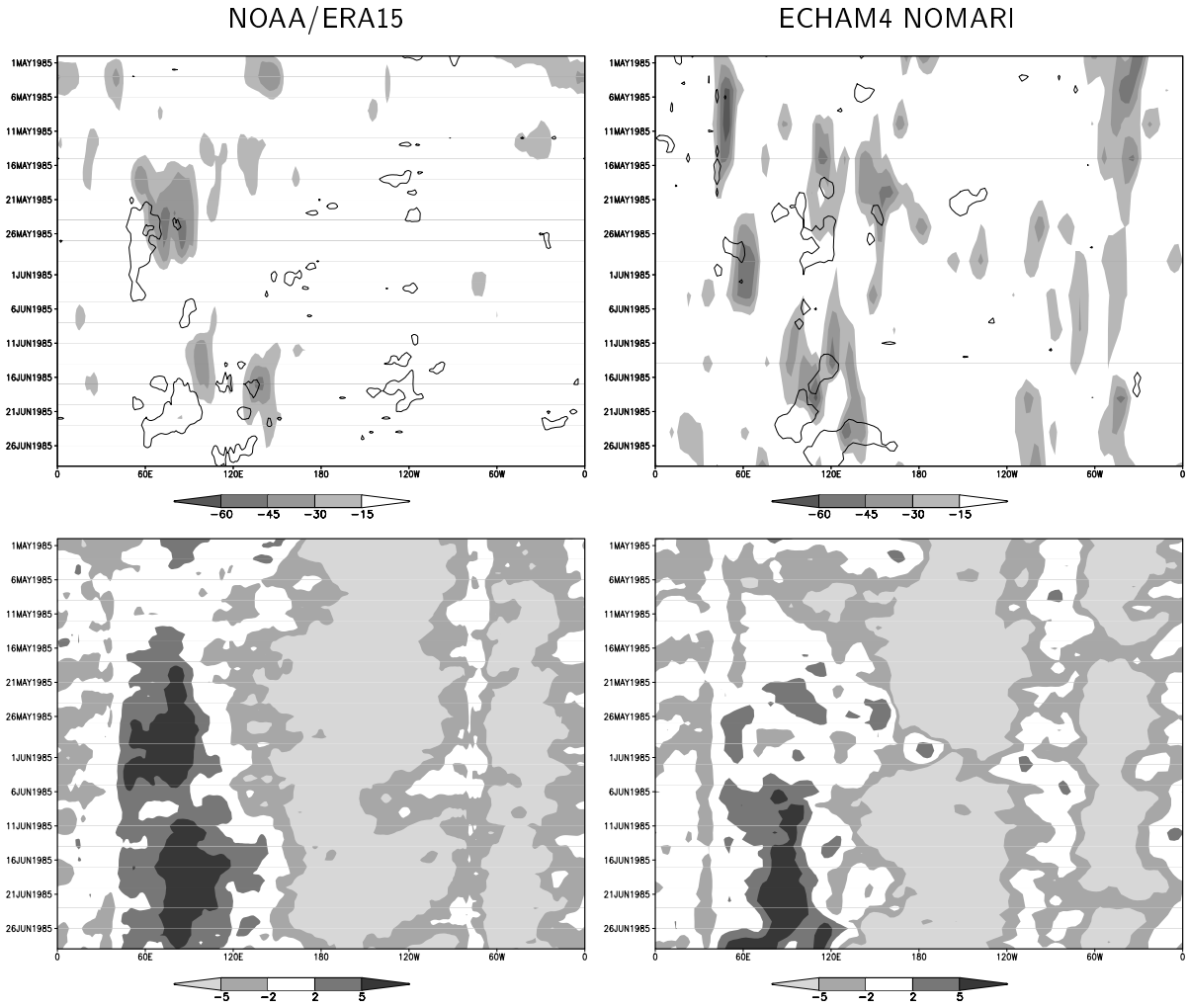

Figure 5.11: *Top: OLR anomaly [W m^{-2}] (shaded) and the 40 W m^{-2} isoline of latent heat flux anomaly. Bottom: 850 hPa zonal wind [m s^{-1}]. All data are averaged between 10°N and 10°S. Left: NOAA OLR and ERA15 latent heat flux and zonal wind, right: ECHAM4 NOMARI data.*

130°E. ERA15 OLR (Figure 5.12, top right) is weaker than the observations. Especially the deep convection over Borneo and New Guinea is underestimated, but the deepest convection to the west of Sumatra is well represented. The control experiment shows a more continuous mean OLR pattern with the deepest convection over Borneo. From the first impression, this seems to be in contrast to the underestimation of the convective anomaly during the passage of an IO. However, it should be noticed that a positive zonal gradient of mean deep convection from the eastern Indian Ocean to the West Pacific warm pool could prevent the eastward propagation of convective anomalies, which are related to the IO, over the maritime continent. A result of the increase in mean surface temperature in ECHAM4 NOMARI is an increase in mean deep convection. The mean OLR pattern in ECHAM4 NOMARI is well represented compared to the NOAA observations. Due to

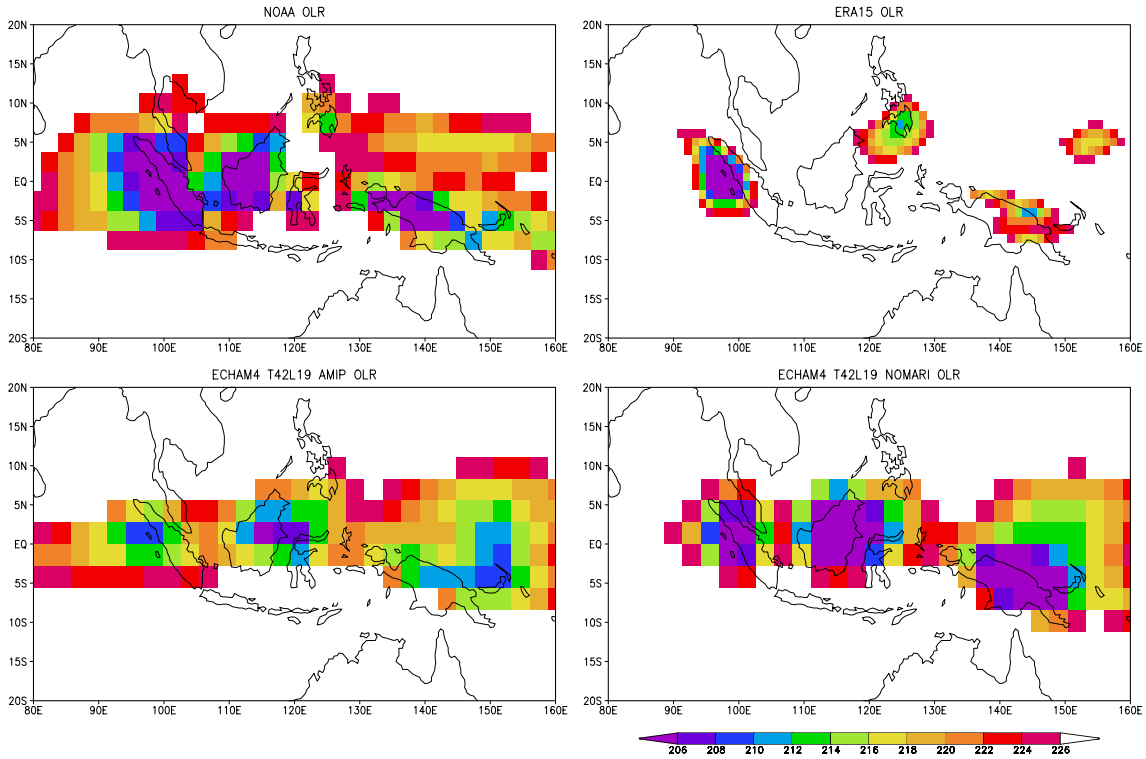

Figure 5.12: *Mean (1984-1988) OLR [W m^{-2}] for NOAA observations, ERA15 reanalysis, ECHAM4 T42L19 AMIP and ECHAM4 T42L19 NOMARI.*

the unchanged orography the deepest convection is still located over the islands.

Although the realistic representation of deep convection is essential for the simulation of the location of the main IO activity, the propagation speed of the IO in ECHAM4 NOMARI still differs from the observed. The increase in deep convection is accompanied by an increase in low-level convergence and surface latent heat flux, since the island regions are being replaced by oceanic regions with higher surface temperature, lower surface friction and an unlimited moisture supply from the surface. Figure 5.13 illustrates the changes in mean 850 hPa divergence and mean surface latent heat flux due to the removal of the islands over the maritime continent. Compared to ERA15, both GCM integrations overestimate 850 hPa convergence and surface latent heat flux. The variability of 850 hPa divergence over the maritime continent in ERA15 is twice as strong as in both the NCEP and NASA reanalyses (see Section 2.1). However, the strong 850 hPa divergence suggests the importance of low-level convection for the reduced propagation speed of the IO. This low-level convection is accompanied by reduced latent heat flux. The deep convection in ECHAM4 NOMARI is accompanied by stronger 850 hPa convergence and latent heat flux than the control experiment. This increases the propagation speed of the IO in this sensitivity study. The weaker WWBs in the case study of ECHAM4 NOMARI indicate

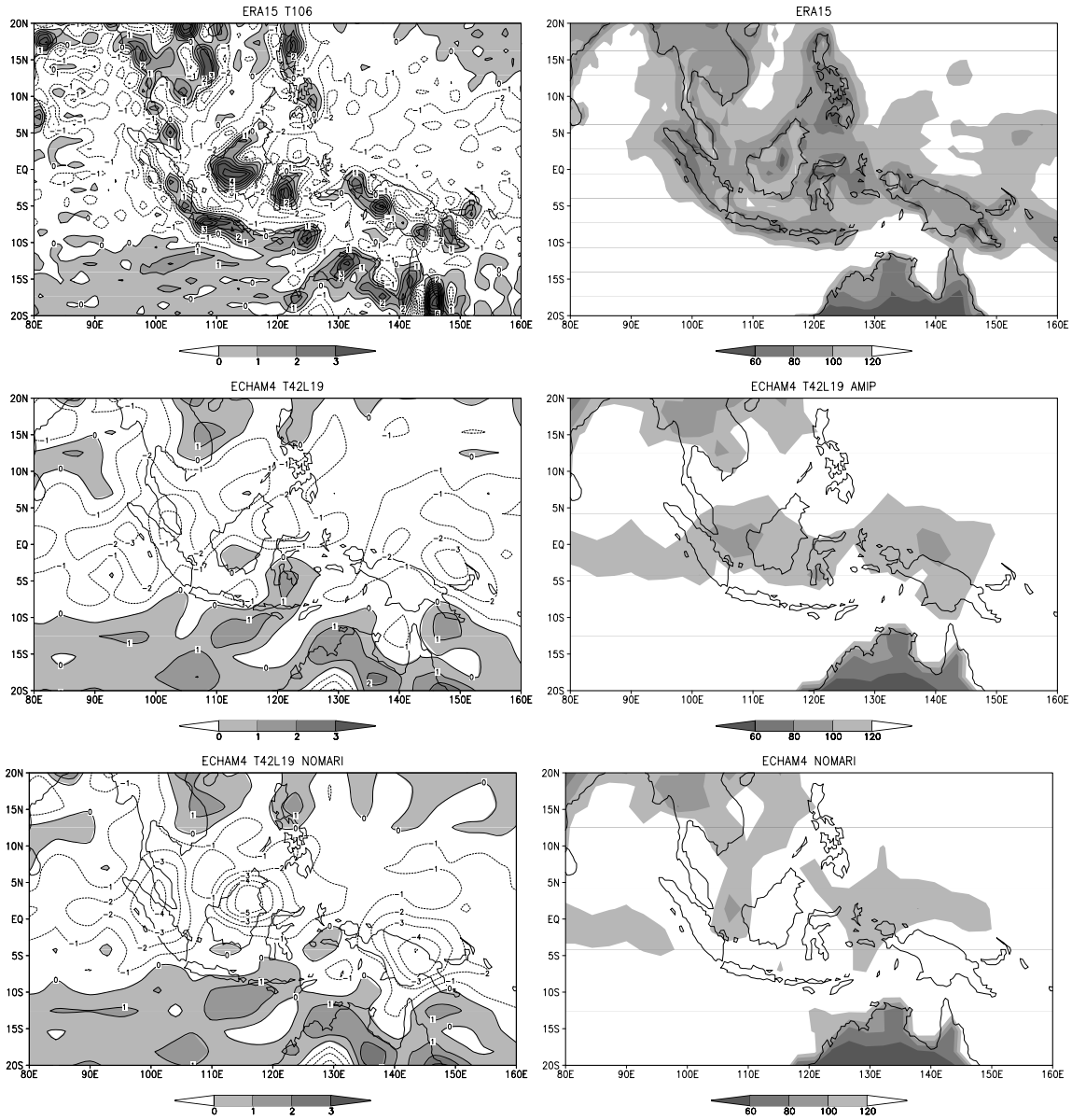

Figure 5.13: *Mean (1984-1988) 850 hPa divergence [10^{-6} s^{-1}] (left) and surface latent heat flux [W m^{-2}] (right) for ERA15 reanalysis, ECHAM4 T42L19 AMIP and ECHAM4 T42L19 NOMARI. Divergence is shaded and convergence dashed. Low values of latent heat flux are dark shaded.*

that the increased 850 hPa convergence is due to the meridional wind field.

The artificial improvements of the spatial structure of the IO and the acceleration of the eastward propagation due to the removal of the maritime continent lead to the assumption that surface forcing, especially due to heating, is an essential component for the realistic representation of the IO in GCMs. Since the IO is driven by deep convection and the convection is very sensitive to changes of the surface temperature (see Section 1.3), the following section deals with the influence of the prescribed SST on the simulation of the IO in ECHAM4.

5.3 On the impact of different SSTs

Sections 5.1 and 5.2 revealed the importance of surface characteristics on the simulation of the IO. Since the IO influences the SST – although in a small amplitude – (see Section 2.2), and the tropical convection is very sensitive to changes in the surface temperature (see Section 1.3), the IO should be considered as a coupled atmosphere-ocean phenomenon. The results of ECHAM4/OPYC3 in Section 3.2 did not provide any improvements of the simulation of the IO in a CGCM, but the following question is left open: Are there coupled atmosphere-ocean processes in the Indian Ocean/West Pacific warm pool region that influence the propagation of the IO, but are not resolved by current CGCMs?

As shown in Section 5.2, the maritime continent is located in a region of strong differences between SST and land surface temperature, and the IO is strongly influenced by the land-sea distribution in this region. Hence, a realistic surface forcing is essential for the simulation of the IO in AGCMs. A map of Indonesia illustrates the small-scale land-sea distribution over the maritime continent (Figure 5.14). Besides Indonesia, also Malaysia, the Philippines and Papua New Guinea belong to the maritime continent. Observations reveal a land area of 1,826,440 km^2 for Indonesia, 328,550 km^2 for Malaysia, 298,170 km^2 for the Philippines and 452,860 km^2 for Papua New Guinea (Central Intelligence Agency, 2001). This is a total of 2,906,020 km^2. With a radius of the earth of 6378 km at the equator, a grid point near the equator at T42 horizontal resolution (128x64 grid points) covers an area of 98,019 km^2. Hence, the 19 grid points representing the maritime continent cover an area of only 1,862,359 km^2 in the GCM, which is about 64% of the total land area over the maritime continent.

Figure 5.15 shows the 5-year mean SST of the years 1984 to 1988 for ERA15 (top left), the AMIP dataset at T106 horizontal resolution (top right) and interpolated to T42 (Figure 5.15, bottom left). The annual mean SST over the region between 90°E, 160°E, 10°N and 10°S for the years 1984 to 1988 is 28.72°C for the ERA15 SST, 28.87°C for AMIP T106 and 28.86°C for AMIP T42. The small increase in annual mean values of 0.14-0.15 K occurs in a temperature range where convection is highly sensitive to surface temperature (see Section 1.3). In the observational dataset used in ERA15, the values over small land areas, which are not resolved by the ERA15 T106 horizontal resolution, may represent a realistic surface heating, but they are extrapolated using a "weaving" algorithm developed at NCEP (Taylor et al., 2001). The wave-structure in the ERA15 SST, especially north east of New Guinea, is necessary to represent the influence of the spectral orography. This is neglected in the AMIP SSTs (E. Roeckner, pers. comm.).

Figure 5.14: *Map of Indonesia (Central Intelligence Agency, 2001).*

The AMIP SST datasets strongly differ between land and sea points, which is necessary to compute the surface processes in a physically correct way. However, the problem of such a strict distinction is the change in the prescribed heating pattern. As a simple example, one could suggest a grid point, that consists of three quarters sea surface with a mean temperature of 28 °C and one quarter land surface with a mean temperature of 26 °C. Due to the larger fraction of sea, this grid point is treated as a sea point in a GCM. An observational dataset would use the mean surface temperature of 27.5 °C over this grid point, whereas the AMIP dataset would use the 28 °C mean SST. Such small changes in mean surface temperature may have relatively strong effects on the development of deep convection. At particular grid points the AMIP SST differs from the observed surface temperature by more than 0.5 K. This is seen especially over the Philippines, the Lesser Sunda Islands east of Java and Sulawesi (Celébes) and the Mollucas between Borneo and New Guinea. To take the effect of small islands into account, which are not resolved by the GCMs; an artificial SST dataset is constructed (CHSST T42), that uses the ERA15 SST horizontally interpolated from T106 to T42, whereby the "SST" is partly influenced by the land surface temperature (Figure 5.15, bottom right). The annual mean SST over the region between 90°E, 160°E, 10°N and 10°S for the years 1984 to 1988 is 28.68 °C for the CHSST T42 dataset, similar to the ERA15 SST dataset.

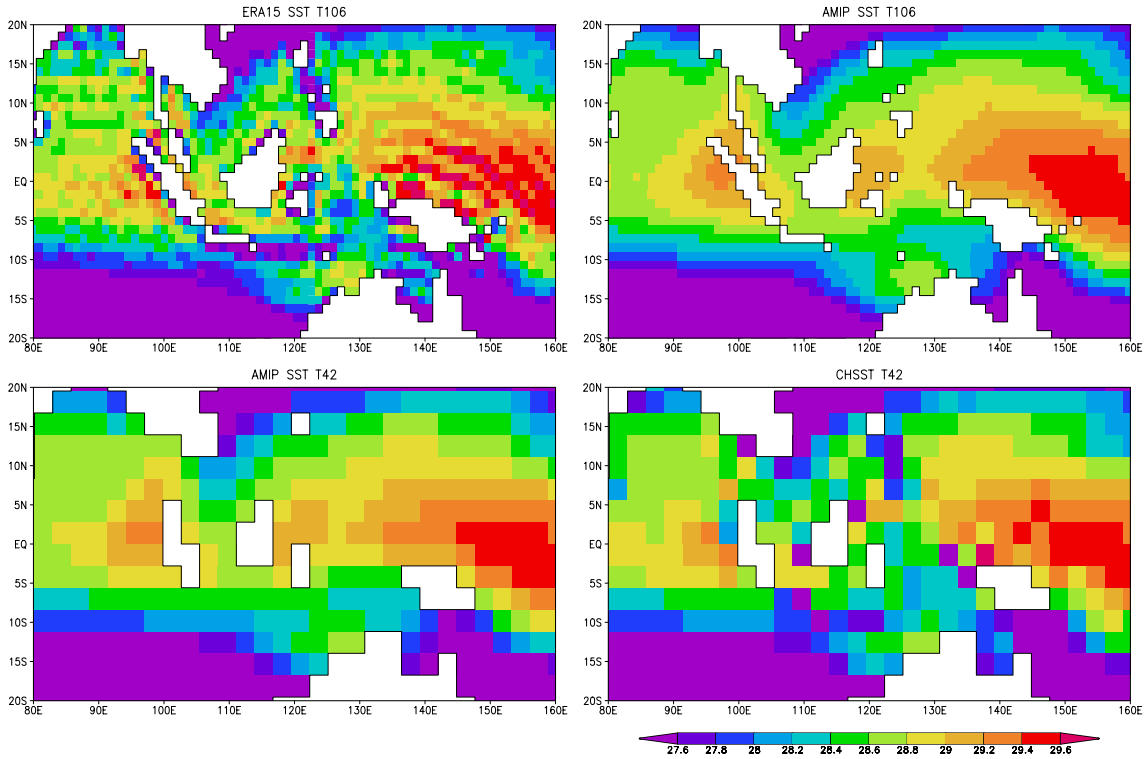

Figure 5.15: *Mean (1984-1988) SST [°C] for ERA15, ECHAM4 T106L19 AMIP, ECHAM4 T42L19 AMIP and ECHAM4 T42L19 CHSST.*

As in the previous chapters, the IO in ECHAM4 CHSST is investigated with the POP analysis of the simulated 15-90 day bandpass filtered 200 hPa velocity potential anomaly. The peaks in the real and imaginary parts of the dominant POP coefficient (Figure 5.16, left) occur at the 48 days period as in the ERA15 data. This is a considerably slower period than in the control experiment (see Figure 3.1). The slower propagation speed of the IO is confirmed in the squared coherence (Figure 5.16, right). It shows a pronounced bimodal spectrum with the period for the slow mode, referred to as the IO mode, shifted from 34 to 48 days compared to the control experiment, and the one of the faster mode shifted from 18 to 24 days. The bandwidth and amplitude for the fast mode remain nearly unchanged, but the bandwidth of the IO mode is broadened to cover a range from 29 to 53 days above the 99% confidence interval and also the maximum is considerably increased. This POP mode has a relatively long e-folding time of about 75 days and explains 53.7% of the total variance.

The composite study (Figure 5.17) describes the simulated IO. The period of 48 days yields a time step of 6 days from one panel to the next, as in ERA15. The position of the main activity of the IO is also much closer to the reanalysis data, compared to the control experiment. The convective anomalies over the maritime continent are present and this

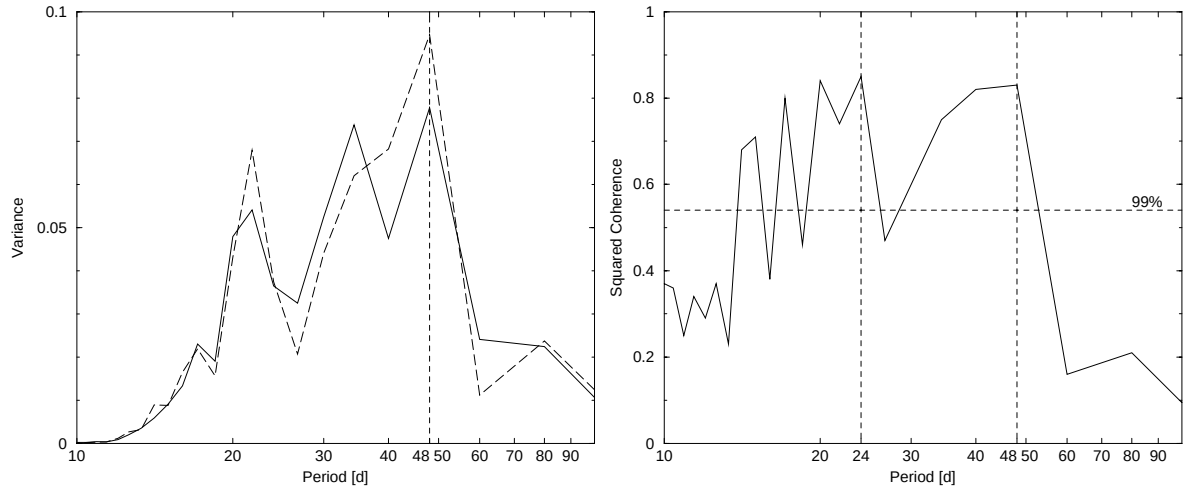

Figure 5.16: *ECHAM4 CHSST: spectra of the real (solid line) and imaginary (long dashed line) dominant POP coefficients (left) and their squared coherence (right). The vertical dashed lines indicate the maxima. The horizontal dashed line depicts the 99% confidence interval of the squared coherence.*

improvement is also confirmed by the EOF analysis (Figure 5.18) with the minimum over the maritime continent at 143°E, similar to the reanalysis data. The similarity of the position of main IO activity in ECHAM4 NOMARI and ECHAM4 CHSST compared to the control experiment suggests that the larger temperature differences between land and sea are responsible for the eastward shift of the IO. The peak in the PC1 time series reveals an IO around the 20th of June 1987 (Figure 5.19, left). Also in the ECMWF analysis data (see Figure 1.2), some weak IO activity is seen in summer 1987. The interannual variability of the IO, as represented by the POP-coefficient time series (Figure 5.19, right), does not show the erroneous peak prior to the 1987 El Niño that is present in the control experiment. The POP-coefficient time series reveal the strongest IO activity during 1985, as in the reanalysis data (see Figure 2.10, right). The observed strong IO activity in spring 1988 is not present in this model version.

The case study of the IO shows the strongest OLR anomaly near the date line in the observations and in ECHAM4 CHSST (Figure 5.20, top). As previously stated, this feature is typical for pre-El Niño conditions. The present case is a good example for the interaction of Kelvin and Rossby waves, as previously described by Nakazawa (1988) and Lau et al. (1989). The super cloud clusters propagate eastward consistent with the Kelvin wave theory. This is seen in the NOAA OLR data (Figure 5.20, top left) from the 5th of July until the 30th of July 1987, when the super cloud cluster propagates from 150°E to 165°W. One Rossby wave propagates slowly westward from 170°E to 150°E from the 30th of June to the 10th of July 1987. Another Rossby wave propagates westward from

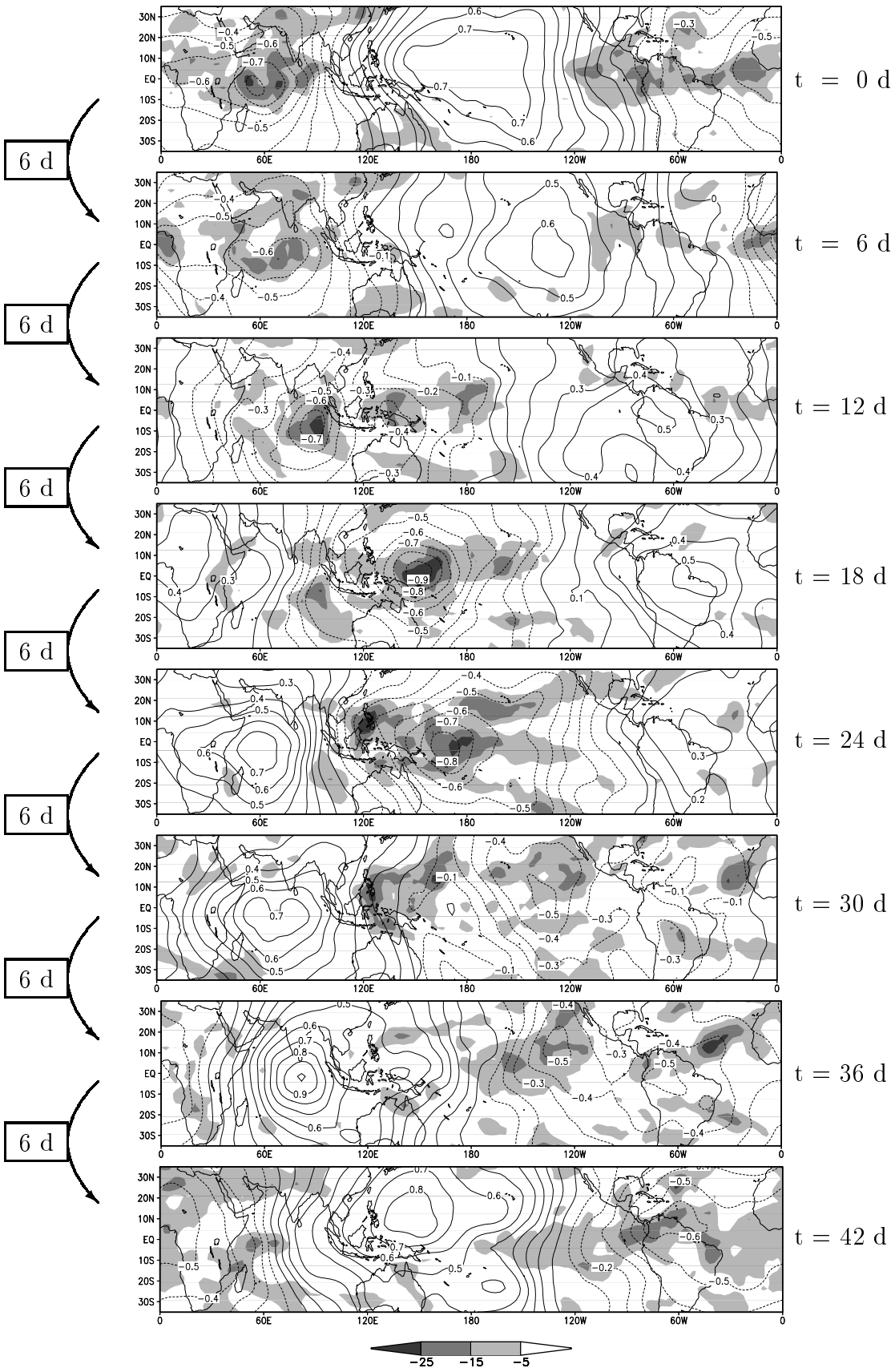

Figure 5.17: *Pseudo-Hovmöller diagrams of ECHAM4 CHSST OLR anomaly [W m^{-2}] and 200 hPa velocity potential anomaly [10^7 m^{2}s^{-1}]. Negative OLR anomaly (shaded) indicates deep convective anomalies and negative velocity potential anomaly (dotted) indicates large-scale divergent flow. Arrows on the left and the scale on the right point out the time step between the panels as derived by the POP analysis.*

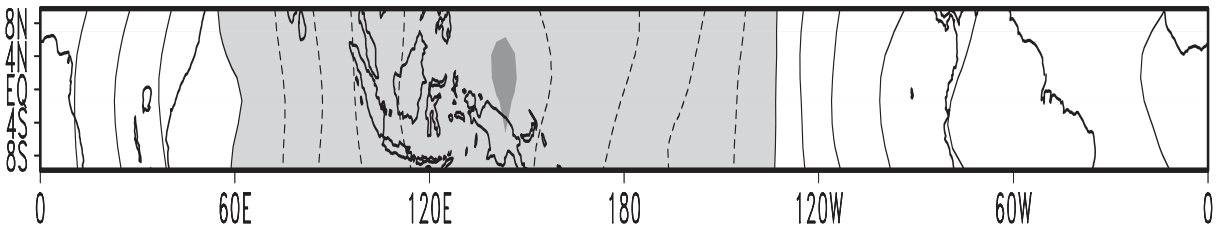

Figure 5.18: *ECHAM4 CHSST first EOF of 200 hPa velocity potential anomaly in the equatorial region. Contour interval is 0.01, negative values are light shaded and the minimum at 143°E is indicated by dark shadings. The EOF pattern explains 33.1% of the total variance.*

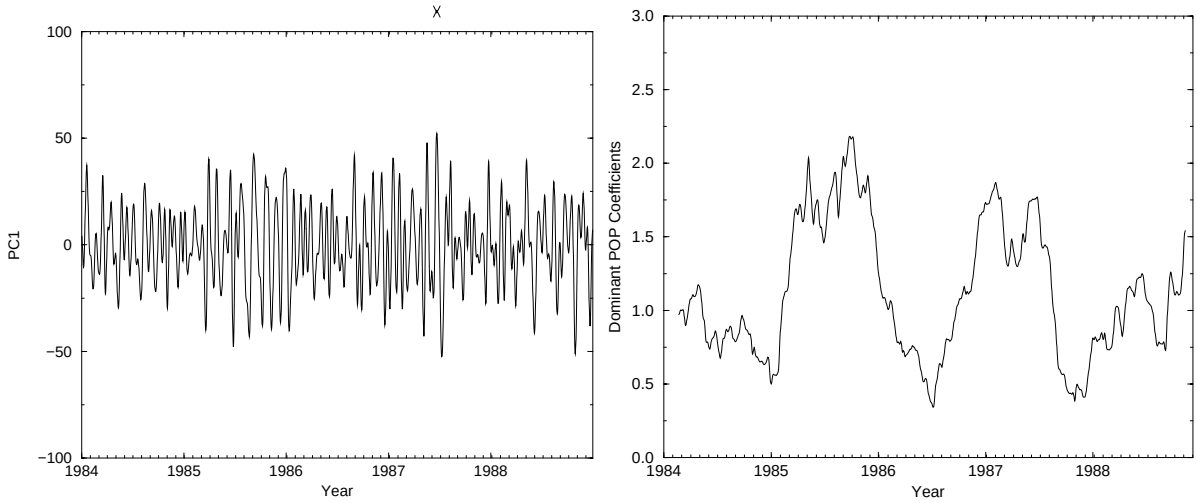

Figure 5.19: *Left: ECHAM4 CHSST PC1 which is used as an index of the activity of the IO. X marks the maximum at the 20th of June 1987 as an identifier for a typical IO. Right: 100-day running mean of the squared amplitude of the POP coefficients of 200 hPa velocity potential anomalies, reflecting the interannual variability of the IO activity.*

the date line to 170°E during the 5th to the 17th of July 1987. As theoretically expected, both Rossby waves produce WWBs and associated positive latent heat flux anomalies to the west of the deep convective anomalies (see Section 1.3). Weak WWB activity is seen around 120°E between the 10th and the 17th of July 1987 (Figure 5.20, bottom). ECHAM4 CHSST simulates two eastward propagating IO events (Figure 5.20, right). Both events have the strongest convective anomaly around 150°E, the first on the 20th of June and the second on the 21st of July 1987. A Rossby wave, initiated by the first IO, is slowly propagating westward from 120°E to 80°E between the 23rd of June and the 12th of July 1987, when it reaches the second IO. As in the reanalysis data, the strong WWBs (Figure 5.20, bottom right) appear mainly below and to the west of the Rossby wave activity.

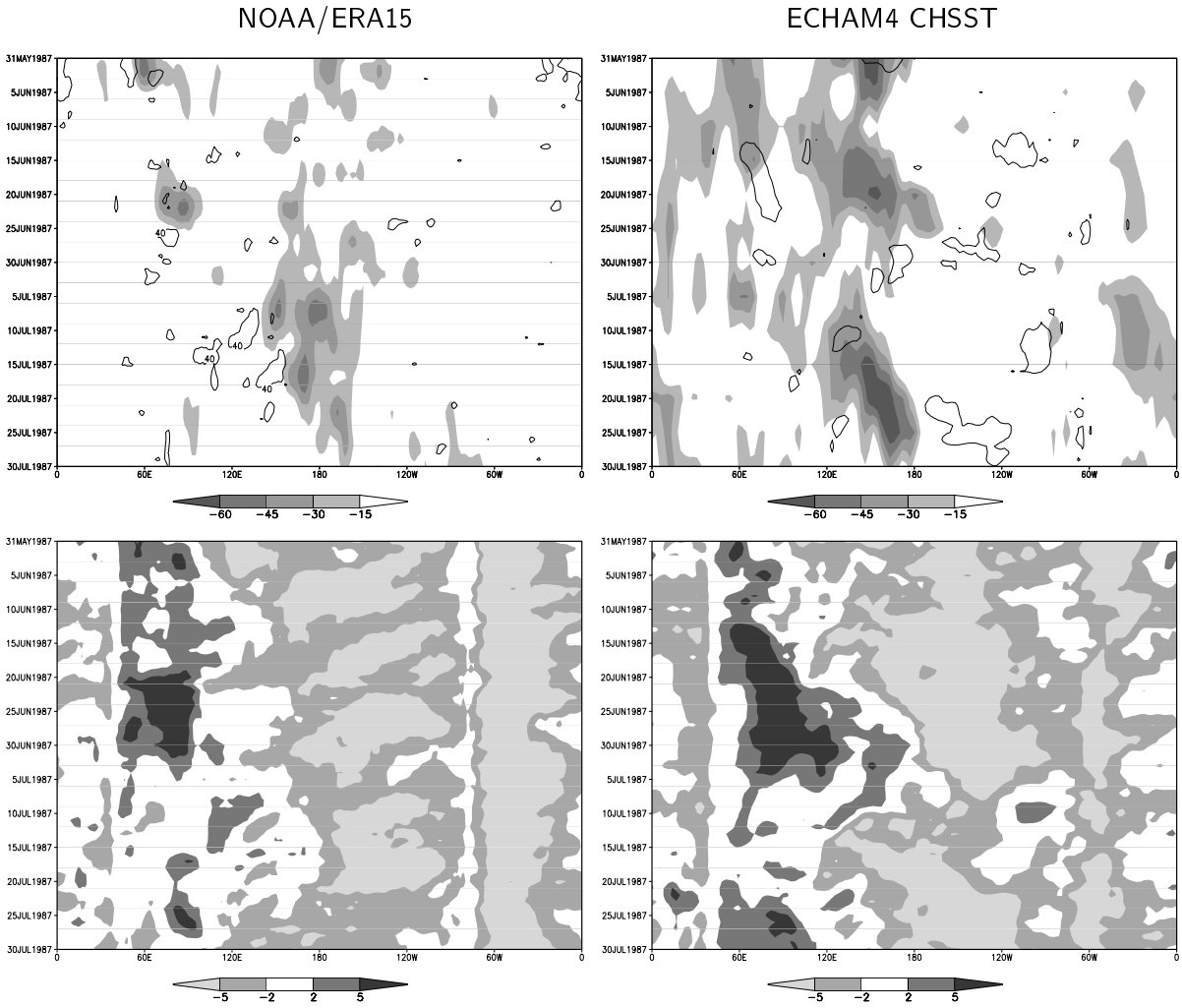

Figure 5.20: *Top: OLR anomaly [W m^{-2}] (shaded) and the 40 W m^{-2} isoline of latent heat flux anomaly. Bottom: 850 hPa zonal wind [m s^{-1}]. All data are averaged between 10°N and 10°S. Left: NOAA OLR and ERA15 latent heat flux and zonal wind, right: ECHAM4 CHSST data.*

The improved simulation of the IO due to in general lower SSTs over the maritime continent region shows the strong impact of the prescribed SST on the IO. Lower mean SSTs result in lower convection, a stronger influence of frictionally dominated surface convergence and by this a slower propagation of the IO (Hendon and Salby, 1994). The lower mean convection over the maritime continent has a peak near 90°E (Figure 5.21, top left), similar to the NOAA satellite observations (see Figure 5.12). The mean surface latent heat flux, which is overestimated in the control experiment over the maritime continent, is reduced in ECHAM4 CHSST (Figure 5.21, top right) due to the more realistic forcing with lower surface heating. The mean 850 hPa divergence over the maritime continent island regions (Figure 5.21, bottom) is also slightly increased compared to the control experiment, especially over New Guinea and the Philippines. An additional experiment

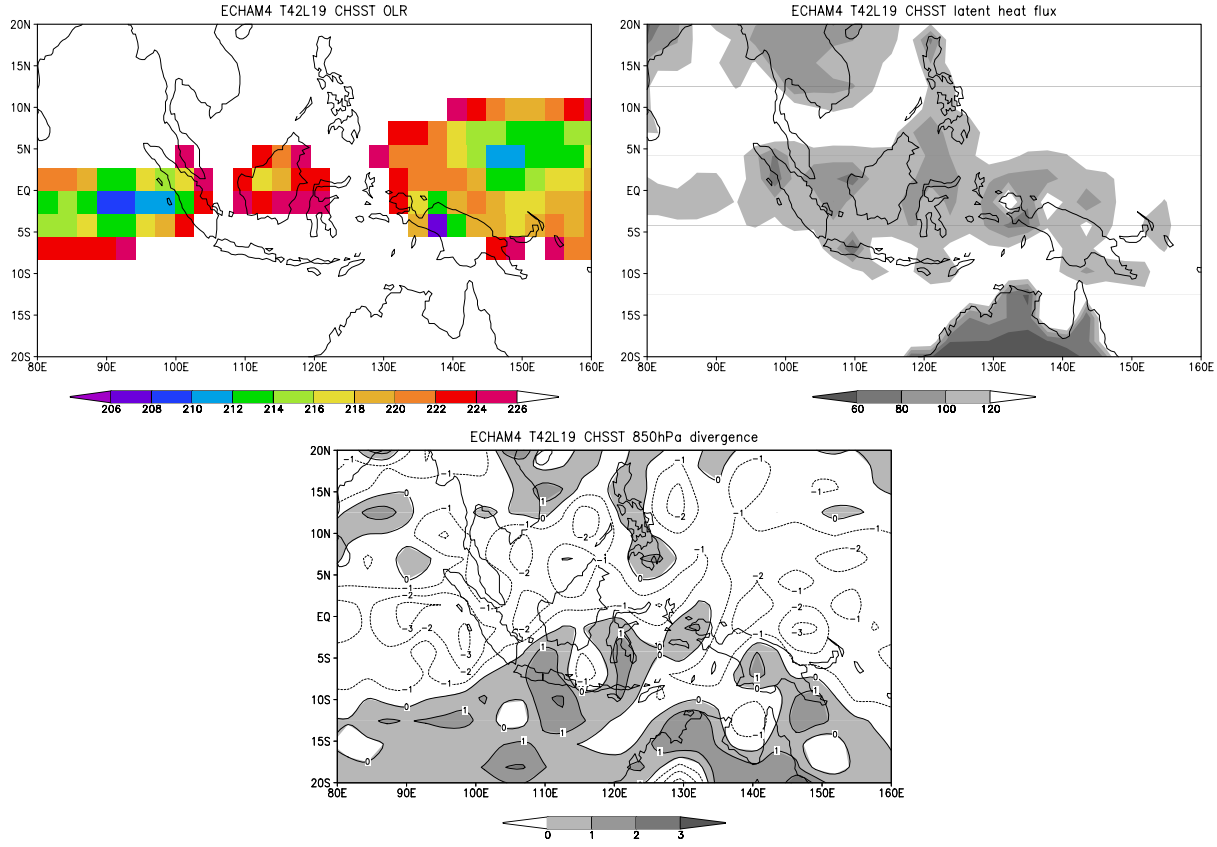

Figure 5.21: *Mean (1984-1988) OLR [W m^{-2}], latent heat flux [W m^{-2}] and 850 hPa divergence [10^{-6} s^{-1}] for ECHAM4 CHSST.*

with OPYC3 SSTs, obtained from the coupled ECHAM4/OPYC3 experiment, resembles the IO in ECHAM4/OPYC3 (not shown), since the simulated SST forcing includes the eastward shift and the too fast propagation of the IO produced by the AGCM (see Figure 3.8). This also proves the strong influence of SST on the IO. As in the control experiment, the strong distinction between land surface temperature and SST leads to higher SSTs over the maritime continent and thus a faster IO.

The results of this section point out the importance of a realistic surface temperature over the maritime continent for the simulation of the IO in GCMs. Even the AMIP SSTs are not able to provide an adequate forcing for a realistic mean surface latent heat flux. However, since the artificial CHSST T42 dataset is obtained by interpolating SSTs and land surface temperatures, ECHAM4 CHSST should not be considered as an improved model version but as a sensitivity experiment to detect the surface heating as a relevant mechanism for the realistic simulation of the IO. Hence, the remaining problem is to resolve the mean observed SST pattern and to consider the distinction between land and sea points at the same time. A possible improvement may be gained with an improved land-sea mask, which resolves more land area or the application of fractional land points

in GCMs, as used in the preliminary version of the new ERA40 reanalysis (S. Hagemann, pers. comm.). In such a scheme, the mean values of surface fluxes and surface temperature over a grid point are calculated as means of the land and sea fraction of the corresponding grid point. Nevertheless, it should be concluded that the change in SST is not the only important necessity for an improved simulation of the IO. The remaining deficiencies of ECHAM4 CHSST are an insufficient representation of the annual cycle of the IO. The bimodal spectrum of the main IO periods is also found by Hayashi and Golder (1993) in observations during the FGGE. Hence, it is questionable if the ERA15 data underestimate this bimodal structure.

Chapter 6

Discussion of the results

A realistic simulation of the IO in GCMs is important for the representation of cloud cover and the resulting precipitation in the tropical eastern hemisphere. In addition, recent studies propose an influence of the IO on the ENSO-cycle and precipitation rates in the midlatitudes (see Section 1.2). Hence, a realistic simulation of the IO gives the opportunity to improve the GCM simulations in this respect, not only in the 30 to 60 day period. The 30 to 60 day – or intraseasonal – period lies between typical life times for weather systems and the seasonal cycle. This feature makes the IO an important link between numerical weather forecasts and climate simulations at least in the tropical eastern hemisphere. The main errors in the representation of the IO in current GCMs are a weaker amplitude, a too fast eastward propagation with phase velocities up to more than twice the observed (Slingo et al., 1996) and an eastward shift of the strongest IO activity from the West Pacific warm pool to the Central Pacific due to an underestimation of intraseasonal variability over the maritime continent (Sperber et al., 1997).

The present study describes the capability of the ECHAM4 GCM to represent the IO. An ECHAM4 integration forced with AMIP SSTs from 1984 to 1988 is compared to the same period in the ERA15 reanalysis. A POP analysis of the 200 hPa equatorial velocity potential between 10°N and 10°S reveals a fairly realistic simulation of the general features of the IO in the ECHAM4 T42L19 standard version. The eastward propagation has an amplitude close to that of the reanalysis data and the seasonal variations are present. However, the model deficiencies are (1) a too fast phase velocity with a period of 34 days in the dominant POP mode compared to 48 days in the ERA15 reanalysis data and (2) an eastward shift of the main IO activity to 170°E compared to 140°E as in ERA15.

Many authors (e.g. Wang and Xie, 1998; Waliser et al., 1999b; Zhang et al., 2001) suggest the coupling of AGCMs to an underlying ocean as an important step towards an improved simulation of the IO. The present study points out that the ECHAM4/OPYC3 CGCM does not improve the representation of the IO compared to AGCM simulations. This result is confirmed in a parallel work by Hendon (2000), who found similar results with the GFDL GCM coupled to an ocean mixed layer model. This leads to the suggestion that the IO is an atmospheric phenomenon.

IO indices based on global winds and convection, necessary as objective measures of the capability of AGCMs to simulate the IO, may not reflect local IO activity in the Pacific (Zhang et al., 2001). The IO indices used in the present study also do not capture the eastward shift of the main IO activity during an El Niño event, since they are confined to a predefined spatial pattern as the first EOF or the dominant POP. The $\overline{u_{200}}$-variance index by Slingo et al. (1996) and Slingo et al. (1999) uses zonal mean values and therefore local zonal variations might be canceled out by each other. Thus, this index generally underestimates the IO. The shift of main IO activity with the extension of the West Pacific warm pool is best seen in Hovmöller diagrams of OLR as in Section 3.3 or upper-level velocity potential anomalies as shown in Appendix B. The location of main IO activity is restricted to the extension of the West Pacific warm pool, which is affected by the ENSO cycle (Picaut and Delcroix, 1995; Delcroix et al., 2000). The WWBs due to the IO may contribute to the development of an oceanic Kelvin wave (e.g. Zhang, 1997) that influences or even triggers the occurrence of an ENSO event (e.g. Nakazawa, 1999; van Oldenborgh, 2000).

Following the suggestions by Tompkins and Emanuel (2000) and Inness et al. (2001) to improve the representation of the trimodal structure of cloud cover distribution as observed by Johnson et al. (1999), the IO is analyzed in an ECHAM4 simulation with an increased vertical resolution of 39 levels. Since the vertical profile of cloud cover is a rather noisy variable, this study uses the instability index introduced by Kemball-Cook and Weare (2001) instead. The ECHAM4 AGCM with 39 layers leads to a noisier spectrum of the IO than the corresponding 19-level version. However, the decrease in phase velocity for the IO is small. Thus, three sensitivity experiments with different temperature changes due to melting of precipitation are performed to investigate the influence of the stable layer near the freezing level.

The temperature changes due to melting of convective precipitation are artificially doubled in the first experiment. This leads to a decrease in mean 500 hPa temperature of 0.4 K over the maritime continent, which is about the same amount as for nearly doubling the

vertical resolution from 19 to 39 levels. This illustrates the sensitivity of the cooling near the freezing level due to melting precipitation on vertical resolution. To confirm the results of this experiment, also the converse experiment is performed with the temperature change due to melting of convective precipitation artificially halved. The warming of the 500 hPa layer is about 0.2 K over the maritime continent in this experiment. However, both sensitivity experiments produce an increase in the phase speed of the IO. Only the amplitude of the IO is slightly increased (decreased) due to the cooling (warming).

In the third experiment, the melting of all precipitation is inhibited. Hence, no stable layer develops. This experiment still produces an – although quite noisy – oscillation similar to the IO. These sensitivity experiments show that a pronounced representation of the energy required for melting precipitation and thus an increased stability near the freezing level does not significantly reduce the phase speed of the simulated IO. In contrast, the phase speeds of the simulated IOs increased for all three experiments due to the disturbed energy cycles. From the experiments described in the next paragraphs, it is suggested that the improved simulation of the 850 hPa divergence and by this the stable layer near 2 km height (not shown) due to the trade wind inversion (Schubert et al., 1995) is responsible for the slower phase velocity in ECHAM4 T30L39 than in ECHAM4 T30L19.

The influence of surface forcing on the IO is investigated in three ways. First, the effect of increased horizontal resolution is analyzed. Second, a sensitivity experiment with the maritime continent substituted by sea points is performed; and third, the importance of the prescribed SST is studied.

Increasing the horizontal resolution from T42, which corresponds to about $2.8° \times 2.8°$horizontal grid mesh, to T106 corresponding to about $1.1° \times 1.1°$horizontal resolution leads to a spatial structure of the IO similar to ERA15. Also the simulation of the interannual cycle is improved. However, the phase velocity is even increased and the amplitude of the IO is reduced, which leads to noisier spectra compared to the ECHAM4 T42 control experiment. The sensitivity study with the maritime continent replaced by sea points also reveals an improved spatial structure of the IO and an increased phase velocity. Neale and Slingo (2001) also found an improved spatial structure of the IO in the HadAM3 GCM with the maritime continent removed. This points to deficiencies in current GCMs in the representation of the maritime continent.

NOAA satellite observations show reduced mean convection over the center of the maritime continent between 120°E and 130°E, which reduces the low-level convergence in this area (Rui and Wang, 1990; Salby and Hendon, 1994). In contrast to this, the ECHAM4

control experiment produces a maximum in mean convection in the region between 110°E and 120°E. It is suggested that this erroneous positive zonal gradient of equatorial deep convection from the Indian Ocean to the West Pacific warm pool prevents the eastward propagation of super cloud clusters over the maritime continent. This results in the erroneous eastward shift of the main IO activity. A sensitivity study is performed with the prescribed AMIP SST replaced with an artificial "SST" dataset obtained by interpolating ERA15 SSTs and land surface temperatures to maintain the observed spatial structure of the surface heating.

The consequence of this different surface forcing is a maximum of mean deep convection over the eastern Indian Ocean, decreasing towards the West Pacific warm pool as in the satellite data. This results in a remarkable improvement in the simulated IO: The spatial structure resembles the observations and the reanalysis data, and also the phase velocity is reduced to about 48 days as in ERA15. The reason for this is the reduced mean convection due to a reduction of mean latent heat flux to values similar to ERA15. Also the 850 hPa divergence is slightly increased, which emphasizes the possible influence of the stable layer near 2 km height due to the trade wind inversion (Schubert et al., 1995) on the propagation of the IO. The remaining deficiencies of the ECHAM4 simulation with reduced SSTs over the maritime continent are a northward shift in main IO activity and a pronounced bimodal structure in the IO spectra with a secondary peak near 24 days. However, observations by Hayashi and Golder (1993) from the FGGE also show this bimodal structure. Thus, only more precise observations and more reliable IO indices might clarify this difference.

The period of the IO and the location of its main activity in ERA15 and the different ECHAM4 versions is summarized in Table 6.1. The sensitivity studies with different melting rates are omitted, since they do not show any improvements in the simulation of the IO. The location of the main IO activity is described by the minimum in the first EOF of the 15-90 day filtered 200 hPa velocity potential anomaly. Within the ECHAM4 versions forced with AMIP SSTs, the slower IO propagation of 34 days is accompanied by an eastward shift of the main IO activity to 170°E for the control experiment and 165°E for ECHAM4 T30L39. The spatial structure near or even west of the observed in ECHAM4 T30L19, ECHAM4 NOMARI, and ECHAM4 T106L19 is connected with an erroneous increase in phase velocity. The improved location of main IO activity in ECHAM4/OPYC3 and the faster IO propagation is suggested to be due to slightly warmer SSTs over the West Pacific warm pool and colder over the Central Pacific in the CGCM (not shown). Only the sensitivity study with reduced SSTs over the maritime continent

Table 6.1: *Main period, range of the periods above the 99% significance interval in the squared coherence and location of the IO, described by the minimum in the first EOF of the 15-90 day filtered 200 hPa velocity potential anomaly.*

	Period of the IO	(99%-range)	Minimum of 1. EOF
ERA15 reanalysis	48 d	(37-67 d)	140°E, 5°S
ECHAM4 T42L19	34 d	(15-38 d)	170°E, 0°N
ECHAM4/OPYC3	27 d	(15-41 d)	145°E, 6°S
ECHAM4 T30L19	27 d	(15-45 d)	148°E, 3°S
ECHAM4 T30L39	34 d	(16-56 d)	165°E, 5°N
ECHAM4 T106L19	24 d	(21-30 d)	117°E, 7°S
ECHAM4 NOMARI	27 d	(15-46 d)	122°E, 8°S
ECHAM4 CHSST	48 d	(29-53 d)	143°E, 3°N

provides an IO period close to the ERA15 dataset due to the increased influence of surface friction. Also the zonal position of the main IO activity is well captured in this realization. The meridional northward shift to 3°N is suggested to be responsible for the overestimation of the IO during northern summer in ECHAM4 CHSST.

Although the annual cycle of IO activity is present in all ECHAM4 versions, the shift towards strongest IO activity during spring and summer compared to winter and spring in ERA15 is evident in all model integrations. However, the annual cycle of IO activity is best represented in ECHAM4 T106L19 and ECHAM4 NOMARI due to the location of main IO activity south of the equator as in ERA15. The explained variance of the dominant POP mode in ECHAM4 T106L19 is with 27.7% similar to the 23.8% in ERA15. The ECHAM4 integrations with lower horizontal resolutions produce stronger explained variances of more than 40%, thus indicating a more distinct oscillation pattern associated with the IO compared to ERA15.

A case study gives further insight into the structure of the IO, although the result can not be generalized due to the great diversity of the IO phenomenon (Wang and Rui, 1990b). To identify the occurrence of strong IO activity, the maximum in the principal component time series of the bandpass filtered 200 hPa velocity potential anomaly is used. As pointed out in Chapter 2, the oscillation of the PC1 time series should not be regarded as the IO, because only the mean pattern of the large-scale divergent flow is depicted, not its eastward propagation. Nevertheless this method leads to the detection of strong IO activity, which occurs mostly in northern spring when tropical SSTs are highest.

The principal component analysis reveals different IO events as typical for the different ECHAM4 versions analyzed in this study. However, since all case studies are compared to observed OLR anomalies and ERA15 data, they illustrate the great diversity of the IO phenomenon. The different IO events are listed in Table 6.2, together with a short description of their characteristics. The case studies reveal the presence of low-level convergence and coinciding WWBs to the west of the convection, which increase the latent heat flux to the west of the convection. This feature is an indicator for the presence of wave-CISK in ERA15 and ECHAM4 as the dominant propagating mechanism of the IO (Sperber et al., 1997).

Since this study points out the importance of a realistic SST forcing, Table 6.3 describes the differences in the SST datasets used in this study. The annual mean values from 1984 to 1988 (model years 251 to 275 for ECHAM4/OPYC3) are averaged over the maritime continent region from 90°E to 160°E and from 10°N to 10°S. The ERA15 SST is obtained from the optimum interpolated SST (OISST) dataset by Reynolds and Smith (1994) and the AMIP SSTs are presented in Gates (1992). The AMIP SSTs at T42 and T30 horizontal resolution are 0.14 K higher than the ERA15 SSTs. The difference is even 0.15 K for the AMIP T106 version. Although these mean differences are relatively small, the strong sensitivity of tropical convection on surface temperatures should be kept in mind. The NOMARI SSTs (see Section 5.2) are interpolated from the AMIP SSTs. Their stronger influence on the ECHAM4 GCM surface temperature over the maritime continent leads to a faster IO in ECHAM4 NOMARI. The changed SST dataset in the last sensitivity

Table 6.2: *Case studies of the IO.*

	PC1 maximum	Characteristics of the IO events in ERA15
ERA15 reanalysis	Mar 23rd 1988	Typical IO event, investigated by many authors (e.g. Matthews et al., 1996).
ECHAM4 T42L19	Mar 8th 1987	Main IO activity shifted to the east, OLR anomalies confined to the date line.
ECHAM4 T30L39	Feb 3rd 1988	Similar to event on Mar 1988, but weaker.
ECHAM4 T106L19	May 1st 1986	Main IO activity shifted to the west, propagation disrupted over maritime continent.
ECHAM4 NOMARI	May 20th 1985	Hardly any eastward propagation in OLR, only in 200 hPa velocity potential anomalies.
ECHAM4 CHSST	July 20th 1987	Interaction of Kelvin and Rossby waves clearly seen.

Table 6.3: *Annual mean SSTs over the maritime continent averaged over the region 90° E, 160° E, 10° N and 10° S. Also the differences to the ERA15 SST are shown.*

	Annual mean SST	Difference to ERA15 SST
ERA15 reanalysis	28.72 °C	0. K
AMIP T42	28.86 °C	0.14 K
ECHAM4/OPYC3	28.94 °C	0.22 K
AMIP T30	28.86 °C	0.14 K
AMIP T106	28.87 °C	0.15 K
NOMARI	28.86 °C	0.14 K
CHSST	28.68 °C	-0.04 K

study is obtained from the ERA15 SST and by this the IO in ECHAM4 CHSST resembles the IO in ERA15. This proves the strong influence of the surface heating on the IO. This study shows that the AMIP SST is not sufficient as a boundary condition for a realistic simulation of the IO. Slingo et al. (1996) used the AMIP SSTs as the boundary forcing for 15 GCMs to analyze their ability to simulate the IO. This might be a reason why most GCMs failed to produce a reasonable realistic IO.

An AMIP2 SST dataset, which accounts for a better representation of the annual cycle of the SST (Taylor et al., 2001), still has an annual mean SST of 28.86 °C for the years 1984 to 1988 over the above described region, and thus no significant improvement of the representation of the IO is found in this model (not shown). It is suggested that only an introduction of fractional land points, as used in the preliminary version of the new ERA40 reanalysis (S. Hagemann, pers. comm.), will help towards solving the problem of a relatively realistic surface heating pattern on one hand, and a physical correct representation of land and sea areas on the other hand.

The IO is sensitive to mean SST changes less than 0.2 K over the whole maritime continent region, which exceed 0.5 K at some grid points, as shown in this study. In addition, it produces SST anomalies in the range of 0.2 to 0.5 K (e.g. Zhang et al., 2001), which is confirmed in the composite studies of observed SSTs. Hence, it is suggested that an investigation with atmosphere-ocean CGCMs might yield further insight into the mechanisms responsible for the development of the IO, if the CGCMs are able to produce a realistic surface heating pattern over the maritime continent.

Chapter 7

Conclusion

Current AGCMs reveal many deficiencies in representing the IO as shown in a model intercomparison by Slingo et al. (1996). Besides the GLA, the GFDL and the UKMO GCMs, the ECHAM4 standard version simulates an IO, which behaves relatively close to observations and reanalysis data compared to other GCMs. However, in ECHAM4 the propagation of the IO is too fast with a period of 34 days compared to 48 days in the ERA15 reanalysis. Also the main IO activity is shifted too far east to about 170°E instead of about 140°E as in ERA15. In addition to composite studies and Hovmöller diagrams, the $\overline{u_{200}}$-variance index by Slingo et al. (1996) and Slingo et al. (1999) and the POP index by Gualdi et al. (1999) are used in this study to describe the interannual variability of the IO. It is shown that the $\overline{u_{200}}$-variance index more strongly underestimates the IO prior and during El Niño events than the POP index. Hence, this study recommends the POP index for representing the interannual variability of the IO. However, since the POP index is also based on specific pattern – the real and imaginary parts of the dominant POP – it is also not able to fully reproduce the zonal shift of the main IO activity due to the change in extension of the West Pacific warm pool during the ENSO cycle. Unlike the ENSO index, currently no standardized index exists for the description of the IO. Despite the limitations of the POP index, it provides a reasonable measure of the annual cycle of the IO in the different model versions. Nevertheless, this study emphasizes that interannual variability should additionally be analyzed with Hovmöller diagrams.

To improve the representation of the IO in atmosphere GCMs, the coupling to ocean GCMs is suggested. The interaction of the IO and ENSO is presented in this study: The IO can influence the onset of an El Niño event and the eastward extension of the SST forcing during an El Niño event influences the position of the main IO activity.

Inness et al. (2001) point out the importance of an increased vertical resolution and by this an improved simulation of the stable layer near the freezing level as important for the reduced propagation speed of the IO in AGCMs. The increase in vertical resolution slightly improves the simulation of the vertical moisture profile, and thus slightly slows down the propagation speed of the IO. However, this result is not confirmed by sensitivity studies with artificially changed stability in the mid-troposphere. Hence, the present study concludes that neither the coupling of the ECHAM4 AGCM to the OPYC3 OGCM nor the increased vertical resolution from 19 to 39 levels has a significant impact on the simulation of the IO in ECHAM4.

ECHAM4 simulates IOs with different spatial structures at different horizontal resolutions: In T30L19 and T106L19 the main IO activity is located over the maritime continent similar to observations, whereas in the T42L19 standard version it is shifted eastward towards the date line. An additional sensitivity experiment with the maritime continent substituted by ocean grid points reveals the importance of the land-sea distribution over the maritime continent on the representation of the IO. As in a parallel work by Neale and Slingo (2001), the spatial structure of the IO is improved by the removal of land points. However, the ECHAM4 integrations with improved spatial structures produce IOs with periods of 24 to 27 days. This is even faster than in the control experiment.

This study also reveals that, averaged over the maritime continent, annual mean AMIP SSTs, which are used as boundary forcing for ECHAM4, are about 0.14 K higher than those observed. Although these mean values seem to be rather small, at single grid points the AMIP dataset can be more than 0.5 K warmer than the observations due to the overly large sea area coverage. In this region, SST is generally higher than land surface temperature. A changed "SST" dataset with a mean pattern and a mean value similar to the ERA15 SST is constructed by interpolating observed ERA15 SSTs and surface temperatures to the T42 grid. An ECHAM4 version with this changed "SST" dataset produces a reasonable well IO with a mean period of 48 days and a main IO activity near 140°E, as in the ERA15 reanalysis. Hence, the strong influence of the SST on the simulation of the IO is shown. The reduced surface heating leads to reduced latent heat flux and by this lower convection. The resulting increase in 850 hPa divergence points to lower vertical circulations and the increased influence of surface friction.

However, the observational OISST dataset used in ERA15 interpolates between land and sea surface temperature (Taylor et al., 2001). Hence, a GCM should also account for subgrid-scale land-sea distributions, where the mean values of surface fluxes and surface temperature over a grid point are calculated as means of the land and sea fraction of the

grid point as in the preliminary version of the new ERA40 reanalysis. In addition to such a development, another future work may be an artificial increase in land points over the maritime continent, since the land-sea mask for ECHAM4 T42 resolves only 64% of the land surface over the maritime continent.

The results of the present study exhibit a classification of the requirements, which are necessary for the simulation of the IO in GCMs: Most important is a fairly realistic surface forcing, namely the prescribed SST, which leads to a remarkable improvement in the simulation of the IO in ECHAM4. Second, a sufficient vertical resolution is required to resolve the stable layers near 2 km height due to the trade wind inversion, near 5 km height due to melting precipitation and near 15-16 km height at the tropopause. The increase in vertical resolution to 39 levels reveals a slight tendency towards slower propagation of the IO in this study. Third, possible improvements due to the coupling to an OGCM may be analyzed. Current AGCMs as ECHAM4 and the GFDL GCM do not show any improvements of the simulation of the IO due to the coupling. However, this may change if a more realistic land-sea distribution and by this a more realistic surface forcing is available, and if the vertical stability profile of the troposphere is improved.

An – of course incomplete – list of current deficiencies and possible future projects to improve the simulation of the IO in GCMs and to gain more insight into its characteristics is presented in Table 7.1. Future studies with AGCMs and CGCMs will be more reliable when these current deficiencies are minimized.

Table 7.1: *Current deficiencies and possible future projects.*

Current deficiencies	Possible future projects
Current IO indices do not account for the zonal displacement of the main IO activity during the ENSO cycle.	Developing a standardized IO index that takes phase velocity, interannual variability and zonal displacement of the main IO activity into account.
Current land area over the maritime continent in ECHAM4 T42 represents only 64% of the observed land area.	Increasing the land area over the maritime continent in the land-sea mask to obtain a more realistic surface heating.
Small islands over the maritime continent may not be resolved even in high resolution GCMs.	Implementing a land surface scheme that uses fractional land points to obtain a more realistic surface heating.
Moisture profiles of reanalysis data differ considerably over areas with sparse observations.	Further improving the convective parameterization.

Table 7.2 describes climate phenomena, which are suggested to interact or at least to be influenced by the IO. Examples of related observational studies are also listed. With the improvements in the IO simulations achieved by this study, these interactions and influences may now be more clearly analyzed.

Table 7.2: *Examples of observational studies about interactions and influences of the IO.*

Phenomenon	Studies
Asian summer monsoon	Lau et al. (1998)
Australian summer monsoon	Hendon and Liebmann (1990a,b)
El Niño / Southern Oscillation	Kessler et al. (1995); Nakazawa (1999)
South Pacific Convergence Zone	Matthews et al. (1996)
Quasi Biennial Oscillation	Wheeler et al. (2000)
Tropical-extratropical interactions	Ferranti et al. (1990)
Californian rainfall	Mo and Higgins (1998a,b)

Acknowledgments

Working in the pleasant and motivating atmosphere of the Physical Climate Systems department at the Max-Planck-Institut für Meteorologie in Hamburg has been an excellent opportunity for me.

I would especially like to thank Prof. Dr. Lennart Bengtsson for making this thesis possible and for his expert advise. His profound knowledge, enthusiastic support and continuous guidance were very helpful and highly motivating.

I am grateful to Prof. Dr. Hartmut Graßl for the examination of this work and his previous teachings during my time at the University of Hamburg.

Many thanks go to Prof. Dr. Duane E. Waliser, Dr. Silvio Gualdi, Dr. Adrian Tompkins and Dr. Pete M. Inness for their valuable help and fruitful scientific discussions.

I greatly appreciate the assistance I received from the staff of the Max-Planck-Institut für Meteorologie and the Meteorological Department of the University of Hamburg, in particular:

Dr. Erich Roeckner, Dr. Ingo Kirchner, Uwe Schulzweida and Dr. Hans-Stefan Bauer provided expertise with the ECHAM4 GCM and general computational support. Prof. Dr. Hans von Storch and Dr. Rainer Schnur is thanked for their advice concerning the POP analysis and other statistical issues of this thesis. Dr. Mojib Latif and Sigrid Schoettle contributed with numerous comments. Dr. Noel Keenlyside, Dr. Silke Dierer, Georg Bäuml and Marko Scholze carefully reviewed the manuscript.

The ECMWF made the radiosonde measurements at Singapore airport available as part of the MARS dataset. The ERA15 and ERA40 reanalysis data were supplied by ECMWF in cooperation with DKRZ. The NOAA satellite data and the NCEP reanalysis data were kindly provided by the CPC.

Most of all, I want to thank my wife Carmen for her love and encouragement, and my friends and family for their continuous support.

Appendix A

List of acronyms

AGCM	Atmosphere General Circulation Model
AMIP	Atmospheric Model Intercomparison Project
ASCII	Air-Sea Convective Intraseasonal Interaction
CGCM	Coupled General Circulation Model
CISK	Conditional Instability of the Second Kind
COARE	Coupled Ocean-Atmosphere Response Experiment
DERF	Dynamical Extended Range Forecast
ECHAM	European Centre Hamburg Atmospheric Model
ECHAM4 0.5xMR	Identifier for the sensitivity experiment with halved melting rate for convective precipitation
ECHAM4 2.0xMR	Identifier for the sensitivity experiment with doubled melting rate for convective precipitation
ECHAM4 CHSST	Identifier for the sensitivity experiment with changed SST
ECHAM4 NOMARI	Identifier for the sensitivity experiment with the land mass of the maritime continent replaced by sea points
ECHAM4 NSMT	Identifier for the sensitivity experiment with no snow melt allowed
ECHAM4 TmLn	Identifier for the sensitivity experiments with different horizontal resolution (wavenumbers higher than m are truncated) or vertical resolution (n vertical levels are resolved)
ECMWF	European Centre for Medium Range Weather Forecasts
ENSO	El Niño/Southern Oscillation
EOF	Empirical Orthogonal Function
ERA15	15 years of ECMWF Reanalysis
ERA40	40 years of ECMWF Reanalysis

FGGE	First GARP Global Experiment
GARP	Global Atmospheric Research Programme
GCM	General Circulation Model
GFDL	Geophysical Fluid Dynamics Laboratory
GLA	Goddard Laboratory for Atmospheres
HadAM	Hadley Centre Atmosphere Model
IO	Intraseasonal Oscillation
ITCZ	Inter-Tropical Convergence Zone
NASA	National Aeronautics and Space Administration
NCAR	National Center for Atmospheric Research
NCEP	National Centers for Environmental Prediction
NINO3	Identifier for the region between 150°W, 90°W, 5°N and 5°S
NOAA	National Oceanic and Atmospheric Administration
NSCAT	NASA Scatterometer
OGCM	Ocean General Circulation Model
OISST	Optimum Interpolated SST
OLR	Outgoing Longwave Radiation
OPYC	Ocean isopycnal model
PC1	The first Principal Component
POP	Principal Oscillation Pattern
SCS	South China Sea
SCSMEX	South China Sea Monsoon Experiment
SLH	Sea Level Height
SPCZ	South Pacific Convergence Zone
SST	Sea Surface Temperature
SSTA	Sea Surface Temperature Anomaly
TAO	Tropical Atmosphere Ocean
TOGA	Tropical Ocean Global Atmosphere
TOPEX	Topography Experiment
UKMO	United Kingdom Meteorological Office
WISHE	Wind-Induced Surface Heat Exchange
WWB	Westerly Wind Burst

Appendix B

Hovmöller diagrams of the IO cycle

Since the present study illustrates the deficiencies of current IO indices, the IO and its interannual variability including the zonal shift during the ENSO cycle should also be viewed in time-longitude Hovmöller diagrams. Figures B.1 to B.4 show the Hovmöller diagrams of the 200 hPa velocity potential anomaly for the ERA15 reanalysis and the selected GCM experiments ECHAM4 T42L19, ECHAM4/OPYC3, ECHAM4 CHSST, ECHAM4 T30L39, ECHAM4 T106L19, ECHAM4 NOMARI and ECHAM4 NSMT, which are previously described in this thesis. No filtering is applied to these data, since the filtering might have a non-negligible effect on the representation of the IO in the data, as shown in Chapter 2.

The ERA15 data resemble the ECMWF analysis in Figure 1.2. Even ECHAM4 NSMT simulates an IO-like oscillation, thus emphasizing the small contribution of the stable layer near 500 hPa on the simulation of the IO. ECHAM4 T42L19, ECHAM4/OPYC3 and ECHAM4 T30L39 show a more frequently occurring underestimation in intraseasonal variability over the maritime continent at about 100°E to 120°E than ERA15, ECHAM4 CHSST, ECHAM4 T106L19 and ECHAM4 NOMARI. Typical IO activity occurs in 1985 and 1986 with strong activity during the equinox periods and weakest activity during boreal summer 1985, except for the ECHAM4 T30L39 and ECHAM4 CHSST simulations, which also show IO activity during this summer period. From October 1986 until December 1987 all datasets depict the eastward shift of the IO activity and the related underestimation of intraseasonal variability over the maritime continent due to the eastward extension of the West Pacific warm pool prior and during the 1987 El Niño as explained by Picaut and Delcroix (1995) and described in Figures 1.3 and 3.16. Conversely, the slight tendency towards a westward shift during 1988 may be explained with the beginning of the westward displacement of the West Pacific warm pool prior and during the 1988 La Niña. The strongest El Niño event in ECHAM4/OPYC3 occurs in winter 273/274, but

the eastward shift of the main IO activity during the ENSO cycle is less than in the reanalysis data, as shown in Section 3.3.

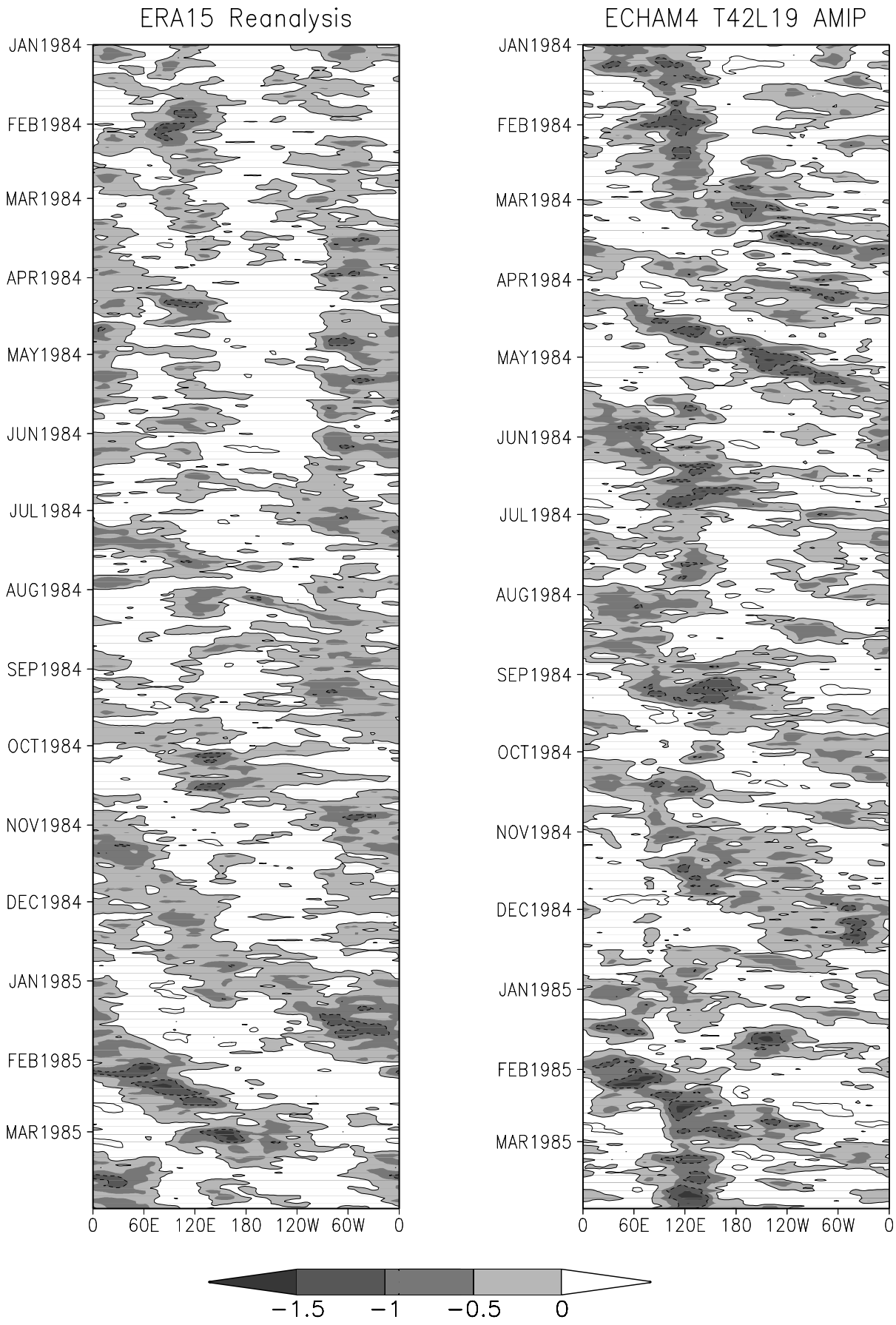

Figure B.1: *Hovmöller diagrams of the IO cycle represented by 200 hPa velocity potential anomaly [10^7 $m^2 s^{-1}$] averaged between 10°N and 10°S. Shown is the period from January 1984 to March 1985 for the ERA15 reanalysis and selected GCM experiments. Negative values are shaded.*

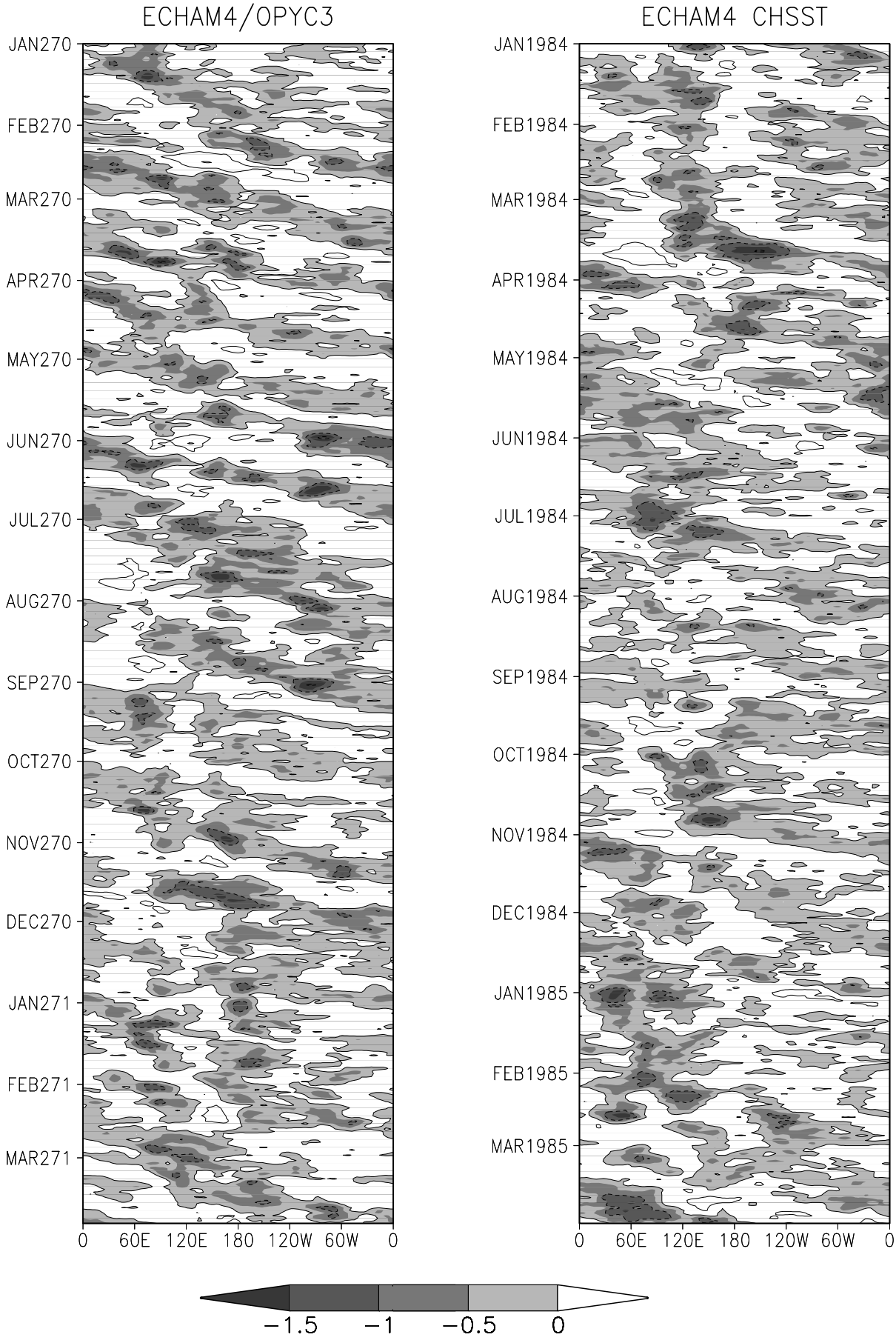

Figure B.1 continued.

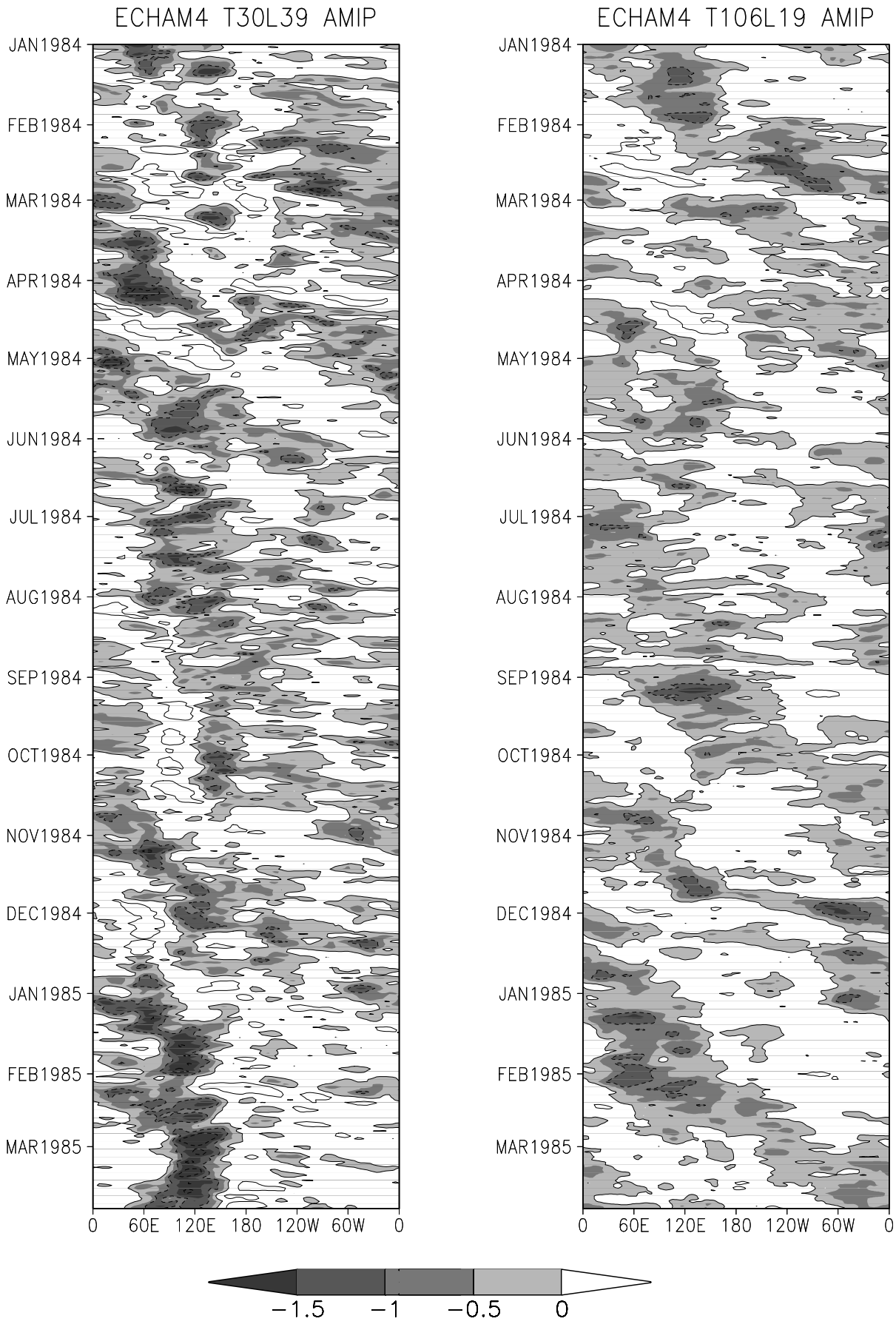

Figure B.1 continued.

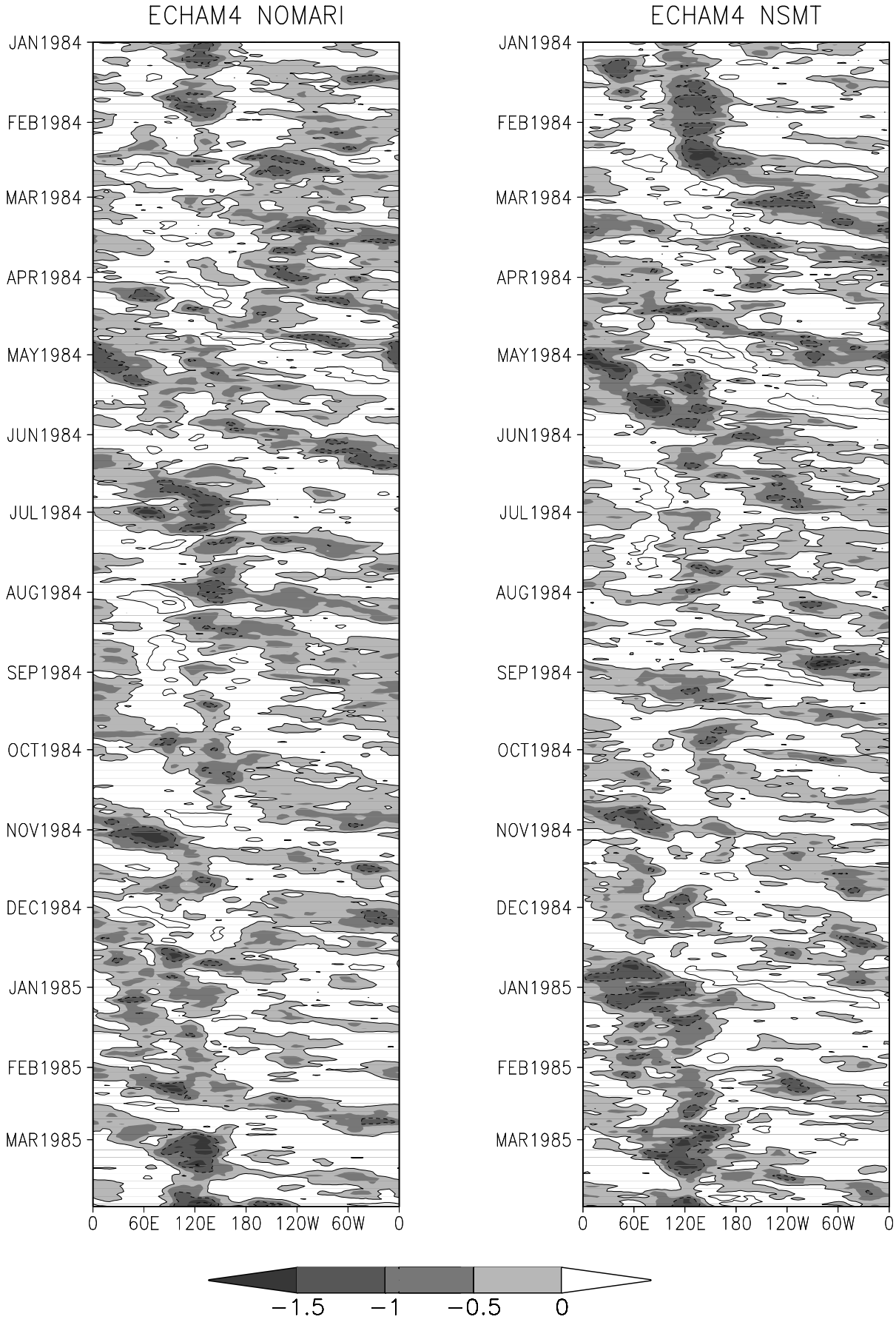

Figure B.1 continued.

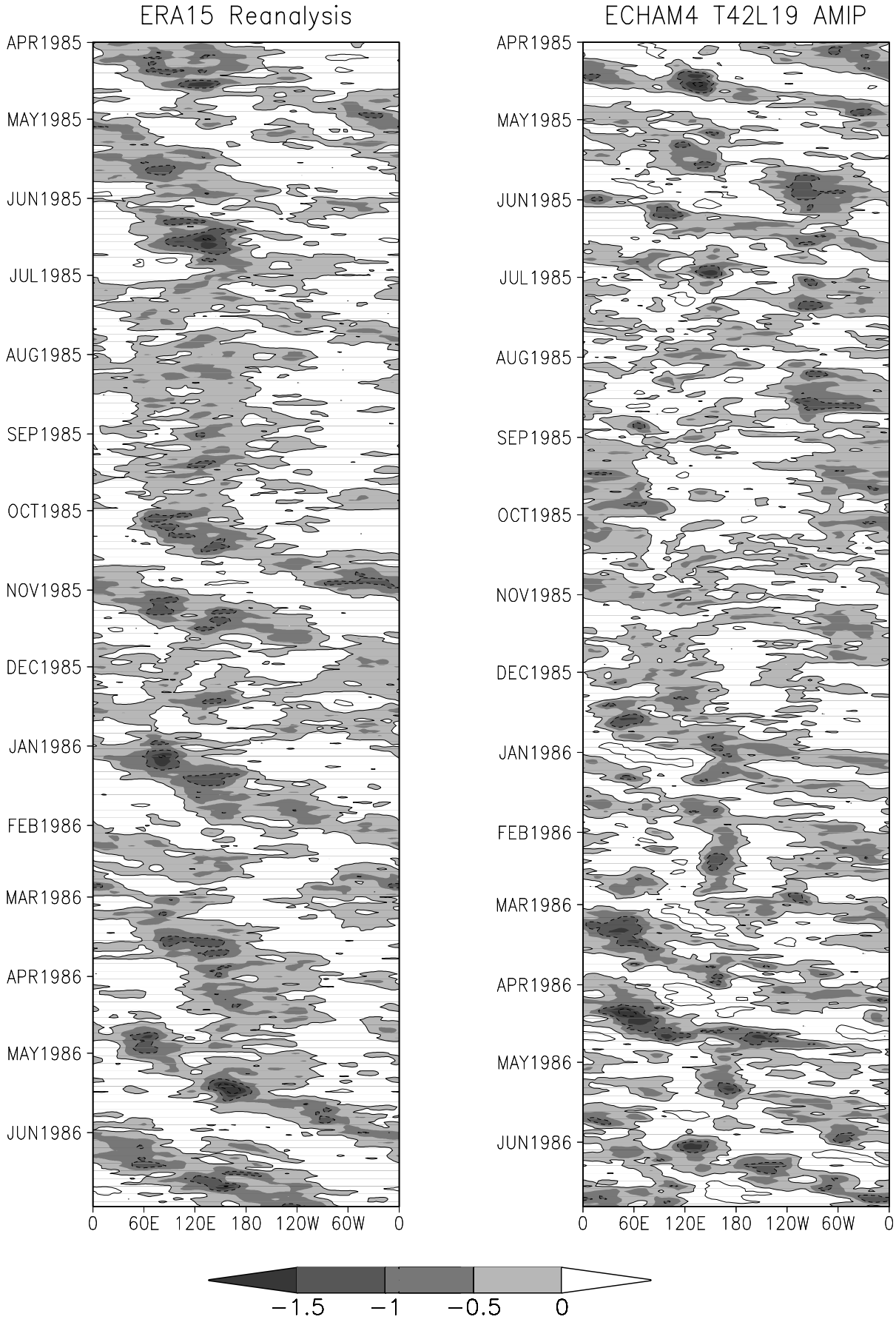

Figure B.2: *As Figure B.1, but for April 1985 to June 1986.*

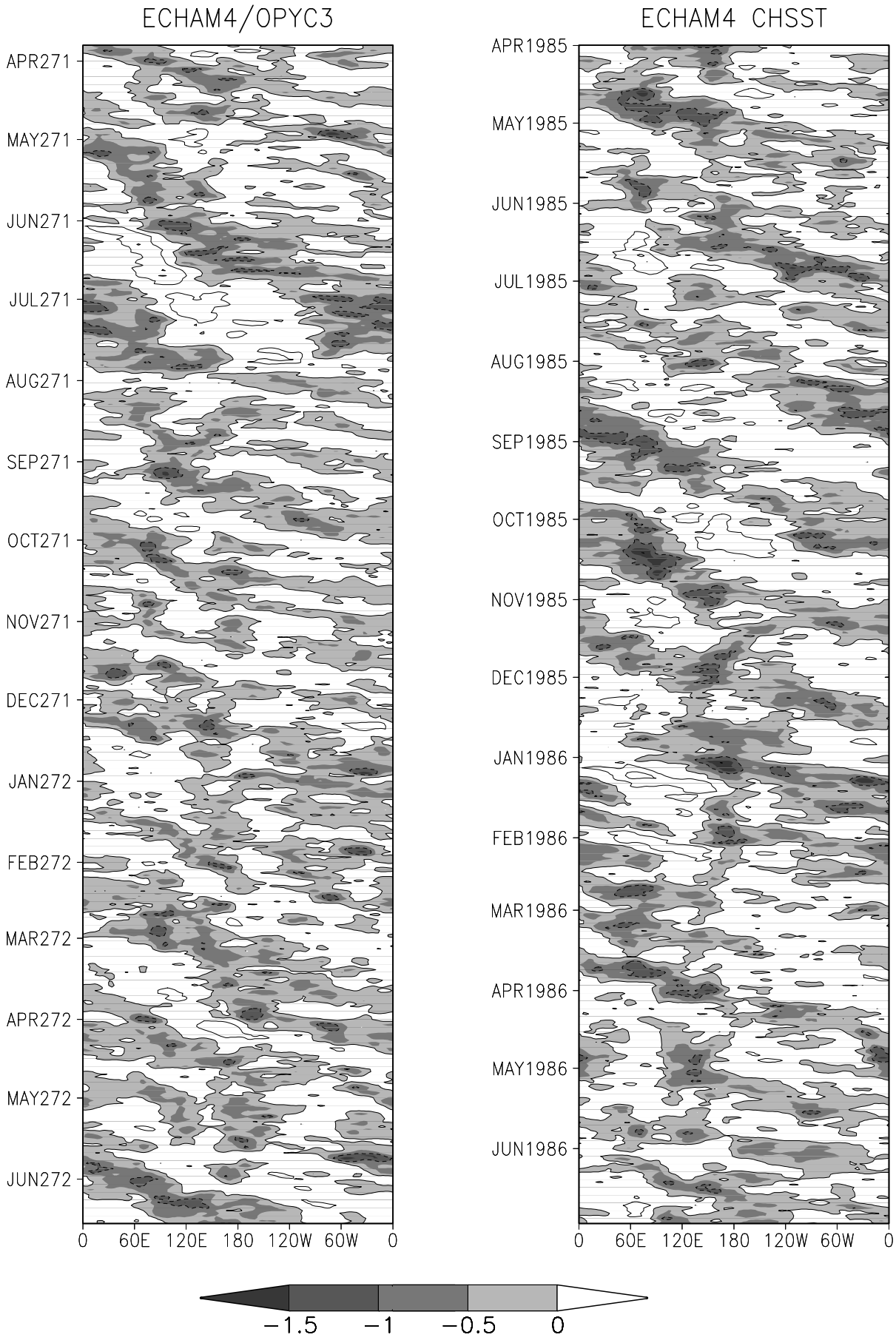

Figure B.2 continued.

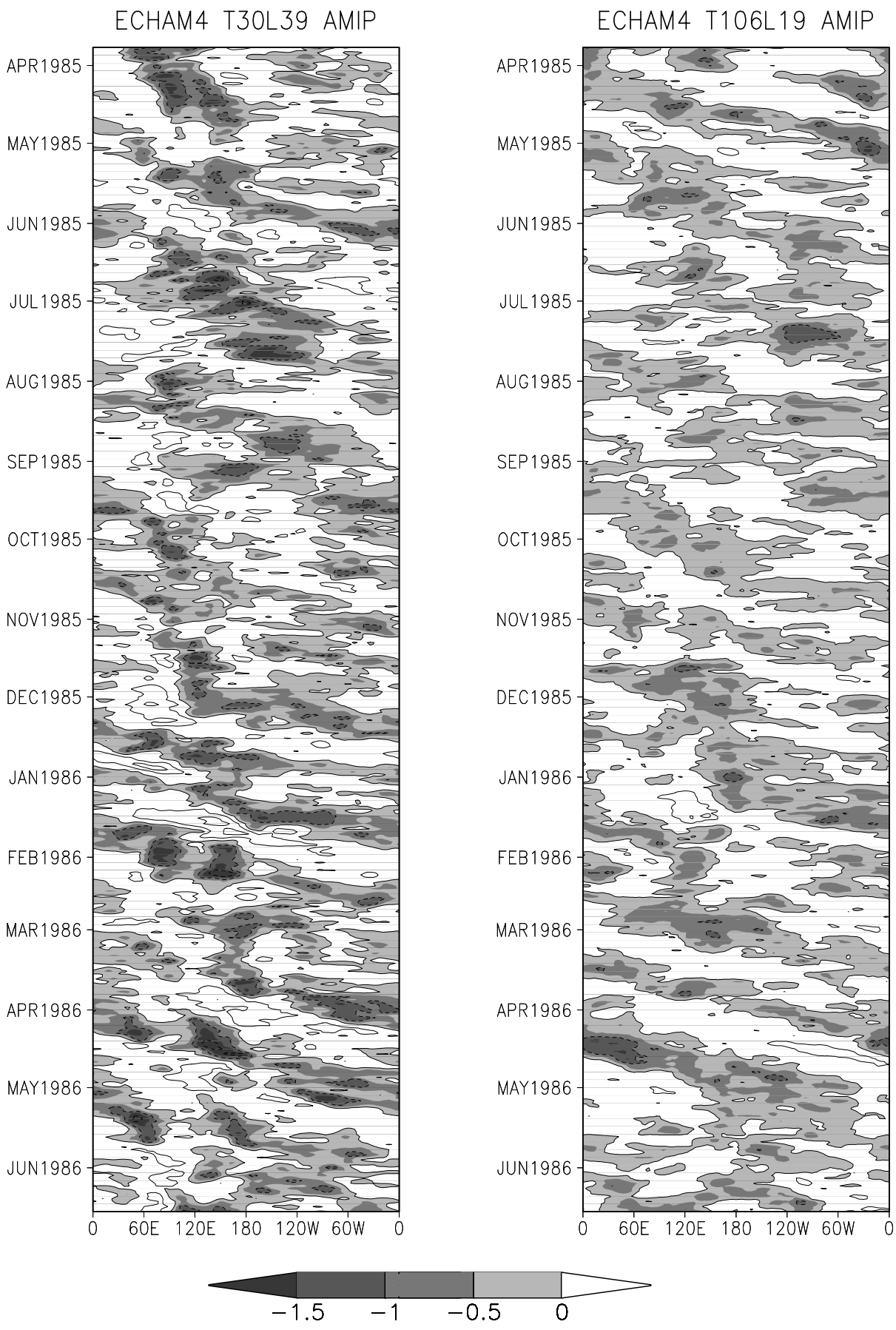

Figure B.2 continued.

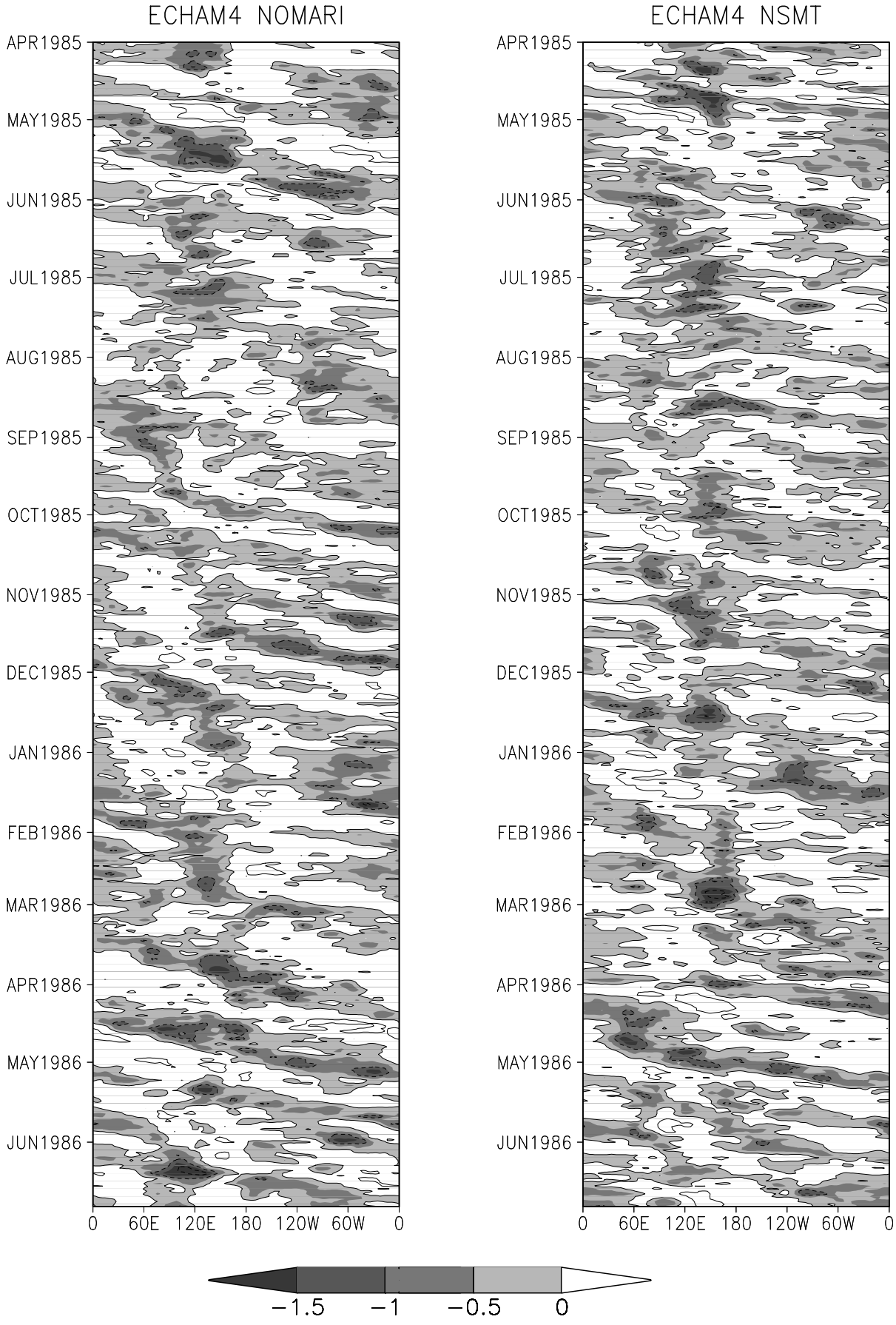

Figure B.2 continued.

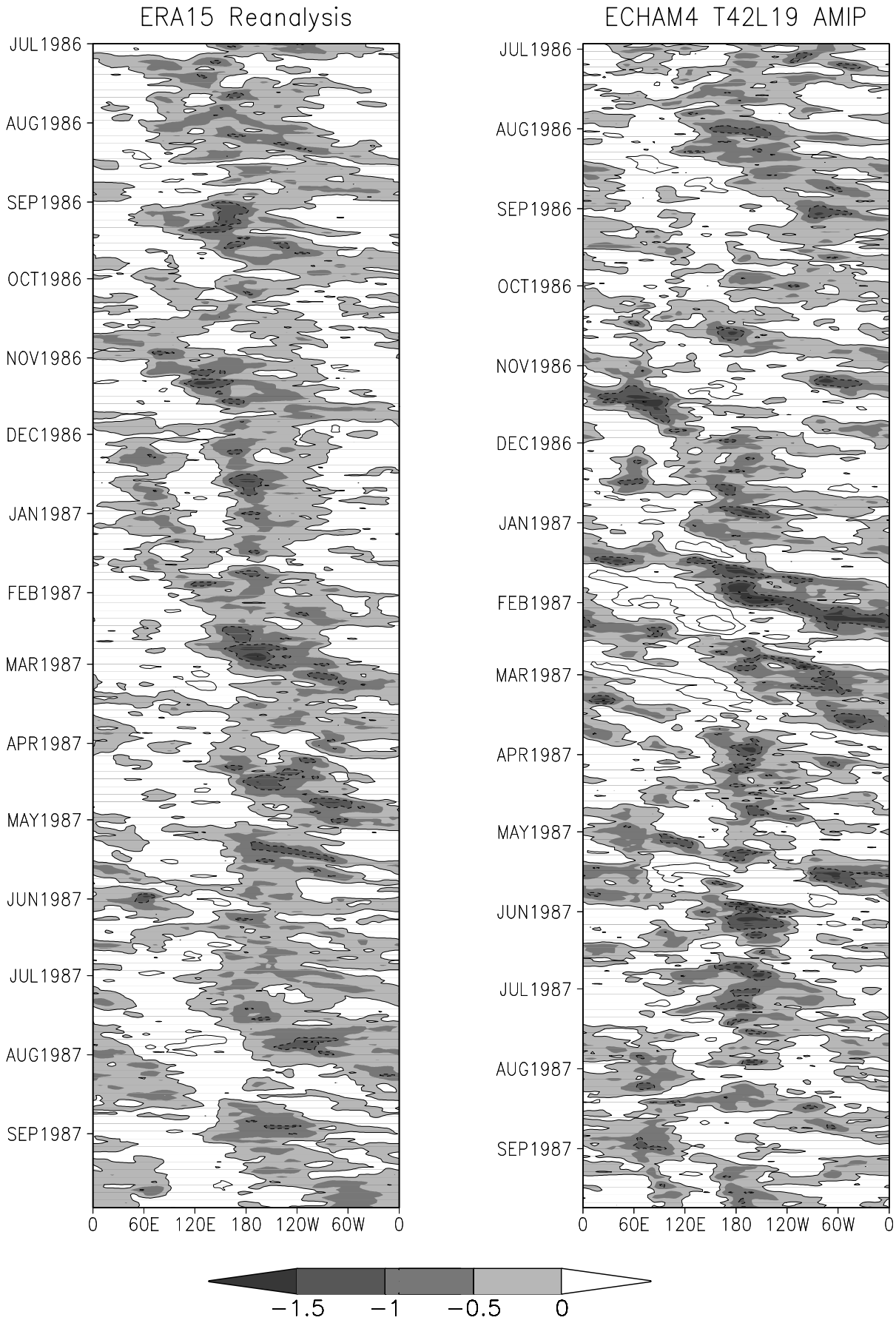

Figure B.3: *As Figure B.1, but for July 1986 to September 1987.*

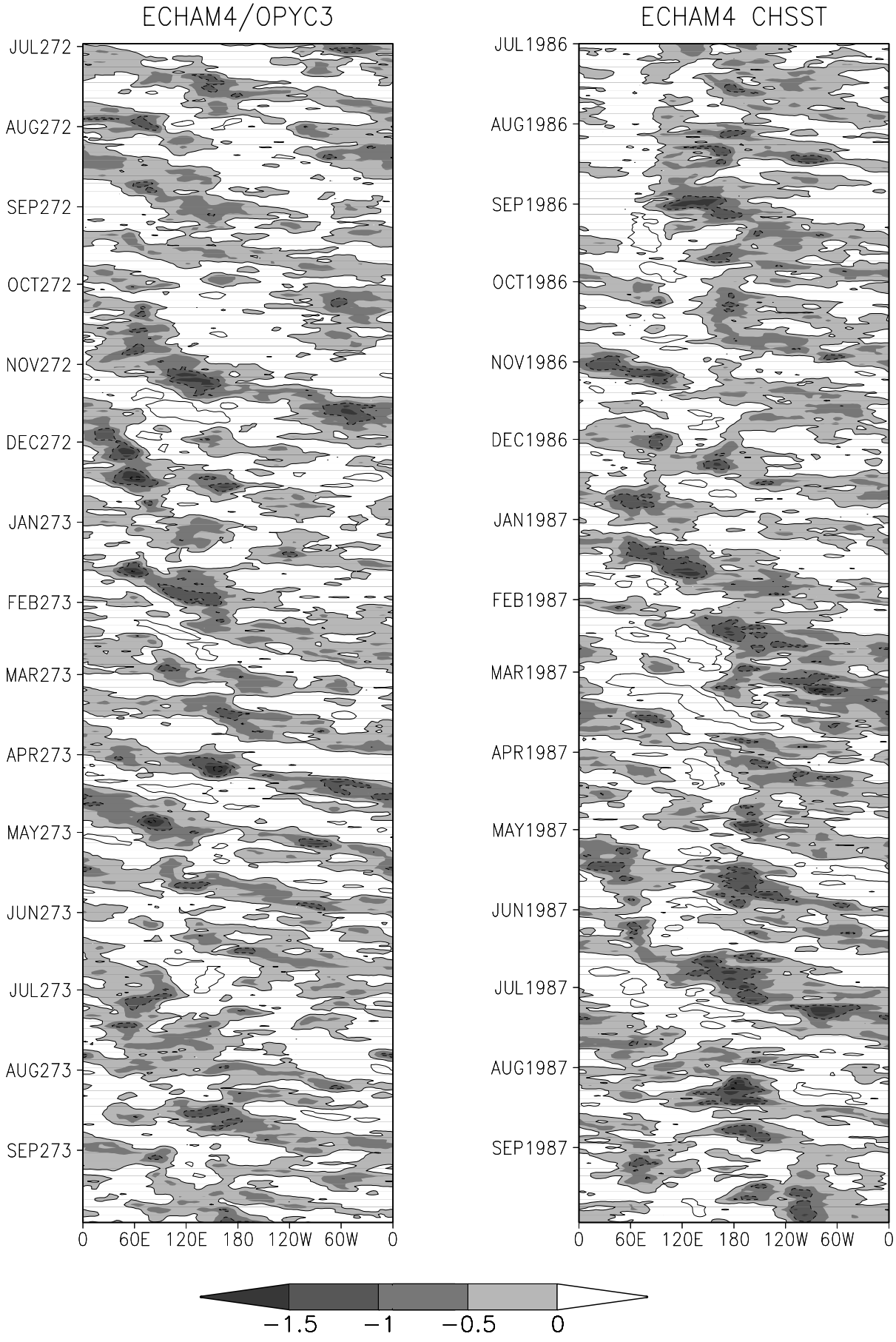

Figure B.3 continued.

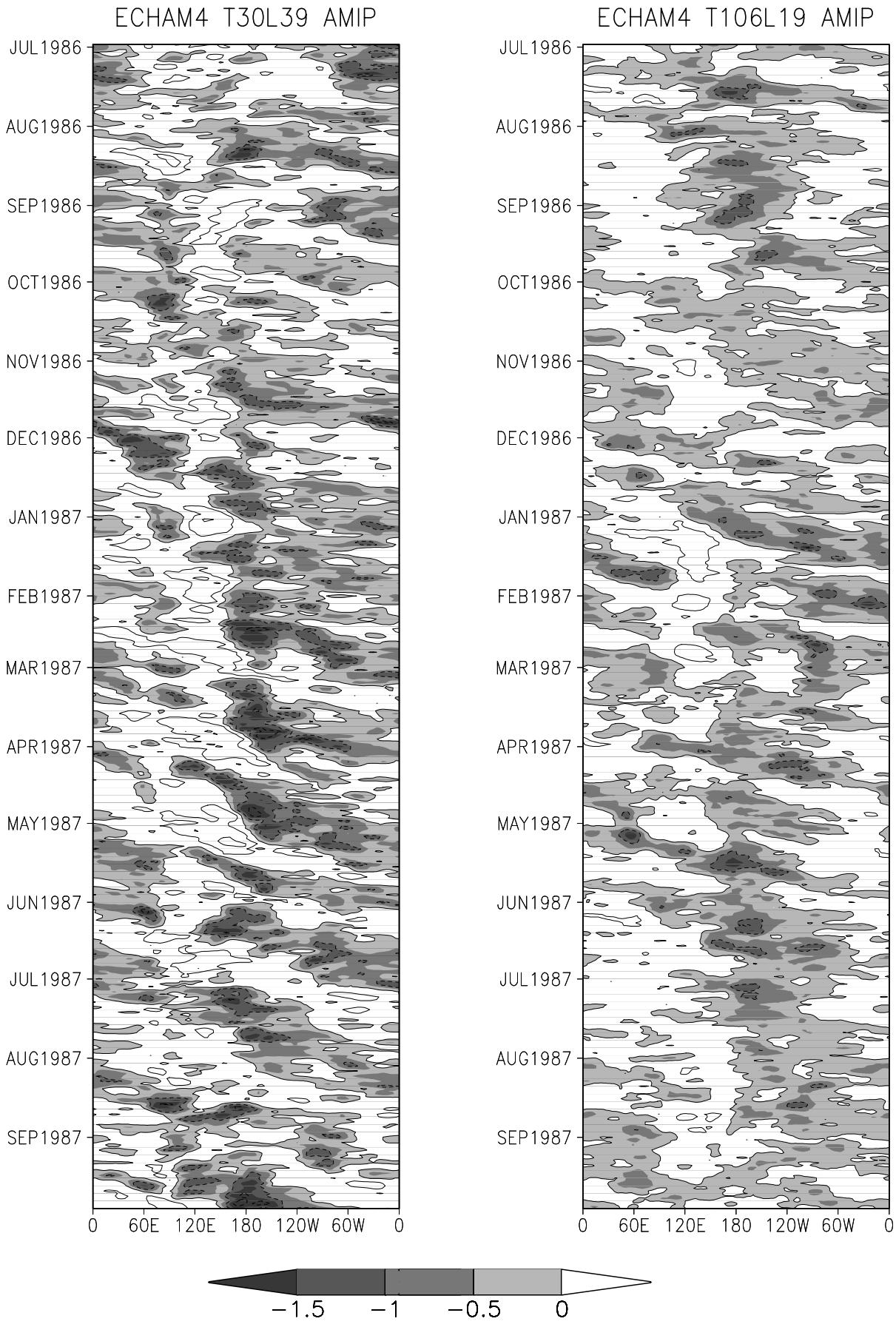

Figure B.3 continued.

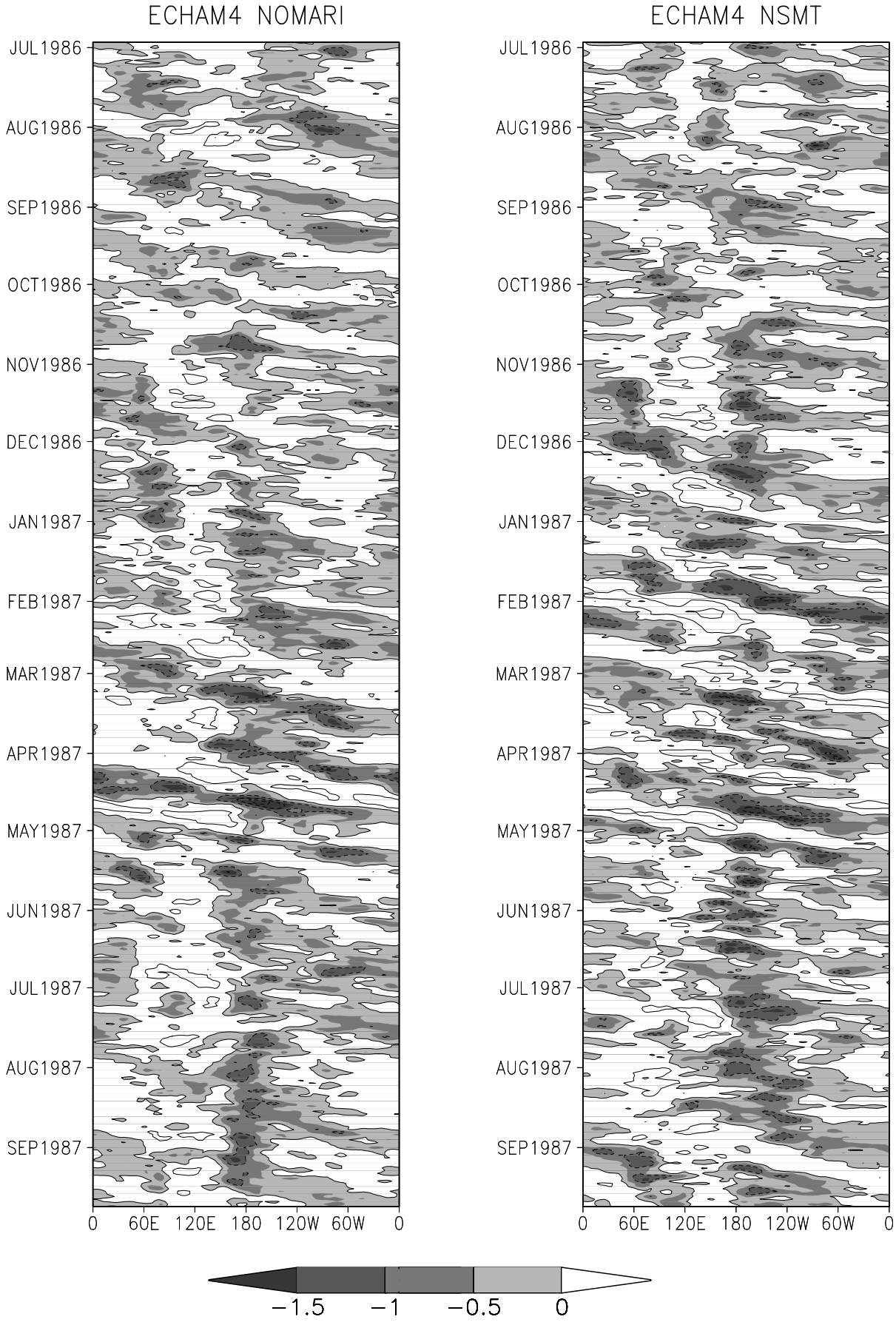

Figure B.3 continued.

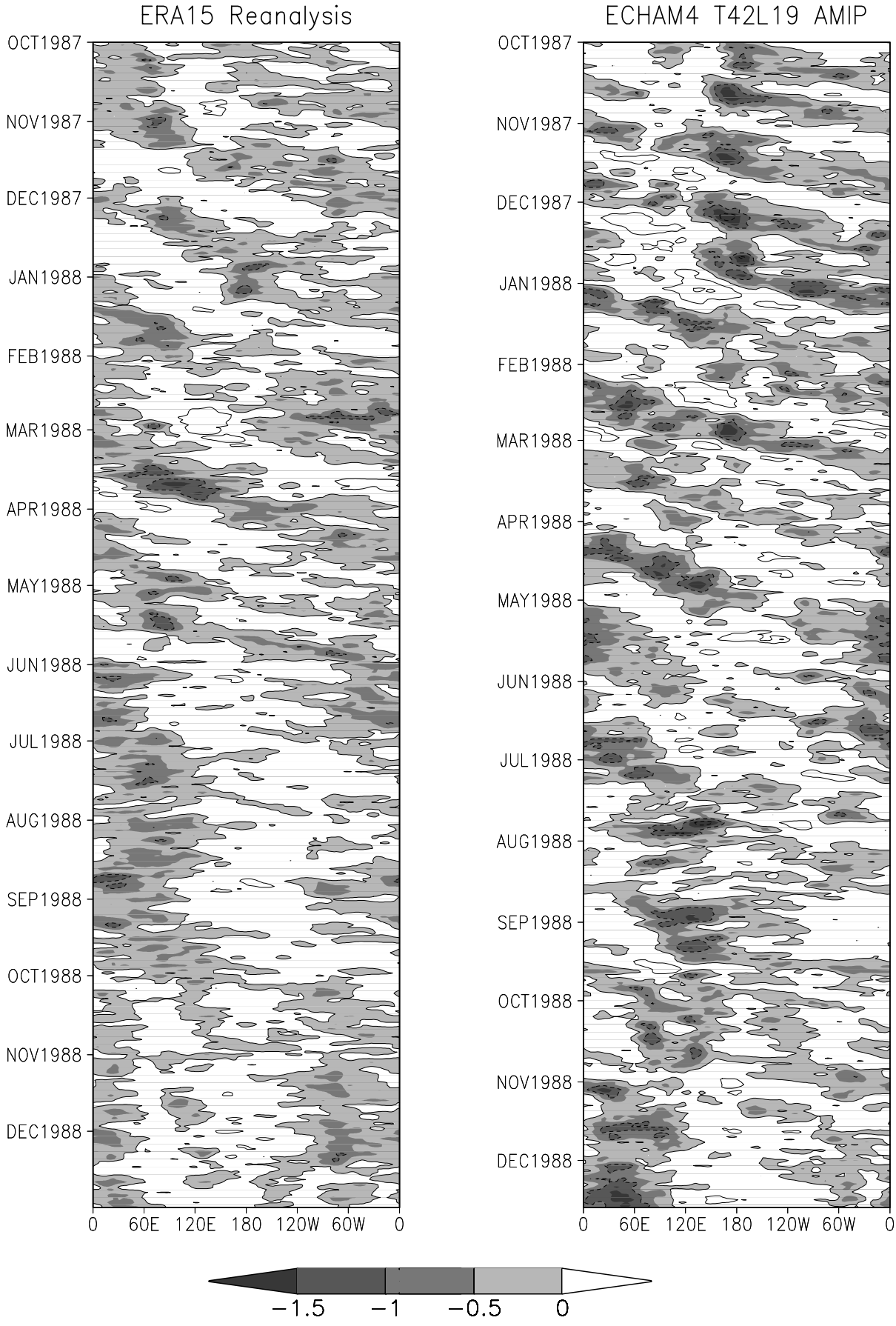

Figure B.4: *As Figure B.1, but for October 1987 to December 1988.*

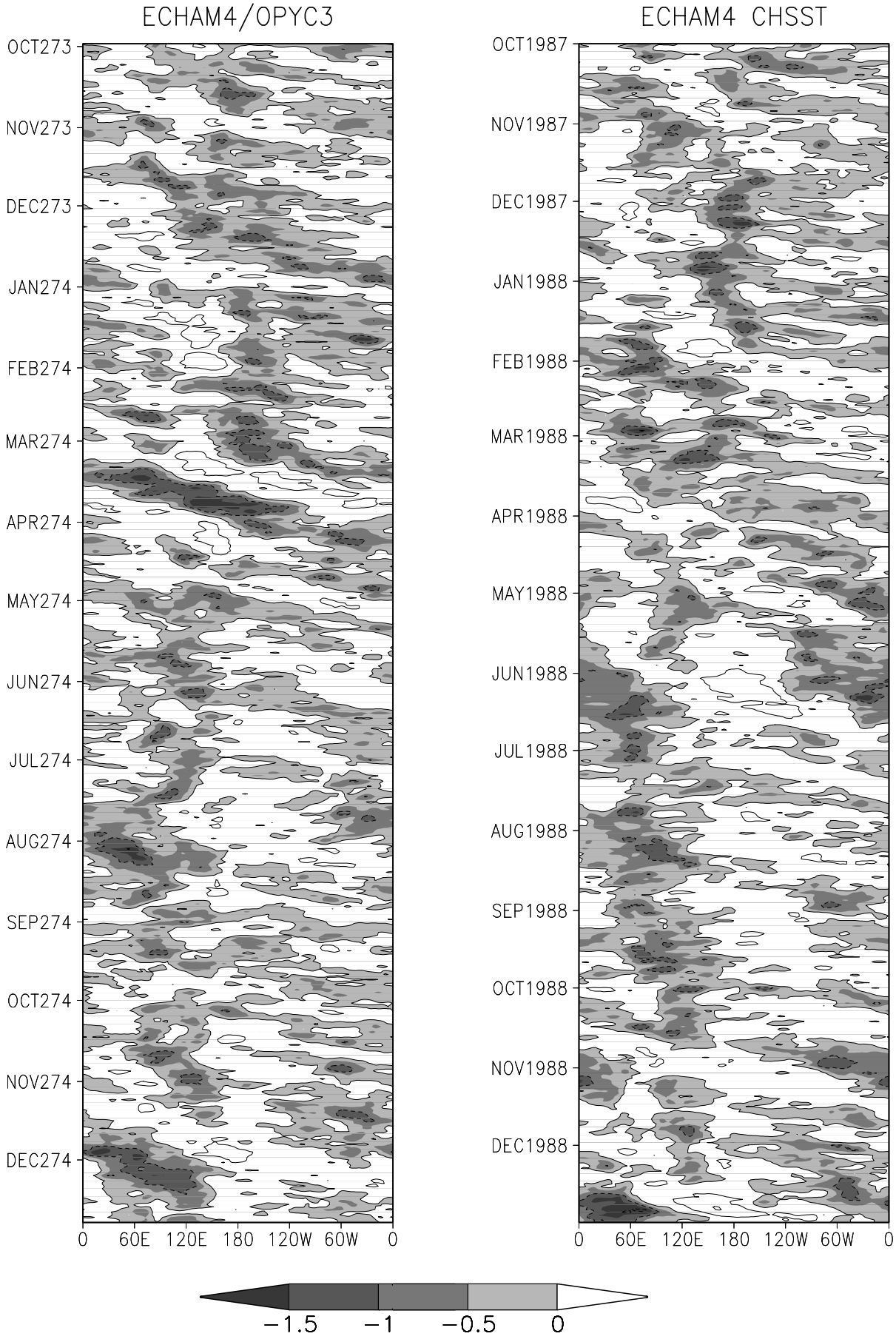

Figure B.4 continued.

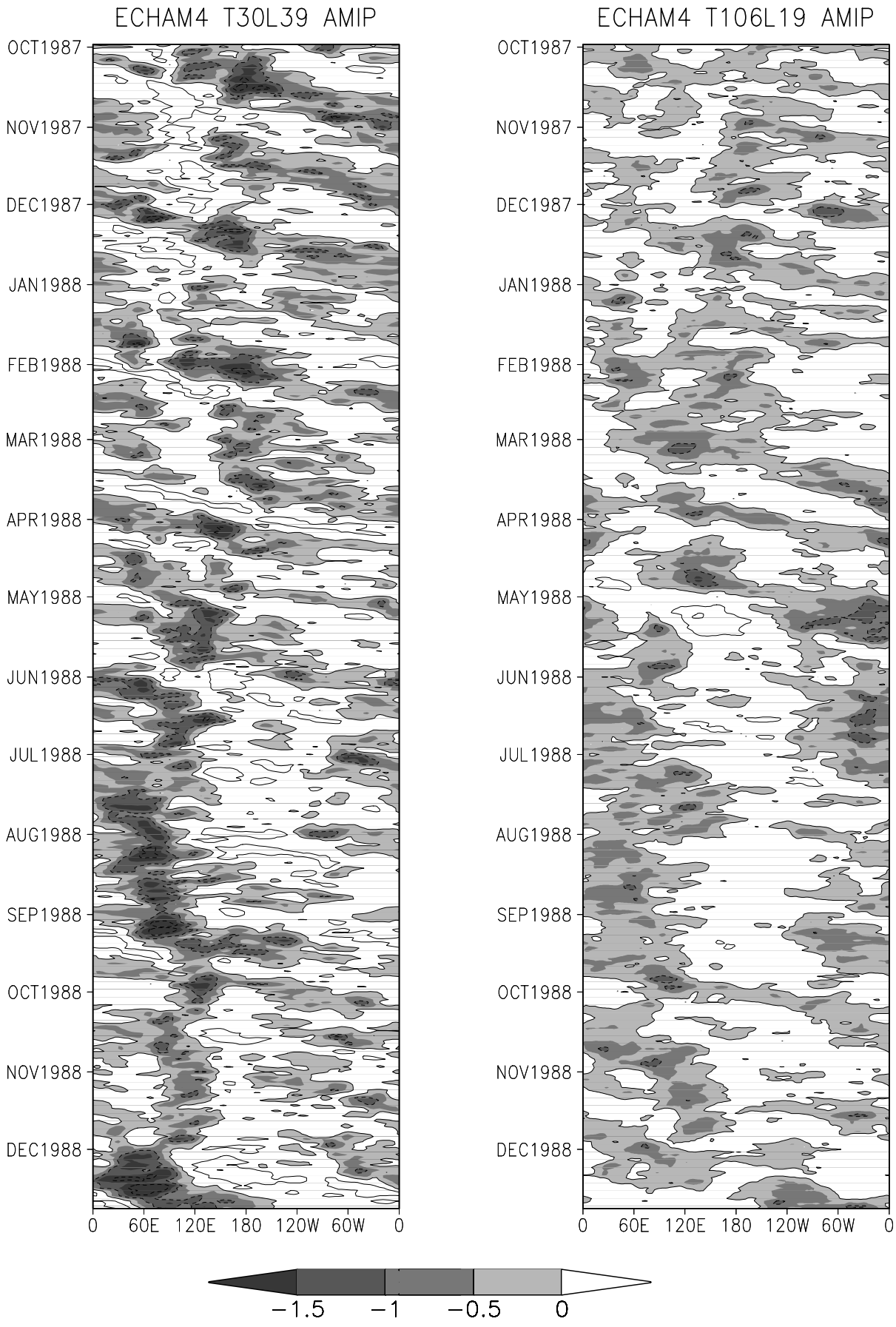

Figure B.4 continued.

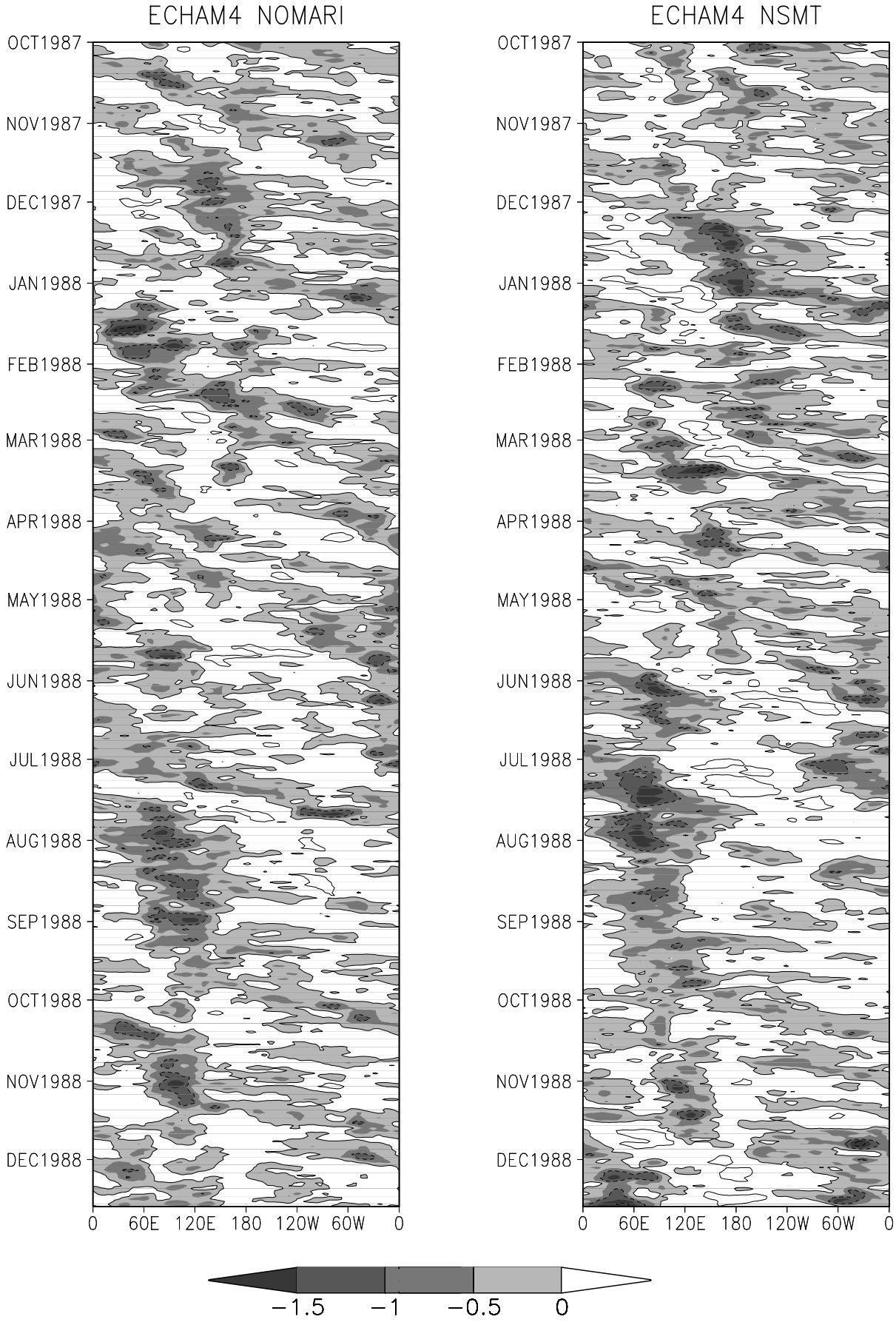

Figure B.4 continued.

Appendix C

The POP analysis

The Principal Oscillation Pattern (POP) analysis (Hasselmann, 1988; von Storch et al., 1988, 1995), used in this study, is a technique for identifying the normal modes (i.e. the characteristic timescales and spatial pattern) of a vector time series. The following paragraphs briefly comprise the basic theory of the POP analysis. A detailed description can be found in Gallagher et al. (1991) and von Storch and Zwiers (1999).

For a large system, the normal modes represent a huge amount of data from which the important characteristics are hard to extract. Hence, the data are transformed to the Empirical Orthogonal Function (EOF) space at first. Then, the EOF space is truncated to n dimensions to reduce the amount of data. In the present study, n is equal to 20 for all datasets, since the first 20 EOFs account for more than 95% of the explained variance of the original datasets in all cases.

The time evolution of the system is explained by the linear vector process

$$\frac{d}{dt}\mathbf{x}(t) \quad = \quad \mathcal{A}\mathbf{x}(t) + \xi(t) \ , \tag{C.1}$$

where $\mathbf{x}(t)$ is the n-dimensional column vector of the EOF-truncated dataset at time t, $\mathcal{A}$ is a constant real $(n \times n)$ matrix and $\xi(t)$ is a noise vector.

The time discretization leads to

$$\mathbf{x}(t+1) \quad = \quad \mathcal{B}\mathbf{x}(t) + \xi(t) \ . \tag{C.2}$$

In this auto regressive process of first order, $\mathcal{B}$ depends on $\mathcal{A}$ and the details of the

discretization. The matrix $\mathcal{B}$ is estimated with the lag 0 and lag 1 covariance matrices $\mathcal{C}_0$ and $\mathcal{C}_1$ of the EOF truncated datasets:

$$\mathcal{B} = \mathcal{C}_1 \mathcal{C}_0^{-1} \tag{C.3}$$

with

$$\begin{aligned} \mathcal{C}_0 &= < \mathbf{x}(t)\ \mathbf{x}(t)^T > \\ \mathcal{C}_1 &= < \mathbf{x}(t+1)\ \mathbf{x}(t)^T > \ . \end{aligned} \tag{C.4}$$

In the absence of noise ($\xi(t) = 0$), Equation (C.2) describes a harmonic oscillation with a mostly complete set of linear independent, but not necessary orthogonal, eigenmodes with eigenvectors $\mathbf{p}^k$ $(k = 1, \ldots, n)$ and corresponding eigenvalues λ_k.

$$\mathcal{B}\mathbf{p}^k = \lambda_k \mathbf{p}^k \tag{C.5}$$

The eigenvectors $\mathbf{p}^k$ of $\mathcal{B}$ are called principal oscillation pattern (POP). $\mathcal{B}$ is in general not symmetric so that λ_k and $\mathbf{p}^k$ may be complex. However, since $\mathcal{B}$ is a real matrix, the complex conjugates λ_k^* and $\mathbf{p}^{k*}$ are also eigenvalues and eigenvectors of $\mathcal{B}$. $\mathbf{P}(t)^k$ is the pattern of $\mathbf{x}(t)$ associated with the corresponding POP k and its pattern coefficient $z(t)$ with

$$\mathbf{P}(t)^k = z(t)_k \mathbf{p}^k + z(t)_k^* \mathbf{p}^{k*} \ . \tag{C.6}$$

Then

$$\mathbf{P}(t)^k = 2z(t)_{k\ re} \mathbf{p}_{re}^k - 2z(t)_{k\ im} \mathbf{p}_{im}^k \ , \tag{C.7}$$

where the subscript re denotes the real part and im the imaginary part. The EOF truncated time series may be reconstructed in terms of the POPs:

$$\mathbf{x}(t) = \sum_{k=1}^{n} a_k(t) \mathbf{p}^k \ , \tag{C.8}$$

where $a_k(t)$ are the complex POP coefficients with a particular POP coefficient defined as $a(t) = z(t)_{re} - iz(t)_{im}$. The vector representation of $a_k(t)$ is depicted in Figure C.1. The diagram describes one oscillation period whereby the initial noise $\xi_k(0)$ is driving only the

real part of the POP. In the data, used in this study, the noise $\xi_k(t)$ drives both parts at every time step. Hence, the POP period that is estimated from the diagram, differs from the actual oscillation period. The actual oscillation period is determined with the spectra of the real and imaginary POP coefficient and their squared coherence (H. von Storch, pers. comm.). It is apparent that the complex pattern represented by $\mathbf{p}^k$ renders the oscillation by the cycle $\mathbf{p}^k_{re} \longrightarrow -\mathbf{p}^k_{im} \longrightarrow -\mathbf{p}^k_{re} \longrightarrow \mathbf{p}^k_{im}$. The compositing technique used in the present study takes only values of $a_k(t)$ greater than $\overline{|a_k|} + 0.8 \times std.dev.(|a_k|)$ into account with k representing the dominant POP mode.

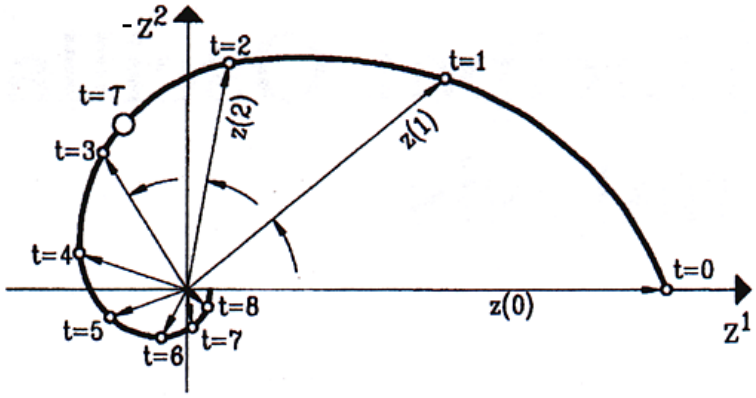

Figure C.1: *Schematic diagram of the time evolution of the POP coefficients z(t) with the initial noise driving only the real part of the POP (z^1). The imaginary part of the POP (z^2) is negatively defined according to Equation C.7. The e-folding time τ is indicated by the large open circle (adapted from Gallagher et al., 1991; von Storch and Zwiers, 1999).*

The composites for the ERA15 200 hPa velocity potential anomaly as discussed in Section 2.2 are obtained from the POPs $\mathbf{p}^k_{im}$ and $\mathbf{p}^k_{re}$ as illustrated in Figure C.2. The spatial pattern of the real and imaginary part of the dominant POP are not orthogonal, as described before. Their time evolution is described in the scatter plot in Figure C.3, similar to Figure C.1. The scatter plot is divided into eight segments and the 200 hPa velocity potential anomaly at every time step in a certain segment with an amplitude of the POP coefficients greater than $\overline{|a_k|} + 0.8 \times std.dev.(|a_k|)$ is allocated to the respective composite. The average of each composite defines the mean IO pattern in the respective phase. It is illustrated as contour lines in Figures 2.5 and 2.6. The resemblance of the contour lines in the top panel of Figure C.2 to the top panels of Figures 2.5 and 2.6 and the reversed pattern in panels five of Figures 2.5 and 2.6 are obvious. The same is true for the resemblance of the bottom panel of Figure C.2 to the third panels of Figures 2.5 and 2.6 and the reversed pattern in panels seven of Figures 2.5 and 2.6.

The advantage of the POP analysis compared to the EOF analysis is the independence of the spatial pattern of the real and imaginary part of the dominant POPs, whereas the first and second EOF pattern are orthogonal by definition. This mathematical constraint

of orthogonality in space and time reduces the physical relevance of the second EOF (Dommenget and M.Latif, 2002). In this study the pattern of the first EOFs are used to illustrate one single position of main IO activity, whereas the dominant POP is used to describe the oscillation with the aid of the complex pattern and thus the advantage to describe the eastward direction of the propagation of the IO.

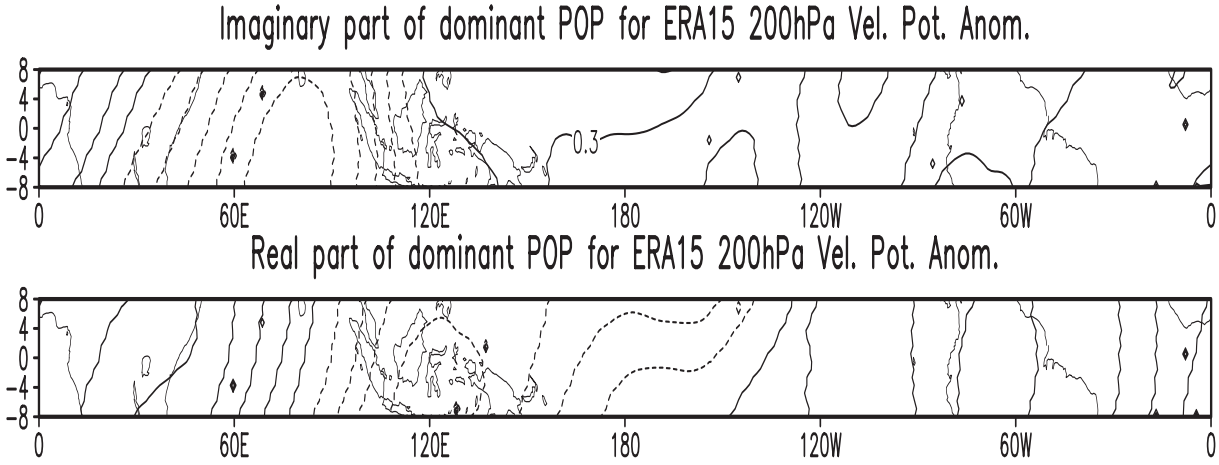

Figure C.2: *Imaginary (top) and real (bottom) part of the dominant POP of 200 hPa velocity potential anomalies. Contour interval is 0.3, negative values are dashed and the pattern explains 23.8% of the total variance.*

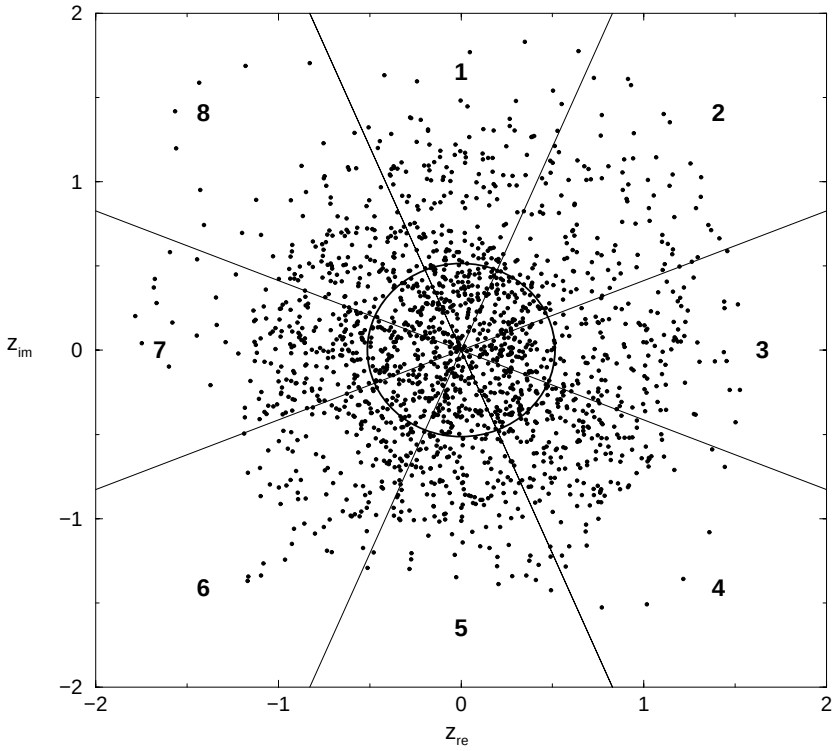

Figure C.3: *Scatter plot of the dominant POP coefficients of ERA15 200 hPa velocity potential anomalies. Numbers in the eight segments indicate the phase of the IO. The circle in the center illustrates the threshold of* $\overline{|a_k|} + 0.8 \times std.dev.(|a_k|)$.

References

Bacher, A., J. M. Oberhuber and E. Roeckner (1998): ENSO dynamics and seasonal cycle in the tropical Pacific as simulated by the ECHAM4/OPYC3 coupled general circulation model. *Climate Dyn.*, **14**, 431–450.

Bengtsson, L. (1999): From short-range barotropic modelling to extended-range global weather prediction: a 40-year perspective. *Tellus*, **51A-B**, 13–32.

Bladé, I. and D. L. Hartmann (1993): Tropical intraseasonal oscillations in a simple nonlinear model. *J. Atmos. Sci.*, **50**, 2922–2939.

Central Intelligence Agency (2001): *The world factbook 2001.* Washington D.C., http://www.cia.gov/cia/publications/factbook.

Charney, J. G. and A. Eliassen (1964): On the growth of the hurricane depression. *J. Atmos. Sci.*, **21**, 68–75.

Chen, T.-C. and J.-M. Chen (1997): On the relationship between the streamfunction and velocity potential of the Madden-Julian oscillation. *J. Atmos. Sci.*, **54**, 679–685.

Cullen, M. J. P. (1993): The Unified Forecast/Climate Model. *Meteor. Mag.*, **122**, 81–94.

Delcroix, T., B. Dewitte, Y. du Penhoat, F. Masia and J. Picaut (2000): Equatorial waves and warm pool displacements during the 1992-1998 El Nino Southern Oscillation events: observation and modeling. *J. Geophys. Res.*, **105**, 26045–26062.

Dommenget, D. and M.Latif (2002): A cautionary note on the interpretation of EOF. *J. Climate*, **15**, 216–225.

Emanuel, K. A. (1987): Air-sea interaction model of intraseasonal oscillations in the Tropics. *J. Atmos. Sci.*, **44**, 2324–2340.

Ferranti, L., T. N. Palmer, F. Molteni and E. Klinker (1990): Tropical-extratropical interaction associated with the 30-60 day oscillation and its impact on medium and extended range prediction. *J. Atmos. Sci.*, **47**, 2177–2199.

Flatau, M., P. J. Flatau, P. Phoebus and P. P. Niiler (1997): The feedback between equatorial convection and local radiative and evaporative processes: The implications for intraseasonal oscillations. *J. Atmos. Sci.*, **54**, 2373–2386.

Fox-Rabinovitz, M. S. and R. S. Lindzen (1993): Numerical experiments on consistent horizontal and vertical resolution for atmospheric models and observing systems. *Mon. Wea. Rev.*, **121**, 264–271.

Gallagher, F., H. von Storch, R. Schnur and G. Hannoschoeck (1991): The POP manual. Technical Report 1, Deutsches Klimarechenzentrum, Hamburg, Germany. 66 pp.

Gates, W. L. (1992): AMIP: The Atmospheric Model Intercomparison Project. *Bull. Amer. Meteor. Soc.*, **73**, 1962–1970.

Gibson, J. K., P. Kållberg, S. Uppala, A. Hernandez, A. Nomura and E. Serrano (1997): Era description. ECMWF Reanal. Proj. Rep. Ser. 1, Eur. Cent. for Medium Range Weather Forecasting, Geneva, Switzerland. 72 p.

Gordon, C. T. and W. F. Stern (1982): A description of the GFDL global spectral model. *Mon. Wea. Rev.*, **110**, 625–644.

Graham, N. and T. P. Barnett (1987): Observations of sea surface temperature and convection over tropical oceans. *Science*, **238**, 657–660.

Gruber, A. and A. F. Krueger (1984): Status of the NOAA outgoing long-wave radiation data set. *Bull. Amer. Meteor. Soc.*, **65**, 958–962.

Gualdi, S., A. Navarra and G. Tinarelli (1999): The interannual variability of the Madden-Julian oscillation in an ensemble of GCM simulations. *Climate Dyn.*, **15**, 643–658.

Gualdi, S., A. Navarra and H. von Storch (1997): Tropical intraseasonal oscillation appearing in operational analysis and in a family of general circulation models. *J. Atmos. Sci.*, **54**, 1185–1202.

Hasselmann, K. (1988): PIPs and POPs: The reduction of complex dynamical systems using principal interaction and oscillation pattern. *J. Geophys. Res.*, **93**, 11015–11021.

Hayashi, Y.-Y. and D. G. Golder (1988): Tropical intraseasonal oscillations appearing in GFDL general circulation model and FGGE data, Pt. 2, Structure. *J. Atmos. Sci.*, **45**, 3017–3033.

Hayashi, Y.-Y. and D. G. Golder (1993): Tropical 40-50- and 25-30-day oscillations appearing in realistic and idealised GFDL climate models and the ECMWF dataset. *J. Atmos. Sci.*, **50**, 464–494.

Hayashi, Y.-Y. and A. Sumi (1986): The 30-40-day oscillations simulated in an "aqua planet" model. *J. Meteor. Soc. Japan*, **64**, 451–467.

Hendon, H. H. (2000): Impact of air-sea coupling on the Madden-Julian Oscillation in a general circulation model. *J. Atmos. Sci.*, **57**, 3939–3952.

Hendon, H. H. and B. Liebmann (1990a): A composite study of onset of the Australian summer monsoon. *J. Atmos. Sci.*, **47**, 2227–2240.

Hendon, H. H. and B. Liebmann (1990b): The intraseasonal (30-50 day) oscillation of the Australian summer monsoon. *J. Atmos. Sci.*, **47**, 2909–2923.

Hendon, H. H., B. Liebmann, M. Newman, J. D. Glick and J. E. Schemm (2000): Medium-range forecast errors associated with active episodes of the Madden-Julian oscillation. *Mon. Wea. Rev.*, **128**, 69–86.

Hendon, H. H. and M. L. Salby (1994): The life cycle of the Madden-Julian oscillation. *J. Atmos. Sci.*, **51**, 2225–2237.

Higgins, R. W., J.-K. E. Schemm, W. Shi and A. Leetmaa (2000): Extreme precipitation events in the western United States related to tropical forcing. *J. Climate*, **13**, 793–820.

Holland, G. J. (1986): Interannual variability of the Australian summer monsoon at Darwin: 1952-82. *Mon. Wea. Rev.*, **114**, 594–604.

Holton, J. R. (1992): *An Introduction to Dynamic Meteorology*, vol. 48 of *International Geophysics Series*. Academic Press, San Diego, CA. 511 pp.

Hsu, H.-H., B. J. Hoskins and F. F. Jin (1990): The 1985/86 intraseasonal oscillation and the role of the extratropics. *J. Atmos. Sci.*, **47**, 823–839.

Hsu, H.-H., C.-T. Terng and C.-T. Chen (1999): Evolution of large-scale circulation and heating during the first transition of Asian summer monsoon. *J. Climate*, **12**, 793–810.

Huang, R.-H. and F. Y. Sun (1992): Impacts of the tropical western Pacific on the East Asian summer monsoon. *J. Meteor. Soc. Japan*, **70**, 243–256.

Inness, P. M., J. M. Slingo, S. J. Woolnough, R. B. Neale and V. D. Pope (2001): Organization of tropical convection in a GCM with varying vertical resolution; implications for the simulation of the Madden-Julian oscillation. *Climate Dyn.*, **17**, 777–793.

Johnson, R. H., P. E. Ciesielski and K. A. Hart (1996): Tropical inversions near the 0 °C level. *J. Atmos. Sci.*, **53**, 1838–1855.

Johnson, R. H., T. M. Rickenbach, S. A. Rutledge, P. E. Ciesielski and W. H. Schubert (1999): Trimodal characteristics of tropical convection. *J. Climate*, **12**, 2397–2418.

Jones, C. (2000): Occurrence of extreme precipitation events in California and relationships with the Madden Julian oscillation. *J. Climate*, **13**, 3576–3587.

Jones, C., D. E. Waliser and C. Gautier (1998): The influence of the Madden-Julian oscillation on ocean surface heat fluxes and sea surface temperature. *J. Climate*, **11**, 1057–1072.

Jones, C., D. E. Waliser, J. E. Schemm and W. K. Lau (2000): Prediction skill of the Madden and Julian oscillation in dynamical extended range weather forecasts. *Climate Dyn.*, **16**, 273–289.

Jones, C. and B. C. Weare (1996): The role of low-level moisture convergence and ocean latent heat fluxes in the Madden-Julian oscillation: An observational analysis using ISCCP data and ECMWF analyis. *J. Climate*, **9**, 3086–3104.

Kalnay, E., R. Balgovind, W. Chao, D. Edelmann, J. Pfaendtner, L. Takacs and K. Takano (1983): Documentation of the GLAs fourth order general circulation model, Volume I. Tech. Memo. 86064, NASA, Goddard Space Flight Center, Greenbelt, MD. 100 p.

Kalnay, E., M. Kanamitsu, R. Kistler, W. Collins, D. Deaven, L. Gandin, M. Iredell, S. Saha, G. White, J. Woollen, Y. Zhu, M. Chelliah, W. Ebisuzaki, W. Higgins, J. Janowiak, K. C. Mo, C. Ropelewski, J. Wang, A. Leetmaa, R. Reynolds, R. Jenne and D. Joseph (1996): The NCEP/NCAR 40-year reanalysis project. *Bull. Amer. Meteor. Soc.*, **77**, 437–471.

Kemball-Cook, S. R. and B. C. Weare (2001): The onset of convection in the Madden-Julian oscillation. *J. Climate*, **14**, 780–793.

Kessler, W. S., M. McPhaden and K. M. Weickmann (1995): Forcing of intraseasonal Kelvin waves in the equatorial Pacific. *J. Geophys. Res.*, **100**, 10613–10631.

Kirtman, B. and A. Vernekar (1993): On wave-CISK and the evaporation-wind feedback for the Madden-Julian oscillation. *J. Atmos. Sci.*, **50**, 2811–2814.

Kistler, R., E. Kalnay, W. Collins, S. Saha, G. White, J. Woollen, M. Chelliah, W. Ebisuzaki, M. Kanamitsu, V. Kousky, H. van den Dool, R. Jenne and M. Fiorino (2001): The NCEP NCAR 50-year reanalysis: Monthly means CD-ROM and documentation. *Bull. Amer. Meteor. Soc.*, **82**, 247–268.

Knutson, T. R. and K. M. Weickmann (1987): 30-60 day atmospheric oscillations: Composite life cycles of convection and circulation anomalies. *Mon. Wea. Rev.*, **115**, 1407–1436.

Koblinsky, C., R. Ray, B. Beckley, A. Brenner, L. Tsaoussi and Y. Wang (1999): NASA Ocean Altimeter Pathfinder Project. Report 2: Data Set Validation. Technical memorandum, NASA/TM-1999-209230.

Koblinsky, C., R. Ray, B. Beckley, Y. Wang, L. Tsaoussi, A. Brenner and R. Williamson (1998): NASA Ocean Altimeter Pathfinder Project. Report 1: Data Processing Handbook. Technical memorandum, NASA/TM-1998-208605.

Krishnamurti, T. N., D. K. Oosterhof and A. V. Mehta (1988): Air-sea interaction on the time scale of 30 to 50 days. *J. Atmos. Sci.*, **45**, 1304–1322.

Land, C., M. Ponater, R. Sausen and E. Roeckner (1999): The ECHAM4.L39(DLR) atmosphere GCM: technical description and model climatology. DLR-Forschungsbericht 31, Institut fur Physik der Atmosphare des DLR, Oberpfaffenhofen, Germany. 45 p.

Lau, K.-M. and L. Peng (1987): Origin of low-frequency (intraseasonal) oscillations in the tropical atmosphere. Part I: Basic theory. *J. Atmos. Sci.*, **44**, 950–972.

Lau, K.-M., L. Peng, C.-H. Sui and T. Nakazawa (1989): Dynamics of super cloud clusters, westerly wind bursts, 30-60-day oscillations, and ENSO: a unified view. *J. Meteor. Soc. Japan*, **67**, 205–219.

Lau, K.-M. and C.-H. Sui (1997): Mechanisms of short-term Sea Surface Temperature regulation: Observations during TOGA COARE. *J. Climate*, **10**, 465–472.

Lau, K.-M., H.-T. Wu and S. Yang (1998): Hydrologic processes associated with the first transition of the Asian summer monsoon: a pilot satellite study. *Bull. Amer. Meteor. Soc.*, **79**, 1871–1882.

Lau, K. M. and S. Yang (1997): Climatology and interannual variability of the of the Southeast Asian summer monsoon. *Adv. Atmos. Sci.*, **14**, 141–162.

Liebmann, B. and C. A. Smith (1996): Description of a complete (interpolated) outgoing longwave radiation dataset. *Bull. Amer. Meteor. Soc.*, **77**, 1275–1277.

Lindzen, R. S. (1974): Wave-CISK in the tropics. *J. Atmos. Sci.*, **31**, 156–179.

Madden, R. A. and P. R. Julian (1971): Detection of a 40-50 day oscillation in the zonal wind in the tropical Pacific. *J. Atmos. Sci.*, **28**, 702–708.

Madden, R. A. and P. R. Julian (1972): Description of global-scale circulation cells in the ropics with a 40-50 day period. *J. Atmos. Sci.*, **29**, 1109–1123.

Madden, R. A. and P. R. Julian (1994): Observations of the 40-50-day tropical oscillation - a review. *Mon. Wea. Rev.*, **122**, 814–837.

Matsuno, T. (1966): Quasi-geostrophic motions in the equatorial area. *J. Meteor. Soc. Japan*, **44**, 25–43.

Matthews, A. J. (2000): Propagation mechanisms for the Madden-Julian Oscillation. *Quart. J. Roy. Meteor. Soc.*, **126**, 2637–2651.

Matthews, A. J., B. J. Hoskins, J. M. Slingo and M. Blackburn (1996): Developement of convection along the SPCZ within a Madden-Julian oscillation. *Quart. J. Roy. Meteor. Soc.*, **122**, 669–688.

Matthews, A. J. and G. N. Kiladis (1999): The tropical-extratropical interaction between high-frequency transients and the Madden-Julian Oscillation. *Mon. Wea. Rev.*.

McPhaden, M. J. and B. A. Taft (1988): Dynamics of seasonal and intraseasonal variability in the eastern equatorial Pacific. *J. Phys. Oceanogr.*, **18**, 1713–1732.

Mo, K. C. and R. W. Higgins (1998a): Tropical influences on California precipitation. *J. Climate*, **11**, 412–430.

Mo, K. C. and R. W. Higgins (1998b): Tropical convection and precipitation regimes in the western United States. *J. Climate*, **11**, 2404–2423.

Nakazawa, T. (1988): Tropical super clusters within intraseasonal variations over the western Pacific. *J. Meteor. Soc. Japan*, **66**, 823–839.

Nakazawa, T. (1999): MJO–a key component in the atmosphere for triggering ENSO. In: *Conference on the TOGA Coupled Ocean-Atmosphere Response Experiment (COARE), Boulder, Colorado, USA, 7-14 July 1998, COARE-98*. Geneva, Switzerland, World Meteorological Organization, WMO/TD 940, pp. 165–166.

Neale, R. and J. Slingo (2001): The Maritime Continent and its role in the global climate: a GCM study. *J. Climate*, submitted.

Neelin, J. D., I. M. Held and K. H. Cook (1987): Evaporation-wind feedback and low-frequency variability in the tropical atmosphere. *J. Atmos. Sci.*, **44**, 2341–2348.

Newman, M., P. D. Sardeshmukh and J. W. Bergman (2000): An assessment of the NCEP, NASA, and ECMWF reanalyses over the tropical west Pacific warm pool. *Bull. Amer. Meteor. Soc.*, **81**, 41–48.

Nitta, T. (1987): Convective activities in the tropical Western Pacific and their impact on the Northern Hemisphere summer circulation. *J. Meteor. Soc. Japan*, **65**, 373–390.

Nordeng, T. E. (1996): Extended versions of the convective parameterization scheme at ECMWF and their impact on the mean and transient activity of the model in the tropics. Tech. Memo. 206, ECMWF Research Department, Eur. Cent. for Medium-Range Weather Forecasts, Reading, England. 41 p.

Ooyama, K. (1964): A dynamical model for the study of tropical cyclone development. *Geofisica International*, **4**, 187–198.

Philander, S. G. (1990): *El Niño, La Niña and the Southern Oscillation*. Academic Press. 293 p.

Philander, S. G. H., D. Gu, D. Halpern, G. Lambert, N.-C. Lau, T. Li and R. C. Pacanowski (1996): Why the ITCZ is mostly north of the equator. *J. Climate*, **9**, 2958–2972.

Picaut, J. and T. Delcroix (1995): Equatorial wave sequence associated with warm pool displacements during the 1986-1989 El Nino-La Nina. *J. Geophys. Res.*, **100**, 18393–18408.

Reynolds, R. W. and T. M. Smith (1994): Improved global sea surface temperature analysis using optimum interpolation. *J. Climate*, **7**, 929–948.

Riehl, H. and J. Malkus (1958): On the heat balance in the equatorial trough zone. *Geophysica*, **6**, 503–537.

Roeckner, E., K. Arpe, L. Bengtsson, S. Brinkop, L. Dümenil, M. Esch, E. Kirk, F. Lunkeit, M. Ponater, B. Rockel, R. Sausen, U. Schlese, S. Schubert and M. Windelband (1992): Simulation of the present-day climate with the ECHAM model: Impact

of model physics and resolution. Report 93, Max-Planck-Institut für Meteorologie, Hamburg, Germany. 172 p.

Roeckner, E., K. Arpe, L. Bengtsson, M. Christoph, M. Claussen, L. Dümenil, M. Esch, M. Giorgetta, U. Schlese and U. Schulzweida (1996a): The atmospheric general circulation model ECHAM4: Model description and simulation of present-day climate. Report 218, Max-Planck-Institut für Meteorologie, Hamburg, Germany. 90 p.

Roeckner, E., J. M. Oberhuber, A. Bacher, M. Christoph and I. Kirchner (1996b): ENSO variability and atmospheric response in a global coupled atmosphere-ocean GCM. *Climate Dyn.*, **12**, 737–754.

Rui, H. and B. Wang (1990): Development characteristics and dynamic structure of tropical intraseasonal convection anomalies. *J. Atmos. Sci.*, **47**, 357–379.

Salby, M. L., R. R. Garcia and H. H. Hendon (1994): Planetary-scale circulations in the presence of climatological and wave-induced heating. *J. Atmos. Sci.*, **51**, 2344–2367.

Salby, M. L. and H. H. Hendon (1994): Intraseasonal behavior of clouds, temperature, and motion in the tropics. *J. Atmos. Sci.*, **51**, 2207–2224.

Schubert, W., P. E. Ciesielski, C. Lu and R. H. Johnson (1995): Dynamical adjustment of the trade wind inversion layer. *J. Atmos. Sci.*, **52**, 2941–2952.

Slingo, J., M. Blackburn, A. Betts, R. Brugge, K. Hodges, B. Hoskins, M. Miller, L. Steenman-Clark and J. Thuburn (1994): Mean climate and transience in the tropics of the UGAMP GCM: sensitivity to convective parametrization. *Quart. J. Roy. Meteor. Soc.*, **120**, 881–922.

Slingo, J. M., D. P. Rowell, K. R. Sperber and F. Nortley (1999): On the predictability of the interannual behaviour of the Madden-Julian oscillation and its relationship with El Niño. *Quart. J. Roy. Meteor. Soc.*, **125**, 583–609.

Slingo, J. M., K. R. Sperber, J. S. Boyle, J.-P. Ceron, M. Dix, B. Dugas, W. Ebisuzaki, J. Fyfe, D. Gregory, J.-F. Gueremy, J. Hack, A. Harzallah, P. Inness, A. Kitoh, W. K.-M. Lau, B. McAvaney, R. Madden, A. Matthews, T. N. Palmer, C.-K. Park, D. Randall and N. Renno (1996): Intraseasonal oscillations in 15 atmospheric general circulation models: Results from an AMIP diagnostic subproject. *Climate Dyn.*, **12**, 325–357.

Sperber, K. R., J. M. Slingo, P. M. Inness and W. K.-M. Lau (1997): On the maintenance and initiation of the intraseasonal oscillation in the NCEP/NCAR reanalysis and the GLA and UKMO AMIP simulations. *Climate Dyn.*, **13**, 769–795.

Sui, C.-H. and K.-M. Lau (1989): Origin of low-frequency (intraseasonal) oscillations in the tropical atmosphere. Part. II: Structure and propagation of mobile wave-CISK modes and their modification by lower boundary forcings. *J. Atmos. Sci.*, **46**, 37–56.

Swinbank, R., T. N. Palmer and M. K. Davey (1988): Numerical simulations of the Madden and Julian oscillation. *J. Atmos. Sci.*, **45**, 774–788.

Tao, S. and L. Chen (1987): A review of recent research in the East Asian summer monsoon in China. In: *Monsoon Meteorology*, C.-P. Chang and T. N. Krishnamurti, Eds., Oxford University Press, pp. 60–92.

Taylor, K. E., D. Williamson and F. Zwiers (2001): AMIP II sea surface temperature and sea ice concentration boundary conditions. http://www-pcmdi.llnl.gov/amip/AMIP2EXPDSN/BCS/amip2bcs.html.

Tiedtke, M. (1989): A comprehensive mass flux scheme for cumulus parameterization in large scale models. *Mon. Wea. Rev.*, **117**, 1779–1800.

Tompkins, A. M. and K. A. Emanuel (2000): The vertical-resolution sensitivity of simulated equilibrium tropical temperature and water-vapor profiles. *Quart. J. Roy. Meteorol. Soc.*, **126**, 1219–1238.

Troup, A. J. (1961): Variations in upper tropospheric flow associated with the onset of Australian summer monsoon. *Indian J. Meteor. Geophys.*, **12**, 217–230.

van Oldenborgh, G. J. (2000): What caused the 1997-1998 El Niño? *Mon. Wea. Rev.*, **128**, 2601–2607.

von Storch, H., T. Bruns, I. Fischer-Bruns and K. Hasselmann (1988): Principal oscillation pattern analysis of the 30- to 60-day oscillation in general circulation model equatorial troposphere. *J. Geophys. Res.*, **93**, 11022–11036.

von Storch, H., G. Bürger, R. Schnur and J. von Storch (1995): Principal oscillation patterns: A review. *J. Climate*, **8**, 377–400.

von Storch, H. and F. W. Zwiers (1999): *Statistical Analysis in Climate Research*. Cambridge University Press, Cambridge. 550 p.

Waliser, D. E., C. Jones, J.-K. E. Schemm and N. E. Graham (1999a): A statistical extended-range tropical forecast model based on the slow evolution of the Madden-Julian oscillation. *J. Climate*, **12**, 1918–1939.

Waliser, D. E., K. M. Lau and J.-H. Kim (1999b): The influence of coupled Sea Surface Temperatures on the Madden-Julian oscillation: A model perturbation experiment. *J. Atmos. Sci.*, **56**, 333–358.

Waliser, D. E., W. Stern, S. Schubert, M. Latif and S. Liess (2001): Exploring the benefits and limits of dynamical predictions of the tropical intraseasonal oscillation: Steps towards an experimental prediction program. A research proposal to the CLIVAR-Pacific Program of the Office of Global Programs/NOAA, 30 p.

Wang, B. (1988): Dynamics of tropical low-frequency waves: An analysis of the moist Kelvin waves. *J. Atmos. Sci.*, **45**, 2051–2065.

Wang, B. and H. Rui (1990a): Dynamics of the coupled moist Kelvin-Rossby wave on an equatorial β-plane. *J. Atmos. Sci.*, **47**, 397–413.

Wang, B. and H. Rui (1990b): Synoptic climatology of transient tropical intraseasonal convection anomalies. *Meteor. Atmos. Phys.*, **44**, 43–61.

Wang, B. and X. Xie (1998): Coupled modes of the warm pool climate system. Part I: The role of air-sea interaction in maintaining Madden-Julian oscillation. *J. Climate*, **11**, 2116–2133.

Webster, P. J. and R. Lukas (1992): TOGA COARE: the Coupled Ocean-Atmosphere Response Experiment. *Bull. Amer. Meteor. Soc.*, **73**, 1377–1416.

Weickmann, K. M. (1991): El Nino/Southern Oscillation and Madden-Julian (30-60 day) oscillations during 1981-1982. *J. Geophys. Res.*, **96**, 3187–3195.

Weickmann, K. M., G. N. Kiladis and P. D. Sardeshmukh (1997): The dynamics of intraseasonal atmospheric angular momentum oscillations. *J. Atmos. Sci.*, **54**, 1445–1461.

Wheeler, M., G. N. Kiladis and P. J. Webster (2000): Large-scale dynamical fields associated with convectively coupled equatorial waves. *J. Atmos. Sci.*, **57**, 613–640.

Wyrtki, K. (1975): El Nino dynamic response of the equatorial Pacific Ocean to atmospheric forcing. *J. Phys. Oceanogr.*, **5**, 572–584.

Wyrtki, K. (1989): Some thoughts about the West Pacific Warm Pool. In: *Proc. of Western Pacific International Meeting and Workshop on TOGA COARE*, J. Picaut et al., Eds., pp. 99–109.

Yamasaki, M. (1969): Large-scale disturbances in a conditionally unstable atmosphere in low latitudes. *Pap. Meteor. Geophys.*, **20**, 289–336.

Zhang, C. (1997): Intraseasonal variability of the upper-ocean thermal structure observed at 0 degrees and 165 degrees E. *J. Climate*, **10**, 3077–3092.

Zhang, C. and H. H. Hendon (1997): Propagating and standing components of the intraseasonal oscillation in tropical convection. *J. Atmos. Sci.*, **54**, 741–752.

Zhang, C., H. H. Hendon, W. S. Kessler and A. J. Rosati (2001): Meeting summary: A Workshop on the MJO and ENSO. *Bull. Amer. Meteor. Soc.*, **82**, 971–976.

ISSN 0938 - 5177